Probing the Structure of Acetylcholinesterase Inhibitors in their Binding Site using Solid State Nuclear Magnetic Resonance

Scott Goodall

Submitted in partial fulfilment of the requirements for the

degree of Doctor of Philosophy

Christ Church, Oxford

Trinity 2002

Every attempt to employ mathematical methods in the study of chemical questions must be considered profoundly irrational and contrary to the spirit of chemistry … if mathematical analysis should ever hold a prominent place in chemistry, an aberration which is happily almost impossible, it would occasion a rapid and widespread degeneration of that science.

Auguste Comte (1798-1857)

Abstract

Probing the Structure of Acetylcholinesterase Inhibitors in their Binding Site using Solid State Nuclear Magnetic Resonance

Scott Goodall, DPhil Thesis

Christ Church, Trinity 2002

Inhibitors of acetylcholinesterase are of commercial and medical interest as pesticides and as therapeutics in the treatment of Alzheimer's Disease. An understanding of the conformation of inhibitors in the binding site enables the rational design of novel inhibitors with increased potency and specificity. Solid state NMR is a novel approach to the investigation of acetylcholinesterase and the binding of acetylcholinesterase inhibitors. Two compounds, 4-amino-5-fluoro-2-methyl-3-(3-trifluoroacetylbenzyl-oxymethyl)quinoline (R414425) and 4-amino-2-methyl-3-(3-trifluoroacetylbenzyl-oxymethyl)quinoline (R414983) were selected for study from a series of structures developed by Syngenta during research into novel pesticides. The series, based around a chimera of tacrine and *m*-(*N,N,N*-trimethylammonio)-2,2,2-trifluoroacetophenone, are ideal candidates for initial studies using solid state NMR since they demonstrate a high potency, have a large degree of conformational freedom and bind covalently to the enzyme at the active-site.

Both compounds, R414425 and R414983 were successfully synthesised with the incorporation of ^{13}C isotopic labels which, in conjunction with the fluorine atoms already present in their structures, provided the potential for homonuclear and heteronuclear distance measurements. The rotational resonance technique was used to determine ^{13}C-^{13}C distances in $^{13}C_5$-R414983 bound to *Electrophorus electricus* AChE. The reliability of distance measurements in the presence of broad spectral linewidths was first examined through the measurement of two rigid internuclear distances, indicating that an accuracy of 0.5 Å could be attained using linewidth based estimation of zero-quantum relaxation parameters. Subsequently, the internuclear distance for the benzyl methylene/2-methyl spin pair was determined to be 3.9 ± 0.5 Å and that for the benzyl methylene/quinoline C2 pair to be 3.5 ± 0.5 Å. The use of a rotational resonance echo showed a low level of zero-quantum relaxation under rotational resonance for one example pair of spins from $^{13}C_5$-R414983 bound to *Electrophorus electricus* AChE. ^{13}C-^{19}F REDOR experiments performed on a dilute rigid standard indicated that a carbon observed scheme where dephasing pulses were also applied to the carbon channel produced significantly more accurate results than similar schemes with dephasing pulses in the fluorine channel. ^{13}C-^{19}F REDOR was then utilised to quantify the separation of the trifluoromethyl function and the ^{13}C atom at the 2-methyl position in $^{13}C_5$-R414983 bound to *Electrophorus electricus* AChE, providing a distance of 7.1 ± 0.5 Å. The error level for each of the distance measurements is unfortunately high. However, modelling suggests that the determination of a single conformation for the bound inhibitor is restricted by the number of distance measurements presently available rather than the precision of the current values.

Significant progress has been made towards elucidation of the first structure for an inhibitor bound to *Electrophorus electricus* acetylcholinesterase and, for the first time, determination of the conformation of an inhibitor bound to acetylcholinesterase through a means other than x-ray crystallography.

Acknowledgements

A great number of individuals have contributed to this work in some way or another. The quick mention of these people, carefully tailored to fit in a single side of A4, doesn't really do justice to them. A reference to ten men in a boat comes to mind, but few people would understand that.

Financial support was provided in the form of a CASE studentship from the Engineering and Physical Sciences Research Council in collaboration with Syngenta. Terry Lewis, Peter Howe, John Taylor and Caroline Personeni from Syngenta supplied me with support and technical advice at various points, for which I am very grateful.

In addition to the opportunity and the infrastructure necessary to complete this work Tony has frequently exceeded his duties as a supervisor, supporting both my interests outside the lab and those of my wife.

A special thanks to those who provided advice on particular areas – Ian, Carsten, Rene, Vincent and Stephan. Paul has helped with multiple sections and has always given freely of his time, while making me do everything the long, hard, correct way. Other members of the lab, past and present, provided helpful discussions on many occasions.

Lastly, a big thanks to my family and friends, especially my parents who put in a lot of hard work over the last 27 years to get me to this point and my wife who has probably suffered more than me over the last few months.

Contents

Abstract ..... **iii**

Acknowledgements ..... **iv**

Abbreviations and Symbols ..... **ix**

Chapter 1 Introduction **1**

1.1 Biological Membranes 1

1.2 Acetylcholine 3

1.2.1 Nerve Signalling 3

1.2.2 Cholinergic Signalling 5

1.3 Acetylcholinesterase 10

1.3.1 Nomenclature 10

1.3.2 Macromolecular Structure and Cellular Localisation 11

1.3.3 Structure of Catalytic Subunits 13

1.3.4 Non-cholinergic Roles of Acetylcholinesterase 19

1.3.5 Acetylcholinesterase Inhibition 19

1.4 Nuclear Magnetic Resonance 21

1.4.1 The NMR Spectrum 21

1.4.2 Solid State NMR 25

1.5 Solid State NMR and Acetylcholinesterase 29

1.6 Project Aims 36

Chapter 2 Synthesis of Labelled Inhibitors **38**

2.1 Overview 38

2.2 Introduction 39

2.2.1 Synthetic Route 39

2.2.2 Labelling Schemes 40

2.2.3 Internuclear Distance Constraints 42

2.3 Synthesis 43

2.3.1 General 43

2.3.2 Synthesis of 4-amino-5-fluoro-2-methyl-3-(3-trifluoroacetylbenzyl-oxymethyl)quinoline (R414425) 43

2.3.3 Synthesis of $^{13}C_5$-4-amino-5-fluoro-2-methyl-3-(3-trifluoroacetylbenzyl-oxymethyl)quinoline ($^{13}C_5$-R414425) 48

2.3.4 Synthesis of 4-amino-2-methyl-3-(3-trifluoroacetylbenzyl-oxymethyl)quinoline (R414983) 52

2.3.5 Synthesis of $^{13}C_5$-4-amino-2-methyl-3-(3-trifluoroacetylbenzyl-oxymethyl)quinoline ($^{13}C_5$-R414983) 56

2.4 Discussion 61

Chapter 3 Characterisation of Inhibitors 63

3.1 Overview 63

3.2 Introduction 64

3.2.1 Acetylcholinesterase Activity Assays 64

3.2.2 Chemical Shift Investigation 65

3.3 Methodology 71

3.3.1 Acetylcholinesterase Assays 71

3.3.2 Solution NMR Experiments 73

3.3.3 Solid-Sate NMR Experiments 74

3.4 Results 78

3.4.1 Activity Assays 78

3.4.2 NMR 83

3.5 Discussion 97

Chapter 4 Rotational Resonance Investigation of $^{13}C_5$-R414983 Bound to Acetylcholinesterase 99

4.1 Overview 99

4.2 Introduction 100

4.2.1 Homonuclear Recoupling 100

4.2.2 Rotational Resonance 101

4.2.3 Data Analysis and Modelling of Distances 107

4.2.4 Rotational Resonance Echos 110

4.3 Methodology 111

4.3.1 Sample Preparation 111

4.3.2 NMR Experiments 112

4.4 Results 114

4.4.1 T_2 Measurement (Hahn Echo) 114

4.4.2 Rotational Resonance 117

4.4.3 Zero-quantum Relaxation Measurement 128

4.5 Discussion 132

Chapter 5 Rotational-Echo Double-Resonance Experiments 137

5.1 Overview 137

5.2 Introduction 138

5.2.1 Heteronuclear Recoupling Methods 138

5.2.2 Rotational-Echo Double Resonance 139

5.3 Methodology 146

5.3.1 Sample Preparation 146

5.3.2 NMR Experiments 147

5.4 Results 149

5.4.1 REDOR Standard 149

5.4.2 $^{13}C_5$-R414983 Bound to Acetylcholinesterase 154

5.5 Discussion....156

Chapter 6 Modelling of R414983 Bound to Acetylcholinesterase 159

6.1 Overview....159

6.2 Introduction....160

6.2.1 Computational Studies on Acetylcholinesterase....160

6.2.2 The Binding of TMTFA and Tacrine to Acetylcholinesterase....164

6.3 Methodology....167

6.3.1 Molecular Dynamics Simulations....167

6.3.2 NMR Restrained Conformations....170

6.4 Results....170

6.4.1 Molecular Dynamics Simulations....170

6.4.2 NMR Restrained Conformations....174

6.5 Discussion....175

Chapter 7 Conclusions....179

7.1 General Conclusions....179

7.2 Future Experiments....181

Bibliography....184

APPENDICES

Appendix 1 – Acetylcholinesterase Publications....206

Appendix 2 – Published Acetylcholinesterase Structures and Species Homology....207

Appendix 3 – Acetylcholinesterase Inhibitors....212

Appendix 4 – Solution NMR Spectra....214

Appendix 5 – Error Analysis....218

Abbreviations and Symbols

ACh	acetylcholine
AChBP	acetylcholine binding protein
AChE	acetylcholinesterase
AChR	acetylcholine receptor
ATCh	acetylthiocholine
b_{IS}	dipolar coupling between nuclear spins I and S
br	broad
BuChE	butyrylcholinesterase
CAT	choline acetyltransferase
CP	cross-polarisation
CSA	chemical shift anisotropy
CW	continuous wave decoupling
d	doublet
*Dm*AChE	*Drosophila melanogaster* acetylcholinesterase
DMF	dimethylformamide
DTNB	5,5'-dithiobis(2-nitrobenzoic acid)
*Ee*AChE	*Electrophorus electricus* acetylcholinesterase
FAS II	fasciculin II inhibitory peptide
FID	free induction decay
GPCR	G-protein coupled receptor
GPI	glycosylphosphatidylinositol
hAChE	human acetylcholinesterase
HPLC	high performance liquid chromatography
$\boldsymbol{I}$	spin quantum number
m	multiplet

$\boldsymbol{m}$	magnetic quantum number
$\boldsymbol{M_0}$	initial net magnetisation
mAChE	mouse acetylcholinesterase
mAChR	muscarinic acetylcholine receptor
MAS	magic angle spinning
*Md*AChE	*Musca domestica* acetylcholinesterase
MD	molecular dynamics
n	a small integer number
nAChR	nicotinic acetylcholine receptor
NMR	nuclear magnetic resonance
q	quartet
r	internuclear distance
R2	rotational resonance
R2TR	rotational resonance in the tilted rotating frame
R404435	4-amino-5-fluoro-2-methyl-3-(3-trifluoroacetylbenzyl-thiomethyl)quinoline
R414425	4-amino-5-fluoro-2-methyl-3-(3-trifluoroacetylbenzyl-oxymethyl)quinoline
R414983	4-amino-2-methyl-3-(3-trifluoroacetylbenzyl-oxymethyl)quinoline
R415657	4-amino-5-fluoro-2-methyl-3-(3-trifluoroacetylbenzyl-methoxymethyl)quinoline
REDOR	rotational echo double resonance
RMSD	root mean square deviation
s	singlet
SSNMR	solid state nuclear magnetic resonance
t	triplet
T_2	transverse relaxation rate
T_2^{ZQ}	zero-quantum relaxation rate
T_r	rotor period
TBDMS	*tert*-butyldimethylsilyl

*Tc*AChE	*Torpedo californica* acetylcholinesterase
TFA	trifluoracetic acid
THF	tetrahydrofuran
TMTFA	*m*-(*N,N,N*-trimethylammonio)-2,2,2-trifluoroacetophenone
TPPM	two-pulse phase modulated proton decoupling
γ	gyromagnetic ratio
η	asymmetry parameter
$\Delta\sigma$	shielding anisotropy
τ_m	mixing time
$\Delta\omega_{IS}$	isotropic chemical shift difference between nuclear spins I and S
ω_{iso}	isotropic chemical shift frequency
ω_r	sample spinning frequency

Chapter 1 Introduction

1.1 Biological Membranes

Biological membranes play an essential role in the life-cycle of all organisms. Far from being a passive means of keeping cells and organelles intact as independent structures, membranes are highly dynamic, allowing complex interactions with the surrounding environment through the selective transfer of nutrients and chemical signals across the membrane.

Membranes are formed through a bilayer arrangement of amphipathic lipids such that the polar headgroups remain exposed to the aqueous environment of the interior or exterior, while the hydrophobic chains orient towards the membrane core. The resulting asymmetric environment is highly impenetrable to ions and polar molecules. However, membrane associated proteins are capable of modulating the local properties of the bilayer.

Early membrane models, in which it was believed that membrane proteins were positioned simply to either side of the lipid bilayer [1], have been superseded by the fluid mosaic model of biological membranes [2] (Figure 1.1). In this case, the lipid bilayer is considered to behave as a two-dimensional fluid where components can diffuse freely within the plane of the membrane, although movement through the membrane and movement from one leaflet of the membrane

to the other is restricted. Membrane proteins may be categorised into two groups – integral and peripheral. Integral proteins have one or more domains which pass through the entire width of the bilayer; peripheral proteins are associated with the membrane through interactions with lipid headgroups or integral membrane proteins, or by covalent attachment through anchors.

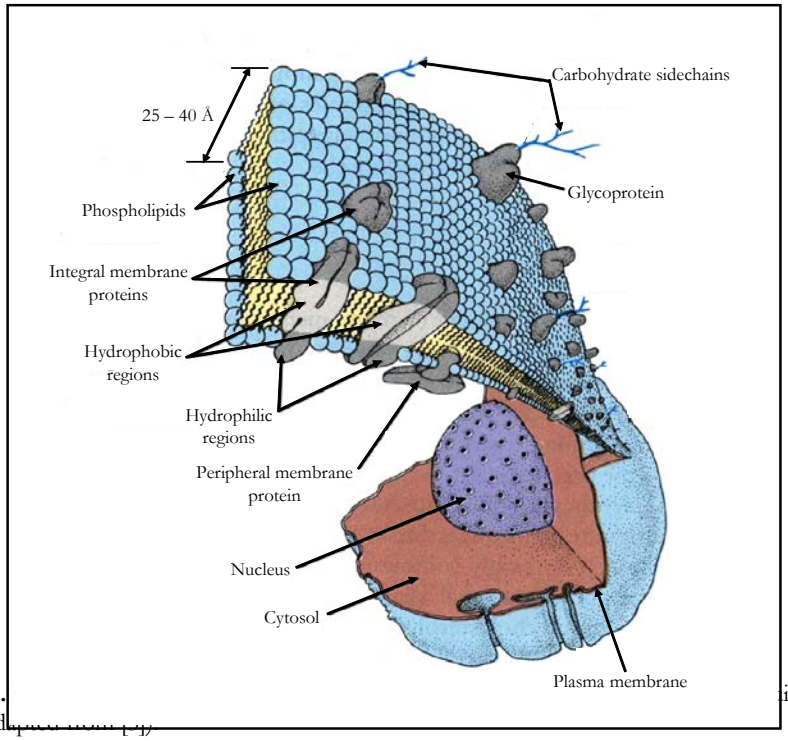

Figure 1. id mosaic model (ad

Recent research has suggested the existence of an additional level of complexity through the concept of lateral heterogeneities known as rafts [4], where increased local protein, sphingolipid and cholesterol compositions may be implicated in the formation of rigid domains.

Between 30% and 50% of most genomes are believed to encode for membrane proteins [5], the polypeptide macromolecules that mediate and control membrane related activities through their roles as channels, pumps, receptors and enzymes. It is estimated that 80% of all cellular

responses are triggered by membrane proteins [6] and it is therefore not surprising that more than 45% of all potential drug targets are expected to be membrane proteins [7]. The structure of these proteins and the mechanisms by which they function is a major area of current research.

1.2 Acetylcholine

1.2.1 Nerve Signalling

The general impermeability of biological membranes to the flow of ions enables the creation of a potential difference or polarisation across the cell membrane. This potential difference, which is demonstrated in all cells and is in the order of -50 mV, can be accounted for by the relative distribution of intracellular and extracellular ions. The application of a depolarising potential across a typical cell membrane will produce a passive and proportional change in the degree of cell polarisation.

A similar response occurs when a depolarisng potential is applied to a nerve cell. However, at a particular threshold value, known as the action potential, a rapid self-sustaining depolarisation is initiated which results in a partial reversal of the resting polarisation state. The transmission of nerve impulses occurs through the propagation of membrane depolarisation along the cell, a feature which is characteristic of nerve cells only.

The arrival of a nerve impulse at a synapse or neuro-muscular junction does not automatically result in the onward transmittance of the impulse, which is generally mediated through the release of transmitter chemicals. Neurotransmitters cover a diverse range of chemical compounds from simple amines (such as dopamine) and amino acids (such as γ-aminobutyric acid) to polypeptides (such as the enkephalins).

In the idealised case (Figure 1.2), the impulse approaches the pre-synaptic terminus along the axon of the pre-synaptic cell, propagated by depolarisation of the membrane. When an action potential reaches the terminal of a pre-synaptic cell, voltage-gated calcium channels are opened. The resulting influx of calcium ions stimulates the exocytosis of synaptic vesicles (400-1200 Å in diameter) which contain the transmitter chemical. These vesicles then fuse with the pre-synaptic membrane, releasing the transmitter into the synaptic cleft (local concentrations of neurotransmitters up to 0.3 mM have been observed [8]).

Binding of the transmitter to post-synaptic receptors subsequently modulates the ion permeability properties and polarisation state of the post-synaptic membrane. If the post-synaptic membrane is depolarised to the threshold of the action potential, an impulse will be generated in the post-synaptic cell which will then be propagated onwards. Transmitter chemicals are recovered, typically through a high affinity active transport system, by the pre-synaptic cell and by neighbouring glial cells [9].

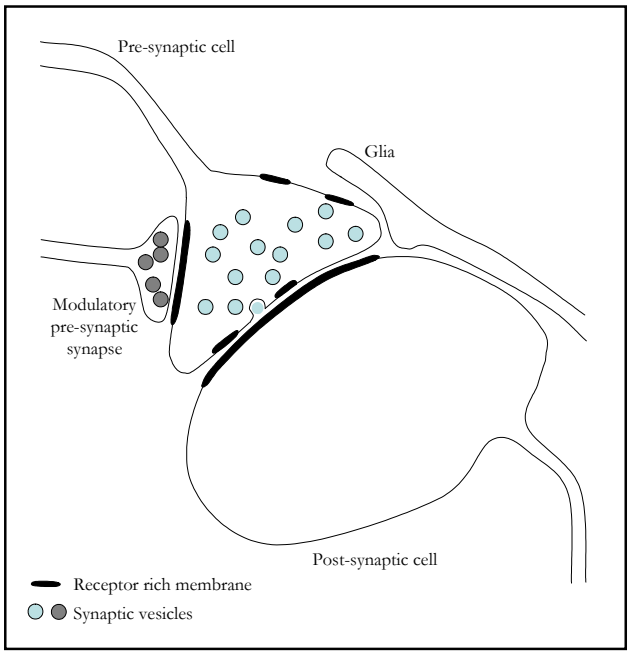

Figure 1.2 – Illustration of an idealised synaptic junction.

It should be noted that the process of signalling is extremely complex:

- Nerve cells do not exist in isolation and the action potential can be achieved through the summation of many contributing factors each of which can be either depolarising or hyperpolarising (neurotransmitters released by distant synapses may reach the local area through intercellular spaces).
- The quantity of transmitter released by the pre-synaptic cell can be modulated through feed-back mechanisms from pre-synaptic receptors [10] or by stimuli (either up or down regulation) from neighbouring nerve cells.
- The persistence of the chemical effects of a transmitter is not only controlled by the rate at which it is recovered both by the pre-synaptic cell and by surrounding glial cells, but also can be modulated through the presence of soluble proteins which bind the transmitter [11].
- The post-synaptic response of the cell to the transmitter is dependent on the number and nature of target receptors – simple, but fast reacting ionophores or slower coupled receptors which have the ability to magnify responses – and whether binding to the particular receptors promotes a depolarisation or hyperpolarisation.
- Finally, the presence of other transmitter or neuromodulator may produce conditional responses (allosteric effects) in the post-synaptic receptors.

1.2.2 Cholinergic Signalling

Acetylcholine (ACh) is one example of a neurotransmitter and is involved in the transfer of nerve impulses across synapses both in the central nervous system and at neuromuscular junctions. ACh is an ester (Figure 1.3) formed through a transesterification reaction of choline with acetyl CoA, a process catalysed by the enzyme choline acetyltransferase (CAT).

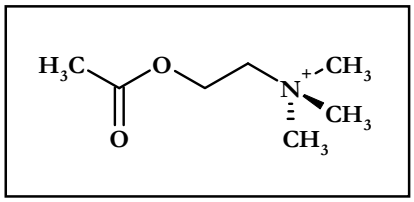

Figure 1.3 – Acetylcholine (ACh).

Two classes of acetylcholine binding receptor exist, identified on the basis of their response to stimulus from muscarine (an alkaloid found in the mushroom *Amanita muscaria*) or from nicotine. In the central nervous system, the muscarinic acetylcholine receptor (mAChR) is implicated in motor control, temperature regulation, cardiovascular regulation and memory; in the periphery it is involved in smooth muscle contraction, glandular secretion and modulation of both cardiac rate and force. Each of the five muscarinic receptor sub-types (M_1-M_5) display the seven transmembrane helix motif (based upon sequence directed structural modelling) which is common among the G-protein coupled receptor family (GPCR) to which they belong. Ligand binding occurs within the outer regions of the transmembrane segment of the protein [12]. Although detailed kinetic and mutation investigations have been performed, there is little direct structural information available for mAChR. To date, x-ray crystallographic studies on GPCRs have been successful only in the case of the dark-state of rhodopsin [13], a single example from a family which includes over 2000 members [14] and is encoded for by ~1% of the mammalian genome.

Nicotinic acetylcholine receptors (nAChR) are cation-selective, ligand-gated ion channels formed from five separate subunits. They belong to a superfamily of ligand-gated channels which includes the 5-HT_3, $GABA_A$, $GABA_C$ and glycine receptors [8]. A number of subunit types exist (designated α, β, γ and δ) and the exact stoichiometry of these depends upon the receptor source. The 'muscle receptor', found in neuromuscular junctions and in the electric organ of the electric ray *Torpedo californica*, comprises an α_2:β:γ:δ ratio, while neuronal receptors

can be homomeric (α_5) or heteromeric (α_2:β_3) [15]. It should be noted that each subunit type can be categorised into further sub-groupings. However, α subunits all possess two adjacent cysteine residues which are critical for acetylcholine binding while the remaining subunits do not [8].

Electron microscopy of tubular nAChR crystals from *Torpedo californica* has provided a valuable insight into the structure of the receptor and the changes which occur upon ligand binding. Early investigations of the receptor in the open and closed states [17, 18] suggest that the channel is activated by binding of ACh within pockets located in the extracellular domains of the α subunits. Ligand binding induces a subtle rotation of the subunits, thereby altering the configuration of the pore-lining M2 helix segments and creating a continuous ion-conducting path across the membrane. More recent work [16], which is approaching atomic resolution, reaffirms this mechanism and indicates how electrostatic interactions may be involved in the guidance of cations through the pore (Figure 1.4).

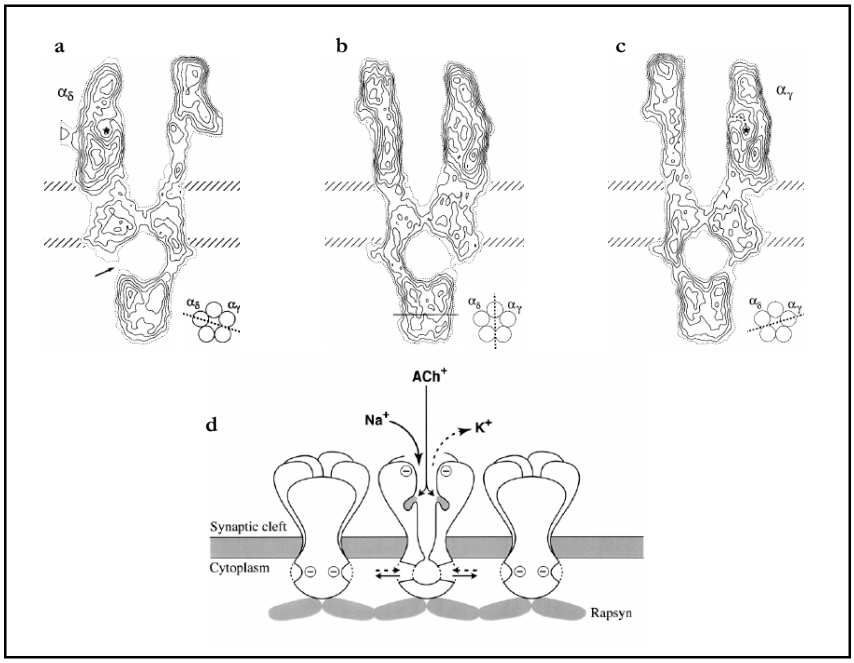

Figure 1.4 – The nicotinic acetylcholine receptor: slices through the electron microscopy density map (a) – (c), schematic illustration of the receptor structure (d) [16].

Acetylcholine molecules are believed to pass through the central vestibule before entering tunnels which lead to their binding sites. The two binding sites can be distinguished both kinetically and in the shape of their associated cavities [16] (Figure 1.5).

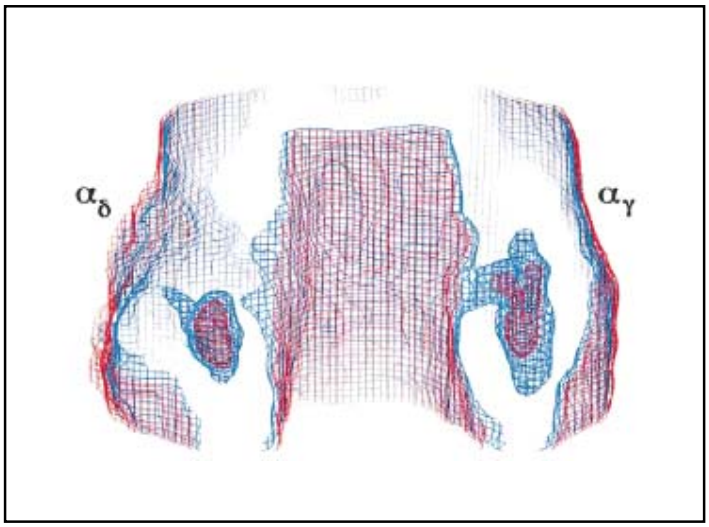

Figure 1.5 – Acetylcholine binding pockets in the nicotinic acetylcholine receptor [16].

Although the resolution of electron microscopy data is insufficient to provide an insight into the mechanism by which ACh binds, methods such as solid-state nuclear magnetic resonance have been used to probe the environment, orientation and dynamics of bound ACh and its analogue bromoacetylcholine [19, 20]. Additionally, the recent x-ray crystal structure (2.7 Å resolution) [15] of a soluble acetylcholine binding protein (AChBP), which is homologous to the extracellular domain of the nicotinic receptor, has determined the arrangement of amino-acids in the region of the binding site (Figure 1.6). Principal binding site residues are located on loop regions within an α subunit, while a number of complementary residues are present on a section of β-sheet from the neighbouring subunit.

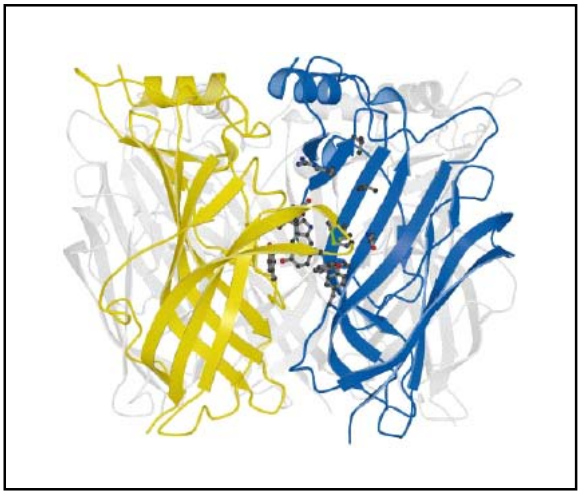

Figure 1.6 – The acetylcholine binding protein: The secondary structure of two subunits is represented in yellow and blue with binding site residues shown in ball and stick form (coloured by atom type). Principal residues are located on the loops of the yellow subunit, although a number of complementary residues are present on the β-sheet of the blue subunit [15].

Receptor responses to ACh binding may be either depolarising or hyperpolarising; both the muscarinic and nicotinic receptors have been implicated in each of these response types [9].

Over 1,000 signals can be transmitted across a synapse each second [21], therefore it is essential that once a signal transmission has occurred the system is reset in the minimum possible period of time. In contrast to other transmitter chemicals, ACh is not directly recovered from synapses by a high-affinity transport system but is first hydrolysed by the enzyme acetylcholinesterase (AChE) before the reuptake of choline and acetate.

AChE is a highly efficient catalyst with a turnover number in the order of 16,000-25,000 s^{-1} [21, 22], a rate approaching the limits imposed by the diffusion of substrate and an enhancement by a factor of 2×10^{13} over the hydrolysis rate in aqueous solution. The obvious importance of AChE in cholinergic signalling has made it the focus of a substantial research effort utilising a range of methodologies, in particular x-ray diffraction [23-48], molecular modelling and simulations [49-67], mutation experiments and kinetics studies [46, 68-91], and the design, synthesis and evaluation of novel inhibitors [43, 60, 92-111]. Relatively minor use

has been made of other techniques, although electron paramagnetic resonance [112], fluorescence spectroscopy [81, 87], atomic force spectroscopy [113], mass spectrometry [114] and solution NMR [115-120] have all contributed to the characterisation of AChE. Appendix 1 shows a summary of the number of acetylcholinesterase related publications each year since 1981.

1.3 Acetylcholinesterase

1.3.1 Nomenclature

Substrate specificity and susceptibility to certain inhibitors varies between cholinesterases from different species. Additionally, a number of species can exhibit more than one type of cholinesterase and in such cases these forms are differentiated by their catalytic properties, inhibition specificities and tissue distributions.

Enzymes which preferentially hydrolyse acetyl esters (such as ACh or acetyl-β-methylcholine) are typically described as acetylcholinesterases, while those which demonstrate a preference for other types of esters (such as butyrylcholine or propionylcholine) are termed butyrylcholinesterases (BuChE). This terminology can be misleading, particularly in the case of non-mammalian enzymes, since a number of exceptions exist. For example, chicken brain acetylcholinesterase hydrolyses both propionylcholine and acetyl-β-methylcholine faster than ACh (butyrylcholinesterases are generally incapable of hydrolysing acetyl-β-methylcholine) [9]. *Drosophila melanogaster* shows a single form of cholinesterase and is classified as an acetylcholinesterase (*Dm*AChE). While efficiently hydrolysing butyrylcholine, *Dm*AChE also displays a number of features which are characteristic of acetylcholinesterases only: it is present in the central nervous system where it is involved in acetylcholine metabolism; it also

demonstrates concentration dependent substrate activation and inhibition (these typical AChE features are discussed later) [68].

No physiological function has been ascribed to butyrylcholinesterase [121]. Individuals lacking the enzyme show no ill effects other than an inability to recover independently from treatment with the anaesthetic succinylcholine [22].

1.3.2 Macromolecular Structure and Cellular Localisation

AChE displays a high degree of polymorphism, derived from alternative splicing from a single gene[*], catalytic subunit oligomerisation and associations with non-catalytic subunits. Three types of catalytic subunit have been found, designated $AChE_S$, $AChE_H$ and $AChE_T$; these differ in their C-terminal functionality, although are based around a conserved core (543 amino acids in humans [123]). A wide range of quaternary structures and methods of membrane attachment result from different post-translational processing of these subunits.

$AChE_S$, which lacks the capacity to form inter-subunit disulphide links, exists only as a soluble monomer (G1) [124]. $AChE_H$ produces a glycophosphatidylinositol (GPI) anchored protein, which may exist either as a membrane associated monomer (G1a-Type I) or disulphide linked dimer (G2a-Type I) [22, 121, 124]. The final subunit type, $AChE_T$, shows the greatest number of quaternary structures, including amphiphilic monomers (G1a-Type II) and dimers (G2a-Type II), soluble tetramers (G4 or G4na), hydrophobic tetramers which have an additional P-subunit (G4a), and large collagen-tailed forms of one to three tetramers (A4, A8 and A12) [22, 121, 124, 125]. Tetramers are formed by electrostatic and hydrophobic interactions between two disulphide bonded dimers (Figure 1.7).

[*] Invertebrates have been found with up to three genes for AChE. Pesticide resistance in some insects has been attributed to a duplication of the AChE gene [122].

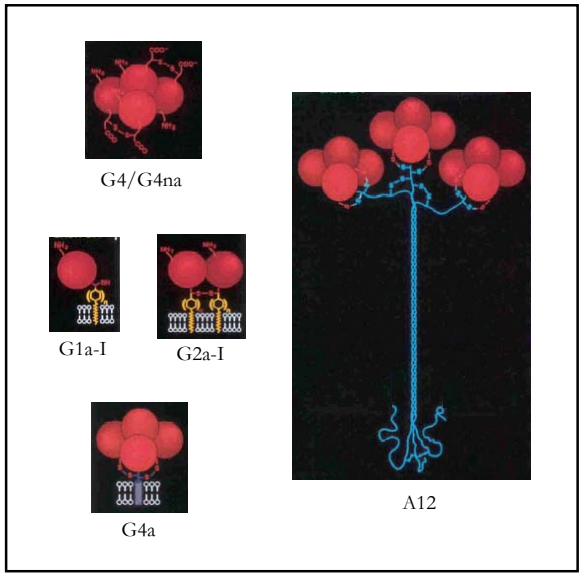

Figure 1.7 – Acetylcholinesterase quaternary structures (adapted from [22]).

Glycophosphatidylinositol anchored AChE from *Torpedo californica* (*Tc*AChE) and human erythrocytes (hAChE) were among the first proteins involved in the characterisation of GPI anchors [126, 127]. A number of studies have shown that the GPI anchor is responsible for routeing to the extracellular leaflet of the membrane and positioning within cholesterol rich regions [128, 129]. Species diversity exists in both the type (alkyl or acyl) and number of lipidic chains involved in the GPI anchor, which can effect their susceptibility to phosphatidylinositol specific phospholipases during attempts at AChE purification [130].

The predominance of particular AChE forms differs not only between species, but also depending on tissue type, developmental stage and external stress factors. The soluble G1 form has been found in the venom of Elapid snakes [124], is expressed in human embryonic and tumour cells, but can also be induced by psychological stress or the presence of AChE inhibitors [123]. *Dm*AChE exhibits only one form, the G2a-Type I amphiphilic GPI anchored dimer [68, 121] (mammalian erythrocytes also demonstrate the G2a-Type I form, although the physiological function of AChE in such cells remains unclear [121]). The hydrophobic G4a

tetramer is the main form in the mammalian central nervous system (70-90% of AChE activity) where it is attached to presynaptic and postsynaptic membranes [121]. Asymmetric collagen-tailed forms are predominant at mammalian neuromuscular junctions [121, 131] and in the electric organ of *Electrophorus electricus* (*Ee*AChE) [34]. In spite of the complex variation in the gross structure and distribution of macromolecular forms, the catalytic activity of each subunit is conserved [121].

1.3.3 Structure of Catalytic Subunits

In 1991 the crystal structure of *Tc*AChE (Figure 1.8) was solved to 2.8 Å resolution [31], revealing a number of interesting structural features of the enzyme.

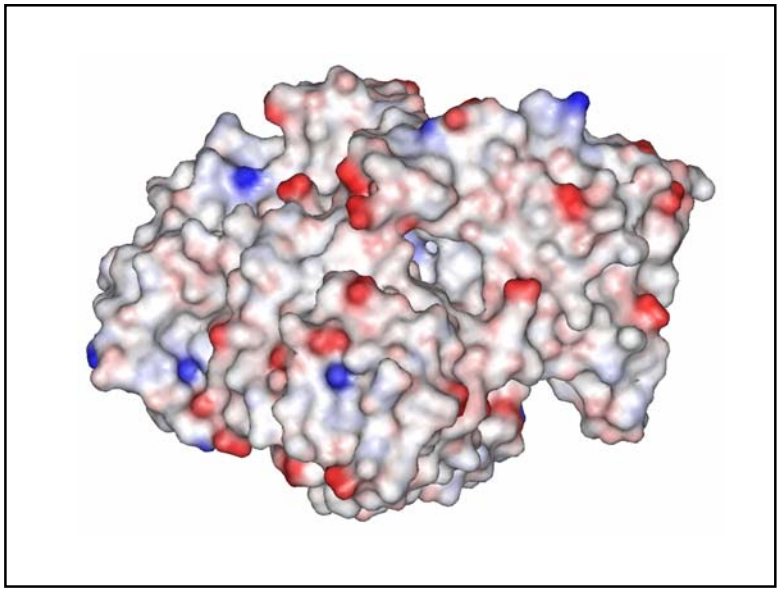

Figure 1.8 – *Torpedo californica* acetylcholinesterase: created from the PDB file 2ACE, showing the solvent accessible surface for a 1.4 Å probe on a single catalytic subunit. The surface is coloured by electrostatic potential – negative potential is shown in red, positive potential in blue.

The enzyme is an α/β hydrolase (containing 537 amino acid residues in the *Tc*AChE form), arranged as a 12-stranded β-sheet surrounded by 14 α-helices (Figure 1.9). The protein is ellipsoidal in shape, with approximate dimensions of 45 Å by 60 Å by 65 Å. Considering the

high turnover of the enzyme, it is surprising that the active site is located around 20 Å from the protein surface, near the base of a narrow gorge lined with 14 aromatic amino acids [31].

Figure 1.9 – *Torpedo californica* acetylcholinesterase secondary structure: created from the PDB file 2ACE, showing the secondary structural motifs of a single catalytic subunit. α-helices are shown as red cylinders, β-sheet as blue arrows. The catalytic triad (Ser200, His440, Glu327) is shown by green stick models.

The active site of *Tc*AChE consists of a number of important sub-sites, namely:

- The esteratic site, comprising the catalytic triad (Ser200, His440 and Glu327[†]) [31]. Substrates bind covalently to the active site serine while the histidine and glutamic acid residues act as proton acceptors/donors during the hydrolysis process. The reaction proceeds through an unstable tetrahedral intermediate state to produce an acetyl-enzyme (releasing choline), before a further tetrahedral intermediate stage returns the enzyme to its initial free form (releasing acetate).

† Unless otherwise stated in the text, it may be assumed that all residue numbering corresponds to the *Tc*AChE amino acid sequence.

- The oxyanion hole (Gly118, Gly119 and Ala201), involved in stabilising tetrahedral intermediates [31].
- An acyl pocket (Phe288 and Phe290), responsible for interactions with the substrate acetyl function [27].
- An anionic binding site (Trp84 and Phe330) where the quaternary ammonium of ACh and other active site ligands interact with the π electrons of aromatic groups [27, 31].

A peripheral ligand binding site also exists (Tyr70, Asp72, Tyr121, Glu199, Trp279 and Phe290) [94], about 14 Å from the active site, near the rim of the gorge. Ligand association at the peripheral site may lead to enzyme inhibition if the entrance of substrate is blocked either by steric hindrance [77, 78] or by charge repulsion (in the case of cationic ligands). Inhibition by an allosteric mechanism which alters the active site conformation has also been proposed [74, 79, 82, 91, 112].

Substrate inhibition has been shown at high concentrations of ACh (> 1 mM, significantly higher than those encountered physiologically), which has been attributed to the binding of ACh at the peripheral site, impeding the release of reaction products from the gorge [68, 72, 77]. However, at lower concentrations of ACh, substrate binding at the peripheral site can lead to an activation of the enzyme [68, 77], due to a combination of allosteric effects which alter the properties of the catalytic site [87, 89] and the transient binding of the substrate *en route* to the catalytic site [77, 84]. Acetylthiocholine has been shown to bind to Asp74 at the peripheral site (human AChE numbering, equivalent to Asp72 in *Tc*AChE) as an initial step towards hydrolysis [82].

Further evidence for the presence of allosteric mechanisms is found in the binding of ligands at the catalytic site, which alters the environment of a surface loop (Cys69-Cys96 in mouse

AChE) located near the mouth of the gorge [90] and alters the properties of a fluorescent marker bound at the peripheral site [87].

Crystal structures suggest that at one point the gorge is too narrow to accommodate a molecule of ACh [50], due to steric hindrance from the aromatic rings of Tyr121, Phe290, Phe330 and Phe331, positioned 12-14 Å from the bottom of the gorge [49, 56]. Molecular dynamics simulations have suggested that these residues form a gate to the active site which opens and closes rapidly [61, 66]. Despite the gate being open between 2.4% [56] and 20% [66] of the time in simulations, it slows ACh binding by only a factor of two, yet confers significant selectivity of substrates [56]. BuChE does not exhibit ligand gating due to substitution of the large aromatic amino acids in the gate region by residues with smaller side chains. Mutagenesis experiments have shown that replacement of appropriate residues in the gate and active site regions of human AChE results in an activity profile which closely resembles that of human BuChE [88]. Figure 1.10 illustrates the positions of the catalytic triad, gate region and peripheral binding site.

Analysis of electrostatic potentials within and around the enzyme shows a combination of a net negative charge under physiological conditions and a significant dipole orientated along the gorge axis. These potentials result in the attraction of the cationic substrate at medium distances and a steering of the molecule towards and down the active site gorge when within shorter range of the protein, providing up to an 80-fold increase in reaction rate compared to models of the enzyme without the dipole [52, 53, 59, 86]. A number of negatively charged groups are located on the protein surface in the region of the gorge entrance. The effect of decreasing surface charges by mutagenesis on the kinetics of substrate hydrolysis has been shown to be minimal [75], since only 40% of the dipole magnitude is dependent upon contributions from surface charges [49].

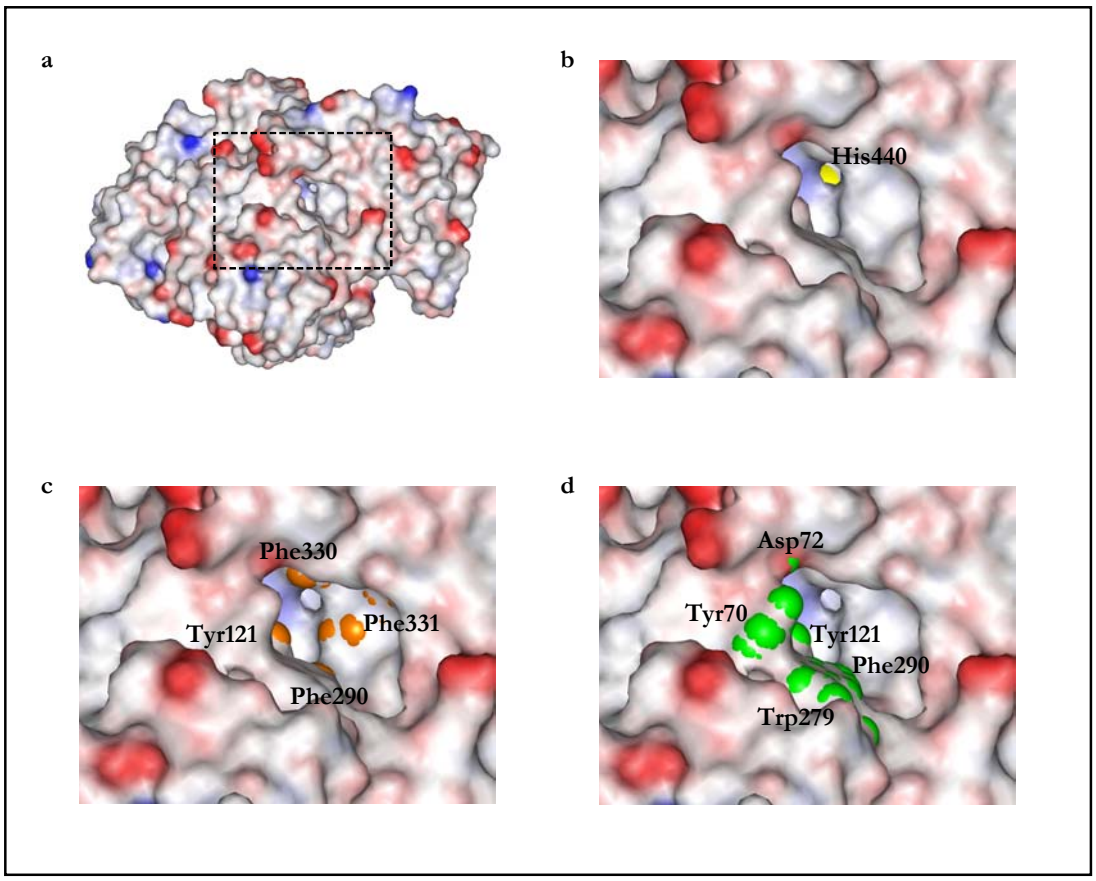

Figure 1.10 – The *Torpedo californica* acetylcholinesterase active site, gate region and peripheral binding site: created from the PDB file 2ACE, showing the solvent accessible surface on a single catalytic subunit for a 1.4 Å probe. The surface is coloured by electrostatic potential, negative potential is shown in red, with positive potential shown by blue. Complete structure (a); the catalytic triad - indicated in yellow, only His440 is visible from this position (b); the gate region - indicated in orange (c); the peripheral binding site - indicated in green (d).

Molecular dynamics (MD) simulations indicate that additional routes to the active site may exist. During simulations, openings large enough to accommodate water molecules have been observed near Trp84, which is situated close to the protein surface [51, 61]. The crystal structures of fasciculin II (FAS II) bound to AChE show the inhibitory peptide completely blocking access to the active site gorge [27, 28], although a residual esterase activity can still be measured [74] (this result was later questioned [91]). Recent molecular dynamics simulations of the acetylcholinesterase/FAS II complex suggests that fasciculin binding promotes the transient opening of multiple routes to the active site which do not involve the main gorge

entrance [63]. Further evidence is found in the crystal structure of *Tc*AChE bound to Mf268 (a physostigimine analogue), where the alkyl chain of one hydrolysis product is found along the upper part of the gorge, blocking access to the active site. However, the bulky eseroline hydrolysis product (released subsequently) is not present within the structure, suggesting that it may have been released through a route other than the main gorge [35].

Crystallographic studies have now been published on AChE from a range of species and a number of AChE/inhibitor complexes, demonstrating that the protein maintains a relatively consistent structure in the enzymes from: *Drosophila melanogaster* [38], *Electrophorus electricus* [34] human [23], mouse [28, 33] and *Torpedo californica* [24-27, 30-32, 35-37, 40-47]. The only significant conformational change observed in the crystal structure of *Tc*AChE bound to the four inhibitors decamethonium, edrophonium, huperzine and tacrine is the orientation of the phenyl sidechain of Phe330 [58]. Edrophonium, huperzine and tacrine bind at the active site [24, 30], whereas decamethonium spans both the active and peripheral sites [30]. Recently, the binding of Huperzine derivatives has provided evidence for the rearrangement of residues within the active-site [48]. Appendix 2 includes a list of published AChE structures available from the Brookhaven Protein Database (Table A2.1) and a list of structures currently awaiting release (Table A2.2).

Amino acid substitutions which have occurred in certain species can lead to changes in activity and in inhibitory characteristics, such as the low binding affinity of fasciculin to avian or insect AChE when compared with mammalian AChE [30, 38], the different properties of greenbug AChE compared with those of many other insect species [132], and benzenesulfonyl fluoride inhibition of mouse AChE but not the *Torpedo californica* enzyme. Figures A2.1 [22] and A2.2 [99], in Appendix 2, illustrate the sequence homology between a range of species, which accounts for these observations.

1.3.4 Non-cholinergic Roles of Acetylcholinesterase

AChE has been implicated in a number of non-cholinergic roles such as cell proliferation, differentiation and responses to stress. The homology of AChE to cell adhesion proteins, gliotactin, gluctactin and the neurexins may form the basis of these implied functional similarities [123, 133-135].

An increased concentration of AChE is observed in the plaques associated with Alzheimer's Disease and AChE has been shown to accelerate the assembly of amyloid-β-peptides into toxic Alzheimer's fibrils. It has been suggested that an area of the protein surface situated near the peripheral site may be responsible for this action, since peripheral site ligands can inhibit fibril formation [136, 137].

The selective synthesis of potent inhibitors has been achieved through combinatorial methods, where a pool of small precursor compounds are allowed to bind with acetylcholinesterase before reaction *in situ* to create a larger molecule [138]. Non-biological applications of the enzyme include the development of sensors for the detection of specific insecticide residues [139]. The high catalytic efficiency of AChE has also prompted attempts to develop smaller non-protein mimics of the catalytic site [140].

1.3.5 Acetylcholinesterase Inhibition

1.3.5.1 Pesticides

The discovery of organophosphate compounds, the first potent synthetic AChE inhibitors, introduced a new era in both chemical weapon and pesticide development. As an enzyme critical to basic life functions, potent AChE inhibitors have an obvious role. A number of pesticide formulations containing AChE inhibitors are currently in commercial use [38], many of which show structural similarity to the original organophosphate nerve agents.

Organophosphates first bind as a trigonal bipyramidal intermediate with the catalytic serine of AChE. This initial structure may persist for a period of days, and in some circumstances may be reversed by the administration of oximes [141]. A hydrolysis process, known as aging, then leads to irreversible enzyme inhibition. Slow hydrolysis of the initial organophosphate complex to the aged form has been explained by steric exclusion, with the active site histidine being forced into a position unsuitable for catalysis [32].

Other pesticide inhibitors, such as the carbamates, bind covalently but reversibly to the active site, and thus are safer for handling and use than organophosphates.

1.3.5.2 Therapeutics

A number of medical disorders can be directly related to a dysfunction of the cholinergic system, or can be treated through modulation of cholinergic function using AChE inhibitors [30, 38]:

- Alzheimer's Disease is the most common form of dementia, with sufferers experiencing increasing impairment of memory, judgement and intellectual function [142]. Senile dementia of the Alzheimer's type has been linked to changes in cholinergic function, including changes in nAChR density, AChE activity and AChE polymorphism. With progressively longer lifespans, diseases such as Alzheimer's which develop later in life are likely to become a more significant problem in the future [40].

- *Myasthenia Gravis* is an incurable muscle disorder estimated to affect 3 in every 10,000 individuals. The muscle weakness is due to poor transfer of nerve impulses across neuromuscular junctions as a direct result of an abnormally low presence of ACh receptors (caused either by auto-immune response or genetic inheritance).

- Glaucoma is a specific pattern of optic nerve damage and visual field loss caused by a number of different eye diseases. Most, but not all, of these eye diseases are characterized by elevated intraocular pressure which may be relieved through treatment with mild AChE inhibitors.

The only compounds presently licensed by the Food and Drug Administration (FDA) for the symptomatic treatment of Alzheimer's Disease are AChE inhibitors (such as tacrine and donepezil) [143-145]. Tacrine binds to the active site of AChE [30], while donepezil binds along the gorge, interacting with both the active and peripheral sites [36, 40]. There is some evidence that AChE inhibitors may actually slow the development of the disease [142, 146-148], but also evidence that AChE may not be the only target of these drugs [149, 150]. The chemical structures for a range of AChE inhibitors are shown in Appendix 3.

1.4 Nuclear Magnetic Resonance

1.4.1 The NMR Spectrum

Nuclear magnetic resonance utilises nuclear spins as a probe to determine the magnetic environment of a nucleus. The behaviour of a spin system can provide an insight into bond angles, internuclear distances and the orientation of nuclei with respect to the external applied field.

The nuclear spin (***I***) can be related to a nuclear magnetic moment by:

$$\mu = \gamma \boldsymbol{I} \eta \qquad \text{Equation 1.1}$$

where: μ = nuclear magnetic moment
$\boldsymbol{I}$ = nuclear spin

γ = gyromagnetic ratio

$\hbar$ = Planck's constant divided by 2π

In the presence of a large externally applied magnetic field a number of orientations can be adopted, described by their magnetic quantum numbers ($\boldsymbol{m}$), which range from $-\boldsymbol{I}$, $-\boldsymbol{I}+1$, … through to $+\boldsymbol{I}$ (a total of $2\boldsymbol{I}+1$ possibilities). For example, in the simplest case of a spin-½ nuclei two alignments exist, parallel and antiparallel to the applied field.

The energy level associated with each alignment differs and, as such, at equilibrium a population difference will exist between states. This population difference produces an overall net magnetisation ($\mathbf{M_0}$), which can be perturbed into a non-equilibrium arrangement through the application of radio-frequency pulses. The subsequent precession of magnetisation around the z-axis as it returns to equilibrium is detected and Fourier transformation translates this time domain information into the frequency domain typically used for the presentation of NMR data (Figure 1.11 represents this procedure for a single isolated spin using both vector and product operator formalisms).

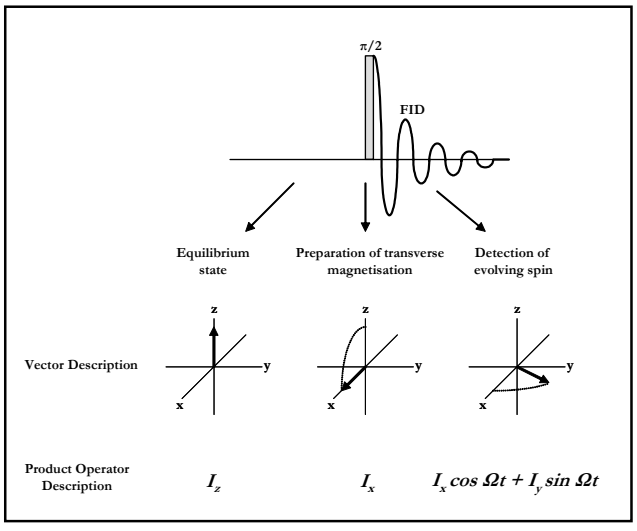

Figure 1.11 – Nuclear spin behaviour during a one pulse experiment (adapted from [151]).

The precise nature of the magnetisation behaviour is dependent upon both internal nuclear properties and external interactions which are characteristic of the spin system under study, and can be described using the general nuclear spin Hamiltonian [152]:

$$H_{TOTAL} = H_Z + H_{CS} + H_J + H_D + H_Q \qquad \text{Equation 1.2}$$

where:
H_Z = Zeeman Hamiltonian
H_{CS} = chemical shift Hamiltonian
H_J = J-coupling Hamiltonian
H_D = dipolar Hamiltonian
H_Q = quadrupolar Hamiltonian

The Zeeman Hamiltonian describes the interaction of the nuclear spin with the static magnetic field ($\boldsymbol{B_0}$). In the case where the applied field is along the z-axis:

$$H_Z = \gamma \eta \boldsymbol{B_0} I_Z \qquad \text{Equation 1.3}$$

The chemical shift Hamiltonian describes the distribution of electrons around the nucleus and is given by:

$$H_{CS} = \gamma \eta \left(\sigma_{11} \sin^2\theta \cos^2\phi + \sigma_{22} \sin^2\theta \sin^2\phi + \sigma_{33} \cos^2\theta\right) \boldsymbol{B_0} I_Z \qquad \text{Equation 1.4}$$

where:
θ, Φ = relate the principle axis system to the laboratory frame
$\sigma_{11}, \sigma_{22}, \sigma_{33}$ = principal tensor elements

The isotropic chemical shift (σ_{iso}) and the shielding anisotropy ($\Delta\sigma$) can be determined from the three principle elements:

$$\sigma_{iso} = \frac{1}{3}\left(\sigma_{11} + \sigma_{22} + \sigma_{33}\right) \qquad \text{Equation 1.5}$$

$$\Delta\sigma = \sigma_{33} - \frac{1}{2}(\sigma_{11} + \sigma_{22}) \qquad \text{Equation 1.6}$$

The asymmetry parameter (η) can then be defined as:

$$\eta = \frac{\sigma_{22} - \sigma_{11}}{\sigma_{33} - \sigma_{iso}} \qquad \text{Equation 1.7}$$

Both the J-coupling and dipolar Hamiltonians relate to interactions between nuclear spins, corresponding to indirect (electron mediated, through bond) and direct (through space) contributions respectively. The J-coupling can be described by:

$$H_J = 2\pi \sum_{I<S} \boldsymbol{I_I J_{IS} I_S} \qquad \text{Equation 1.8}$$

where: $\boldsymbol{J_{IS}}$ = indirect spin coupling tensor

The J-coupling may be split into its isotropic (H_J^{iso}) and anisotropic components (H_J^{aniso}):

$$H_J^{iso} = 2\pi \sum_{I<S} \boldsymbol{I_I} J_{IS} \boldsymbol{I_S} \qquad \text{Equation 1.9}$$

where: J_{IS} = isotropic indirect spin coupling tensor

$$H_J^{aniso} = 2\pi \sum_{I<S} \boldsymbol{I_I} J_{IS}^{aniso} \boldsymbol{I_S} \qquad \text{Equation 1.10}$$

where: J_{IS}^{aniso} = anisotropic indirect spin coupling tensor

Under the high field approximation, the dipolar Hamiltonian may be truncated such that:

$$H_D = \sum_{I<S} b_{IS} \frac{1}{2}\left(1 - 3\cos^2\theta_{IS}\right)\left(3I_{I_Z} I_{S_Z} - \boldsymbol{I_I I_S}\right) \qquad \text{Equation 1.11}$$

$$b_{IS} = \left(\frac{\mu_0}{4\pi}\right)\frac{\gamma_I \gamma_S \eta}{r^3_{IS}} \qquad \text{Equation 1.12}$$

where: b_{IS} = dipolar coupling between nuclear spins I and S
μ_0 = permeability of free space
r_{IS} = distance between nuclear spins I and S

In cases relating to heteronuclear spin interactions only, the dipolar Hamiltonian (H_D^{het}) may be further simplified:

$$H_D^{het} = b_{IS}\left(1 - 3\cos^2\theta_{IS}\right) I_{I_Z} I_{S_Z} \qquad \text{Equation 1.13}$$

The remaining term in the nuclear spin Hamiltonian, the quadrupolar Hamiltonian (H_Q), is only applicable to NMR investigations of nuclei which are not spin-½; it will not, therefore, be described in detail as it is not of relevance in the current study.

$$H_Q = \sum_{I=1}^{N} \boldsymbol{I_I Q_I I_I} \qquad \text{Equation 1.14}$$

1.4.2 Solid State NMR

The rapid isotropic motions generally observed in the solution state result in an averaging of those terms in the Hamiltonian which have an angular dependency. Under these conditions the Hamiltonian may be simplified, such that:

$$H_{TOTAL} = H_Z + H_{CS} + H_J \qquad \text{Equation 1.15}$$

Resonance linewidths are therefore narrow, and splitting due to the relatively small scalar couplings is easily discerned.

However, conventional solution state NMR is of limited use for structural studies on large proteins, membrane proteins and solid materials, where long correlation times or restricted motions lead to incomplete averaging of the anisotropic interaction terms and the full form of the Hamiltonian must be applied.

$$H_{TOTAL} = H_Z + H_{CS} + H_J + H_D + H_Q \qquad \text{Equation 1.2}$$

In this situation, as in the case of static solid state NMR (SSNMR), spectra are dominated by broadening from the anisotropic interactions (Table 1.1). Specific resonances are difficult to resolve individually and spectra are of limited use (Figure 1.12 includes an example of a static SSNMR spectrum).

Table 1.1 – Typical orders of magnitude for NMR interactions.

Interaction	Order of magnitude (ν)
Zeeman	10^8 Hz
Chemical Shift	10^3 Hz
Scalar (J-coupling)	1-100 Hz
Dipolar	10^3 Hz
Quadrupolar	10^6 Hz

A number of techniques may be utilised to improve the NMR spectra of solid samples, by increasing sensitivity and resolution, enabling the investigation of the structural and dynamic properties of proteins and of their ligands.

1.4.2.1 Magic angle spinning

Early work in the field of SSNMR demonstrated that motional averaging could be introduced into a system through macroscopic sample rotation [153, 154]. Sample rotation about an axis aligned at 57.4° to the applied magnetic field, the 'magic angle', effectively removes the inhomogeneous anisotropic terms with a dependency upon $[1-(3\cos^2\theta)]$ when the spinning

speed (ω_r) exceeds the magnitude of the interaction (Table 1.1) [155]. The impact of magic angle spinning (MAS) is twofold, since the reduced linewidths not only enable resonances to be resolved, but also produce a significant improvement in signal to noise levels. Incomplete averaging, observed at slower rotation speeds where ($0 < \omega_r < \nu$), leads to the creation of spinning sidebands.

Figure 1.12 illustrates the effect of MAS on an NMR spectrum. Not all of the resonances are obvious in the static spectrum; only two resonances are clearly visible. Sample spinning causes the spectrum to separate into isotropic components, which are masked at slow speeds by their spinning sidebands (located at intervals equal to the spinning speed, ω_r). At higher speeds the sideband pattern becomes clearer and a larger proportion of magnetisation is found within the isotropic peaks. Only two resonances (those with the greatest CSA) still have associated sidebands at the highest spinning speed.

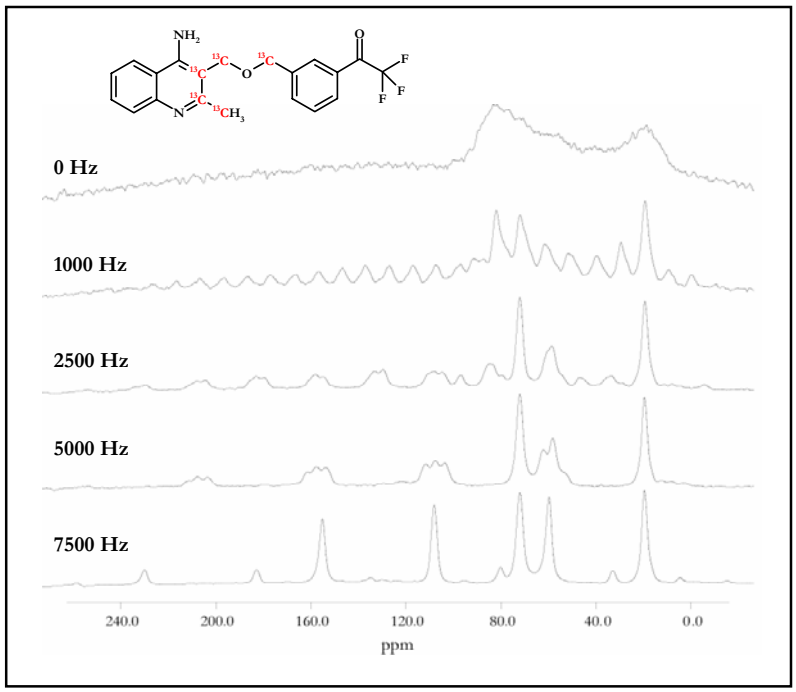

Figure 1.12 – Magic angle sample spinning: ^{13}C NMR spectra of a selectively labelled solid compound (see inset), acquired at 125 MHz and room temperature, using a ramped cross-polarisation experiment. 128 acquisitions were made for each spinning speed. Spectra are not shown to scale.

Dipolar interactions between nuclei are key to the determination of interatomic distances and molecular orientations. However, MAS suppresses these interactions to permit the resonances from individual atomic sites to be resolved. Many SSNMR experiments are therefore based on the selective reintroduction of dipolar couplings whilst still retaining a high resolution spectrum through MAS (such schemes are discussed later in Chapter 4 and Chapter 5).

1.4.2.2 Cross-polarisation

The sensitivity of a particular nucleus to NMR experiments may be related to its gyromagnetic ratio (γ). Unfortunately, many nuclei of interest in biological NMR have relatively low γ values. Cross-polarisation (CP) [156] involves the creation of transverse magnetisation on the abundant high γ protons, before transfer to low γ spins and subsequent observation. Magnetisation transfer is achieved by the simultaneous application of a spin-lock on both the proton and low γ channels, such that the Hartmann-Hahn condition is met [157]:

$$\gamma_I B_{1_I} = \gamma_S B_{1_S} \qquad \text{Equation 1.16}$$

where: B_1 = applied field strength

The sensitivity gain compared to direct generation of transverse magnetisation depends on the ratio of γ values; in the case of proton/carbon transfer a four-fold increase in signal to noise is possible [151]. Additionally, the delay between acquisitions may be reduced since magnetisation is dependent upon proton relaxation (which is typically faster than carbon relaxation rates), thereby increasing the number of acquisitions which may be completed within a given time period.

Precise selection of applied field strengths for the Hartmann-Hahn condition is important for efficient CP, in particular under MAS where the match condition breaks down into a series of sharp peaks separated by the sample spinning frequency [158]. A number of schemes have

been developed to reduce the dependency of magnetisation transfer on an exact match, such as ramped CP [159], variable amplitude CP [160] and amplitude-modulated CP [161].

1.4.2.3 Proton decoupling

Although heteronuclear dipolar couplings are effectively averaged by MAS, the heteronuclear proton couplings behave in an homogeneous manner and are not significantly averaged. In order to achieve narrow linewidths approaching those found in solution NMR experiments, proton couplings with the nuclei of interest must be disrupted. Decoupling is often performed through the application of a strong, continuous wave radio-frequency field on the proton channel. However, advanced schemes such as TPPM [162] and its related super-cycles [163] may offer improvements in some experimental circumstances.

Decoupling of the proton-proton homonuclear interactions provides a second approach to the removal of proton heteronuclear couplings and correspondingly reduces linewidths in SSNMR spectra [164]. In the presence of efficient homonuclear proton decoupling, the heteronuclear coupling behaves in a more inhomogeneous manner and is therefore effectively averaged through MAS.

1.5 Solid State NMR and Acetylcholinesterase

Crop losses due to pests are estimated to represent up to 50% of yields on a worldwide basis [38]. The widespread use of anticholinesterase pesticides over many years has resulted in a number of pests developing resistant strains [122, 165, 166], highlighting the need for continued development of new pesticide products. The inherent toxicity of organophosphates to humans is demonstrated by the fact that 220,000 deaths are believed to occur each year from single short-term exposure to organophosphate pesticides [38, 141]. Chronic exposure

has also been shown to have serious effects including psychiatric symptoms and delayed neuropathy [167]. Species-specific anticholinesterases could lead to pesticides that are of low risk to humans and those organisms outside the design intention.

The cholinergic hypothesis makes AChE an important medical target for the treatment of Alzheimer's Disease. Non-specific interactions of AChE inhibitors are thought to be responsible for many of the side effects associated with tacrine and donepezil treatment [36, 143, 144]. Detailed knowledge of the mechanisms through which acetylcholinesterase interacts with inhibitors, and the subtle changes in these interactions which occur between different species, provides a basis for the optimisation of existing compounds and the design of novel inhibitors with increased potency and selectivity [29, 40, 58].

Despite the wealth of information available on acetylcholinesterase, current research methodologies have a number of limitations which may be addressed through the application of SSNMR, an approach which has not been tried previously.

While crystallographic studies on AChE are becoming more routine and the number of published structures available is constantly increasing (36 structures are currently available from the Brookhaven Protein Data Bank compared to 28 in July 2000), a review of published structures illustrates that the majority involve the *Torpedo californica* enzyme (see Appendix 2). Only a small number of other species have been investigated and, while the availability of enzyme may have been a limiting factor, it is studies of the insect and mammalian strains which are likely to be of more relevance in the development of novel pesticides and therapeutics. X-ray diffraction experiments require the preparation of high quality protein crystals, a non-trivial process which is normally the limiting step in such structural studies. Co-crystallisation can often improve the quality of crystals. The first published mouse AChE structure [28] and both published human AChE structures [23] involved complexes with the FAS II peptide.

Considering the body of evidence which suggests that inhibitor binding at the peripheral site alters the conformation of the active site through an allosteric mechanism [74, 79, 82, 91, 112], such as the case with FAS II, these complexes may be misleading when used as a model for the development of novel inhibitors.

The importance of subtle interactions in ligand binding is demonstrated by the inability of computational methods to predict accurately the binding modes of inhibitors. Donepezil was developed after an extensive study involving the investigation of structure-activity relationships and modelling of inhibitor binding [96]. Although donepezil did prove to be a potent inhibitor, the binding mode predicted during its development was found to be markedly different from the actual bound conformation later derived using x-ray diffraction [36, 40]. Additionally, simulations of the binding of galanthamine, which is a rigid molecule, have only recently been able to produce a structure which matches x-ray crystallography data [41, 64]. A greater pool of AChE structures with bound ligands will allow the deconvolution of key binding interactions, aiding the accuracy of computational predictions.

NMR investigations of AChE to date have involved solution state experiments which are inherently restricted by the size of the enzyme (~65 kDa per catalytic unit). These experiments include: the monitoring of linewidth changes as a means of following the hydrolysis reaction [115]; chemical shift changes demonstrating the covalent binding of an inhibitor as a tetrahedral transition state mimic [120]; the use of chemical shifts to identify the nature of aged and non-aged organophosphate complexes [119]; the comparison of relaxation rates for two inhibitors to infer different binding modes [118]; and the appearance of a resonance upon inhibitor binding to demonstrate the formation of a short, strong hydrogen bond at the active site [116, 117] (although the accuracy suggested by the authors appears to be greater than that demonstrated in the study on which their work is based [168]). While the TROSY NMR

experiment [169] and the application of carefully selected labelling schemes [170] enable the molecular weight boundaries associated with solution NMR to be pushed back (~50 kDa), solution NMR is unlikely to be of significant importance in AChE research.

SSNMR is a novel approach to the investigation of AChE and its inhibitors but has been used extensively in the determination of orientation, dynamics, bond angles and distance constraints in other biological systems. Selected examples include: the orientation of deuterated bromoacetylcholine when bound to nAChR [20], the ground-state and photo-activated orientations of retinal in rhodopsin [171] and helix orientation of the colicin E1 channel domain [172]; the dynamics of the colicin Ia channel domain [173] and of loop motions in triosphosphate isomerase [174]; and the secondary structure determination of a silk, based on torsion angles [175]. However, the determination of internuclear distances is likely to be of most value with respect to AChE research – the introductions to Chapter 4 (homonuclear distance measurements) and Chapter 5 (heteronuclear distance measurements) cover previous examples of such work in detail.

In contrast to other techniques, SSNMR:

- is not hindered by molecular size, as is the case with solution NMR;
- does not require the high degree of macroscopic order necessary for crystallographic studies (providing the option for studies on forms of the enzyme which have so far eluded attempts at crystallisation);
- involves the investigation of either natural abundance signals or non-perturbing labels, unlike mutation experiments or fluorescence labelling;
- involves non-destructive analysis of samples;

- can resolve dynamic effects within the system and may be applied to the investigation of ligands which are hydrolysed at a rate which is too rapid for the preparation of crystals;

- through chemical shifts, can provide an indication of the electronic environment which each nuclei experiences;

- has the potential to determine the absolute conformation of inhibitors within the binding site and the position of inhibitors with respect to the protein;

- may be applied to samples in either frozen solutions, freeze-dried solids or even directly to the membrane tethered form of AChE (this 'natural' state is ultimately of greatest interest).

Information about the binding site of AChE may also help in understanding the recognition of ACh by proteins such as the acetylcholine receptors, which are intriguing in that although ACh is a common ligand, few inhibitors of the esterase act as receptor agonists (galanthamine is one such example [42]).

The active site, peripheral binding site and gorge are all potential targets for the design of novel AChE inhibitors. It has been shown that compounds which simultaneously interact with the peripheral and catalytic sites demonstrate greater potency when compared with compounds which interact with a single site [40, 95, 96, 176]. As part of the development of novel pesticides, Syngenta produced a library of compounds which were predicted (and later confirmed) to be strong inhibitors of acetylcholinesterase [43]. The compounds are based around a chimera of two previously known inhibitor structures – tacrine, which binds non-covalently in the lower gorge [30] and *m*-(*N,N,N*-trimethylammonio)-2,2,2-

trifluoroacetophenone (TMTFA), which binds covalently to the catalytic serine mimicking a transition state structure [27] (Figure 1.13).

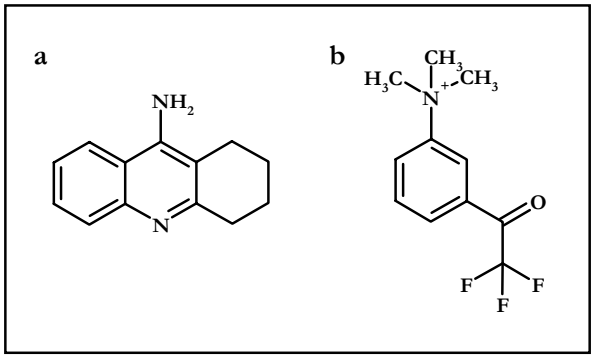

Figure 1.13 – Tacrine (a) and (trimethylammonio)trifluoroacetophenone (b).

In a collaboration between Syngenta, Israel Silman and Joel Sussman, x-ray diffraction was used to determine the conformation of two of the compounds in the series, R404435 and R415657 (Figure 1.14), when bound to acetylcholinesterase. R404435 was characterised while bound to *Tc*AChE [43] and R415657 while bound to *Dm*AChE (unpublished).

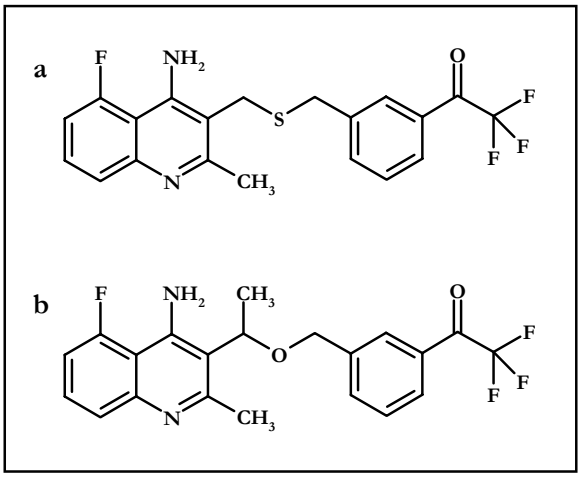

Figure 1.14 – Syngenta acetylcholinesterase inhibitors: R404435, 4-amino-5-fluoro-2-methyl-3-(3-trifluoroacetylbenzyl-thiomethyl)quinoline (a) R415657, 4-amino-5-fluoro-2-methyl-3-(3-trifluoroacetylbenzyl-methoxymethyl)quinoline (b).

Despite these two compounds being closely related, their crystal structures indicate markedly different binding conformations (Figure 1.15).

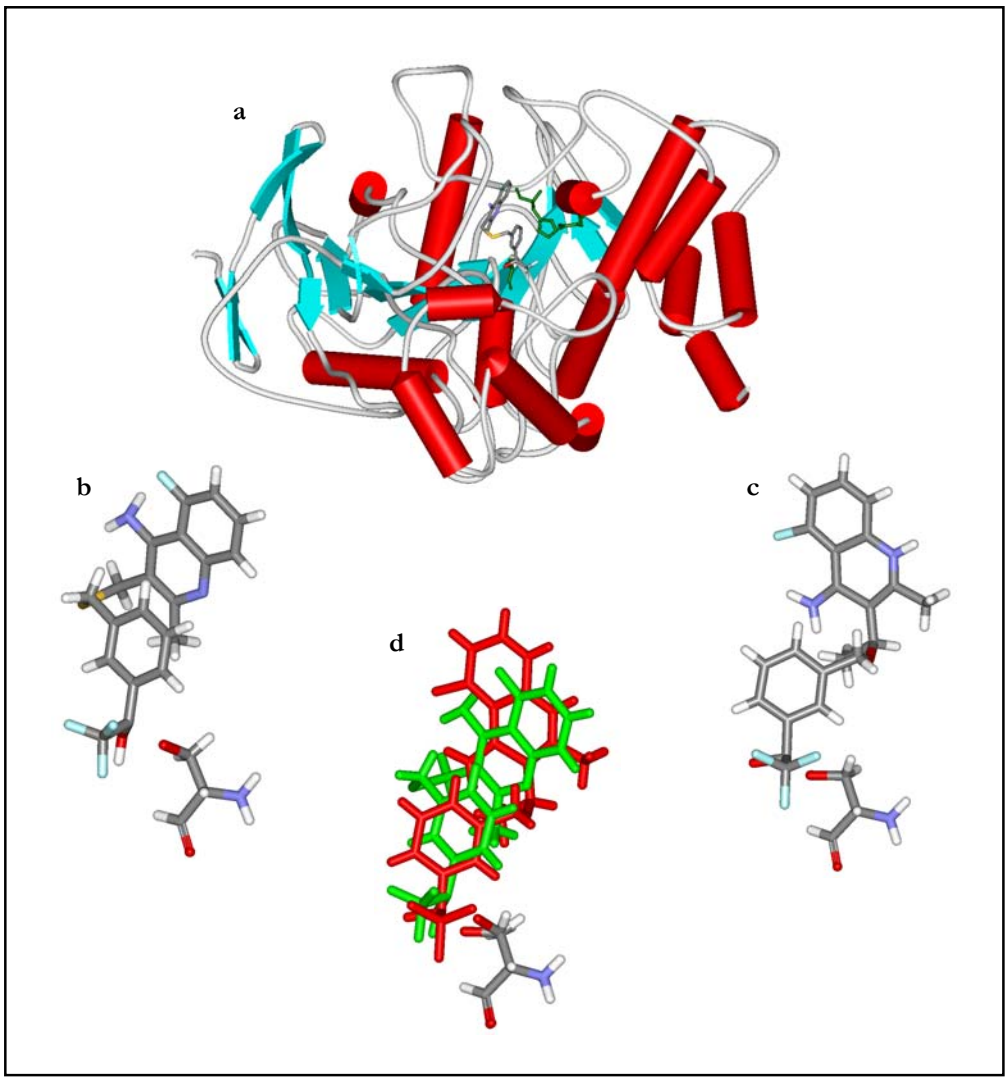

Figure 1.15 – Crystal structures of Syngenta compounds bound to acetylcholinesterase: R404435 with *Tc*AChE - the enzyme secondary structure is shown, with the catalytic triad indicated by green stick models and the inhibitor coloured by atom type (a); R404435 and the active site serine from *Tc*AChE (b), R415657 and the active site serine from *Dm*AChE (c); overlay of the two structures based on a common alignment of the serine residues - R404435 is shown in green, R415657 is shown in red (d).

Further members of the same family of inhibitors which have not been investigated using x-ray crystallography are available, R414425 and R414983 (Figure 1.16); their structures in the

binding site have yet to be determined. These inhibitors provide interesting subjects for study since, on the basis of the conformations for R404435 and R415657, their orientations within the binding site cannot be predicted easily.

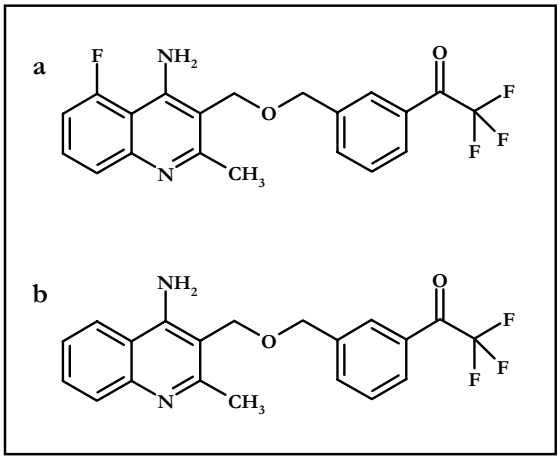

Figure 1.16 – Syngenta acetylcholinesterase inhibitors: R414425, 4-amino-5-fluoro-2-methyl-3-(3-trifluoroacetylbenzyl-oxymethyl)quinoline (a) R414983, 4-amino-2-methyl-3-(3-trifluoroacetylbenzyl-methoxymethyl)quinoline (b).

1.6 Project Aims

This project aims, for the first time, to develop SSNMR methodologies for the investigation of AChE and its ligands, and to demonstrate the potential contribution from SSNMR to the field of AChE research through the synthesis of isotopically labelled R414425 and R414983, the determination of internuclear distances for labelled R414983 while bound to *Electophorus electricus* acetylcholinesterase, and the incorporation of these solid state NMR derived distances in a model for its bound state.

Following on from this introduction to acetylcholinesterase and solid state NMR:

- Chapter 2 describes the selection of isotopic labelling schemes for the two inhibitors R414425 and R414983 in order to maximise the opportunities for defining their conformation when bound to acetylcholinesterase. It also covers the synthesis of

R414425 and R414983, together with their isotopically labelled counterparts, $^{13}C_5$-R414425 and $^{13}C_5$-R414983.

- Chapter 3 involves the characterisation of the inhibitors, both in relation to their potency (acetylcholinesterase activity assays) and to their basic NMR properties (assignment of resonances and a discussion of the chemical shift changes observed between solution, solid and acetylcholinesterase bound states).

- Chapter 4 introduces the first internuclear distance measurements on acetylcholinesterase bound $^{13}C_5$-R414983 through homonuclear recoupling using the rotational resonance (R2) scheme.

- Chapter 5 covers heteronuclear distance determinations on acetylcholinesterase bound $^{13}C_5$-R414983 using rotational-echo double-resonance (REDOR) experiments.

- Chapter 6 focuses on the range of conformations which the inhibitor R414983 can adopt, applying molecular dynamics simulations to the free compound and acetylcholinesterase bound inhibitor, and discusses how the distance measurements determined in Chapters 4 and 5 restrain the conformational freedom of R414983 when bound to acetylcholinesterase.

- Chapter 7 reviews the work performed, discusses what has been achieved and also addresses the future perspectives for the project.

Chapter 2 Synthesis of Labelled Inhibitors

2.1 Overview

The NMR active isotope of carbon, ^{13}C, comprises approximately 1% of the natural abundance carbon. For the purposes of NMR investigations, the incorporation of an increased proportion of ^{13}C provides significantly improved signal to noise and, when used selectively, can aid in the differentiation of particular sites from their natural abundance counterparts. Fortunately, ^{19}F is NMR active and is 100% of natural abundance fluorine.

A protocol for the synthesis of the compounds R414425 and R414983 (Figure 2.1) was provided by Syngenta (personal communication, although some of this work was later published [43]). The range of potential labelling schemes is limited by the availability of precursor chemicals and a scheme providing the greatest range of potential distance measurements for both inhibitors was chosen.

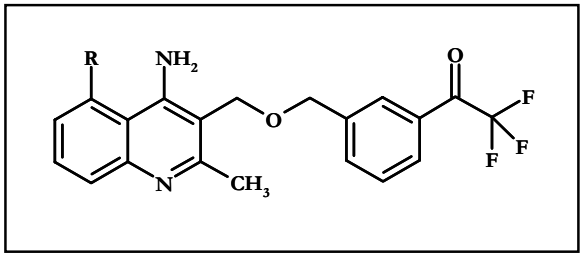

Figure 2.1 – Syngenta acetylcholinesterase inhibitors: R414425 (R = F), R414983 (R = H).

2.2 Introduction

2.2.1 Synthetic Route

The general synthetic route used is shown in Figure 2.2. Minor modifications to the scheme supplied by Syngenta were necessary as a result of the differing reaction scales, however, the reactants and conditions were retained.

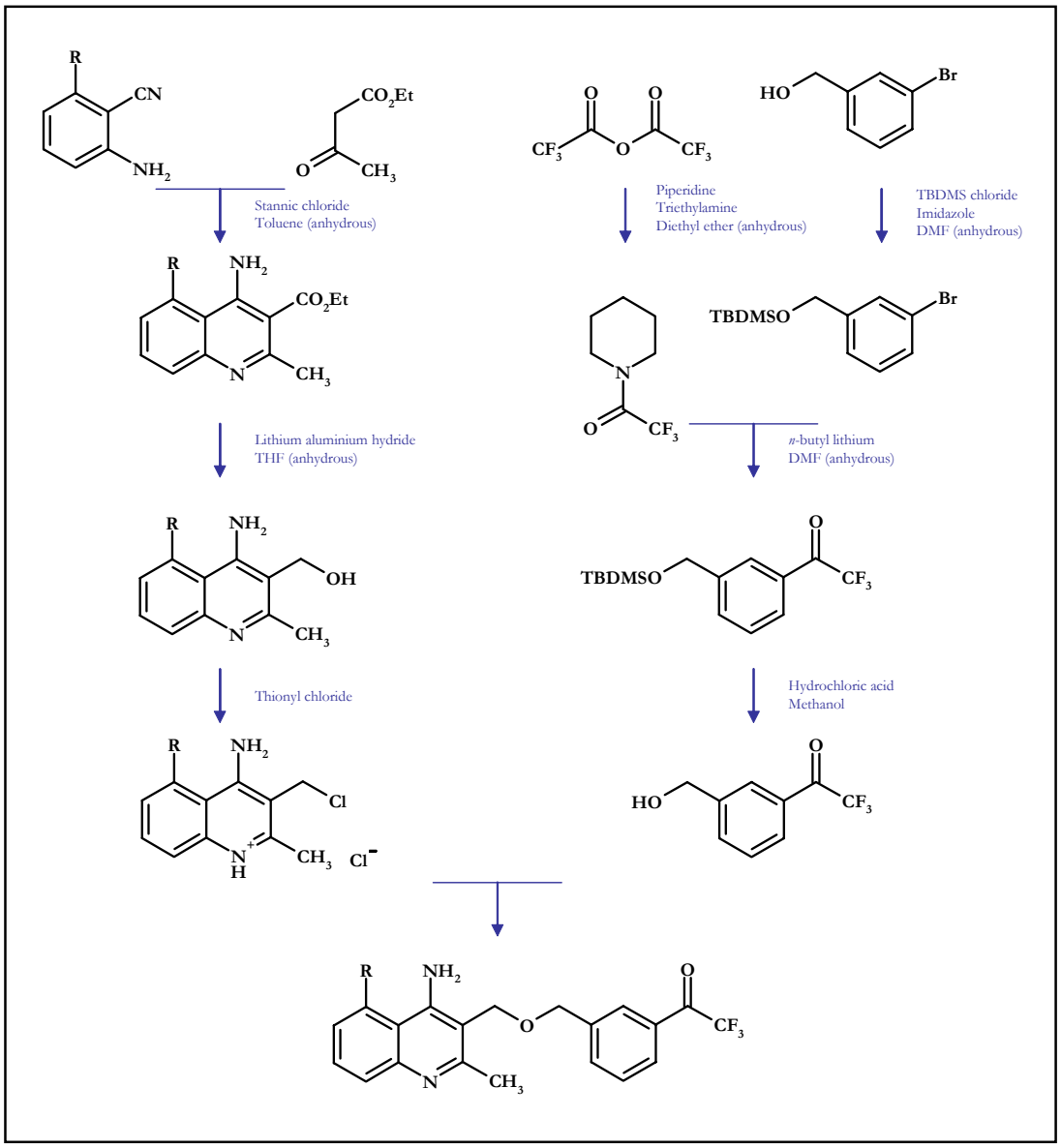

Figure 2.2 – General synthetic steps for the production of Syngenta acetylcholinesterase inhibitors R414425 (R = F) and R414983 (R = H).

2.2.2 Labelling Schemes

Conformational flexibility exists in two main regions of the R414425 and R414983 molecules, around the central ether linkage and the trifluoroacetyl function. It is therefore desirable to incorporate isotopic labels such that internuclear distance measurements (both homonuclear and heteronuclear) can be made to restrict, or ideally to define precisely, the conformation in these areas.

Of the four starting materials which are combined to form the final structures, labelling opportunities only exist for ethyl acetoacetate and 3-bromobenzyl alcohol (anthranilonitrile/2-amino-6-fluorobenzonitrile and trifluoroacetic anhydride are not commercially available or easily synthesised with ^{13}C enrichment). Ethyl acetoacetate is available with a range of ^{13}C label combinations, in positions 3, (1,3), (2,4) and (1,2,3,4). Figure 2.3 illustrates how these positions relate to the final structures.

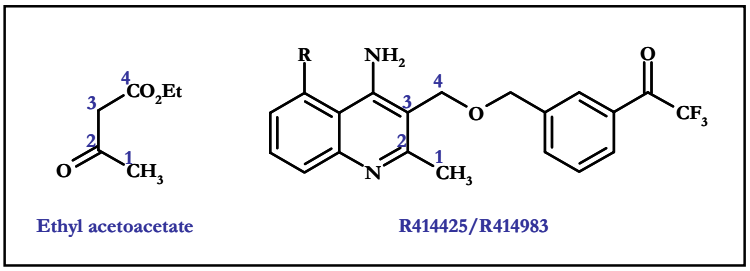

Figure 2.3 – Ethyl acetoacetate label positions and their corresponding locations in the final inhibitor structures.

The 2-methyl and quinoline C2 inhibitor sites (C1 and C2 ethyl acetoacetate sites respectively) are of most interest because of their more distant location in relation to the ether linkage. Only fully labelled ethyl acetoacetate incorporates labels in both of these positions and the presence of the additional C3 and C4 labels (corresponding to the quinoline C3 and quinoline methylene) is unlikely to be a problem in the final structures since they are in chemically (and therefore NMR) distinct locations.

Isotopically labelled 3-bromobenzyl alcohol, while not available itself, can be produced in two steps by modification of benzoic acid (Figure 2.4) [177, 178]. Benzoic acid is available either uniformly labelled at all six aromatic ring positions or singly labelled at the α-carbon. Uniform labelling, while introducing the potential for a greater number of distance measurements, is likely to make the measurement of specific distances more difficult (the aromatic carbons will have similar resonances, which may not be resolved). Benzoic acid with a single label at the α position was therefore chosen.

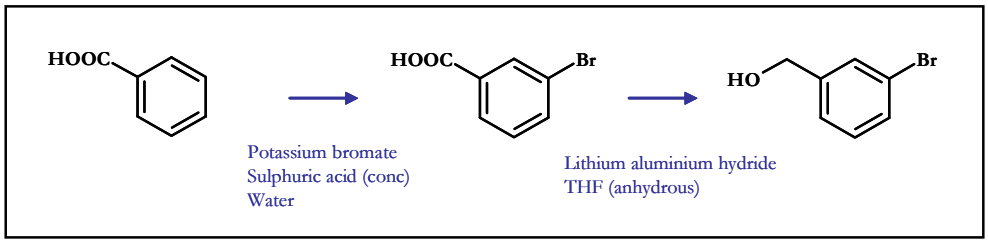

Figure 2.4 – Additional synthetic steps required for the incorporation of isotopic labels.

The inclusion of 1,2,3,4-$^{12}C_4$-ethyl acetoacetate and α-^{13}C-benzoic acid into the synthesis results in the labelled structures shown in Figure 2.5.

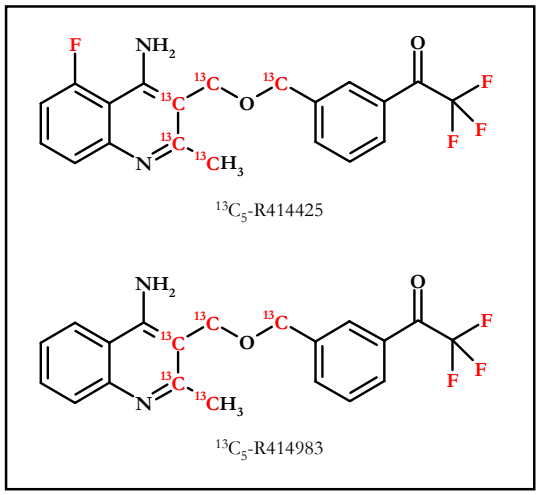

Figure 2.5 – Final labelled inhibitor structures - NMR active nuclei are shown in red.

2.2.3 Internuclear Distance Constraints

The arrangement of NMR active nuclei in the chosen labelling schemes raises the possibility of both homonuclear and heteronuclear distance determinations (Figure 2.6).

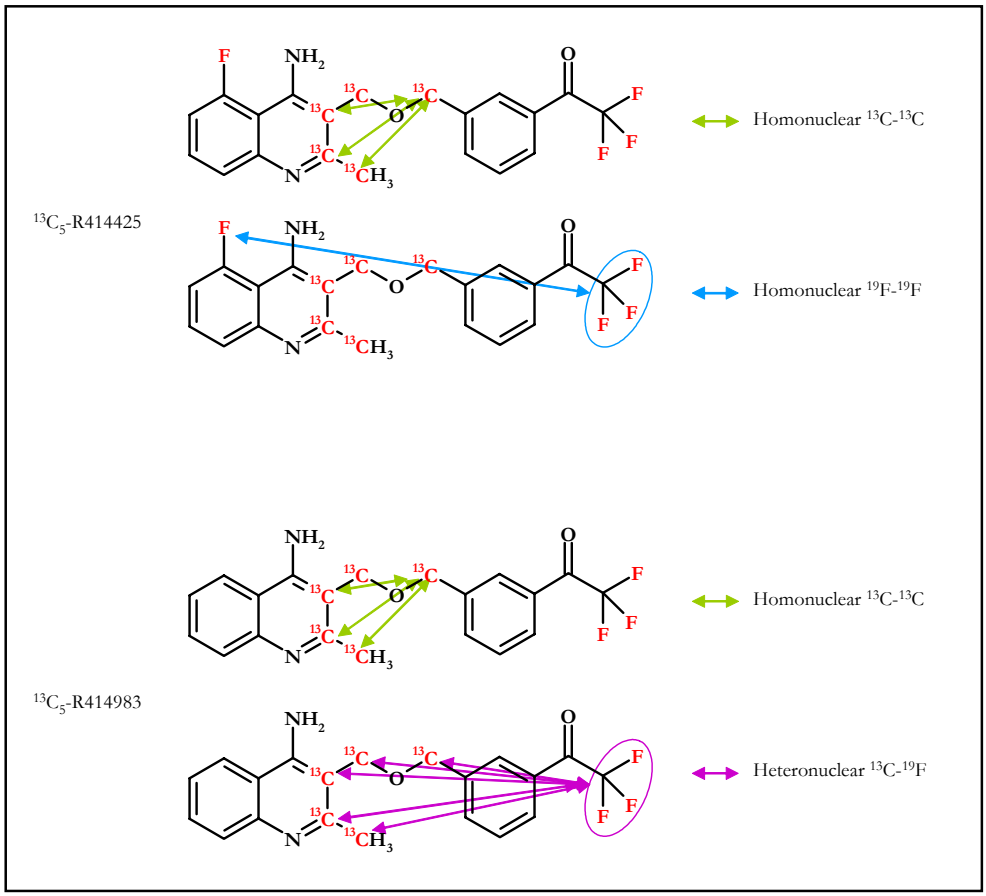

Figure 2.6 – Potential distance constraints based on the chosen labelling schemes.

However, it should be noted that in neither case is it possible to define a single conformation using the labelling schemes proposed but only to restrict the range of conformations which the inhibitors can adopt. Some degree of freedom is likely to remain, particularly in the region of the benzyl ring.

2.3 Synthesis

2.3.1 General

The products of each reaction step were confirmed using ^{1}H NMR (200 MHz Bruker Gemini) and APCI mass spectrometry (Micromass Platform) where appropriate.

The final compounds (R414425, $^{13}C_5$-R414425, R414983 and $^{13}C_5$-R414983) were purified by reverse phase HPLC on a HiChrom Kromasil C_{18} column (100 mm x 21 mm). Solvent A was the aqueous phase (containing 0.1% TFA) and solvent B acetonitrile (containing 0.1% TFA). A linear gradient from 20-40% B, over a period of 20 minutes, was followed by a linear gradient from 40-60% B over 3 minutes and then maintained for a further 3 minutes. A total flow of 20 ml/min was used, with 30-50 mg of product loaded for each run in a minimum volume of 75% A/25% B. Fractions were collected and analysed by ^{1}H NMR (200 MHz Bruker Gemini) and APCI mass spectrometry (Micromass Platform), those containing the desired compound were pooled and dried by rotary evaporation.

2.3.2 Synthesis of 4-amino-5-fluoro-2-methyl-3-(3-trifluoroacetylbenzyl-oxymethyl)quinoline (R414425)

2.3.2.1 3-bromobenzoic acid

Benzoic acid (3.0 g, 24 mmoles) and potassium bromate (4.1 g, 24 mmoles) were dissolved in water (18 ml) and heated to 90 °C. Concentrated sulphuric acid (22 ml) was added dropwise over a period of 1 hour, after addition was completed the temperature was maintained at 90 °C for a further 2 hours. Heating was removed and the mixture was allowed to cool before the addition of water (50 ml) and the extraction of the product with diethyl ether (4 x 25 ml). Ether fractions were combined, washed with sodium metabisulphate solution, then dried over magnesium sulphate before evaporation under reduced pressure.

The product at this point, an off-white solid, was purified to remove unreacted benzoic acid. The solid was repeatedly shaken with hot water (3 x 50 ml, 90 °C) and the undissolved material collected by filtration and dried, providing an pale brown powder (1.95 g, 39% yield): ^{1}H NMR (DMSO) δ 7.39 (1H, t), 7.77 (1H, d), 8.07 (1H, d), 8.28 (1H, s); M-H$^-$ (APCI-) 199 (1 Br).

2.3.2.2 3-bromobenzyl alcohol

Lithium aluminium hydride (1.26 g, 32 mmoles) was mixed with anhydrous diethyl ether (60 ml), and a solution of 3-bromobenzoic acid (1.95 g, 9.6 mmoles) in anhydrous diethyl ether (40 ml) was added dropwise to the stirred mixture over a period of 30 minutes at 18-25 °C, under a nitrogen atmosphere. The mixture was refluxed for 1 hour, before being cooled and the reaction quenched with wet diethyl ether. Following acidification by the addition of sulphuric acid (1 M, 45 ml), the ether layer was removed and the aqueous layer extracted with diethyl ether (3 x 30 ml). The extracts were combined, dried over magnesium sulphate and evaporated under reduced pressure to give a light brown oil (1.70 g, 94% yield): ^{1}H NMR ($CDCl_3$) δ 4.61 (2H, s), 7.10-7.60 (4H, m).

2.3.2.3 *N*-trifluoroacetylpiperidine

Trifluoroacetic anhydride (5.65 g, 26 mmoles) was added dropwise over a period of 30 minutes to a stirred solution of piperidine (2.75 g, 32 mmoles) and triethylamine (2.72 g, 27 mmoles) in anhydrous diethyl ether (20 ml), maintained between 15-20 °C and under a nitrogen atmosphere. After addition was completed the solution was stirred at room temperature for a further 2 hours. A combination of ice and water (60 ml) was then added and the mixture well shaken. The ether fraction was removed and washed with dilute hydrochloric acid until the washings became acidic (0.1 M, 6 x 15 ml). The organic fraction was then washed with water (3 x 10 ml), dried over magnesium sulphate and evaporated under reduced pressure to produce a clear yellow oil (2.66 g, 62% yield: MH$^+$ (APCI+) 182.

2.3.2.4 1-bromo-3-(*tert*-butyldimethylsilyloxymethyl)benzene

tert-butyldimethylsilyl chloride (0.89 g, 5.9 mmoles) in anhydrous DMF (4 ml) was slowly added to a stirred solution of imidazole (0.94 g, 13.8 mmoles) in anhydrous DMF (2 ml). 3-bromobenzyl alcohol (1.0 g, 5.3 mmoles) in anhydrous DMF (2 ml) was then slowly added, with the temperature maintained below 20 °C. The resulting mixture was stirred at 50 °C for 20 hours. Upon completion the mixture was cooled, water (25 ml) added and the product extracted with hexane (4 x 10 ml). Organic extracts were combined, washed with water (5 x 5 ml) and then dried over magnesium sulphate. Hexane was removed by evaporation to produce a clear colourless oil (1.22 g, 76% yield): ^{1}H NMR ($CDCl_3$) δ 0.12 (6H, s), 0.94 (9H, s), 4.82 (2H, s), 7.30-7.81 (4H, m).

2.3.2.5 1-trifluoroacetyl-3-(*tert*-butyldimethylsilyloxymethyl)benzene

n-butyl lithium (2.5 M in hexanes, 1.46 ml, 3.6 mmoles) was added over a period of 15 minutes to a stirred solution of 1-bromo-3-(*tert*-butyldimethylsilyloxymethyl)benzene (1.0 g, 3.3 mmoles) in anhydrous diethyl ether (11 ml), maintained between 0-5 °C under a nitrogen atmosphere. The resulting clear yellow solution was allowed to warm to 10 °C over 30 minutes before being recooled to 0 °C. *N*-trifluoroacetylpiperidine (0.60 g, 3.3 mmoles) in anhydrous diethyl ether (3 ml) was added over a period of 30 minutes with the temperature maintained between 0-5 °C, followed by stirring at room temperature for 1 hour. After cooling to 0-5 °C the reaction quenched with saturated ammonium chloride solution (5 ml). The aqueous portion was extracted with ether, extracts were combined, washed with ammonium chloride solution, then washed with water before drying over magnesium sulphate and evaporation to give a red-brown oil (1.02 g, 96% yield).

2.3.2.6 3-trifluoroacetylbenzyl alcohol

Concentrated hydrochloric acid (0.74 ml) was added dropwise to a stirred solution of 1-trifluoroacetyl-3-(*tert*-butyldimethylsilyloxymethyl)benzene (0.92 g, 2.9 mmoles) in methanol (7.4 ml) at 10-20 °C. The mixture was stirred at room temperature for 30 minutes before being reduced in volume (approx. 50%) on a rotary evaporator. The residue was diluted with diethyl ether (25 ml) and neutralised with a slurry of sodium bicarbonate/water before washing with water and drying over magnesium sulphate. Evaporation under reduced pressure resulted in a yellow oil (0.55 g, 93% yield): ^{1}H NMR ($CDCl_3$) δ 4.80 (2H, s), 7.40-7.80 (4H, m).

2.3.2.7 4-amino-3-carboxyethyl-5-fluoro-2-methylquinoline

2-amino-6-fluorobenzonitrile (1.0 g, 7.4 mmoles) was dissolved in anhydrous toluene (20 ml) and ethyl acetoacetate added (0.96 g, 7.4 mmoles). Stannic chloride (3.83 g, 15 mmoles) was added over a period of 5 minutes with the temperature maintained around 20-22 °C. Following addition, the mixture was stirred under reflux for 5 hours before cooling and the supernatant removed. The residue was triturated with ethyl acetate (21 ml) and a yellow solid collected by filtration. The solid was stirred with sodium hydroxide solution (2 M, 28 ml) for 30 minutes, before extraction into ethyl acetate (4 x 25 ml). Extracts were washed with water before drying over magnesium sulphate and evaporation to give a yellow solid (1.54 g, 85% yield): ^{1}H NMR ($CDCl_3$) δ 1.44 (3H, t), 2.79 (3H, s), 4.42 (2H, q), 6.90-7.75 (5H, m); MH^+ (APCI+) 249.

2.3.2.8 4-amino-5-fluoro-3-hydroxymethyl-2-methylquinoline

4-amino-3-carboxyethyl-5-fluoro-2-methylquinoline (1.0 g, 4.0 mmoles) in anhydrous THF (10 ml) was added over a period of 1 hour to a cooled (18-25°C) solution of lithium aluminium hydride powder (0.182 g, 4.8 mmoles) in anhydrous THF (26 ml), under a nitrogen atmosphere. The mixture was stirred at room temperature for 3 hours, before quenching with the cautious addition of water and acidification with hydrochloric acid (2 M, 5 ml). The

subsequent addition of saturated sodium hydroxide solution (2 ml) was then followed by removal of the THF layer. The organic layer was dried over magnesium sulphate and evaporated to produce a pale yellow powder (0.54 g, 65% yield): ^{1}H NMR ($CDCl_3$) δ 2.58 (3H, s), 4.89 (2H, s), 6.05 (2H, br s), 7.40-7.70 (3H, m); MH^+ (APCI+) 207; $M\text{-}H^-$ (APCI-) 205.

2.3.2.9 4-amino-3-chloromethyl-5-fluoro-2-methylquinoline

4-amino-5-fluoro-3-hydroxymethyl-2-methylquinoline powder (0.52 g, 2.5 mmoles) was added slowly to vigorously stirred thionyl chloride (2.4 ml). The resulting mixture was stirred under reflux for 1.5 hours, before cooling and evaporation under reduced pressure. The residue was triturated with ethanol-free chloroform, the resulting solid filtered and dried in air to produce an off-white powder (0.49 g, 74% yield): ^{1}H NMR (DMSO) δ 2.78 (3H, s), 4.89 (2H, s), 7.30-7.95 (3H, m); MH^+ (APCI+) 221 (1 Cl).

2.3.2.10 4-amino-5-fluoro-2-methyl-3-(3-trifluoroacetylbenzyl-oxymethyl)quinoline

4-amino-3-chloromethyl-5-fluoro-2-methylquinoline (0.11 g, 0.42 mmoles) was mixed with 3-trifluoroacetylbenzyl alcohol (0.43 g, 2.1 mmoles) and stirred at 125-130 °C for 4 hours. After cooling, the gum was stirred with water (5 ml) and diethyl ether (5 ml) until two clear layers were obtained. The aqueous portion was extracted with diethyl ether (5 x 5 ml), before addition of sodium hydroxide solution (2 M) such that the alkalinity exceeded pH 10. The white precipitate was extracted into DCM (5 x 5 ml). After drying over magnesium sulphate, the DCM extracts were evaporated to give an off-white solid (0.15 g, 89% yield). After HPLC purification an off-white solid remained (48 mg, 28% yield): ^{1}H NMR ($CDCl_2$) δ 2.60 (3H, s), 4.62 (2H, s), 4.86 (2H, s), 6.00 (2H, br s), 6.90-8.15 (7H, m); MH^+ (APCI+) 393.

2.3.3 Synthesis of $^{13}C_5$-4-amino-5-fluoro-2-methyl-3-(3-trifluoroacetylbenzyl-oxymethyl)quinoline ($^{13}C_5$-R414425)

2.3.3.1 α-^{13}C-3-bromobenzoic acid

α-^{13}C-benzoic acid (3.0 g, 24 mmoles) and potassium bromate (4.1 g, 24 mmoles) were dissolved in water (18 ml) and heated to 90 °C. Concentrated sulphuric acid (22 ml) was added dropwise over a period of 1 hour, after addition was completed the temperature was maintained at 90 °C for a further 2 hours. Heating was removed and the mixture was allowed to cool before the addition of water (50 ml) and the extraction of the product with diethyl ether (4 x 25 ml). Ether fractions were combined, washed with sodium metabisulphate solution, then dried over magnesium sulphate before evaporation under reduced pressure. The crude solid was repeatedly shaken with hot water (3 x 50 ml, 90 °C) and the undissolved material collected by filtration and dried, providing an pale brown powder (1.36 g, 27% yield): ^{1}H NMR (DMSO) δ 7.38 (1H, t), 7.78 (1H, d), 8.05 (1H, m), 8.27 (1H, m); M-H$^-$ (APCI-) 200 (1 Br).

2.3.3.2 α-^{13}C-3-bromobenzyl alcohol

Lithium aluminium hydride (0.88 g, 22 mmoles) was mixed with anhydrous diethyl ether (40 ml), and a solution of α-^{13}C-3-bromobenzoic acid (1.36 g, 6.8 mmoles) in anhydrous diethyl ether (28 ml) was added dropwise to the stirred mixture over a period of 30 minutes, at 18-25 °C, under a nitrogen atmosphere. The mixture was refluxed for 1 hour, before being cooled and the reaction quenched with wet diethyl ether. The mixture was acidified by the addition of sulphuric acid (1 M, 30 ml), the ether layer was removed and the aqueous layer extracted with diethyl ether (3 x 20 ml). The extracts were combined, dried over magnesium sulphate and evaporated under reduced pressure to give a clear light brown oil (1.26 g, 100% yield).

2.3.3.3 *N*-trifluoroacetylpiperidine

Trifluoroacetic anhydride (20 g, 95 mmoles) was added dropwise over a period of 30 minutes to a stirred solution of piperidine (10.3 g, 116 mmoles) and triethylamine (10 g, 98 mmoles) in diethyl ether (approx. 72 ml) maintained between 15-20 °C and under a nitrogen atmosphere. After addition was completed the solution was stirred at room temperature for a further 2 hours. A combination of ice and water (approx. 200 ml) was then added and the mixture well shaken. The ether fraction was removed and washed with dilute HCl until the washings became acidic (0.1M, 6 x 45 ml). The organic fraction was then washed with water (3 x 30 ml), dried over magnesium sulphate and evaporated under reduced pressure to produce a clear yellow oil (13.9 g, 64% yield: MH^+ (APCI+) 182.

2.3.3.4 α-^{13}C-1-bromo-3-(*tert*-butyldimethylsilyloxymethyl)benzene

tert-butyldimethylsilyl chloride (1.12 g, 7.4 mmoles) in anhydrous DMF (5 ml) was slowly added to a stirred solution of imidazole (1.18 g, 17.3 mmoles) in anhydrous DMF (2.5 ml). α-^{13}C-3-bromobenzyl alcohol (1.26 g, 6.7 mmoles) in anhydrous DMF (2.5 ml) was then slowly added, with the temperature maintained below 20 °C. The resulting mixture was then stirred at 50 °C for 20 hours. Upon completion the mixture was cooled, water added (30 ml) and the product extracted with hexane (4 x 10 ml). Organic extracts were combined, washed with water (5 x 5 ml) and then dried over magnesium sulphate. Hexane was removed by evaporation to produce a clear colourless oil (1.71 g, 85% yield): ^{1}H NMR ($CDCl_3$) δ 0.12 (6H, s), 0.96 (9H, s), 4.87 (2H, d), 7.10-7.60 (4H, m).

2.3.3.5 α-^{13}C-1-trifluoroacetyl-3-(*tert*-butyldimethylsilyloxymethyl)benzene

n-butyl lithium (2.5 M in hexanes, 2.48 ml, 6.1 mmoles) was added over a period of 15 minutes to a stirred solution of α-^{13}C-1-bromo-3-(*tert*-butyldimethylsilyloxymethyl)benzene (1.70 g, 5.6 mmoles) in anhydrous diethyl ether (19 ml) maintained between 0-5 °C, under a nitrogen

atmosphere. The resulting clear yellow solution was allowed to warm to 10 °C over 30 minutes before being recooled to 0 °C. *N*-trifluoroacetylpiperidine (1.02 g, 5.6 mmoles) in anhydrous diethyl ether (5 ml) was then added over a period of 30 minutes with the temperature maintained between 0-5 °C, followed by stirring at room temperature for 1 hour. The solution was then recooled to 0-5 °C and the reaction quenched with saturated ammonium chloride (8 ml). The aqueous portion was extracted with ether, extracts were combined, washed with ammonium chloride solution, then washed with water before drying over magnesium sulphate and evaporation to give a red-brown oil (1.78 g, 99% yield).

2.3.3.6 α-^{13}C-3-trifluoroacetylbenzyl alcohol

Concentrated hydrochloric acid (1.44 ml) was added dropwise to a stirred solution of α-^{13}C-1-trifluoroacetyl-3-(*tert*-butyldimethylsilyloxymethyl)benzene (1.78 g, 5.6 mmoles) in methanol (14.4 ml) at 10-20 °C. The mixture was stirred at room temperature for 30 minutes before reduction in volume (approx. 50%) on a rotary evaporator. The residue was diluted with diethyl ether (50 ml) and neutralised with a slurry of sodium bicarbonate/water before washing with water and drying over magnesium sulphate. Evaporation under reduced pressure resulted in a yellow oil (0.76 g, 65% yield): ^{1}H NMR ($CDCl_3$) δ 4.80 (2H, d), 7.10-8.10 (4H, m).

2.3.3.7 $^{13}C_4$-4-amino-3-carboxyethyl-5-fluoro-2-methylquinoline

2-amino-6-fluorobenzonitrile (1.07 g, 7.9 mmoles) was dissolved in anhydrous toluene (21 ml) and 1,2,3,4-$^{13}C_4$-ethyl acetoacetate added (1.00 g, 7.5 mmoles). Stannic chloride (3.90 g, 15 mmoles) was added over a period of 5 minutes with the temperature maintained around 20-22 °C. Following addition the mixture was stirred under reflux for 5 hours before cooling and the supernatant removed. The residue was triturated with ethyl acetate (21 ml) and a yellow solid collected by filtration. The solid was stirred with sodium hydroxide solution (2 M, 28 ml) for 30 minutes, before extraction into ethyl acetate (4 x 25 ml). Extracts were washed with water

before drying over magnesium sulphate and evaporation to give a yellow solid (1.38 g, 73% yield): ^{1}H NMR ($CDCl_3$) δ 1.44 (3H, t), 2.79 (3H, m), 4.41 (2H, q), 7.05 (2H, br s), 7.40-7.90 (3H, m); MH^+ (APCI+) 253.

2.3.3.8 $^{13}C_4$-4-amino-5-fluoro-3-hydroxymethyl-2-methylquinoline

$^{13}C_4$-4-amino-3-carboxyethyl-5-fluoro-2-methylquinoline (1.38 g, 5.6 mmoles) in anhydrous THF (14 ml) was added over a period of 1 hour to a cooled (18-25°C) solution of lithium aluminium hydride powder (0.26 g, 6.8 mmoles) in anhydrous THF (36 ml), under a nitrogen atmosphere. The mixture was stirred at room temperature for 3 hours, before quenching with the cautious addition of water and subsequent acidification with hydrochloric acid (2 M, 7 ml). Following the addition of saturated sodium hydroxide solution (3 ml), the THF layer was removed. The organic layer was then dried over magnesium sulphate and evaporated to produce a pale yellow powder (0.90 g, 78% yield): ^{1}H NMR ($CDCl_3$) δ 2.54 (3H, m), 4.86 (2H, m), 6.05 (2H, br s), 7.40-7.70 (3H, m); MH^+ (APCI+) 211.

2.3.3.9 $^{13}C_4$-4-amino-3-chloromethyl-5-fluoro-2-methylquinoline

$^{13}C_4$-4-amino-5-fluoro-3-hydroxymethyl-2-methylquinoline powder (0.64 g, 3.05 mmoles) was added slowly to vigorously stirred thionyl chloride (2.9 ml). The resulting mixture was stirred under reflux for 1.5 hours, before cooling and evaporation under reduced pressure. The residue was triturated with ethanol-free chloroform, the remaining solid filtered and dried in air to produce an off-white powder (0.76 g, 94% yield): ^{1}H NMR (DMSO) δ 2.78 (3H, m), 5.03 (2H, m), 7.40-7.09 (3H, m); MH^+ (APCI+) 225 (1 Cl).

2.3.3.10 $^{13}C_5$-4-amino-5-fluoro-2-methyl-3-(3-trifluoroacetylbenzyl-oxymethyl)quinoline

$^{13}C_4$-4-amino-3-chloromethyl-5-fluoro-2-methylquinoline (0.27 g, 1.04 mmoles) was mixed with α-^{13}C-3-trifluoroacetylbenzyl alcohol (1.07 g, 5.2 mmoles) and stirred at 125-130 °C for 4

hours. After cooling, the gum was stirred with water (10 ml) and diethyl ether (10 ml) until two clear layers were obtained. The aqueous portion was extracted with diethyl ether (5 x 10 ml)‡, before addition of sodium hydroxide solution (2 M) such that the alkalinity exceeded pH 10. The white precipitate was extracted into DCM (5 x 10 ml). After drying over magnesium sulphate, the DCM extracts were evaporated to give an off-white solid (0.32 g, 80% yield). After HPLC purification an off-white solid remained (100 mg, 25% yield): ^{1}H NMR ($CDCl_2$) δ 2.59 (3H, m), 4.62 (2H, m), 4.86 (2H, m), 6.00 (2H, br s), 6.90-8.15 (7H, m); MH^+ (APCI+) 398.

2.3.4 Synthesis of 4-amino-2-methyl-3-(3-trifluoroacetylbenzyl-oxymethyl)quinoline (R414983)

2.3.4.1 3-bromobenzoic acid

Benzoic acid (3.0 g, 24 mmoles) and potassium bromate (4.1 g, 24 mmoles) were dissolved in water (18 ml) and heated to 90 °C. Concentrated sulphuric acid (22 ml) was added dropwise over a period of 1 hour, after addition was completed the temperature was maintained at 90 °C for a further 2 hours. Heating was removed and the mixture was allowed to cool before the addition of water (50 ml) and the extraction of the product with diethyl ether (3 x 40 ml). Ether fractions were combined, washed with sodium metabisulphate solution, then dried over magnesium sulphate before evaporation under reduced pressure. The crude solid was repeatedly shaken with hot water (3 x 50 ml, 90 °C) and the undissolved material collected by filtration and dried, providing an pale brown powder (2.85 g, 57% yield): ^{1}H NMR (DMSO) δ 7.37 (1H, t), 7.78 (1H, d), 8.06 (1H, m), 8.25 (1H, m); $M\text{-}H^-$ (APCI-) 199 (1 Br).

‡ The starting material α-^{13}C-3-trifluoroacetylbenzyl alcohol is present in a 5:1 molar ratio to the second reactant, combination of ether extracts at this point, followed by drying over magnesium sulphate and rotary evaporation allows unreacted material to be recovered.

2.3.4.2 3-bromobenzyl alcohol

Lithium aluminium hydride (1.80 g, 46 mmoles) was mixed with anhydrous diethyl ether (85 ml), and a solution of 3-bromobenzoic acid (2.80 g, 13.8 mmoles) in anhydrous diethyl ether (60 ml) was added dropwise to the stirred mixture over a period of 30 minutes at 18-25 °C, under a nitrogen atmosphere. The mixture was refluxed for 1 hour, before being cooled and the reaction quenched with wet diethyl ether. The mixture was acidified by the addition of sulphuric acid (1 M, 65 ml), the ether layer was removed and the aqueous layer extracted with diethyl ether (3 x 45 ml). The extracts were combined, dried over magnesium sulphate and evaporated under reduced pressure to give a clear light brown oil (2.34 g, 90% yield): ^{1}H NMR ($CDCl_3$) δ 4.60 (2H, s), 7.10-7.60 (4H, m).

2.3.4.3 *N*-trifluoroacetylpiperidine

Trifluoroacetic anhydride (10 g, 47 mmoles) was added dropwise over a period of 30 minutes to a stirred solution of piperidine (5.1 g, 58 mmoles) and triethylamine (5 g, 49 mmoles) in diethyl ether (approx. 36 ml), maintained between 15-20 °C and under a nitrogen atmosphere. After addition was completed the solution was stirred at room temperature for a further 2 hours. A combination of ice and water (approx. 100 ml) was then added and the mixture well shaken. The ether fraction was removed and washed with dilute HCl until the washings became acidic (0.1M, 6 x 20 ml). The organic fraction was then washed with water (3 x 15 ml), dried over magnesium sulphate and evaporated under reduced pressure to produce a clear yellow oil (6.6 g, 61% yield: MH^+ (APCI+) 182.

2.3.4.4 1-bromo-3-(*tert*-butyldimethylsilyloxymethyl)benzene

tert-butyldimethylsilyl chloride (2.00 g, 13.2 mmoles) in anhydrous DMF (8 ml) was slowly added to a stirred solution of imidazole (2.13 g, 31.2 mmoles) in anhydrous DMF (4 ml). 3-bromobenzyl alcohol (2.30 g, 12.0 mmoles) in anhydrous DMF (4 ml) was then slowly added,

with the temperature maintained below 20 °C. The resulting mixture was stirred at 50 °C for 20 hours. Upon completion, the mixture was cooled, water added (50 ml) and the product extracted with hexane (4 x 20 ml). Organic extracts were combined, washed with water (4 x 10 ml) and then dried over magnesium sulphate. Hexane was removed by evaporation to produce a clear colourless oil (2.54 g, 69% yield): ^{1}H NMR ($CDCl_3$) δ 0.11 (6H, s), 0.96 (9H, s), 4.84 (2H, d), 7.10-7.60 (4H, m).

2.3.4.5 1-trifluoroacetyl-3-(*tert*-butyldimethylsilyloxymethyl)benzene

n-butyl lithium (2.5 M in hexanes, 3.7 ml, 9.1 mmoles) was added over a period of 20 minutes to a stirred solution of 1-bromo-3-(*tert*-butyldimethylsilyloxymethyl)benzene (2.50 g, 8.4 mmoles) in anhydrous diethyl ether (30 ml) maintained between 0-5 °C, under a nitrogen atmosphere. The resulting clear yellow solution was allowed to warm to 10 °C over 30 minutes before being recooled to 0 °C. *N*-trifluoroacetylpiperidine (1.51 g, 8.4 mmoles) in anhydrous diethyl ether (7 ml) was then added over a period of 30 minutes with the temperature maintained between 0-5 °C, followed by stirring at room temperature for 1 hour. The solution was then recooled to 0-5 °C and the reaction quenched with saturated ammonium chloride (15 ml). The aqueous portion was extracted with ether, extracts were combined, washed with ammonium chloride solution, then washed with water before drying over magnesium sulphate and evaporation to give a red-brown oil (2.39 g, 90% yield).

2.3.4.6 3-trifluoroacetylbenzyl alcohol

Concentrated hydrochloric acid (2.0 ml) was added dropwise to a stirred solution of 1-trifluoroacetyl-3-(*tert*-butyldimethylsilyloxymethyl)benzene (2.3 g, 7.3 mmoles) in methanol (20 ml) at 10-20 °C. The mixture was stirred at room temperature for 30 minutes before being reduced in volume (approx. 50%) on a rotary evaporator. The residue was diluted with diethyl ether (60 ml) and neutralised with a slurry of sodium bicarbonate/water before washing with

water (2 x 20 ml) and drying over magnesium sulphate. Evaporation under reduced pressure resulted in a yellow oil (1.22 g, 83% yield): ^{1}H NMR ($CDCl_3$) δ 4.81 (2H, d), 7.20-8.10 (4H, m); $MH+H_2O^+$ (APCI+) 220.

2.3.4.7 4-amino-3-carboxyethyl-2-methylquinoline

2-amino-benzonitrile (0.88 g, 7.5 mmoles) was dissolved in anhydrous toluene (20 ml) and ethyl acetoacetate added (1.00 g, 7.5 mmoles). Stannic chloride (3.90 g, 15 mmoles) was added over a period of 5 minutes with the temperature maintained around 20-22 °C. Following addition, the mixture was stirred under reflux for 5 hours before cooling and the supernatant removed. The residue was triturated with ethyl acetate (20 ml) and a yellow solid collected by filtration. The solid was stirred with sodium hydroxide solution (2 M, 28 ml) for 30 minutes, before extraction into ethyl acetate (4 x 25 ml). Extracts were washed with water before drying over magnesium sulphate and evaporation to give a yellow solid (1.47 g, 85% yield): ^{1}H NMR ($CDCl_3$) δ 1.44 (3H, t), 2.86 (3H, m), 4.43 (2H, m), 7.00 (2H, br s), 7.40-7.95 (3H, m); MH^+ (APCI+) 231.

2.3.4.8 4-amino-3-hydroxymethyl-2-methylquinoline

4-amino-3-carboxyethyl-2-methylquinoline (1.40 g, 6.0 mmoles) in anhydrous THF (15 ml) was added over a period of 1 hour to a cooled (18-25°C) solution of lithium aluminium hydride powder (0.242 g, 6.5 mmoles) in anhydrous THF (40 ml), under a nitrogen atmosphere. The mixture was stirred at room temperature for 3 hours, before quenching with the cautious addition of water and acidification with hydrochloric acid (2 M, 8 ml). The subsequent addition of saturated sodium hydroxide solution (3 ml) was then followed by removal of the THF layer. The organic layer was dried over magnesium sulphate and evaporated to produce a pale yellow powder (1.13 g, 97% yield): ^{1}H NMR ($CDCl_3$) δ 2.62 (3H, m), 4.79 (2H, m), 7.00 (2H, br s), 7.30-8.10 (3H, m); MH^+ (APCI+) 189.

2.3.4.9 4-amino-3-chloromethyl-2-methylquinoline

4-amino-3-hydroxymethyl-2-methylquinoline (1.10 g, 5.7 mmoles) was added slowly to vigorously stirred thionyl chloride (5.6 ml). The resulting mixture was stirred under reflux for 1.5 hours, before cooling and evaporation under reduced pressure. The residue was triturated with ethanol-free chloroform, the solid then filtered and dried in air to produce an off-white powder (0.88 g, 75% yield): MH^+ (APCI+) 203 (1 Cl).

2.3.4.10 4-amino-2-methyl-3-(3-trifluoroacetylbenzyl-oxymethyl)quinoline

4-amino-3-chloromethyl-2-methylquinoline (0.30 g, 1.45 mmoles) was mixed with 3-trifluoroacetylbenzyl alcohol (1.22 g, 6.7 mmoles) and stirred at 125-130 °C for 4 hours. After cooling, the gum was stirred with water (10 ml) and diethyl ether (10 ml) until two clear layers were obtained. The aqueous portion was extracted with diethyl ether (4 x 10 ml), before addition of sodium hydroxide solution (2 M) such that the alkalinity exceeded pH 10. The white precipitate was extracted into DCM (4 x 10 ml). After drying over magnesium sulphate, the DCM extracts were evaporated to give an off-white solid (0.38 g, 76% yield). After HPLC purification an off-white solid remained (95 mg, 19% yield): ^{1}H NMR ($CDCl_2$) δ 2.66 (3H, m), 4.61 (2H, m), 4.90 (2H, m), 7.35-8.10 (7H, m); MH^+ (APCI+) 375.

2.3.5 Synthesis of $^{13}C_5$-4-amino-2-methyl-3-(3-trifluoroacetylbenzyl-oxymethyl)quinoline ($^{13}C_5$-R414983)

2.3.5.1 α-^{13}C-3-bromobenzoic acid

α-^{13}C-benzoic acid (6.0 g, 48 mmoles) and potassium bromate (8.2 g, 48 mmoles) were dissolved in water (35 ml) and heated to 90 °C. Concentrated sulphuric acid (40 ml) was added dropwise over a period of 1 hour, after addition was completed the temperature was maintained at 90 °C for a further 2 hours. Heating was removed and the mixture was allowed to cool before the addition of water (100 ml) and the extraction of the product with diethyl

ether (3 x 50 ml). Ether fractions were combined, washed with sodium metabisulphate solution, then dried over magnesium sulphate before evaporation under reduced pressure. The crude solid was repeatedly shaken with hot water (3 x 100 ml, 90 °C) and the undissolved material collected by filtration and dried, providing an pale brown powder (5.95 g, 59% yield): ^{1}H NMR (DMSO) δ 7.38 (1H, t), 7.78 (1H, d), 8.05 (1H, m), 8.27 (1H, m); M-H^{-} (APCI-) 200 (1 Br).

2.3.5.2 α-^{13}C-3-bromobenzyl alcohol

Lithium aluminium hydride (3.85 g, 96 mmoles) was mixed with anhydrous diethyl ether (175 ml), and a solution of α-^{13}C-3-bromobenzoic acid (5.95 g, 29 mmoles) in anhydrous diethyl ether (120 ml) was added dropwise to the stirred mixture over a period of 30 minutes at 18-25 °C, under a nitrogen atmosphere. The mixture was refluxed for 1 hour, before being cooled and the reaction quenched with wet diethyl ether. The mixture was acidified by the addition of sulphuric acid (1 M, 120 ml), the ether layer was removed and the aqueous layer extracted with diethyl ether (3 x 90 ml). The extracts were combined, dried over magnesium sulphate and evaporated under reduced pressure to give a clear light brown oil (4.6 g, 86% yield).

2.3.5.3 *N*-trifluoroacetylpiperidine

Trifluoroacetic anhydride (10 g, 47 mmoles) was added dropwise over a period of 30 minutes to a stirred solution of piperidine (5.1 g, 58 mmoles) and triethylamine (5.0 g, 49 mmoles) in diethyl ether (approx. 36 ml) maintained between 15-20 °C and under a nitrogen atmosphere. After addition was completed the solution was stirred at room temperature for a further 2 hours. A combination of ice and water (approx. 100 ml) was then added and the mixture well shaken. The ether fraction was removed and washed with dilute HCl until the washings became acidic (0.1M, 6 x 20 ml). The organic fraction was then washed with water (3 x 15 ml),

dried over magnesium sulphate and evaporated under reduced pressure to produce a clear yellow oil (5..9g, 54 % yield: MH^+ (APCI+) 182.

2.3.5.4 α-^{13}C-1-bromo-3-(*tert*-butyldimethylsilyloxymethyl)benzene

tert-butyldimethylsilyl chloride (4.04 g, 26.7 mmoles) in anhydrous DMF (18 ml) was slowly added to a stirred solution of imidazole (4.25 g, 62.3 mmoles) in anhydrous DMF (7 ml). α-^{13}C-3-bromobenzyl alcohol (4.55 g, 24.1 mmoles) in anhydrous DMF (7 ml) was then slowly added, with the temperature maintained below 20 °C. The resulting mixture was stirred at 50 °C for 20 hours. Upon completion the mixture was cooled, water (100 ml) added and the product extracted with hexane (4 x 35 ml). Organic extracts were combined, washed with water (4 x 20 ml) and then dried over magnesium sulphate. Hexane was removed by evaporation to produce a clear colourless oil (5.90 g, 81% yield): ^{1}H NMR ($CDCl_3$) δ 0.11 (6H, s), 0.96 (9H, s), 4.86 (2H, d), 7.10-7.60 (4H, m).

2.3.5.5 α-^{13}C-1-trifluoroacetyl-3-(*tert*-butyldimethylsilyloxymethyl)benzene

n-butyl lithium (2.5 M in hexanes, 8.60 ml, 21.2 mmoles) was added over a period of 25 minutes to a stirred solution of α-^{13}C-1-bromo-3-(*tert*-butyldimethylsilyloxymethyl)benzene (5.90 g, 19.5 mmoles) in anhydrous diethyl ether (65 ml) maintained between 0-5 °C, under a nitrogen atmosphere. The resulting clear yellow solution was allowed to warm to 10 °C over 30 minutes before being recooled to 0 °C. *N*-trifluoroacetylpiperidine (3.54 g, 19.4 mmoles) in anhydrous diethyl ether (18 ml) was then added over a period of 30 minutes with the temperature maintained between 0-5 °C, followed by stirring at room temperature for 1 hour. The solution was then recooled to 0-5 °C and the reaction quenched with saturated ammonium chloride (25 ml). The aqueous portion was extracted with ether, extracts were combined, washed with ammonium chloride solution, then washed with water before drying over magnesium sulphate and evaporation to give a red-brown oil (5.77 g, 92% yield).

2.3.5.6 α-^{13}C-3-trifluoroacetylbenzyl alcohol

Concentrated hydrochloric acid (5.0 ml) was added dropwise to a stirred solution of α-^{13}C-1-trifluoroacetyl-3-(*tert*-butyldimethylsilyloxymethyl)benzene (5.70 g, 18 mmoles) in methanol (50 ml) at 10-20 °C. The mixture was stirred at room temperature for 30 minutes before reduced in volume (approx. 50%) on a rotary evaporator. The residue was diluted with diethyl ether (150 ml) and neutralised with a slurry of sodium bicarbonate/water before washing with water and drying over magnesium sulphate. Evaporation under reduced pressure resulted in a yellow oil (3.28 g, 88% yield): ^{1}H NMR ($CDCl_3$) δ 4.80 (2H, d), 7.20-8.15 (4H, m); $MH+H_2O^+$ (APCI+) 221.

2.3.5.7 $^{13}C_4$-4-amino-3-carboxyethyl-2-methylquinoline

2-amino-benzonitrile (0.88 g, 7.5 mmoles) was dissolved in anhydrous toluene (20 ml) and 1,2,3,4-$^{13}C_4$-ethyl acetoacetate added (1.00 g, 7.5 mmoles). Stannic chloride (3.90 g, 15 mmoles) was added over a period of 5 minutes with the temperature maintained around 20-22 °C. Following addition the mixture was stirred under reflux for 5 hours before cooling and the supernatant removed. The residue was triturated with ethyl acetate (20 ml) and a yellow solid collected by filtration. The solid was stirred with sodium hydroxide solution (2 M, 28 ml) for 30 minutes, before extraction into ethyl acetate (4 x 25 ml). Extracts were washed with water before drying over magnesium sulphate and evaporation to give a yellow solid (1.40 g, 81% yield): ^{1}H NMR ($CDCl_3$) δ 1.46 (3H, t), 2.85 (3H, m), 4.43 (2H, m), 7.05 (2H, br s), 7.40-7.95 (3H, m); MH^+ (APCI+) 235.

2.3.5.8 $^{13}C_4$-4-amino-3-hydroxymethyl-2-methylquinoline

$^{13}C_4$-4-amino-3-carboxyethyl-2-methylquinoline (1.40 g, 6.0 mmoles) in anhydrous THF (15 ml) was added over a period of 1 hour to a cooled (18-25°C) solution of lithium aluminium hydride powder (0.242 g, 6.5 mmoles) in anhydrous THF (40 ml), under a nitrogen

atmosphere. The mixture was stirred at room temperature for 3 hours, before quenching with the cautious addition of water and acidification with hydrochloric acid (2 M, 8 ml). The subsequent addition of saturated sodium hydroxide solution (3 ml) was then followed by removal of the THF layer. The organic layer was dried over magnesium sulphate and evaporated to produce a pale yellow powder (1.15 g, 99% yield): ^{1}H NMR ($CDCl_3$) δ 2.62 (3H, m), 4.79 (2H, m), 7.05 (2H, br s), 7.30-8.10 (3H, m); MH^+ (APCI+) 193.

2.3.5.9 $^{13}C_4$-4-amino-3-chloromethyl-2-methylquinoline

$^{13}C_4$-4-amino-3-hydroxymethyl-2-methylquinoline powder (1.15 g, 5.95 mmoles) was added slowly to vigorously stirred thionyl chloride (5.8 ml). The resulting mixture was stirred under reflux for 1.5 hours, before cooling and evaporation under reduced pressure. The residue was triturated with ethanol-free chloroform, the resulting solid filtered and dried in air to produce an off-white powder (0.81 g, 66% yield): MH^+ (APCI+) 207 (1 Cl).

2.3.5.10 $^{13}C_5$-4-amino-2-methyl-3-(3-trifluoroacetylbenzyl-oxymethyl)quinoline

$^{13}C_4$-4-amino-3-chloromethyl-2-methylquinoline (0.55 g, 2.67 mmoles) was mixed with α-^{13}C-3-trifluoroacetylbenzyl alcohol (2.20 g, 12 mmoles) and stirred at 125-130 °C for 4 hours. After cooling, the gum was stirred with water (20 ml) and diethyl ether (20 ml) until two clear layers were obtained. The aqueous portion was extracted with diethyl ether (5 x 20 ml)[§], before addition of sodium hydroxide solution (2 M) such that the alkalinity exceeded pH 10. The white precipitate was extracted into DCM (5 x 20 ml). After drying over magnesium sulphate, the DCM extracts were evaporated to give an off-white solid (0.64 g, 63% yield). After HPLC

[§] The starting material α-^{13}C-3-trifluoroacetylbenzyl alcohol is present in a 5:1 molar ratio to the second reactant, combination of ether extracts at this point, followed by drying over magnesium sulphate and rotary evaporation allows unreacted material to be recovered.

purification an off-white solid remained (170 mg, 17% yield): ^{1}H NMR ($CDCl_2$) δ 2.64 (3H, m), 4.62 (2H, m), 4.90 (2H, m), 7.40-8.15 (7H, m); MH^+ (APCI+) 380.

2.4 Discussion

Considering the small scale under which synthesis was performed, the yields obtained are within the expected range. A relatively large quantity, in comparison the amounts required for NMR studies, of both the unlabelled and labelled inhibitors was successfully produced (Table 2.1). The subsequent purification of the compounds by HPLC has ensured that they only contain trace amounts of impurities (confirmed by both solution NMR and mass spectrometry).

Table 2.1 – Summary of synthesis yields.

Compound	Mass of product (mg)	Moles of product (mM)
R414425	48	0.12
$^{13}C_5$-R414425	100	0.25
R414983	95	0.25
$^{13}C_5$-R414983	170	0.45

The presence of ^{19}F and ^{13}C isotopic labels in the final inhibitor structures provides the opportunity for a range of NMR experiments to investigate internuclear separations when the inhibitors are bound to acetylcholinesterase. Homonuclear and heteronuclear distance determinations are both possible: ^{13}C-^{13}C in both $^{13}C_5$-R414425 and $^{13}C_5$-R414983; ^{19}F-^{19}F in $^{13}C_5$-R414425; ^{13}C-^{19}F in $^{13}C_5$-R414983.

The restriction imposed on the choice of labelling schemes by the availability of isotopically labelled reactants is limiting. Distance measurements based on the current schemes can only provide constraints which, although significantly reducing the range of conformations which

the inhibitors could potentially adopt, cannot be used to determine the absolute conformation whilst at their binding sites.

Chapter 3 Characterisation of Inhibitors

3.1 Overview

The potency of acetylcholinesterase inhibitors is largely maintained across different species, although exceptions are known to exist (see Chapter 1). Neither of the two compounds R414425 and R414983 has previously been tested as an inhibitor of *Electrophorus electricus* acetylcholinesterase. Monitoring of the rate of substrate hydrolysis in the presence of a range of inhibitor concentrations enables the determination of the inhibitor concentration where 50% of enzyme activity remains (the IC_{50}). Additionally, the impact of steps used in the preparation of samples for NMR studies on the activity of acetylcholinesterase is examined (such as freezing, freeze drying and dialysis).

The chemical shift of an NMR resonance is a sensitive probe of the electronic environment around a nucleus and is reflected in the isotropic and anisotropic part of the interaction. Chemical shifts of the labelled inhibitors $^{13}C_5$-R414425 and $^{13}C_5$-R414983 are investigated in solid form, in solution and when bound to acetylcholinesterase. The variation in chemical shifts between these states may provide an insight to the conformational changes which occur during binding of the inhibitors.

3.2 Introduction

3.2.1 Acetylcholinesterase Activity Assays

The chemical and physical properties of acetylcholine, its related esters and their hydrolysis products are such that assays involving natural substrates are particularly difficult. However, it is generally accepted that thio analogues of substrates, such as acetylthiocholine or butyrylthiocholine, provide appropriate replacements. These compounds report hydrolysis rates closely matching their natural counterparts yet are suitable for simple photometric monitoring of the reaction process [179]. The methodology may be applied to protein extracts, homogenates or suspensions of whole cells.

Acetylthiocholine (present in excess) is hydrolysed by acetylcholinesterase to form acetate and thiocholine. Subsequently, the thiocholine reacts with 5,5'-dithiobis(2-nitrobenzoic acid) (DTNB) and releases the strongly coloured 5-thio-2-nitrobenzoic acid (in anion form). The second reaction step is not rate limiting, therefore the development of absorbance at 412 nm can be directly related to enzyme activity. Figure 3.1 shows the reactions involved in the assay process.

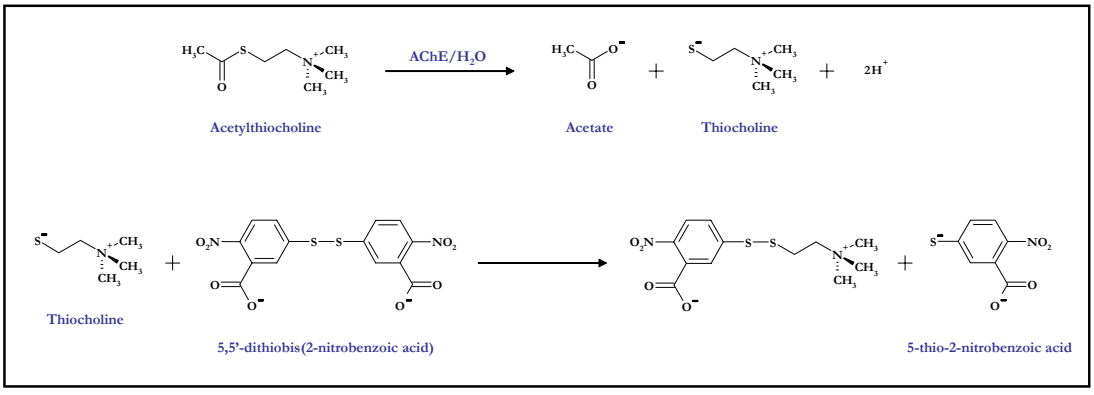

Figure 3.1 – The Ellman Assay [179]: acetylcholinesterase activity is measured through a coupled reaction involving the acetylcholine analogue acetylthiocholine.

3.2.2 Chemical Shift Investigation

3.2.2.1 Chemical shifts

In a uniform applied magnetic field the movement of electrons around a nucleus results in the generation of a secondary magnetic field. This secondary field is opposed to the applied field and causes a nucleus to experience a reduced net magnetic field, the exact value of which is dependent upon the degree of shielding provided by the associated electrons. The chemical shift of a nucleus is therefore a sensitive indicator of its local electronic environment and, as such, is also a potential source of structural information.

Chemical shifts are dominated by the type of atom under investigation (which defines the ground-state electron arrangement) and the nature of chemical bonding to neighbouring atoms (which determines both hybridisation of electron orbitals and the degree of electron withdrawal, donation or delocalisation). For structural studies on biological samples it is the more subtle effects which are of greatest interest, such as perturbations arising from molecular conformation or intermolecular interactions.

^{1}H, ^{13}C and ^{15}N chemical shifts in peptides show a marked dependency upon the relative orientation of the peptide planes (Figure 3.2) defined by the angles Φ and Ψ.

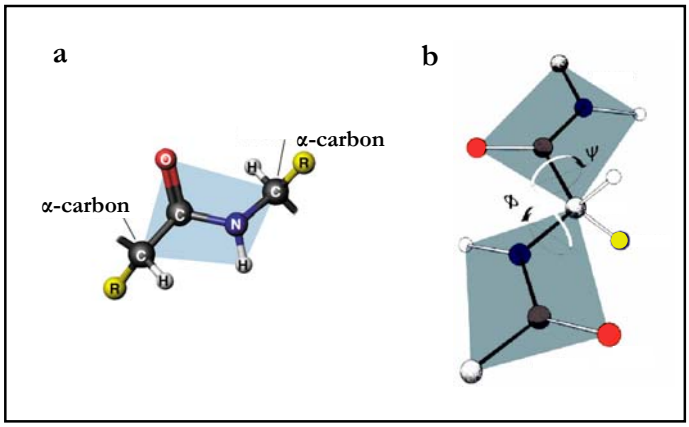

Figure 3.2 – The peptide plane: a rigid plane is formed due to the double bond character of the carbon-nitrogen peptide bond [180].

Since secondary structural motifs have different associated arrangements of their peptide planes, the chemical shift of a nucleus can be used to derive the backbone structure by comparison with known data (Figure 3.3) [181-183]. The combination of multiple chemical shifts from a single residue ($^{13}C\alpha$, $^{13}C\beta$, $^{13}C'$, $^{1}H\alpha$ and ^{15}N) and comparison with data from only homologous proteins can provide a more reliable estimate of Φ and Ψ angles, accurate to within 15° of x-ray crystallography results [184].

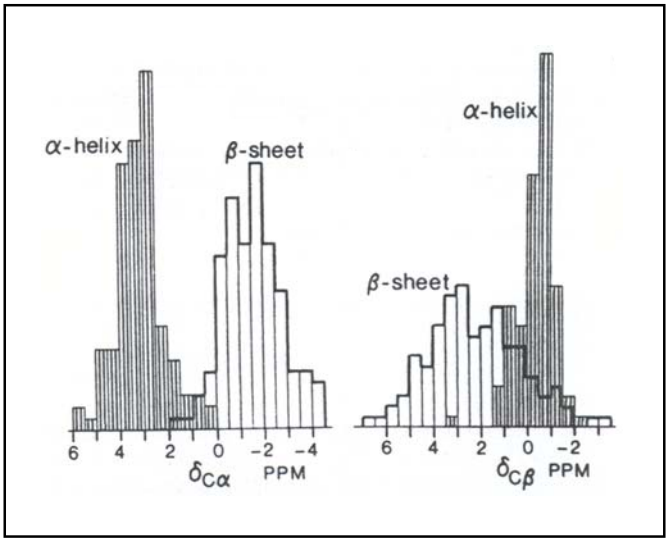

Figure 3.3 – Conformationally dependent chemical shifts: histograms of secondary shift distribution in α-helix and β-sheet [183].

The C16 and C17 methyl groups of retinal, the chromophore of rhodopsin, demonstrate identical chemical shifts in solution (28.8 ppm, in heptane) although are resolved as two inequivalent sites in the dark-state of rhodopsin (occurring at 30.8 and 26.4 ppm) [185]. Figure 3.4 illustrates the positions of the two methyl groups with respect to the β-ionone ring. Steric interaction between the axial methyl (C17) and the axial proton at the C3 position is responsible for the different shifts.

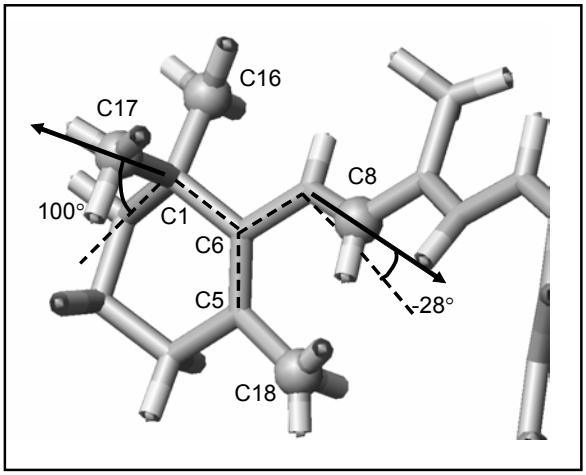

Figure 3.4 – Proposed conformation of the β-ionone ring of retinal in the dark-state of rhodopsin: the C16 and C17 methyl groups occupy equatorial and axial positions with respect to the ring, causing inequivalence in their chemical shifts [185].

In practice, the presence of multiple effects can make deconvolution of specific interactions difficult (including steric interactions, ring currents, electrostatics and hydrogen bonding). Solid-state NMR has an advantage over solution studies in relation to the investigation of chemical shifts due to the absence of CSA averaging. As a result, both the isotropic chemical shift and the anisotropy can be characterised, enabling a more detailed analysis of the electronic shielding distribution within a system.

3.2.2.2 Determining chemical shift parameters

Methods are available for the extraction of the principal chemical shift tensor elements from a spinning sideband pattern [186]. However, it is first necessary for the sideband intensities to be determined accurately. In the current study, involving small quantities of a multiply labelled ligand bound to protein, this process is complicated by the presence of a protein background and overlapping sideband envelopes.

The protein background may be removed through the preparation of a second sample, prepared in parallel to the protein-inhibitor complex but lacking the labelled inhibitor.

Subtraction of the 'protein only' spectrum from that of the complex reliably compensates for the protein background, providing a spectrum comparable to the bound form of the inhibitor alone.

To determine the tensor elements accurately, the sample spinning speed must be selected so that a sufficient number of sidebands remain for each of the labelled positions. However, at such low speeds the spectrum becomes significantly more complex. Since the strength of magnetic shielding scales linearly with the applied magnetic field, the advantages of higher frequency spectrometers are clear:

- increased sensitivity
- increased resolution
- greater number of sidebands at a given spinning frequency

2D-PASS [187] is a two dimensional NMR experiment which separates spinning sidebands by their order. This is achieved through the manipulation of sideband phases by the application of five π pulses with variable spacings (Figure 3.5). Pulses are initially spaced evenly throughout a single rotor cycle. In subsequent increments the pulse positions are varied in a complex manner. It is important to note that the 2D-PASS experiment is susceptible to the effects of residual dipolar couplings - a weakness which may prove significant in the network of multiple labels presently under investigation.

Symmetry based radio-frequency cycles, based on either C sequences (where the net impact of each cycle element on spins is a 360^{o} rotation of spins) or R sequences (an 180^{o} rotation), enable the design of new experiments which select specific spin interactions [188, 189]. Each interaction is selected on the basis of its relationship to the molecular framework (Space rank), nuclear spin polarisation (Spin rank) and rotations of the external magnetic field (Field rank).

The values of these parameters for homonuclear spin interactions are shown in Table 3.1 (corresponding values are also available for heteronuclear interactions) [188].

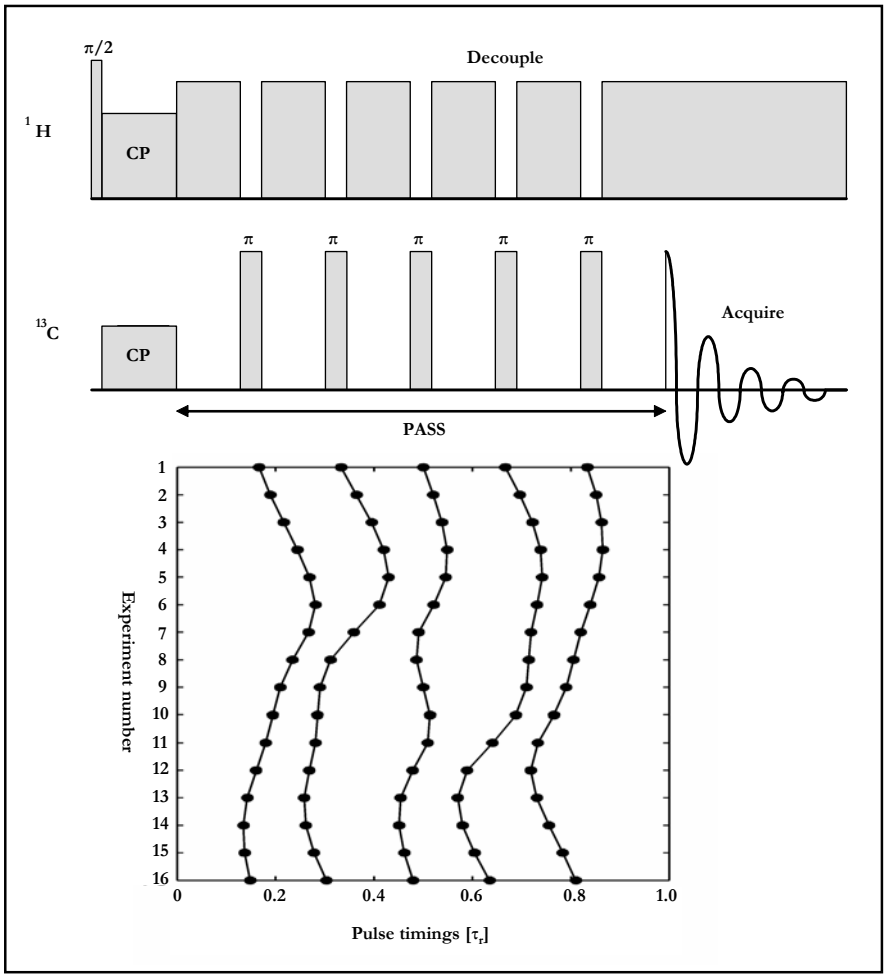

Figure 3.5 – Pulse sequence for the 2D-PASS experiment.

Table 3.1 – Rotational signatures of homonuclear spin interactions in diamagnetic systems of spin-½.

Interaction	Space rank, *l*	Spin rank, λ	Field rank
Isotropic chemical shift	0	1	1
Chemical shift anisotropy	2	1	1
J-coupling	0	0	0
Dipole-dipole coupling	2	2	0

Each sequence is described using the notation XN^{ν}_{n}, where X denotes the use of either C or R elements, and n describes the number of sample revolutions into which N equal intervals are

each filled with a radio-frequency based π rotation around the x-axis. The final parameter, ν, denotes the phase shift of the radio-frequency pulses for the segments. Many of the 'traditionally' designed experiments can be described using symmetry notation - RFDR (see Chapter 4) corresponds $R4^1_4$, while the REDOR scheme (see Chapter 5) corresponds to $R4^1_2$. The C7 scheme, specifically $C7^2_1$ in the current study, recouples the homonuclear dipolar interaction and can be used for the development of double quantum coherences for DQF and correlation experiments.

The $R12^4_5$ experiment (Figure 3.6) recouples the chemical shift anisotropy, while suppressing the isotropic chemical shift and homonuclear dipolar couplings. However, in the absence of radio-frequency pulses on the non-observed spins, heteronuclear interactions are also recoupled by the scheme [188].

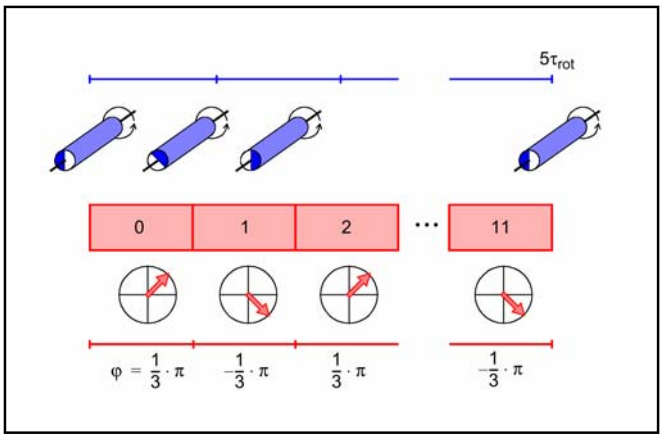

Figure 3.6 – The $R12^4_5$ scheme: Five rotor cycles are split evenly into 12 elements (each of which has the effect of a 180° rotation of spins), RF phases are alternated between ±1/3 π.

3.2.2.3 Modelling of chemical shifts

Advances in computational power mean that semi-empirical methods for the estimation of NMR parameters [190] have become relatively fast. Software packages are available which can calculate chemical shifts based on a given input molecular structure and conformation (such as deMon, from the University of Montreal).

The chemical shifts of the labelled sites within $^{13}C_5$-R414983, and their variation with changes in the conformation of the molecule, are presently under investigation by Dr Rene Verel (Oxford). It is hoped that values for chemical shifts and CSA tensor elements determined experimentally on the solid inhibitor and for the inhibitor bound to acetylcholinesterase can be correlated with changes in the inhibitor conformation and environment upon binding. This modelling work is currently at a preliminary stage and will not be discussed further here.

3.3 Methodology

3.3.1 Acetylcholinesterase Assays

3.3.1.1 General

Acetylcholinesterase activity and inhibition assays were performed according to the Ellman method [179]. Acetylthiocholine (ATCh) iodide solution (0.075 M, 21.67 mg/ml) was prepared in water. 5,5'-dithiobis(2-nitrobenzoic acid) (DTNB) (0.1 M, 3.96 mg/ml) was dissolved in pH 7.0 phosphate buffer (0.1 M) containing 0.15% (w/v) sodium bicarbonate. A concentrated AChE solution was prepared by dissolving 100 units of lyophilised *Electrophorus electricus* AChE (Sigma-Aldrich, Type V-S) in 25 ml of 0.2% aqueous gelatine, dilution of this concentrate with water was performed before use (typically 1:1) such that the final enzyme activity comprised between 0.15 and 0.10 AU/min. Serial dilutions of the test compounds (R414425, R414983, tacrine and galanthamine) were prepared in water at 3.14 times their desired final concentrations (1 mM – 10 fM).

Phosphate buffer (1.0 ml, 0.1 M, pH 8.0) was first mixed with DTNB solution (50 µl) and AChE (10 µl) before the addition of either an inhibitor test solution or water (0.5 ml) as appropriate. Following preincubation at 25 °C for 10 minutes, 10 µl of ATCh solution was

added. The absorbance at 412 nm was followed for a period of 10 minutes, using a Beckman-Coulter DU 640 spectrophotometer. Data was corrected for non-enzymatic contributions to hydrolysis by the use of a blank containing all components except for AChE.

3.3.1.2 Inhibitor assays

For each concentration of the four inhibitors tested, five samples were analysed. IC_{50} values, defined as the inhibitor concentration were 50% of enzyme activity remains, were determined by non-linear least squares fitting of a sigmoidal function (Equation 3.1) to the experimental results using Microcal Origin version 5.0.

$$y = \min + \frac{\max - \min}{1 + e^{-k(x - Xmid)}} \qquad \text{Equation 3.1}$$

Where x and y are variables, max and min define the data range, with Xmid the value of x at y=(max+min)/2. In the case of an ideal dose response curve, max and min correspond to 1 and 0 respectively, while Xmid is the IC_{50}.

3.3.1.3 AChE stability

Five aliquots of AChE solution (1 ml) were subjected to different treatments to examine the susceptibility of the enzyme to damage as a result of handling steps such as those involved during the preparation of samples for NMR analysis:

- a control sample was maintained at 4 °C for 3 hours
- to test the effects of slow freezing, a sample was placed in a freezer (-20 °C) for 3 hours
- a sample was quickly frozen by rotating a round bottom flask in liquid nitrogen
- a sample was quickly frozen (as above) and subsequently lyophilised
- a final sample was maintained at 25 °C for 3 hours

The lyophilised sample was reconstituted to its initial volume before testing. The first four samples were tested three times to determine acetylcholinesterase activity, while the room temperature sample was examined at 30 minute intervals.

3.3.2 Solution NMR Experiments

3.3.2.1 Pure labelled inhibitors

^{13}C and ^{19}F spectra of the isotopically labelled inhibitors, $^{13}C_5$-R414425 and $^{13}C_5$-R414983, were recorded using a 250 MHz (^1H frequency, 63 MHz for carbon, 235 MHz for fluorine) Bruker DPX spectrometer. Samples were prepared at a concentration between 1-2 mg/ml in either deuterium oxide or deuterated chloroform. Approximately 700 µl was used for analysis. ^{13}C spectra were acquired with proton decoupling (400-1200 transients) and ^{19}F without decoupling (60-150 transients).

3.3.2.2 $^{13}C_5$-R414983 bound to acetylcholinesterase

Musca domestica acetylcholinesterase* (*Md*AChE), at an initial concentration of 1.0 mg/ml, was reduced in volume from 5 ml to approximately 400 µl using Amicon Centricons (3 kDa molecular weight cut-off) while maintained at 4 °C. A 50:1 molar excess of $^{13}C_5$-R414983 was added to the concentrate (1.5 ml of aqueous solution at a concentration of 1 mg/ml) and the mixture left at room temperature for 15 minutes. After cooling to 4 °C the volume was again reduced to 400 µl. Excess inhibitor was removed by dialysis in 100 ml of buffer solution (20 mM phosphate, pH 7.0, 0.5 mM EDTA, 0.02% NaN_3) for 12 hours at 4 °C. 300 µl of the protein solution was placed in a susceptibility matched NMR tube and a ^{19}F spectrum recorded, over 20480 acquired, using a 500 MHz (^1H frequency, 470 MHz for fluorine) Varian

* *Md*AChE exists mainly in the G2a-I form (covalently linked GPI-anchored dimers). The enzyme utilised was a C575S mutant, which is unable to form covalent link between monomer units and therefore remains as a monomer in solution.

Infinity spectrometer. ^{19}F spectra of the protein sample with additional inhibitor (a nominal quantity) and the pure inhibitor solution were also recorded (20480 and 16 transients respectively) for the purposes of spectral assignment.

3.3.3 Solid-Sate NMR Experiments

3.3.3.1 Pure labelled inhibitors

^{13}C spectrum of $^{13}C_5$-R414425

Solid $^{13}C_5$-R414425 (10 mg) was placed within a 4 mm Bruker MAS rotor and a ^{13}C spectrum acquired on a 200 MHz (^1H frequency, 50 MHz for carbon) Chemagnetics spectrometer. The probe and spinning module were supplied by Bruker. 1024 scans were recorded at room temperature using a CP experiment with TPPM decoupling, ω_r 12000 Hz,.

^{13}C spectrum of $^{13}C_5$-R414983

Solid $^{13}C_5$-R414983 (22 mg) was placed within a 4 mm Chemagnetics MAS rotor and a ^{13}C spectrum acquired on a 500 MHz (^1H frequency, 125 MHz for carbon) Chemagnetics spectrometer. 1000 scans were recorded at room temperature using a standard single pulse experiment with continuous wave (CW) proton decoupling and 9000 Hz spinning speed.

2-D correlation experiments

A two dimensional C7 experiment [191, 192] was performed on solid labelled R414983 for the assignment of resonances. 3.5 mg of $^{13}C_5$-R414983 was placed within a 4 mm Bruker MAS rotor and a ^{13}C spectrum acquired on a 200 MHz (^1H frequency, 50 MHz for carbon) Chemagnetics spectrometer. The probe and spinning module were supplied by Bruker. Figure 3.7 shows the sequence used. Initial proton magnetisation, generated using an 85 kHz field, was transferred to carbon spins during a 1 ms period of cross-polarisation (85 kHz field on

both channels). During τ_1 and acquisition TPPM decoupling was applied, while CW decoupling was utilised during the C7 cycle (85 kHz proton field strength in both cases). A carbon field strength of 70 kHz was used during the C7 cycle. 128 τ_1 increments were recorded for each of three mixing times (0.6 ms, 1.2 ms and 2.4 ms), with 128 acquisitions taken in each slice. The spinning speed was maintained at 10000 Hz.

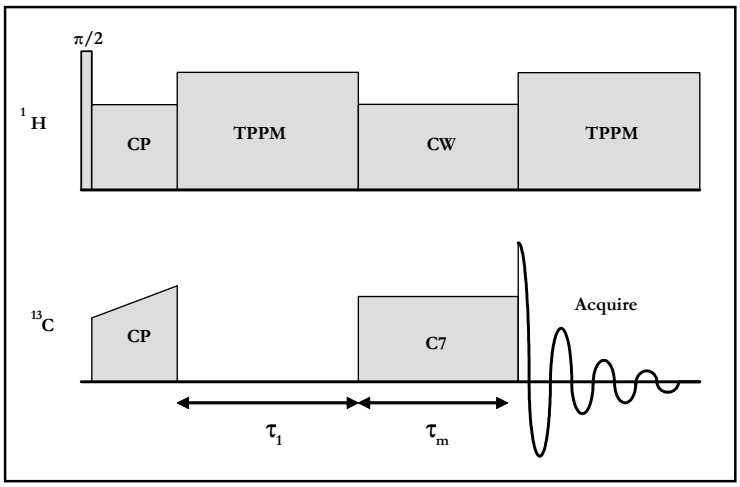

Figure 3.7 – Pulse sequence for a two-deimensional C7 experiment.

^{19}F spectra of $^{13}C_5$-R414425 and $^{13}C_5$-R414983

Solid $^{13}C_5$-R414983 (22 mg) or $^{13}C_5$-R414425 (80 mg) was placed within a 6 mm Chemagnetics MAS rotor and a ^{19}F spectrum acquired on a 500 MHz (^{1}H frequency, 470 MHz for fluorine) Chemagnetics spectrometer with a triple channel (HFX) MAS probe. 400 acquisitions were recorded at room temperature using a standard single pulse experiment with CW proton decoupling at spinning frequencies from 6000-9000 Hz. A 63 kHz field was used for generation of fluorine magnetisation, with a 63 kHz decoupling field applied on the proton channel during acquisition.

3.3.3.2 $^{13}C_5$-R414983 bound to acetylcholinesterase

Sample preparation

Lyophilised *Electrophorus electricus* AChE (50,000 units, Sigma-Aldrich Type V-S, approximately 30 mg/400 nmoles protein) were dissolved in distilled water (8 ml) and divided between two previously prepared Float-a-lyzers (3500 Da limit) for dialysis (4 hours, 4 °C, 5 litres of 25 mM potassium phosphate, 0.05 mM EDTA at pH 7.1).

The dialysed solutions were first combined, then divided again into two equal volumes. An excess (approximately 10:1 molar ratio) of $^{13}C_5$- labelled R414983 was added to one half of the enzyme (1 ml, 1 mg/ml), with buffer solution (1 ml, 25 mM potassium phosphate, 0.05 mM EDTA, pH 7.1) added to the remaining enzyme). Both solutions were left to equilibrate (30 min, 25 °C) before dialysis using two further Float-a-lyzers (3500 Da limit) to remove the unbound excess inhibitor (12 hours, 4 °C, 5 litres of 25 mM potassium phosphate, 0.05 mM EDTA at pH 7.1). After completion of the second dialysis step the enzyme samples were frozen quickly in liquid nitrogen and lyophilised.

NMR experiments

Experiments were performed on a Chemagnetics 500 MHz (^{1}H frequency - 125 MHz for ^{12}C and 470 MHz for ^{19}F) spectrometer using either a 4 mm dual channel Chemagnetics Apex MAS probe for ^{13}C experiments or a 6 mm triple channel (HFX) MAS probe for ^{19}F observe experiments. The temperature was maintained at -30 °C.

^{13}C spectra of the protein and protein/inhibitor samples were acquired using a ramped CP experiment. A 63 kHz field was used to generate initial proton magnetisation and during CP, while a 100 kHz field was applied for decoupling during the relaxation decay and a 63 kHz field during acquisition. A carbon field strength of 63 kHz was applied for CP, modulated by a

20% linear ramp. The spinning speed was set to 7500 Hz, with 2000 acquisitions were made on each sample. Spectral subtractions were performed using the FELIX software package.

^{19}F spectra of the protein/inhibitor sample were acquired using a ramped CP experiment. A 63 kHz field was used to generate initial proton magnetisation, a 42 kHz field during CP and a 63 kHz field was for decoupling during acquisition. A fluorine field strength of 42 kHz was applied for CP, modulated by a 20% linear ramp. Two experiments were performed, with the spinning speed set to 9000 Hz (6144 transients) and 6500 Hz (12288 transients).

3.3.3.3 Anisotropy investigation

PASS experiment

A 750 MHz (^1H frequency, 188 MHz for carbon) Bruker DSX spectrometer was used to examine a sample of solid $^{13}C_5$-R414983 (20 mg) using the PASS sequence†. A 4 mm dual channel MAS probe was utilised. The PASS pulse sequence was supplied by Bruker Analytik (CPPASS) and was used without modification. A 55 kHz field was used for initial generation of proton magnetisation, during CP and decoupling. A 55 kHz field was applied on the carbon channel during CP and a 60 kHz field for π pulses. 81 scans were acquired in each of 16 slices in the indirect dimension. The temperature was maintained at 0 ^oC and a spinning speed of 2000 Hz was used.

$R12^4_5$ experiment

Figure 3.5 shows the general form of the pulse sequence for the $R12^4_5$ experiment. Inversions during each R segment were achieved by the application of a composite pulse (90_0270_{180}). A

† The protein/inhibitor complex and protein background samples were also examined. However, the signal to noise from these samples was insufficient for sideband analysis. The results are therefore not included here, although it is intended that further experiments are performed with these samples.

sample of solid $^{13}C_5$-R414983 (20 mg) was examined on a 500 MHz (^{1}H frequency, 125 MHz for ^{13}C) Chemagnetics spectrometer using a 4 mm dual channel Apex MAS probe. A 100 kHz field was used to generate initial proton magnetisation and during CP, while a 100 kHz field was applied for decoupling. A carbon field strength of 100 kHz was used for CP (modulated by a 10% linear ramp), with a 28 kHz field used during the recoupling sequence. The spinning speed was set to 15000 Hz. 320 acquisitions were made in each of 33 slices.

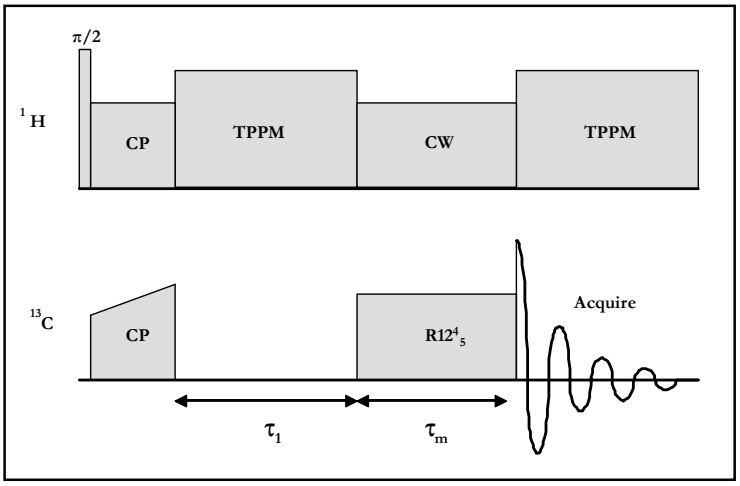

Figure 3.8 – Pulse sequence for a two-dimensional R12$^4_5$ experiment.

3.4 Results

3.4.1 Activity Assays

3.4.1.1 Inhibitor testing

Dose response curves for each of the four inhibitors tested are shown in Figure 3.9-Figure 3.12. The IC_{50} values derived from these results are summarised in Table 3.2 and compared to published data where available.

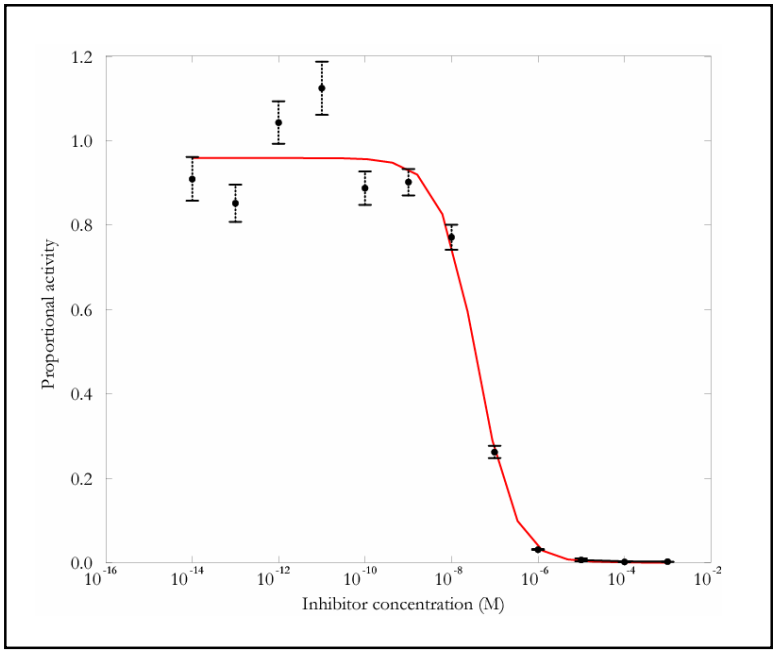

Figure 3.9 – Dose response curve showing tacrine inhibition of *Electrophorus electricus* AChE: Experimental points (an average of 5 data sets) are shown as black filled circles with the standard deviation indicated by error bars. A sigmoidal fit to the experimental data is shown in red (R = 0.9882).

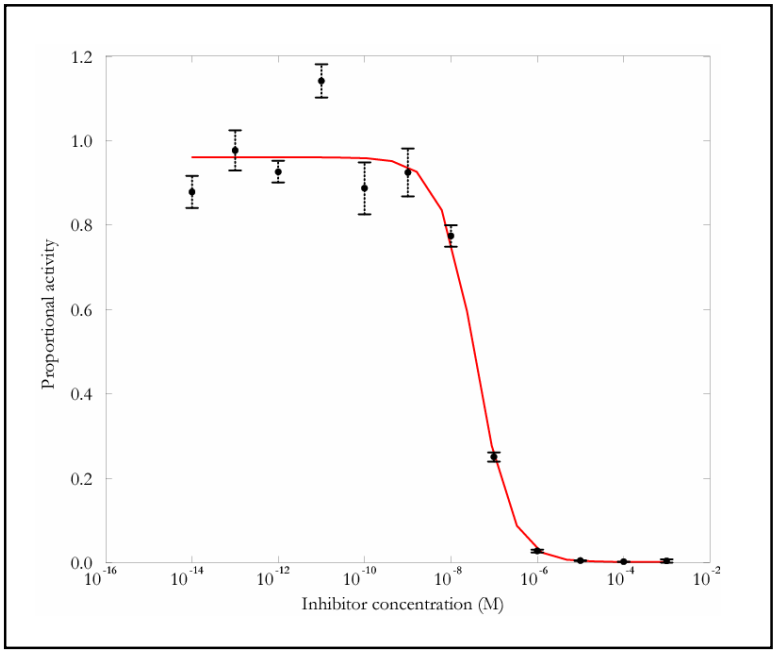

Figure 3.10 – Dose response curve showing galanthamine inhibition of *Electrophorus electricus* AChE: Experimental points (an average of 5 data sets) are shown as black filled circles with the standard deviation indicated by error bars. A sigmoidal fit to the experimental data is shown in red (R = 0.9900).

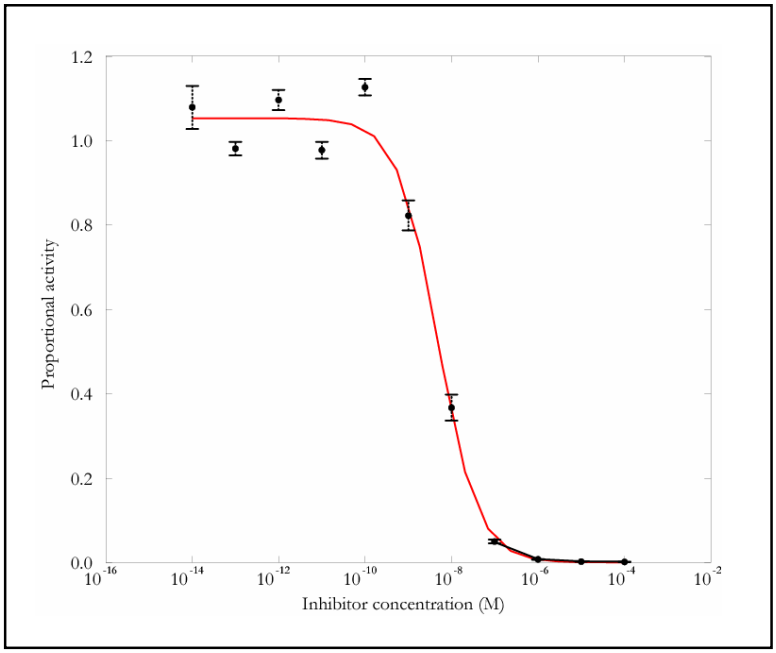

Figure 3.11 – Dose response curve showing R414425 inhibition of *Electrophorus electricus* AChE: Experimental points (an average of 5 data sets) are shown as black filled circles with the standard deviation indicated by error bars. A sigmoidal fit to the experimental data is shown in red (R = 0.9951).

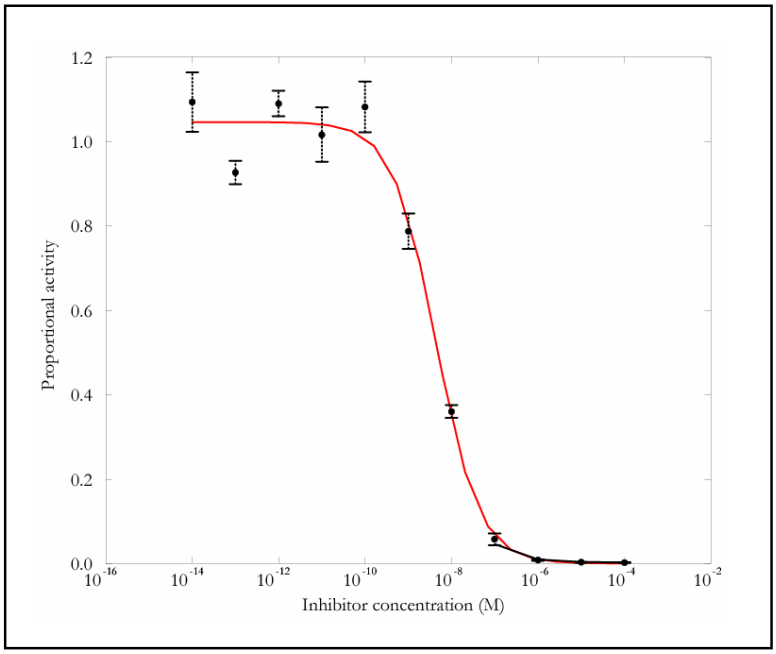

Figure 3.12 – Dose response curve showing R414983 inhibition of *Electrophorus electricus* AChE: Experimental points (an average of 5 data sets) are shown as black filled circles with the standard deviation indicated by error bars. A sigmoidal fit to the experimental data is shown in red (R = 0.9947).

Table 3.2 – Comparison of measured inhibitor IC_{50} values, with standard deviation, for *Electrophorus electricus* acetylcholinesterase with literature values for *Electrophorus electricus* and *Torpedo californica*.

Inhibitor	Measured IC_{50} (nM)	Literature IC_{50} (nM)	
		Electrophorus electricus	*Torpedo californica*
tacrine	38 ± 14	50 ± 4 [176]	8.2 [43]
galanthamine	37 ± 13	360 ± 10 [176]	-
R414425	4.8 ± 1.2	-	3.8 [43]
R414983	4.4 ± 1.2	-	3.0 [43]

Throughout the four test series, the data show a sigmoidal curve which is characteristic of simple inhibition kinetics. The standard deviation of the data is typically small in the presence of inhibitor concentrations approaching or higher than the IC_{50}, while at lower inhibitor concentrations a greater range in the data distribution is observed.

The IC_{50} of the Alzheimer's Disease drug tacrine was found to be 38 ± 14 nM. This value is similar to that determined previously for tacrine inhibition of *Electrophorus electricus* AChE (50 ± 4 nM)[176]. The IC_{50} for tacrine inhibition of *Torpedo californica* AChE is 8.2 nM [43], a possible explanation for the different inhibitory potency between species could be amino-acid substitution in the region where tacrine binds (see Chapter 6).

The IC_{50} for galanthamine, the second Alzheimer's Disease drug used for comparison, was determined to be 37 ± 13 nM. There is some discrepancy between the value determined here and that available in the literature (360 ± 10 nM [176]). It is not clear where this difference may arise, although the similarity between values for tacrine inhibition of *Ee*AChE in both studies suggests that the methodology used is comparable.

A step change is apparent when comparing the inhibition by tacrine and galanthamine to that of R414425 and R414983, both of these Syngenta compounds are extremely potent with IC_{50} values of 4.8 ± 1.2 nM and 4.4 ± 1.2 nM respectively. The published IC_{50} values for inhibition of *Tc*AChE are marginally lower (R414425 3.8 nM and R414983 3.0 nM [43]) but show the

same trend, with R414983 demonstrating a subtly greater level of enzyme inhibition than R414425.

3.4.1.2 Acetylcholinesterase stability

Storage of *Ee*AChE at room temperature results in a marked decrease in the enzyme activity after a relatively short period of time (Figure 3.13). An exponential fit to the data provides a time constant of 5.00 ± 0.25 hrs.

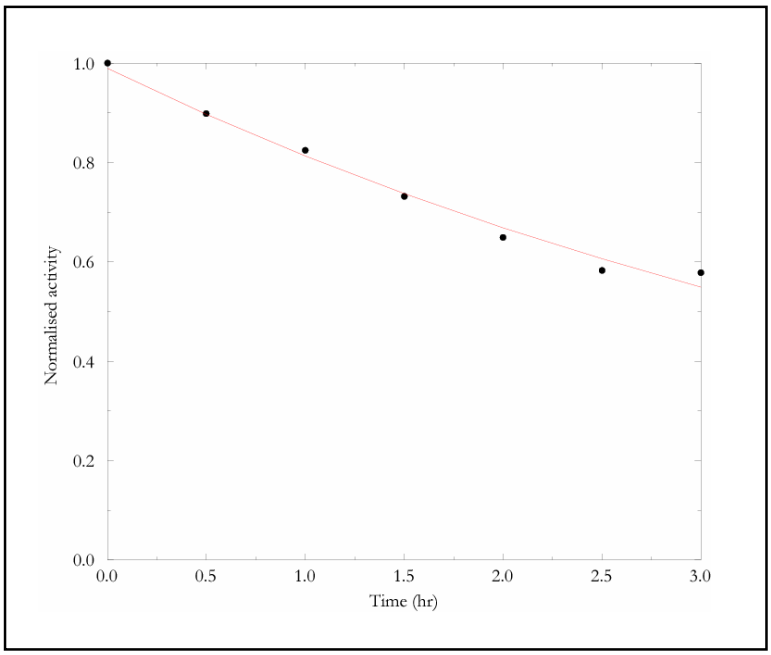

Figure 3.13 – Acetylcholinesterase activity as a function of time at room temperature: data points are shown as black dots, with an exponential fit in red (R = 0.9905).

The effect of steps such as freezing and freeze-drying on enzyme activity is of great interest, since it is desirable that samples analysed by NMR are representative of the AChE in its natural state. Table 3.3 shows that slow freezing, rapid freezing and freeze-drying are reversible processes which have no deleterious effect on the activity of the enzyme.

Table 3.3 – The effect of preparative steps on AChE activity.

Sample treatment	Normalised activity
Maintained at 4 °C	1.0 ± 0.07
Slowly frozen	1.02 ± 0.04
Rapidly frozen in liquid nitrogen	0.91 ± 0.08
Rapidly frozen and lyophilised	1.06 ± 0.07

3.4.2 NMR

3.4.2.1 ^{13}C NMR

Solid state experiments

The spectrum of solid $^{13}C_5$-R414425 (Figure 3.14) benefits from the use of a low frequency spectrometer and a high sample spinning speed, J-couplings are resolved for a number of the resonances. The relatively narrow linewidths suggest the absence of significant structural heterogeneity in the sample. The C2, C3 and 2-methyl resonances appear within isolated regions of the spectrum and are therefore assigned easily. Resonances arising from the benzyl methylene and quinoline methylene labels both fall within the same region of the spectrum, although they may be assigned on the basis that the quinoline methylene is coupled to the quinoline C3 position (therefore appearing as a doublet) while the benzyl methylene is isolated (singlet).

Figure 3.15 shows the spectrum of solid $^{13}C_5$-R414983. Spectral linewidths are broader than observed previously for $^{13}C_5$-R414425 (Figure 3.14), due to a combination of effects such as a slower spinning frequency, higher field spectrometer and sample heterogeneity. Coupling between labelled sites is not resolved and, although the two methylene positions could be assigned with reference to the $^{13}C_5$-R414425 spectrum, homonuclear double-quantum correlation experiments are otherwise necessary to distinguish the benzyl methylene and quinoline methylene in the solid state.

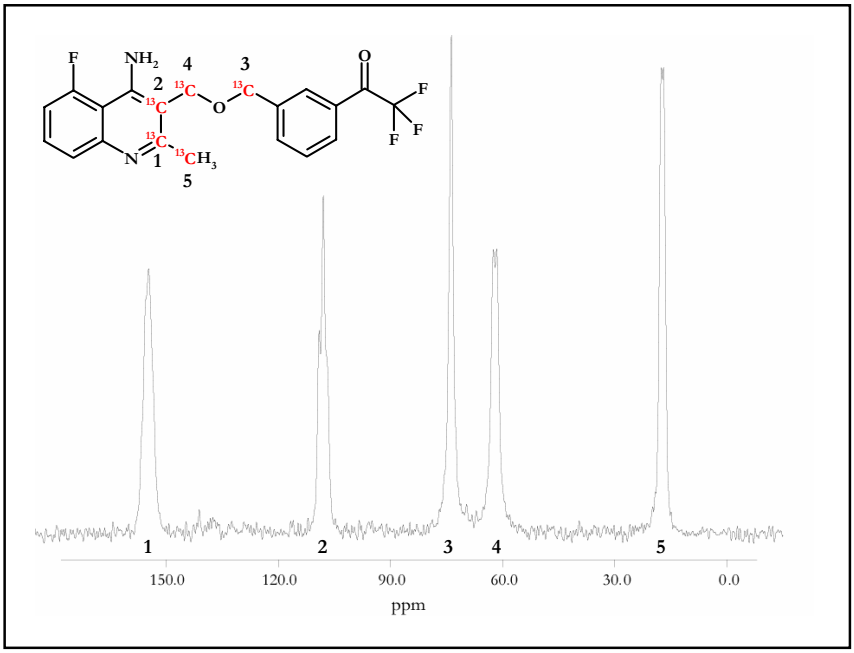

Figure 3.14 – ^{13}C NMR spectrum of solid $^{13}C_5$-R414425: 1024 transients were acquired on a 200 MHz (^1H frequency, 50 MHz for carbon) spectrometer using 10 mg of inhibitor and a sample spinning speed of 12000 Hz.

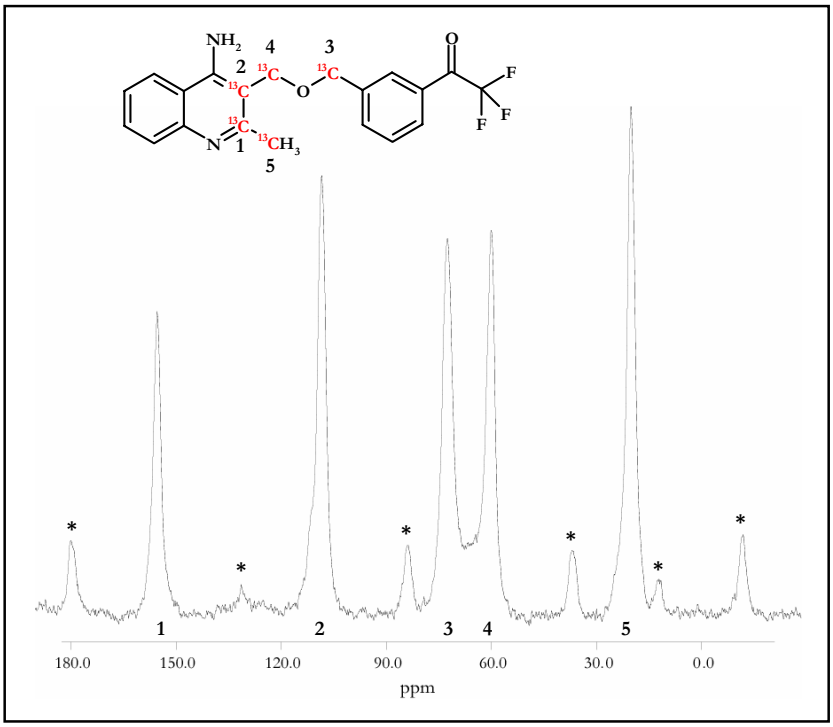

Figure 3.15 – ^{13}C NMR spectrum of solid $^{13}C_5$-R414983: 1000 transients were acquired on a 500 MHz (^1H frequency, 125 MHz for carbon) spectrometer using 22 mg of inhibitor and a sample spinning speed of 9000 Hz. Spinning sidebands are indicted by *.

Use of the pulse scheme applied for the two-dimensional correlation experiments generates cross-peaks which alternate in phase depending upon the number of bonds separating atoms. Figure 3.16a was acquired with a mixing period of 0.6 ms. Only three cross-peaks are present at this time point (2-methyl/C2, C2/C3 and C3/quinoline methylene) but they are sufficient for the unequivocal assignment of resonances.

Figure 3.16 – ^{13}C homonuclear correlation experiments on solid $^{13}C_5$-R414983: A two-dimensional C7 sequence was used to investigate 3.5 mg of inhibitor on a 200 MHz spectrometer (^1H frequency, 50 MHz for carbon). A sample spinning speed of 10000 Hz was used. The homonuclear coupling is reintroduced during a variable mixing time of 0.6 ms (a) 1.2 ms (b) and 2.4 ms (c). Positive intensity is shown in black and negative intensity in red.

At longer mixing times additional cross-peaks appear, initially those corresponding to two bond internuclear separations (τ_m 1.2 ms, seen with positive phase in Figure 3.16b) and later couplings via three bonds (τ_m 2.4 ms, seen with negative phase in Figure 3.16c).

Figure 3.17a shows the spectrum of $^{13}C_5$-R414983 bound to acetylcholinesterase. Comparison with the spectrum of the enzyme alone (Figure 3.17b) provides an indication of the level of signal arising from natural abundance ^{13}C within the protein. Subtraction of the control spectrum from that of the inhibitor with acetylcholinesterase provides a spectrum representative of the inhibitor in the binding site.

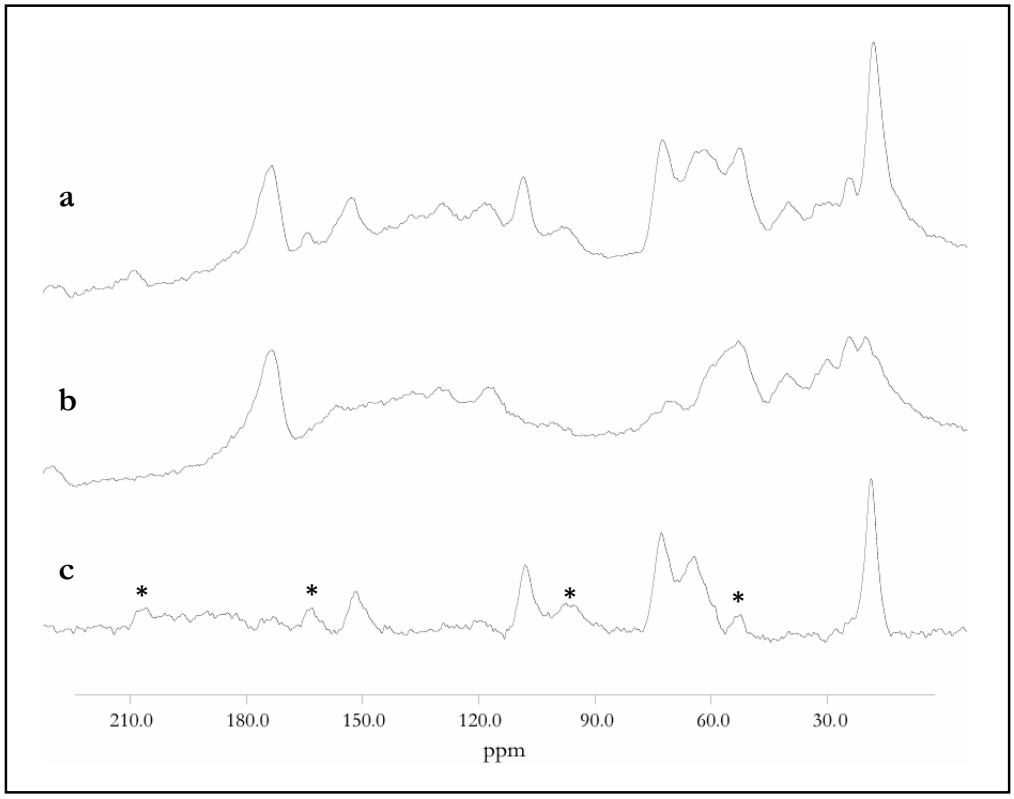

Figure 3.17 – ^{13}C NMR spectra of $^{13}C_5$-R414983 bound to acetylcholinesterase: acquired on a 500 MHz (^1H frequency, 125 MHz for carbon) spectrometer at a sample spinning speed of 7500 Hz – acetylcholinesterase with bound inhibitor (a), acetylcholinesterase control (b), difference spectrum (c).

Solution state experiments

^{13}C observed solution NMR spectra of the inhibitors are shown in Figure A4.1-Figure A4.4 in Appendix 4. The spectra are all typical of solution experiments on pure low molecular weight samples, demonstrating narrow linewidths and easily resolving homonuclear J-couplings‡.

Isotropic chemical shifts

The chemical shifts determined during ^{13}C NMR experiments on the labelled inhibitors are listed in Table 3.4. The multitude of interactions which contribute to the chemical shift of a resonance make it difficult to reach specific conclusions on the basis of the results. However, a number of observations can be made.

Table 3.4 – Summary of ^{13}C NMR chemical shifts for the inhibitors $^{13}C_5$-R414425 and $^{13}C_5$-R414983.

Compound	State	Chemical shift (ppm)				
		C2	C3	Benzyl CH_2	Quinoline CH_2	Methyl
$^{13}C_5$-R414425	solid	154.8 (br s)	108.0 (t)	73.8 (s)	62.1 (d)	17.3 (d)
"	D_2O	153.4 (q)	108.5 (q)	72.4 (s)	63.6 (d)	18.0 (d)
"	$CDCl_3$	158.8 (t)	108.8 (t)	70.8 (s)	66.9 (d)	24.1 (d)
$^{13}C_5$-R414983	solid	155.5	108.5	72.6	60.1	20.1
"	D_2O	153.3 (q)	107.7 (q)	72.4 (s)	63.7 (d)	18.1 (d)
"	$CDCl_3$	157.9 (t)	108.8 (t)	70.8 (s)	67.2 (d)	24.2 (d)
"	*Ee*AChE bound	152.6	108.2	73.0	64.4	18.3

The chemical shifts of both $^{13}C_5$-R414425 and $^{13}C_5$-R414983 are similar in solid form. While the presence of the fluorine atom on the quinoline ring of R414425 is responsible, in part, for the differences, sample preparation may also be a contributing factor since the chemical shifts are more closely matched in either D_2O or $CDCl_3$ solution.

‡ Attempts were made to resolve ^{13}C resonances for the bound ligand using solution NMR experiments (^1H-^{13}C heteronuclear single quantum correlation). However, these experiments were unsuccessful.

The inequivalence of the electronic environments of the benzyl and quinoline methylene labels is highlighted by their changes in chemical shift in solution (Table 3.5). In D_2O the benzyl methylene resonances move to lower frequency, while the quinoline methylene resonances moving to higher frequency. These shift changes are more pronounced in $CDCl_3$, with the benzyl methylene moving further in the low frequency direction and the quinoline methylene resonances moving further in the high frequency direction. The chemical shift difference between the two methylene positions in solid form therefore decreases in D_2O and to a greater extent in $CDCl_3$.

Table 3.5 – Summary of chemical shift changes for the benzyl and quinoline methylene labels in solution (values are in ppm).

Compound	Chemical shift change relative to solid				Difference in chemical shifts		
	Benzyl methylene		Quinoline methylene		Solid	D_2O	$CDCl_3$
	D_2O	$CDCl_3$	D_2O	$CDCl_3$			
$^{13}C_5$-R414425	-1.4	-3.0	1.5	4.8	11.7	8.8	3.9
$^{13}C_5$-R414983	-0.2	-1.8	3.6	7.1	12.5	8.7	3.6

For both labelled compounds, splitting of the C2 and C3 resonances due to the J-coupling is resolved as a quartet for both compounds in D_2O, but only as a triplet in $CDCl_3$ (arising from unresolved overlapping doublets).

Resonances for the C3 and benzyl methylene positions are marginally shifted for the enzyme bound $^{13}C_5$-R414983 compared to the solid $^{13}C_5$-R414983 inhibitor alone (by -0.3ppm and 0.4 ppm respectively), in contrast to substantial shifts for the C2, quinoline methylene and 2-methyl positions (-2.9 ppm, 4.3 ppm and -1.9 ppm respectively).

3.4.2.2 ^{19}F NMR

Solid state experiments

The fluorine spectra of solid $^{13}C_5$-R414425 indicate the presence of three inequivalent fluorine sites (Figure 3.18). Based on the structure of the compound this result may at first seem surprising, though it may be explained easily.

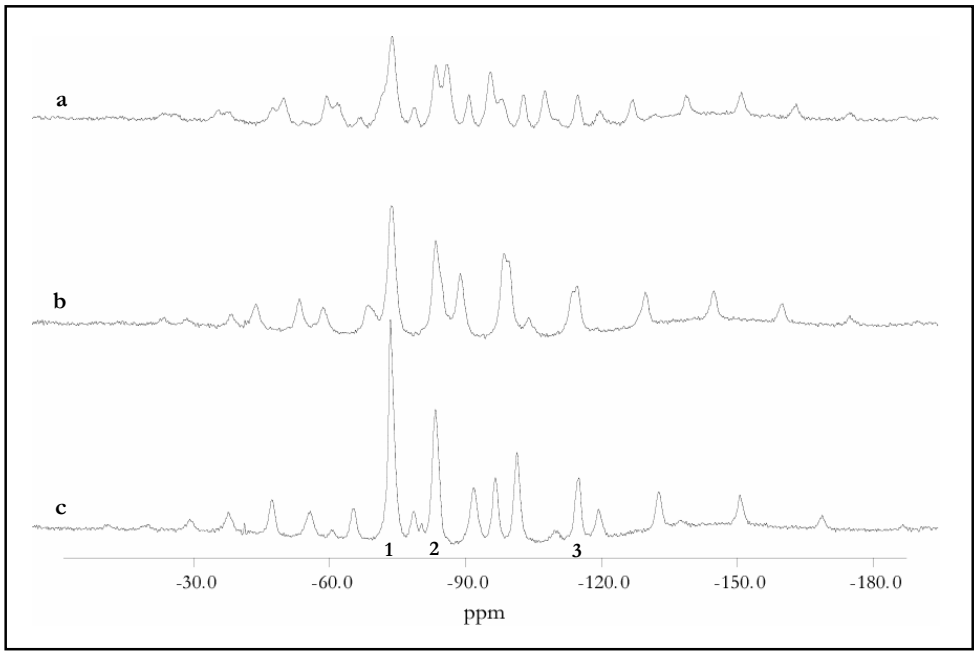

Figure 3.18 – ^{19}F NMR spectra of solid $^{13}C_5$-R414425: 400 transients were acquired on a 500 MHz (^{1}H frequency, 470 MHz for fluorine) spectrometer using 80 mg of inhibitor and sample spinning speeds of 6000 Hz (a) 7500 Hz (b) and 9000 Hz (c). The three isotropic peaks are numbered (1 - ketone, 2 - hydrate, 3 - aromatic.

The trifluoromethyl function is critical for inhibitor potency and substitution of the group for an unfluorinated methyl decreases the IC_{50} of inhibitors in the series by a factor of over 3000-fold [43]. The fluorine atoms withdraw electron density, making the ketone accessible to nucleophilic attack from the catalytic serine and stabilising the covalently bonded tetrahedral structure. This susceptibility to nucleophilic attack is demonstrated by the formation of a

hydrate in aqueous solution (Figure 3.19). Incomplete drying of the sample, prepared from a water/MeCN solution, is therefore responsible for the third resonance.

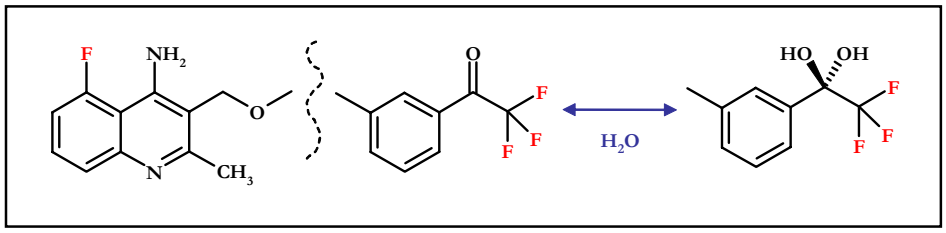

Figure 3.19 – Hydrate formation in the presence of water: the aromatic fluorine and the trifluoromethyl groups from the free ketone and hydrate produce distinct NMR resonances (the three fluorines within each trifluoromethyl group are equivalent).

Spectra of solid $^{13}C_5$-R414983 show a single fluorine resonance with its associated sideband pattern (Figure 3.20). The single form present in the sample is the hydrate, not the free ketone, on the basis of the isotropic chemical shift.

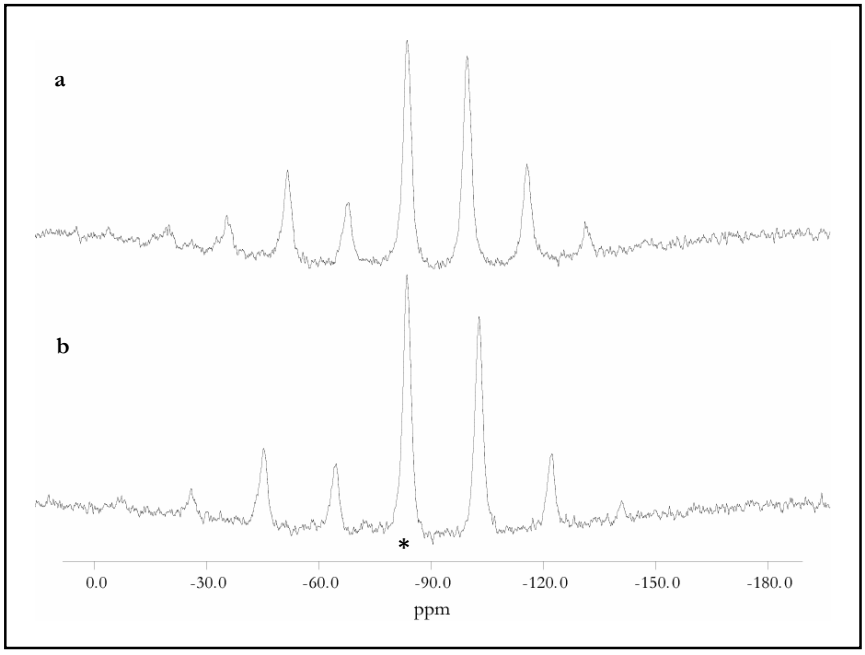

Figure 3.20 – ^{19}F NMR spectra of solid $^{13}C_5$-R414983: 400 transients were acquired on a 500 MHz (^{1}H frequency, 470 MHz for fluorine) spectrometer using 10 mg of inhibitor and a sample spinning speeds of 7500 Hz (a) and 9000 Hz (b). The isotropic peak is indicated by *.

Figure 3.21 shows the fluorine NMR spectrum of $^{13}C_5$-R414983 bound to *Ee*AChE. Comparison of the peaks at two spinning speeds suggests the presence of a single fluorine resonance, although it should be noted that the broad spectral linewidths (1300 Hz, ~3 ppm) make it impossible to distinguish between resonances from the serine bound and unbound hydrate forms of the inhibitor (unlike in the case with solution NMR, Figure 3.22).

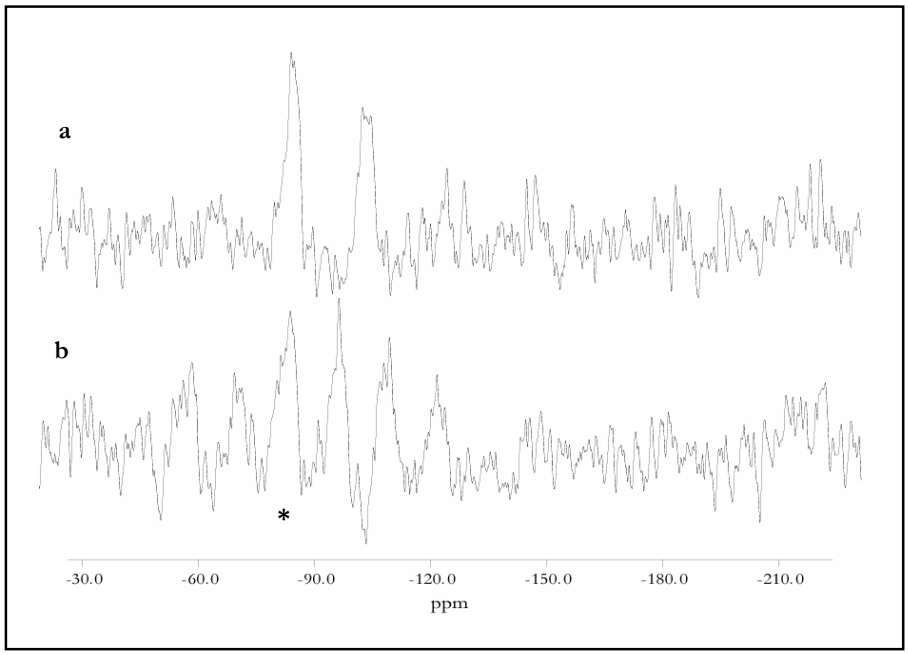

Figure 3.21 – ^{19}F solid state NMR spectra of $^{13}C_5$-R414983 bound to *Ee*AChE: acquired on a 500 MHz (^{1}H frequency, 470 MHz for fluorine) spectrometer with a sample spinning speed of 6500 Hz (a) and 9000 Hz (b). The isotropic peak is indicated by *.

Solution state experiments

^{19}F NMR spectra of the pure inhibitors in D_2O and $CDCl_3$ solution are included as Figure A4.5-Figure A4.8 in Appendix 4. Linewidths are narrow in all four spectra and, in contrast to the ^{13}C solution NMR experiments which were performed on the same sample, separate resonances are observed in D_2O corresponding to the hydrate and free ketone forms of the

inhibitor (the presence of both forms can also be observed in ^{1}H spectra, the results of which are not included here).

Solution NMR spectra of $^{13}C_5$-R414983 bound to *Md*AChE are particularly interesting (Figure 3.22). As a result of the high viscosity of the concentrated protein solution, linewidths are broader in the presence of the protein (Figure 3.22a and Figure 3.22b) than for the spectrum of the inhibitor alone (Figure 3.22c). Despite this, peaks relating to the trifluoromethyl function of the protein bound inhibitor and free unbound inhibitor (in hydrate form) are resolved. The protein bound resonance is broadened in relation to the free inhibitor as a result of its impeded mobility.

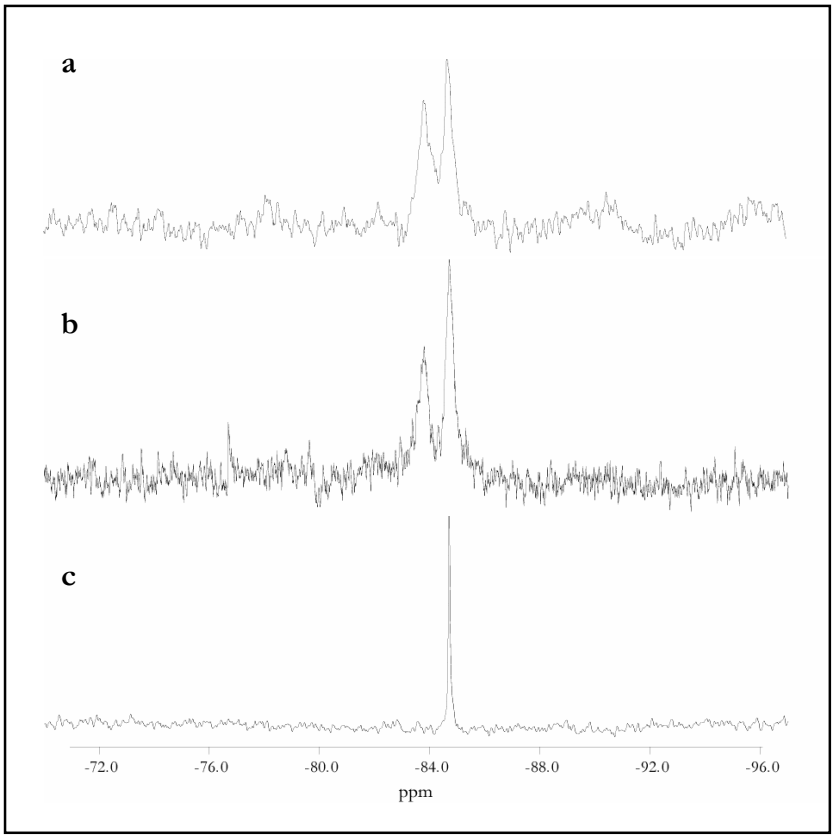

Figure 3.22 – ^{19}F solution state NMR spectra of $^{13}C_5$-R414983 bound to *Md*AChE: acquired on a 500 MHz (^{1}H frequency, 470 MHz for fluorine) spectrometer showing the sample after dialysis (a) doped with additional inhibitor (b) and inhibitor alone (c).

Isotropic chemical shifts

Table 3.6 combines the isotropic chemical shift results from the ^{19}F NMR experiments for comparison. Again, the interactions which determine the isotropic chemical shift are complex and limit analysis.

Table 3.6 – Summary of ^{19}F NMR chemical shifts for the inhibitors $^{13}C_5$-R414425 and $^{13}C_5$-R414983.

Compound	State	Chemical shift (ppm)		
		Trifluoromethyl		Aromatic
		Ketone	Hydrate	
$^{13}C_5$-R414425	solid	-73.6	-83.4	-114.8
"	D_2O	-76.1(6%)	-84.7 (94%)	-113.7
"	$CDCl_3$	-71.8	Not present	-116.6
$^{13}C_5$-R414983	solid	Not present	-83.5	NA
"	D_2O	Not present	-84.7	NA
"	$CDCl_3$	-71.8	Not Present	NA
"	*Ee*AChE bound (solid)	Not Present	-84.3	NA
"	*Md*AChE bound (solution)	Not Present	-83.8 (bound) -84.7 (free)	NA

Fluorine nuclei posses a large chemical shift range and chemical shifts are very sensitive to factors such as solvent polarity and ionic strength [120], a feature highlighted by the fact that free ketone and tetrahedral hydrate forms are not resolved in ^{13}C NMR experiments but are in ^{19}F NMR. The location of the fluorine atoms, in close proximity to the hydration site, obviously contributes to this sensitivity but ^{1}H resonances from the 2-methyl or quinoline methylene positions can also distinguish the two forms (data not shown). The chemical shift difference between the ketone and hydrate is measured to be 9.8 ppm (based on solid $^{13}C_5$-R414425).

The detection of a resonance which can be ascribed to the protein bound ligand has been shown previously using solution state fluorine NMR for the binding of 3-octyl-thio-1,1,1-trifluoropropan-2-one to *Ee*AChE [120]. It has also been successfully performed here, with a

resonance at -83.8 ppm for the tetrahedral enzyme bound inhibitor and -84.7 ppm for the free tetrahedral hydrate.

3.4.2.3 Anisotropy investigation

2D-PASS

The results of the 2D-PASS experiment on the pure inhibitor ($^{13}C_5$-R414983) are shown in Figure 3.23. The inequivalence of the two methylene sites is of particular interest, due to their contrasting chemical shift changes upon binding, and a full analysis of the sideband distribution for these positions is shown in Figure 3.24. While the remaining sites have not been analysed in detail, a number of points are apparent in the 2D-PASS results.

The isotropic peaks show a large variation in intensity between the labelled positions, with the aromatics and quinoline methylene being significantly smaller than the benzyl methylene and 2-methyl. Differential magnetisation transfer during cross-polarisation may contribute to the intensity variation, though the dominant effect arises from the chemical shift anisotropy of the positions. Twelve sidebands are visible for each of the aromatic positions, seven for the quinoline methylene, five/six for the benzyl methylene and four for the 2-methyl.

A plot of the methylene sideband manifolds and Herzfeld-Berger [186] analysis of their intensities enables the chemical shift anisotropy and asymmetry parameters to be quantified (Figure 3.24). The benzyl methylene has a shielding anisotropy ($\Delta\sigma$) of 43.8 ppm and an asymmetry parameter (η) of 0.37, the quinoline methylene has a much larger shielding anisotropy of 62.4 ppm and an asymmetry parameter of 0.60.

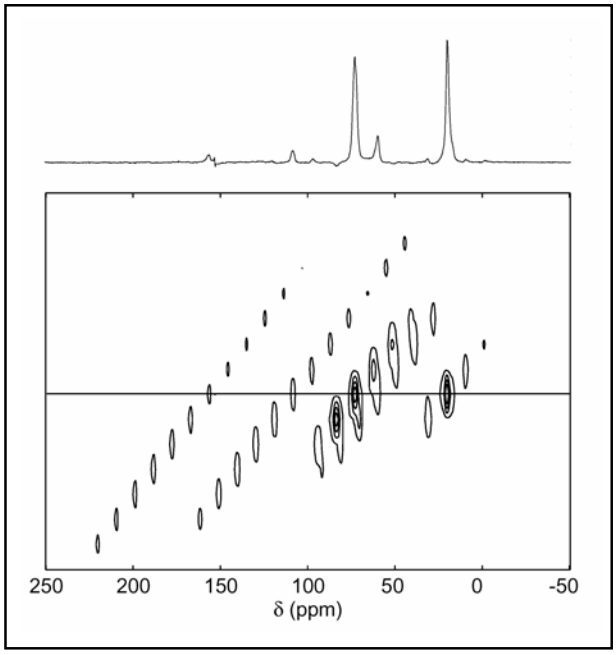

Figure 3.23 – 2D-PASS series for solid $^{13}C_5$-R414983: acquired on a 750 MHz spectrometer (^{1}H frequency, 183 MHz for carbon) at a spinning speed of 2000 Hz. A single slice through the isotropic peaks is also shown.

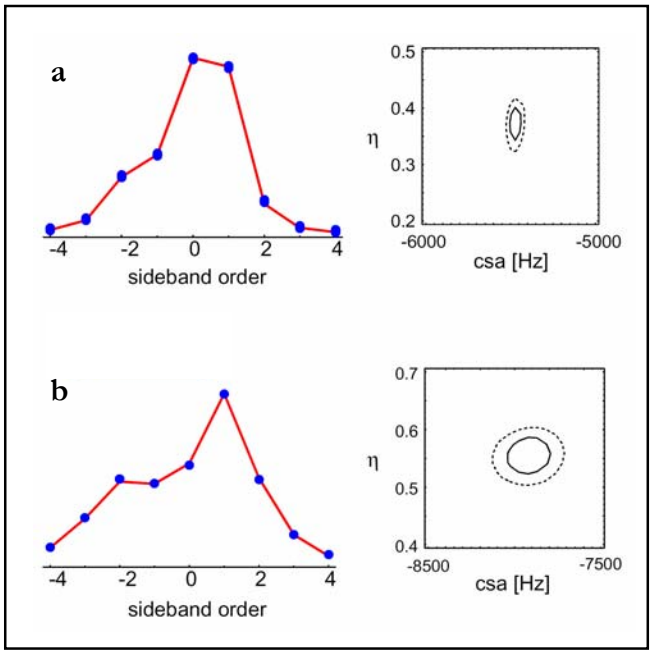

Figure 3.24 – Extraction of chemical shift anisotropy parameters from sideband manifolds: based on the results of the 2D-PASS experiments on solid $^{13}C_5$-R414983, using Herzfeld-Berger deconvolution [186] for the benzyl methylene (a) and quinoline methylene (b). A solid line represents 68% and a dotted line 95% confidence limits.

$R12^4_5$

The results of the $R12^4_5$ experiment are illustrated in Figure 3.25. Using this scheme, the recoupled CSA is observed in the indirect dimension as an overlapped doublet, symmetrical around the centre and scaled by a factor of 0.13. Slices through the benzyl methylene (Figure 3.25b) and quinoline methylene (Figure 3.25c) highlight the differences in both the shielding anisotropy and their asymmetry.

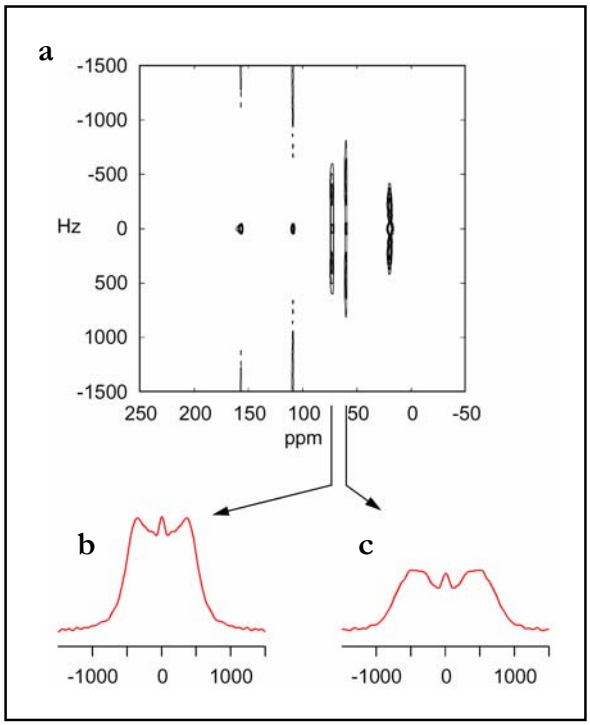

Figure 3.25 – CSA recoupling using the $R12^4_5$ sequence: spectra were acquired on a 500 MHz spectrometer (^{1}H frequency, 125 MHz for carbon) at a spinning speed of 15000 Hz (a). Slices through the benzyl methylene (b) and quinoline methylene (c) are also shown (under this scheme the CSA is scaled by a factor of 0.13 and appears as a symmetrical 'doublet').

Fitting of simulated powder patterns to the peaks is impeded by the central spike, an artefact arising from a DC offset in the time domain. Although it is possible to compensate for this offset, this cannot be done in a way that the anisotropy parameters are guaranteed to remain unchanged.

3.5 Discussion

Each of the two compounds, R414425 and R414983, is an extremely potent inhibitor of *Electrophorus electricus* acetylcholinesterase (IC_{50} values of 4.8 ± 1.2 nM and 4.0 ± 1.2 nM respectively). The high degree of homology between the enzymes from *Electrophorus electricus* and *Torpedo californica* is shown by the similarity of the IC_{50} values determined here with those previously published for *Tc*AChE (only one residue is altered in the region where the inhibitors bind – Phe331 in *Tc*AChE, which is equivalent to Tyr337 in *Ee*AChE). The IC_{50} values are almost an order of magnitude smaller than that of tacrine, the drug used in the treatment of Alzheimer's Disease, upon which the Syngenta compounds are based. While the difference between the IC_{50} values of R414425 and R414983 for *Ee*AChE is within experimental error, previous work also noted the subtly greater potency of R414983 [43]. Structurally, a single substitution of a fluorine atom at the 5 position of the quinoline ring is responsible for this change in potency.

The chemical shifts of the labelled inhibitors, based on both ^{13}C and ^{19}F NMR in solution and solid state, show a marked dependence upon their environment. The complexity of the interactions which contribute to the chemical shift limits a full analysis. For this reason, it is best to focus on the benzyl and quinoline methylene positions. These sites are chemically similar, yet demonstrate contrasting chemical shift behaviour such as their opposite shift changes in solution, different shift changes with bonding to AChE and their dissimilar electronic environments (illustrated by both the shielding anisotropy and asymmetry parameters). Interpretation of a structural basis for these differences is presently not possible.

To date, attempts at crystallisation of the Syngenta inhibitors have proved unsuccessful, possibly due to the presence of a mixture of the hydrate and free forms. The narrow linewidths observed in the ^{13}C NMR spectrum of pure $^{13}C_5$-R414425 suggest a low level of local structural

heterogeneity, it may therefore be possible to determine the conformation of the solid inhibitors using NMR without the need for macro-crystalline material. After the development of a model for the inhibitors bound to AChE it may then be possible to simulate the electronic environment for both unbound and protein bound inhibitors, explaining the chemical shift changes which have been observed. Additional instrument time is required before 2D-PASS experiments on the enzyme bound inhibitor have sufficient signal for the analysis of sideband manifolds, enabling the investigation of anisotropy changes which may also occur upon binding of the inhibitor.

Spectral linewidths for lyophilised $^{13}C_5$-R414983 bound to acetylcholinesterase are broad. The sensitivity of the isotopic labels to their environment, coupled with a less well defined binding pocket in this dehydrated state may be responsible. However, the large chemical shift changes observed for certain positions when compared to the pure solid inhibitor (such as 4.3 ppm for the quinoline methylene) shows that although some heterogeneity is present, it is unlikely to be structurally significant in later distance measurements.

Chapter 4 Rotational Resonance Investigation of $^{13}C_5$-R414983 Bound to Acetylcholinesterase

4.1 Overview

Determination of ^{13}C-^{13}C internuclear distances for the acetylcholinesterase bound inhibitor R414983 is an important step in the development of a model for its bound state.

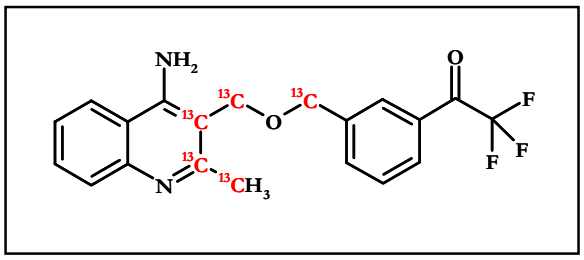

Figure 4.1 – $^{13}C_5$-R414983, 4-Amino-2-methyl-3-(3-triflouroacetylbenzyl-oxymethyl) quinoline.

Three pairs of spins are located such that their separation is dependent upon the relative orientation of the quinoline and benzyl functionalities of the molecule (benzyl methylene/2-methyl, benzyl methylene/quinoline C2 and benzyl methylene/quinoline C3), the relative positions of the remaining pairs of spins is fixed through the rigid network of covalent bonds.

4.2 Introduction

4.2.1 Homonuclear Recoupling

Dipolar couplings are inversely proportional to the cube of the separation between spins (Chapter 1 – Equation 1.12). Elucidation of the dipolar coupling strength between pairs of spins is therefore key in the determination of internuclear distances. Under the magic-angle spinning conditions required for high spectral resolution, dipolar couplings are effectively averaged to zero. Thus, reintroduction of the interaction is necessary in order that distance measurements can be performed.

Interference with the averaging process of magic-angle spinning, and thereby a recoupling of the dipolar interaction, can be achieved through the use of rotor synchronised radio-frequency pulses or by mechanical means where the spinning frequency is carefully selected. The importance of the dipolar interaction, not only in the determination of internuclear distances, but also in the assignment of coupled networks of spins or the creation of multiple-quantum coherences, has led to the development of a wealth of schemes for its recovery [193, 194].

Early radio-frequency based recoupling methods, such as the DRAMA experiment [195] in which two $\pi/2$ pulses are applied during each rotor period or SEDRA/RFDR [196-198] which employ a single π pulse in each rotor period, are all particularly susceptible to pulse imperfections, chemical shift anisotropy, chemical shift offsets and difficulties with calibration. Later schemes including MELODRAMA [199], CEDRA [200], RIL [201] and DRAWS [202] incorporate improvements to ensure a more broad-banded recoupling efficiency. Despite the fact that precise distance determination using these sequences has been demonstrated on ideal systems, broad-banded recoupling restricts their practical application to distance determination in samples incorporating a single pair of labelled nuclei or for multidimensional correlation

experiments [203-205] (narrow-banded versions of the RFDR and SEDRA experiments have recently been proposed [206]).

The dipolar interaction is also utilised in double quantum filtering (DQF) experiments, where coherences between coupled spins are promoted and exclusively selected, suppressing signals such as those arising from a natural abundance background [191, 192, 207-210]. While in theory the rate of double quantum evolution could be correlated to the strength of the dipolar coupling, the complex analysis required has ensured that this method is not employed for internuclear distance determination.

Mechanical recoupling of the dipolar interaction, known as rotational resonance, is more appropriate for distance determination in a multiply labelled spin system such as that used in the current study [211].

4.2.2 Rotational Resonance

4.2.2.1 The rotational resonance method

First observed through its effects on relaxation times and line broadening [212, 213], when the frequency difference between the isotropic chemical shifts of two nuclei is equal to an integer multiple of the sample spinning speed the rotational resonance condition is met ($\Delta\omega_{IS} = n\,\omega_r$). Under these conditions nuclei may undergo rapid cross-relaxation and magnetisation exchange through reintroduction of the dipolar interaction.

In suitable circumstances, with sufficient spectral resolution, a dipolar splitting resulting from rotational resonance [214] can be observed directly in the standard one-dimensional spectrum (see Figure 4.2 below). While measurement of the dipolar splitting is a relatively simple method for the determination of internuclear distances, which has been proven on crystalline systems [215] and successfully applied in at least one biological system [216], it is not commonly utilised

in biological systems where large resonance line widths and relatively weak dipolar couplings limit the potential for accurate measurements.

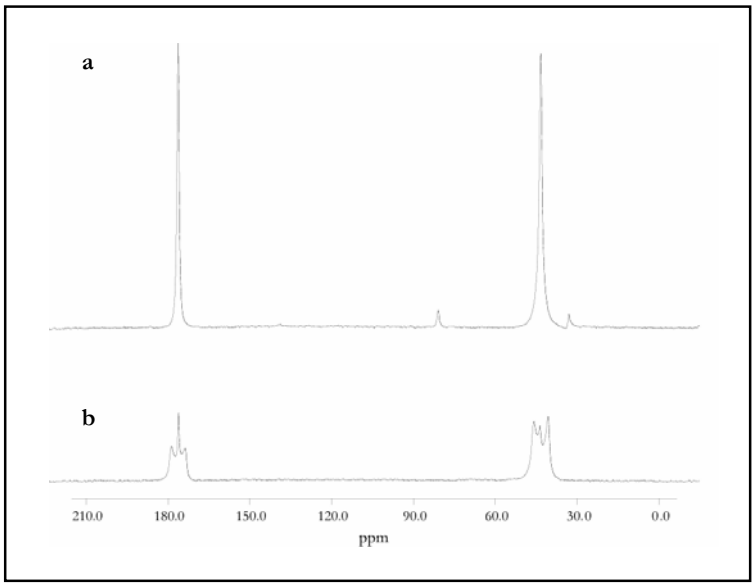

Figure 4.2 – Dipolar splitting under rotational resonance: ^{13}C spectra acquired at 125 MHz (500 MHz for ^{1}H) of $^{13}C_2$-glycine diluted 1:19 with unlabelled glycine and crystallized from aqueous solution - off rotational resonance, ω_r = 12000 Hz (a) on rotational resonance at the n = 1 condition, ω_r = 16720 Hz (b).

The first inter-atomic distance measurement for an integral membrane protein from solid-state NMR was determined in bacteriorhodopsin by investigation of magnetisation exchange between a pair of spins under rotational resonance [217]. In contrast to the line shape effects discussed above, significant magnetisation exchange can occur even in systems with weak dipolar couplings. The basis of this magnetisation exchange and the interpretation of an exchange profile in terms of the strength of the dipolar coupling between spins are discussed later (Section 4.2.3).

Figure 4.3 illustrates the general form of the pulse scheme used for rotational resonance magnetisation exchange experiments [151, 214]. Initial proton magnetisation is transferred to the dilute spins during a period of cross-polarisation (in this case using ramped CP). Following

a non-selective 90° pulse on the ^{13}C channel which aligns the spins along the +Z axis, a selective inversion is performed on one of the pair of ^{13}C spins (the DANTE scheme is frequently used [185, 218], though other methods involving long weak pulses [214], time delays [219] or three pulse sequences have also been applied [220]). A mixing time of variable length (τ_m) allows magnetisation exchange to occur, before magnetisation is returned to the transverse plane and an FID is acquired. Efficient proton decoupling is required throughout the course of the experiment, though particularly during the exchange period to minimise the influence of zero-quantum relaxation (discussed later in Section 4.2.3.2).

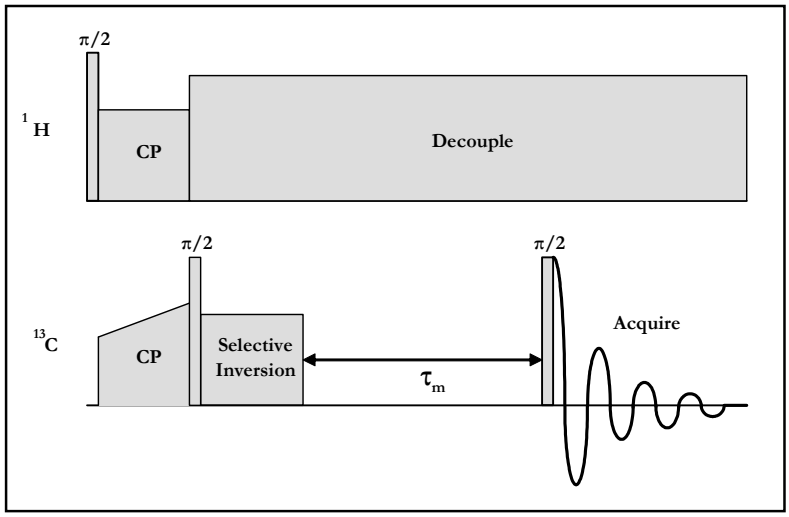

Figure 4.3 – The rotational resonance pulse sequence [151, 214].

Recoupling of the dipolar interaction by rotational resonance allows the transfer of Zeeman magnetisation between sites during the mixing period (Figure 4.4), in cases where the coupling is strong it is often possible to observe oscillations in the exchange. One advantage of rotational resonance is that the dipolar recoupling is highly frequency selective. Recoupling (and therefore magnetisation exchange) is strongly suppressed at spinning frequencies away from the rotational resonance condition (it is absent 500-1000 kHz from the match).

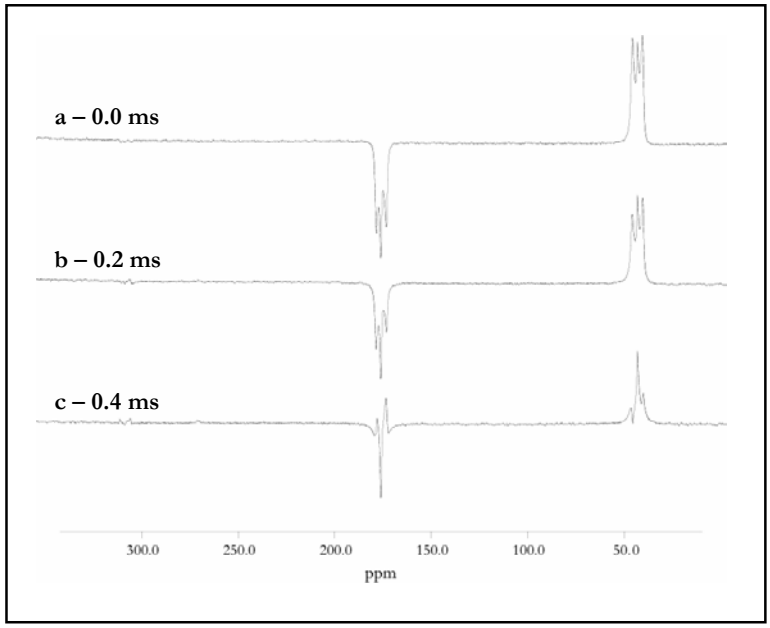

Figure 4.4 – Magnetisation exchange under rotational resonance: ^{13}C spectra of $^{13}C_2$-glycine diluted 1:19 with unlabelled glycine and crystallized from aqueous solution acquired at 125 MHz (500 MHz for ^{1}H) on rotational resonance at the $n = 1$ condition, $\omega_r = 16720$ Hz, showing rotational resonance exchange following inversion of the carbonyl peak and after $\tau_m = 0.0$ ms (a) $\tau_m = 0.2$ ms (b) $\tau_m = 0.4$ ms (c).

Internuclear distances of up to 6.5 Å can be determined at an accuracy as high as 0.01 Å [214, 221], enabling the investigation of protein and peptide structure [160, 217, 222] or the conformation of protein bound ligands [185, 223]. Due to the reintroduction of a single dipolar coupling, it is feasible to apply the rotational resonance technique to specific distance measurements within multiply labelled samples.

Experiments involving large proteins, or even those with smaller proteins and peptides if in the presence of membrane lipids, can be complicated by contributions from the natural abundance background. The need to discern the resonances of interest from the background for accurate quantification requires the preparation and measurement of two samples in parallel, one containing and the other without the labelled component.

4.2.2.2 Modified rotational resonance sequences

A number of advanced rotational resonance sequences have been proposed. One of the most conceptually simple is the constant-time experiment (Figure 4.5) [224], which in addition to the variable mixing time under which magnetisation exchange proceeds (τ_m) introduces a further time delay (τ_d). The sum of these delays is maintained at a constant value during variation in the mixing time, ensuring that samples experience a consistent level of heating from the strong decoupling applied and can remove the requirement for a separate background spectrum for each mixing time (a reliable background spectrum is still required, but the single spectrum may be applied to all of the data points).

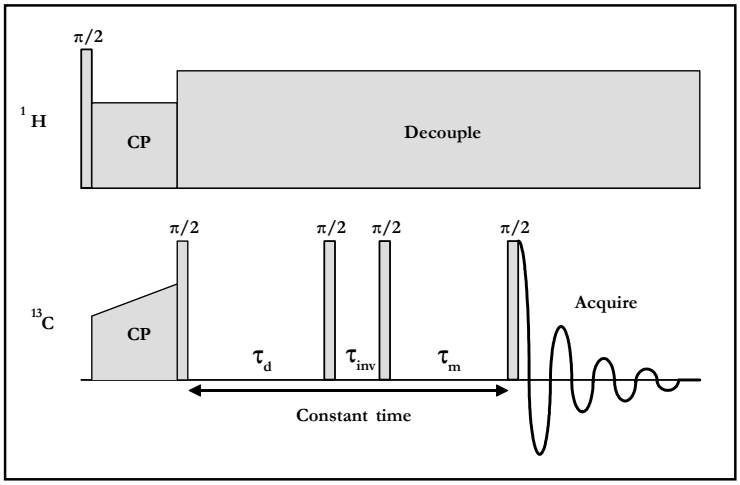

Figure 4.5 – The constant time rotational resonance experiment pulse sequence [224].

In systems with multiple spins where the chemical shift difference between a pair of spins is small, the low sample spinning speed required for traditional rotational resonance measurements may result in an incomplete removal of residual homonuclear dipolar couplings. Rotational resonance in the tilted rotating frame (R2TR) allows spinning speeds which are many kilohertz away from rotational resonance to be used [225-227]. An additional advantage of R2TR, which also results from the higher spinning frequency, is the suppression of sideband intensities.

R2TR features a constant weak radio-frequency field during the mixing period (Figure 4.6), compensating for a sample spinning speed offset from normal rotational resonance conditions. Rapid switching of the radio-frequency field strength provides the potential for multidimensional experiments, where data acquisition for different pairs of spins is possible without requiring changes in sample spinning speed. This technique has been successfully demonstrated in the determination of the absolute conformation of a uniformly labelled dipeptide [228].

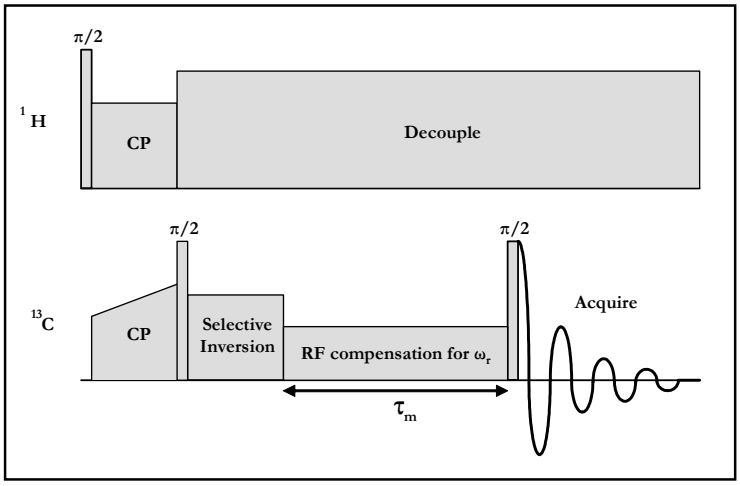

Figure 4.6 – The rotational resonance in the tilted frame (R2TR) pulse sequence [225].

The dependency of spin dynamics under rotational resonance on zero-quantum parameters (see Section 4.2.3.2 below) can be reduced by the use of rotational resonance tickling [219]. In this case the spinning speed is again offset from rotational resonance (though by a relatively small amount compared to R2TR), while a variable radio-frequency field ramps through a rotational resonance condition.

Combination of DQF methods with a traditional rotational resonance experiment can also remove the need for a background sample. In addition to the radio-frequency based DQF methods discussed earlier, it has recently been proposed that rotational resonance can itself be

utilised to create double-quantum coherences [229-231]. Unfortunately, the efficiency of DQF is limited in practical circumstances, and it is often more effective to split the available material into two samples (to provide a sample for measurement and a background or control sample) than to apply such super-sequences*.

4.2.3 Data Analysis and Modelling of Distances

4.2.3.1 The dipolar interaction under rotational resonance

The theoretical basis of the line shape effects and magnetisation transfer phenomena which occur under rotational resonance have been investigated in detail [232]. In a two spin system under magic-angle spinning conditions where the dipolar coupling is smaller than the isotropic chemical shift difference, the dipolar coupling can be effectively removed (it is dominated by $\Delta\omega_{IS}$, behaving in an inhomogeneous manner and is easily averaged by moderate sample spinning). Nuclear spins are normally unable to achieve rapid mutual spin flips through the dipolar coupling because of the energy mismatch for nuclear transitions.

At spinning speeds which satisfy the rotational resonance condition, energy levels associated with the macroscopic sample rotation match the energy disparity between spin states. As such, truncation of the dipolar interaction by the isotropic shift difference no longer applies, restoring its true homogenous nature. Spectral broadening and splitting become visible in the normal one dimensional spectrum, while the non-equilibrium state of Zeeman magnetisation prepared in the exchange experiment undergoes transfer through a zero-quantum flip-flop process.

* Strongly coupled resonances pass through DQF with a greater efficiency. Initial experiments performed here with DQF suggested that of the labelled sites in $^{13}C_5$-R414983 the four directly bonded positions produced much stronger signals than the isolated methylene. The isolated methylene is involved in each of the three variable distance measurements and a large differential in initial magnetisation is likely to affect the quality of any distance measurements obtained.

4.2.3.2 Correlation of exchange with internuclear distances

The dynamics of the difference magnetisation exchange process depend upon a number of variables: the strength of the dipolar coupling between sites (b_{IS}), the zero-quantum relaxation rate (T_2^{ZQ}), the principle values of the chemical shift tensors, the orientation of the chemical shift tensors relative to both the dipolar coupling and to each other, and the through bond J-coupling [151, 232].

The J-coupling has a relatively small influence on magnetisation exchange and may be easily estimated from typical solution NMR data, while operating at the $n = 1$ condition ensures that the dependence upon chemical shift parameters is minimised. Reliable determination of the dipolar coupling from a simulated fit to the experimental data [232] therefore often depends mainly on the zero-quantum relaxation value and it has been shown that errors of over ±1 Å can be directly attributed to the incorrect estimation of this term [222].

Since magnetisation exchange occurs through a zero-quantum coherence process, zero-quantum relaxation retards the rate of exchange. Zero-quantum relaxation is suppressed (i.e. T_2^{ZQ} is maximised) by the use of strong decoupling fields but remains a significant factor in its uncertainty, especially in situations where the dipolar couplings are weak. A number of methods are commonly utilised to estimate T_2^{ZQ}: summation of the individual line widths, which is generally an underestimate and produces a larger dipolar coupling than in reality [217]; summation of single-quantum (T_2) relaxation rates, typically an overestimate which can result in underestimation of the dipolar coupling [151, 160, 185, 233]; and also calculation of T_2^{ZQ} through experiments on analogous systems with known distances (such as determined by x-ray crystallography), which is limited by the degree of similarity between the examples used [222]. Recently experiments have been proposed for the direct measurement of zero-quantum relaxation [220, 234] and these methods are discussed later in more detail (Section 4.2.4).

Stability of the sample spinning speed is important to ensure a consistent match of the rotational resonance condition, deviations from the condition can have significant effects on the observed magnetisation exchange. Sample inhomogeneity is a further factor which must be considered since the rotational resonance condition is relatively narrow (offset effects can be observed as little as 50 Hz from the match, particularly on crystalline standards with narrow linewidths) and broad spectral lines may not undergo rotational resonance exchange at a uniform rate across their full width. It has been proposed that simulations of experimental data should incorporate inhomogeneity correction factors [218, 222], although for relatively long internuclear distances a high correlation of fitted parameters is observed which may still result in good quality fits without incorporation of this additional factor. The scale of such corrections factors can be determined from known calibration distances, typically short internuclear distances where it may be discerned independently of other parameters, although it must be assumed that these values are directly transferable to the intended distance measurement.

After successfully fitting a simulated exchange to the experimental data [151] the value of the dipolar coupling can be related to the internuclear distance, as discussed previously:

$$b_{IS} = \left(\frac{\mu_0}{4\pi}\right)\frac{\gamma_I \gamma_S \eta}{r^3_{IS}} \qquad \text{Equation 1.12}$$

where:

	b_{IS}	=	dipolar coupling between nuclear spins I and S
	μ_0	=	permeability of free space
	γ_I	=	gyromagnetic ratio of spin I
	γ_S	=	gyromagnetic ratio of spin S
	$\hbar$	=	Planck's constant divided by 2π
	r_{IS}	=	distance between nuclear spins I and S

Which, for a ^{13}C homonuclear spin pair, can be simplified to:

$$r_{IS} = \sqrt[3]{\frac{7.59382 \times 10^3}{b_{IS}}} \qquad \text{Equation 4.1}$$

where b_{IS} is specified in Hz and r_{IS} in Å.

4.2.4 Rotational Resonance Echos

The apparent 'loss' of magnetisation which results from Zeeman exchange during rotational resonance occurs through a coherent process which can in fact be reversed [220, 234]. Figure 4.7 illustrates such a scheme, where after an initial time delay (τ_1) under which normal rotational resonance exchange occurs, a radio-frequency cycle is performed. The cycle may be considered to lock spins in space and lasts for one half of a rotor period, as a result of sample rotation it therefore leads to a π shift of the spins relative to the z-axis (proton decoupling may be turned off during the cycle to minimise CP effects, although it can still be utilised if relatively high ^{13}C field strengths are applied). In a second delay period (τ_2) the zero-quantum state vectors continue along their initial trajectories, but the inclusion of the π shift ensures that they are now refocused.

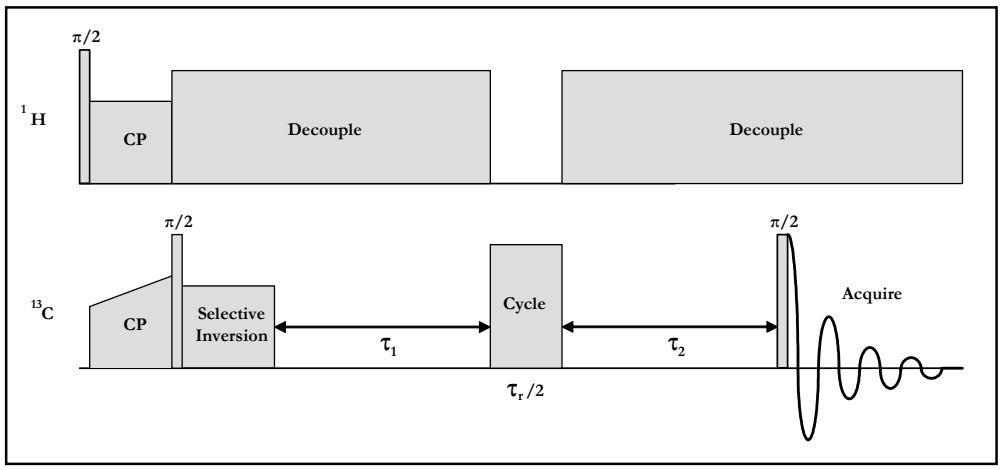

Figure 4.7 – The rotational resonance echo pulse sequence [234].

In the case where the two mixing times are equal ($\tau_1 = \tau_2$) a rotational resonance echo will occur (see Figure 4.8). However, the magnitude of the echo is not equal to the initial level of difference magnetisation as a result of zero-quantum relaxation. Comparison of rotational resonance echo intensity across different time delays is therefore a means of directly measuring T_2^{ZQ}.

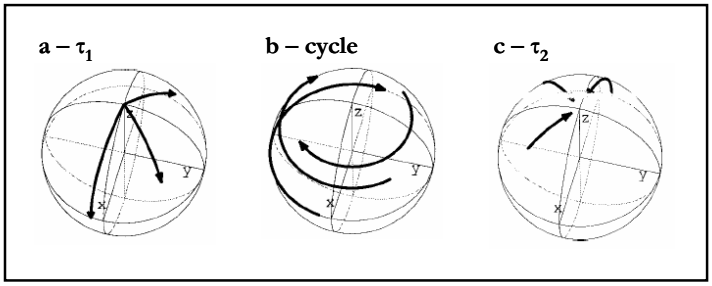

Figure 4.8 – Rotational resonance echoes depicted a fictitious zero-quantum frame (adapted from [220]): zero-quantum state vectors spread during the initial rotational resonance exchange period, observed a decrease of Zeeman difference magnetisation (a) the refocusing cycle shifts zero-quantum state vectors around the z-axis (b) the vectors refocus by continuing along their initial trajectories during the second exchange period (c).

The cycle applied in rotational resonance echoes has also been utilised in creating double-quantum coherences under rotational resonance conditions [229-231]. There are currently no published examples of the application of either rotational resonance echoes or double-quantum excitation under rotational resonance to real biological systems.

4.3 Methodology

4.3.1 Sample Preparation

4.3.1.1 Glycine

1,2-$^{13}C_2$-glycine was diluted with unlabelled glycine (1:19 molar ratio) and repeatedly crystallised from aqueous solution to ensure that a single crystal form was obtained. Dried crystals were

powdered using a mortar and pestle and packed into a 4 mm Chemagnetics MAS rotor, using standard Teflon spacers.

4.3.1.2 Acetylcholinesterase

Lyophilised *Electrophorus electricus* AChE (50,000 units, Sigma-Aldrich, Type V-S, approximately 400 nmoles protein) were dissolved in distilled water (8 ml) and divided between two previously prepared Float-a-lyzers (3500 Da limit) for dialysis (4 hours, 4 °C, 5 litres of 25 mM potassium phosphate, 0.05 mM EDTA at pH 7.1).

The dialysed solutions were first combined, then divided again into two equal volumes. An excess (approximately 10:1 molar ratio) of ^{13}C labelled R414983 was added to one half of the enzyme (1 ml, 1 mg/ml), with buffer solution (1 ml, 25 mM potassium phosphate, 0.05 mM EDTA, pH 7.1) added to the remaining enzyme). Both solutions were left to equilibrate (30 min, 25 °C) before dialysis using two further Float-a-lyzers (3500 Da limit) to remove the unbound excess inhibitor (12 hours, 4 °C, 5 litres of 25 mM potassium phosphate, 0.05 mM EDTA at pH 7.1).

After completion of the second dialysis step the enzyme samples were frozen quickly in liquid nitrogen and lyophilised. Each sample was then placed in a 4 mm Chemagnetics MAS rotor with the volume restricted appropriately using additional Teflon inserts.

4.3.2 NMR Experiments

4.3.2.1 General conditions

All experiments were performed on a Chemagnetics 500 MHz (^{1}H frequency, 125 MHz for ^{13}C) spectrometer using a 4 mm dual channel Chemagnetics Apex MAS probe. Unless otherwise noted, the temperature for experiments was maintained at -30 °C. Typically, 64 transients were acquired per data point on labelled glycine samples and 2000 transients

acquired on both the protein and protein/inhibitor samples. Integral intensities were determined by peak fitting using the FELIX software package.

4.3.2.2 T_2 measurement

A Hahn spin echo experiment [235] was used to measure single-quantum relaxation rates. A 63 kHz field was used to generate initial proton magnetisation and during CP, while a 100 kHz field was applied for decoupling during the relaxation decay and a 63 kHz field during acquisition. A carbon field strength of 63 kHz was applied throughout the experiment, although this was modulated by a 20% linear ramp during CP. Time delays for relaxation were synchronised to whole rotor periods. A spinning speed of 9000 Hz was used. Time constants were determined by least squares fitting of an exponential curve.

4.3.2.3 Rotational resonance experiments

The rotational resonance scheme discussed earlier (Section 4.2.2.1, Figure 4.3) was applied to the investigation of internuclear distances in both glycine and for acetylcholinesterase bound $^{13}C_5$-R414983. Field strengths were applied at the same levels as during T_2 experiments. Rotor spinning frequencies were carefully chosen to match the $n = 1$ condition for the spin pair of interest and the DANTE inversion was optimised separately in each experimental case. Magnetisation loss at a spinning speed off rotational resonance was found to be negligible. An appropriate range of mixing times were chosen in each case such that a suitable degree of magnetisation exchange was observed. Multiple points were taken close to 0 ms and averaged to provide the initial time point.

Simulated exchange curves were fitted to the experimental data using the RR FIT program [236], an adaptation of CC2 (Malcolm Levitt, Southampton) derived from the original theoretical treatment [232]. Tensor values were taken from the range typical for the sites under

consideration, while T_2^{ZQ} was estimated using both the combination of individual linewidths and measured relaxation rates (T_2).

4.3.2.4 Rotational resonance echo experiments

The variation of difference magnetisation intensity during the rotational resonance echo experiment was investigated using the sample of labelled glycine, since the scheme has not previously been applied to a biological system. The impact of the time delays in the rotational resonance echo scheme discussed earlier (Section 4.2.2.1, Figure 4.7) was first investigated with τ_1 kept constant while the τ_2 period was arrayed. Values were chosen such that τ_1 was synchronised to an integral number of rotor periods, while τ_2 was varied across a range of time points corresponding to both an integral number of rotor periods and points falling between whole rotor periods.

After the scheme was shown to be performing as expected [220], zero-quantum relaxation rates were then determined for the labelled glycine and one pair of spins from bound $^{13}C_5$-R414983 by performing a range of echo decay experiments ($\tau_1 = \tau_2$). Field strengths were applied at the same levels as during the other experiments, with proton decoupling turned off during the refocusing cycle.

4.4 Results

4.4.1 T_2 Measurement (Hahn Echo)

4.4.1.1 Labelled glycine

The single-quantum relaxation rate for the C1 position (carbonyl) was determined to be 5.44 ± 0.68 ms while the corresponding rate for the C2 position (α) was 3.76 ± 0.24 ms (Figure 4.9). Both of these values are lower, as expected, than would be typical for an isolated ^{13}C spin (~10

ms). The faster decay associated with the C2 position is a result of heteronuclear coupling with its directly bonded protons which has not been completely suppressed by the combination of magic-angle spinning and the decoupling field.

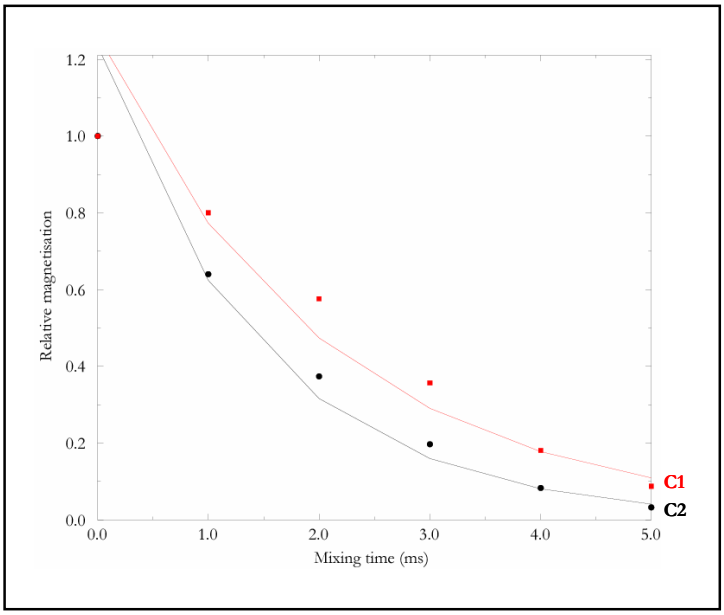

Figure 4.9 – T_2 decay curves for $^{13}C_2$-glycine diluted 1:19 with unlabelled glycine: intensity values have been normalised to the initial time point. Data for the C1 (carbonyl) position are shown as red squares and a red line (T_2 5.44 ms, R = 0.9786) while the C2 (α) position is indicated by black filled circles, with the appropriate exponential fit as a black line (T_2 3.76 ms, R = 0.9898).

4.4.1.2 $^{13}C_5$-R414983 bound to acetylcholinesterase

Data from experiments on the background sample (acetylcholinesterase without bound ligand) were subtracted from the results for acetylcholinesterase with bound $^{13}C_5$-R414983 to produce spectra for the bound ligand alone. The integral intensities of these spectra were used to produce relaxation curves shown in (Figure 4.10), relaxation rates are summarised in Table 4.1.

Table 4.1 – T_2 relaxation rates (with standard deviation) for ^{13}C labelled positions within $^{13}C_5$-R414983 bound to AChE.

Label position	Relaxation rate (ms)
Quinoline methylene	2.03 ± 0.20
Benzyl methylene	3.19 ± 0.08
Quinoline C2	3.91 ± 0.67
Quinoline C3	3.53 ± 0.18
2-methyl	4.09 ± 0.27

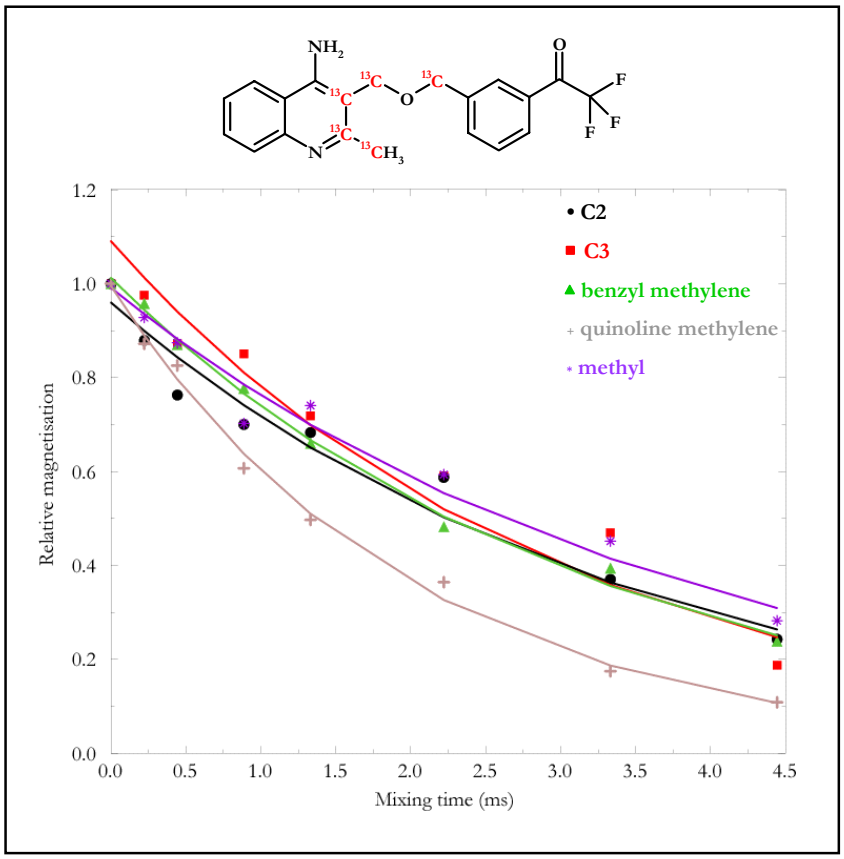

Figure 4.10 – T_2 decay curves for $^{13}C_5$-R414983 bound to acetylcholinesterase: intensity values have been normalised to the initial time point (C2 R=0.9840, C3 R=0.9569, benzyl R=0.9951, quinoline R=0.9977, methyl R=0.9850)..

All of the resonances show relaxation rates which are well below the normal range for isolated ^{13}C spins (~10 ms). The 2-methyl position relaxes at the slowest rate (4.09 ms) as it is directly bonded to only one other labelled carbon and is able to undergo free rotation which ensures that it is effectively decoupled from its attached protons. The two aromatic positions (C2, C3) and the benzyl methylene relax at an intermediate rate (3.91, 3.53 and 3.19 ms respectively). In

the case of the aromatic carbons, enhanced relaxation is due to the effect of the strong homonuclear coupling to multiple directly bonded sites. For the benzyl methylene, increased relaxation is due to heteronuclear coupling to its attached protons. The quinoline methylene experiences the effects of both a strong homonuclear coupling to the C3 position and strong heteronuclear couplings, therefore relaxing at the fastest rate (2.03 ms).

4.4.2 Rotational Resonance

4.4.2.1 Labelled glycine

The short distance separating the directly bonded spins in the labelled glycine sample ensures that magnetisation exchange proceeds at a rapid rate. The strength of the coupling is such that oscillations of both resonances around the baseline can be observed (Figure 4.11).

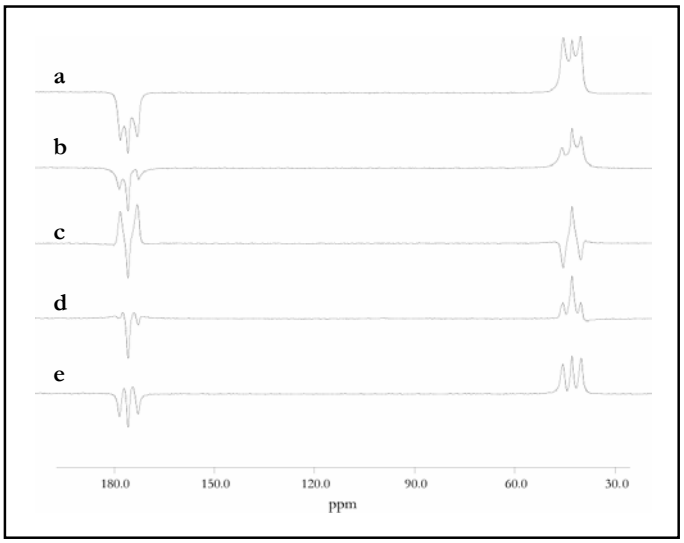

Figure 4.11 – Magnetisation oscillations of $^{13}C_2$-glycine resonances under rotational resonance exchange: at rotational resonance at the $n = 1$ condition, $\omega_r = 16720$ Hz., showing rotational resonance exchange following inversion of the $^{13}C{=}O$ peak and after $\tau_m = 0.0$ ms (a) $\tau_m = 0.3$ ms (b) $\tau_m = 0.6$ ms (c) $\tau_m = 0.9$ ms (d) $\tau_m = 1.4$ ms (e).

After initial magnetisation is prepared with the carbonyl resonance inverted (Figure 4.11a), rotational resonance exchange results in a progressive decrease of peak intensities and net magnetisation (Figure 4.11b). Resonances then pass through the baseline and develop inverted

intensities. Net magnetisation increases in this inverted state (Figure 4.11c), before decreasing again as the spins continue to undergo exchange (Figure 4.11d). The oscillatory profile continues as magnetisation then develops in the initial direction, increasing the net magnetisation but not to the extent observed at the outset of the experiment (Figure 4.11e).

Due to the well defined oscillating profile in magnetisation transfer (Figure 4.12) it is possible to create a simulated fit without the need to restrain the zero-quantum parameter since there is likely to be a low correlation with the dipolar coupling strength [218].

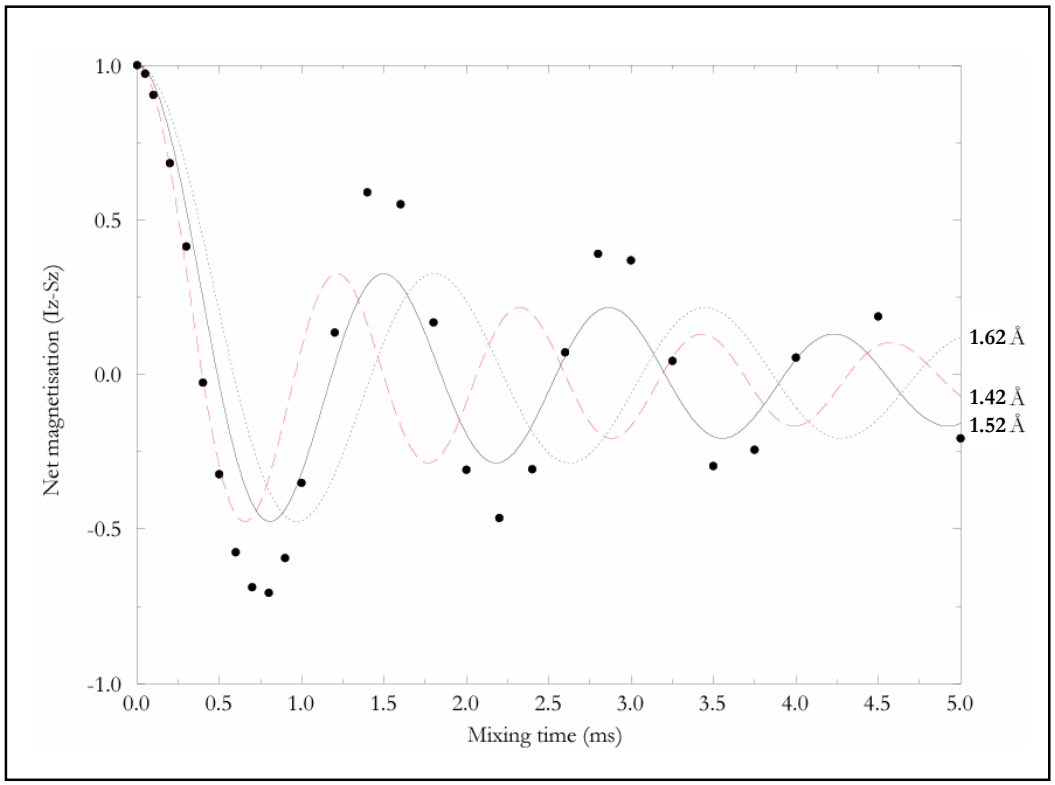

Figure 4.12 – Rotational resonance exchange curve for $^{13}C_2$-glycine: experimental data is shown as black dots, with the appropriate fit (1.52 Å) as a solid black curve, R=0.9487. Simulated exchange curves for 1.42 Å (dashed red line) and 1.62 Å (dotted blue line) internuclear distances are also shown.

The results of the data fit are shown in Figure 4.12. The dipolar coupling of 2149 Hz corresponds to a C1-C2 internuclear distance of 1.52 Å (applying Equation 4.2), which is in

good agreement with previous measurements† performed using x-ray diffraction (1.52 Å) [237], neutron diffraction (1.53 Å) [238] and NMR (1.54 Å) [239]. Theoretical curves for internuclear distances of 1.42 Å and 1.62 Å are also shown and demonstrate that experiments performed under these 'ideal' conditions are likely to have relatively low levels of uncertainty.

The discrepancy between intensities of the simulated and experimental data is common for strongly coupled spin pairs and is a result of the simulation methodology. The effect of this discrepancy on the dipolar coupling is negligible since, under the strongly coupled conditions for which the discrepancy occurs, the frequency of intensity oscillations are more characteristic than the absolute intensity values (the simulated curves corresponding to 1.42 and 1.62 Å both have similar ranges of intensity oscillations, but demonstrate these oscillations at a higher and lower frequency respectively).

4.4.2.2 $^{13}C_5$-R414983 bound to acetylcholinesterase

The spectra of $^{13}C_5$-R414983 bound to acetylcholinesterase reveal particularly broad resonances (Figure 4.13), probably as a result of local structural inhomogeneity in the sample (T_2 measurements show that relaxation rates are not the limiting factor for the linewidths). It is therefore important to examine a number of the fixed internuclear distances, in order to quantify the possible effect of inhomogeneity on distance measurements (i.e. the extent of off-resonance effects in magnetisation exchange) and determine whether it is possible to incorporate an inhomogeneity parameter in simulations if necessary.

Table 4.2 lists the rotational resonance match condition for each spin combination at n = 1, 2 and 3. The data demonstrates that for each spin pair chosen for investigation, the closest

† The dipolar coupling is also resolved in the one-dimensional spectrum as a 562 Hz splitting of the C1 carbonyl resonance and a 637 Hz splitting of the C2 resonance. These values, taken directly from the line shape, suggest a dipolar coupling [215, 232] of 1589 Hz and 1801 Hz, giving distances of 1.68 Å and 1.62 Å respectively.

match is a minimum of 795 Hz away. The distance measurements obtained from rotational resonance experiments are summarised in Table 4.3 and subsequently discussed in detail.

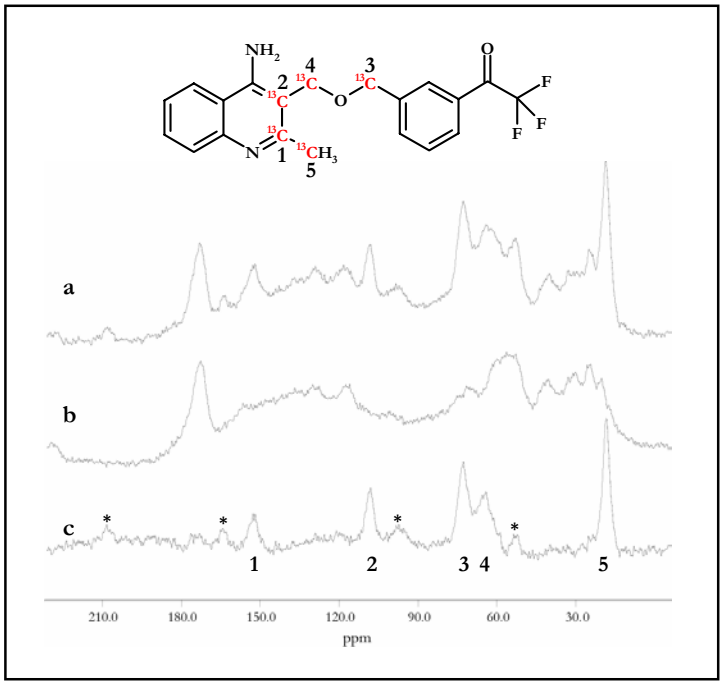

Figure 4.13 – ^{13}C spectra of acetylcholinesterase bound $^{13}C_5$-R414983: a ramped cross-polarisation experiment was used, ω_r = 7500 Hz. Spectrum of acetylcholinesterase with bound ligand (a) spectrum of acetylcholinesterase background (b) background subtracted spectrum, showing the five ^{12}C labelled sites within the inhibitor, * indicates a spinning sideband (c).

Table 4.2 – Rotational resonance match conditions (values are given in Hz).

Spin pair	Isotropic chemical shift difference (n = 1)	n = 2	n = 3
Quinoline C2/quinoline C3 (1/2)	5875	2938	1958
Quinoline C2/benzyl methylene (1/3)	10400	5200	3467
Quinoline C2/quinoline methylene (1/4)	11195	5598	3732
Quinoline C2/2-methyl (1/5)	17250	8625	5750
Quinoline C3/benzyl methylene (2/3)	4525	2263	1508
Quinoline C3/quinoline methylene (2/4)	5320	2660	1773
Quinoline C3/2-methyl (2/5)	11375	5688	3792
Benzyl methylene/quinoline methylene (3/4)	795	398	265
Benzyl methylene/2-methyl (3/5)	6850	3425	2283
Quinoline methylene/2-methyl (4/5)	6055	3028	2018

Table 4.3 – Summary of rotational resonance distance measurements.

Spin pair	ω_r (Hz)	Expected distance (Å)	T_2^{ZQ} (ms)		Measured distance (Å)	
			linewidth	T_2	linewidth	T_2
Quinoline methylene/2-methyl	6055	2.95	0.231	1.35	3.0	4.0
Quinoline C3/2-methyl	11375	2.53	0.315	1.89	3.0	4.0
Benzyl methylene/2-methyl	6850	<5.63	0.303	1.79	3.9	5.2
Quinoline C2/benzyl methylene	10400	2.91-5.13	0.174	1.88	3.5	5.1
Quinoline C3/benzyl methylene	4525	3.14-3.79	-	-	-	-

4.4.2.2.1 Internal calibration measurements

Quinoline methylene/2-methyl spin pair

The frequency difference between the isotropic chemical shifts for the quinoline methylene and the 2-methyl labels is 6055 Hz. Figure 4.14 shows an example of the spectra obtained during rotational resonance on the quinoline methylene/2-methyl spin pair. These spectra are representative of all other experiments on the protein and protein/inhibitor samples.

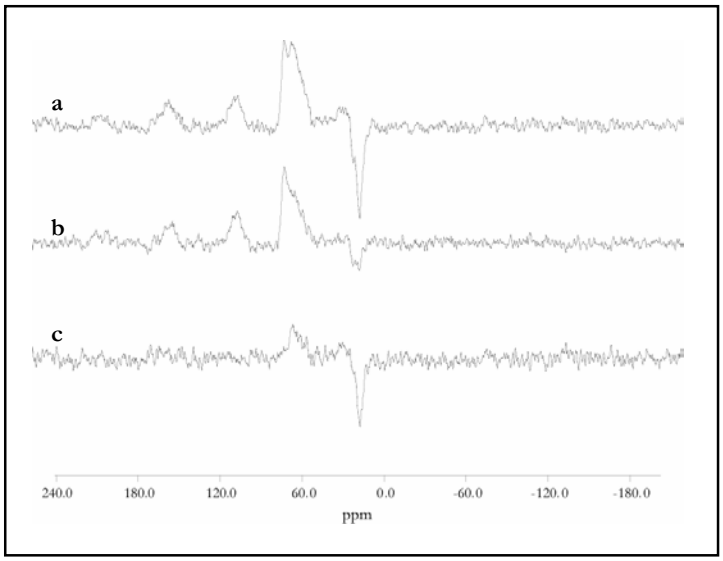

Figure 4.14 – ^{13}C rotational resonance spectra the quinoline methylene/2-methyl spin pair in bound $^{13}C_5$-R414983: the rotational resonance sequence was used at the n = 1 match (ω_r = 6055 Hz), spectra are produced by subtraction of the control acetylcholinesterase spectra from those of acetylcholinesterase with bound ligand τ_m = 0 ms (a) τ_m = 22 ms (b) difference spectrum illustrating magnetisation exchange during the 22 ms mixing period (c).

At the n = 1 rotational resonance condition (ω_r = 6055 Hz), as a result of the longer internuclear distance and thereby a weaker dipolar coupling, magnetisation exchange occurs over a significantly longer period of time than for the directly bonded spin pair in the labelled glycine sample.

A simulated fit of the experimental data is shown in Figure 4.15. Using the combined spectral linewidths as an estimate for T_2^{ZQ} (0.231 ms) produces a dipolar coupling of 287 Hz (corresponding to an internuclear distance of 3.0 Å). In the case where single-quantum relaxation rates are used to estimate T_2^{ZQ}, the combination of T_2 values for the two sites leads to an estimate of 1.35 ms (Section 4.4.1.2), a dipolar coupling of 119 Hz then provides the most suitable fit (4.0 Å). The distance is expected to be 2.95 Å (corresponding to b_{IS} = 296 Hz) [43], which suggests that T_2^{ZQ} estimation using spectral linewidths is much more reliable (< 0.1 Å error) than using single-quantum relaxation rates (1 Å error), in the absence of explicitly including inhomogeneity effects in the analysis.

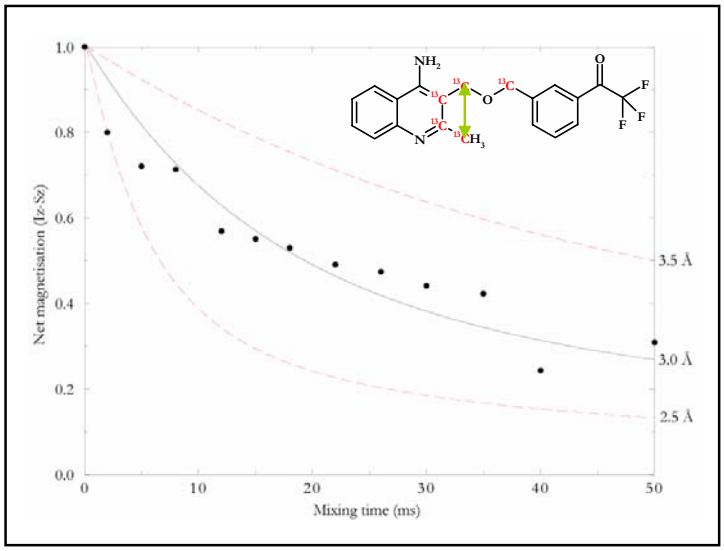

Figure 4.15 – Rotational resonance exchange curve for quinoline methylene/2-methyl label pair: experimental data is shown as black dots, with the appropriate fit (3.0 Å) as a solid black curve. Simulated exchange curves for 2.5 Å and 3.5 Å internuclear distances are shown as dashed red lines. Simulations are based on the use of spectral linewidths for estimation of zero-quantum relaxation, R=0.9691.

Incorporating a dipolar coupling value based on the expected distance into the simulation allows the determination of an apparent T_2^{ZQ}. This value, found to be 0.230 ms, was later used in simulating a fit for the variable benzyl methylene/2-methyl spin pair which can be expected to have similar spin dynamics.

Appendix 5 uses this data set to demonstrate that the statistical error introduced by noise in the rotational resonance results is relatively small, and that systematic errors (such as the method of T_2^{ZQ} estimation) are the major source of deviation in distance determinations.

Quinoline C3/2-methyl spin pair

At the n = 1 condition for the quinoline C3/2-methyl spin pair (11375 Hz), a simulated fit (Figure 4.16) using the combined spectral linewidths for T_2^{ZQ} (0.315 ms), produces a dipolar coupling of 281 Hz (corresponding to an internuclear distance of 3.0 Å). In the case where single-quantum relaxation rates are used to estimate T_2^{ZQ} (1.89 ms), a dipolar coupling of 115 Hz provides the best fit (a 4.0 Å separation).

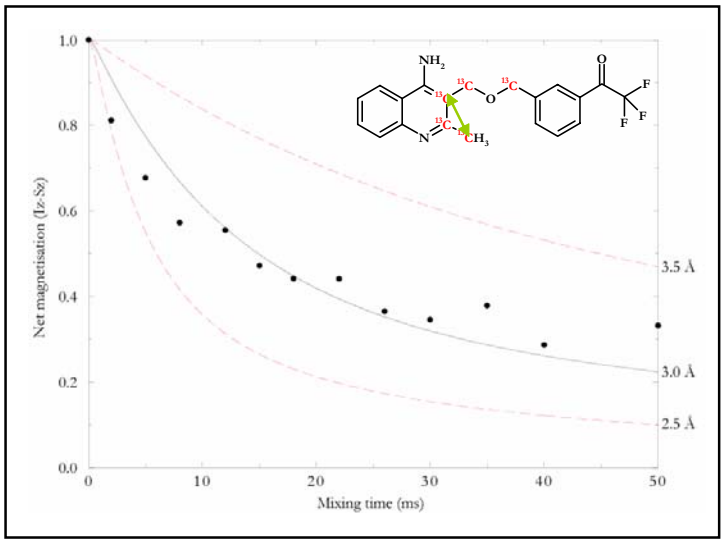

Figure 4.16 – Rotational resonance exchange curve for quinoline C3/2-methyl label pair: experimental data is shown as black dots, with the appropriate fit (3.0 Å) as a solid black curve. Simulated exchange curves for 2.5 Å and 3.5 Å internuclear distances are shown as dashed red lines. Simulations are based on the use of spectral linewidths for estimation of zero-quantum relaxation., R=0.9774

Crystal data indicates a separation of 2.53 Å (with an expected dipolar coupling of 469 Hz) [43]. Again, T_2^{ZQ} estimation using spectral linewidths produces a better result (0.5 Å error) than using single-quantum relaxation rates (1.5 Å error). The good quality of the simulated fit to the experimental results suggests that the errors do not arise from random variation in the data but are due to a systematic inaccuracies arising from T_2^{ZQ} estimation or inhomogeneity which affects all time points. Subtle oscillations in the exchange profile are visible, these are frequently observed and are probably due to a small residual dipolar couplings between the spin pair of interest and the other labelled sites with the inhibitor (incompletely averaged by magic-angle spinning), though these are unlikely to contribute significantly to the distance error [240].

Estimation of zero-quantum relaxation

Considering that T_2^{ZQ} estimation from single-quantum relaxation consistently underestimated the coupling strength for both fixed distance measurements (errors of 1.0 and 1.5 Å when compared to x-ray crystallography distances), while estimation using linewidths were significantly more accurate (errors of < 0.1 and 0.5 Å), it is therefore likely that the linewidth based method provides the most accurate result for the variable distance measurements.

4.4.2.2.2 Variable distance measurements

Benzyl methylene/2-methyl spin pair

The first pair of spins with a conformationally dependent separation, benzyl methylene/2-methyl, are separated in the spectrum by a frequency difference of 6850 Hz. The magnetisation exchange profile correlates to a dipolar coupling of 131 Hz (corresponding to a separation of 3.9 Å) based on T_2^{ZQ} estimation from the combined linewidths (0.303 ms), a coupling of 55 Hz (5.2 Å) from the measured T_2 (1.79 ms) based estimation and a coupling of 150 Hz (3.7 Å) if

the value for T_2^{ZQ} is taken from the quinoline methylene/2-methyl calibration experiment (0.230 ms). The internuclear distance can reach a potential maximum of 5.63 Å in the most extended conformational form, based on typical bond lengths from crystal data.

As discussed earlier, the linewidth based approach is likely to be the most accurate measurement. Additional support for this approach comes from applying the apparent T_2^{ZQ} from the quinoline methylene/2-methyl spin pair, which has a relatively high degree of similarity in the chemical environments for the two nuclei. However, due to the differences in dipolar coupling values an error in internuclear distance of 0.5 Å may be possible.

Oscillations in the exchange profile (Figure 4.17) are observed, again probably due to residual dipolar couplings from other ^{13}C labels in close proximity to the sites under rotational resonance. This variation results in a relatively low correlation value (R=0.8623), although is taken into account with the limits of ± 0.5 Å.

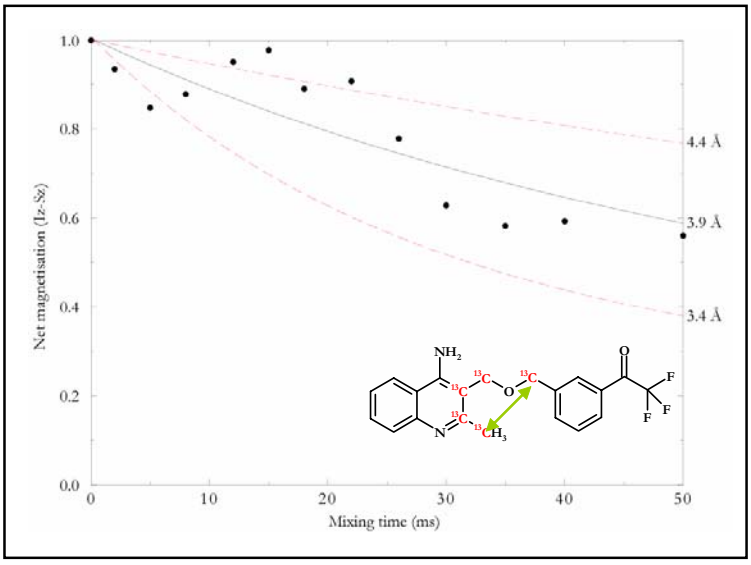

Figure 4.17 – Rotational resonance exchange curve for benzyl methylene/2-methyl spin pair: experimental data is shown as black dots, with the appropriate fit (3.9 Å) as a solid black curve. Simulated exchange curves for 3.4 Å and 4.4 Å internuclear distances are shown as dashed red lines. Simulations are based on the use of spectral linewidths for estimation of zero-quantum relaxation, R=0.8623.

Quinoline C2/benzyl methylene spin pair

The $n = 1$ rotational resonance condition for the quinoline C2/benzyl methylene resonances is met at a spinning frequency of 10400 Hz. The magnetisation exchange profile is shown in Figure 4.18. The spread of experimental points is larger than during previous distance measurements, with R=0.7764. However, a fit to the data based on T_2^{ZQ} estimation from the combined linewidths (0.174 ms) produces a dipolar coupling of 182 Hz (3.5 Å). Again, use of the Hahn echo measured T_2 (1.88 ms) provides a much longer distance value (b_{IS} = 56 Hz, corresponding to 5.1 Å) which is likely to be an overestimate. Based on crystal structure data, the distance is expected to fall within the range of 2.91-5.13 Å.

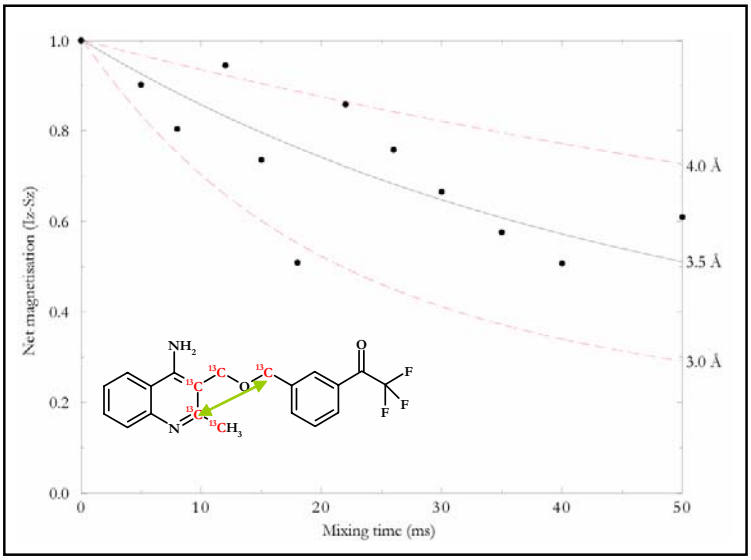

Figure 4.18 – Rotational resonance exchange curve for quinoline C2/benzyl methylene pair: experimental data is shown as black dots, with the appropriate fit (3.5 Å) as a solid black curve. Simulated exchange curves for 3.0 Å and 4.0 Å internuclear distances are shown as dashed red lines. Simulations are based on the use of spectral linewidths for estimation of zero-quantum relaxation, R=0.7764.

Both pairs of nuclei involved in the calibration experiments are chemically different, which may invalidate the use of their apparent zero-quantum relaxation rates to this particular case (the first fixed distance is between methylene and methyl sites while for the second fixed

distance, although it involved a methylene-aromatic measurement, the C3 aromatic has a very different chemical environment to the C2 position). However, it is likely that inhomogeneity effects dominate contributions dependant upon the nature of the nuclei and these inhomogeneity effects are expected to be similar. Application of the apparent T_2^{ZQ} from the quinoline methylene/2-methyl pair (0.230 ms) results in a dipolar coupling of 158 Hz (3.6 Å), while the quinoline C3/2-methyl data (0.111 ms) suggests a coupling of 228 Hz (3.2 Å). These two values are similar to the 3.5 Å determined using spectral linewidths for T_2^{ZQ} estimation.

Quinoline C3/benzyl methylene spin pair

Due to the relatively small frequency separation between the aromatic quinoline C3 and benzyl methylene position (4525 Hz) at the $n = 1$ condition a large proportion of intensity for resonances occurs within rotational sidebands i.e. the spinning frequency is small compared to the chemical shift anisotropy. Superposition of rotational sidebands with isotropic resonances for inverted and non-inverted nuclei causes a reduction of spectral intensity. Combined with the effects from residual dipolar couplings, which are also amplified at lower spinning speeds, this results in a greatly reduced level of signal to noise across the whole spectrum and ensures that accurate deconvolution of peak intensities is not possible.

Figure 4.19 shows a representative spectrum. The isotropic peaks of the aromatic positions, in particular, are significantly reduced in intensity because of their high CSA.

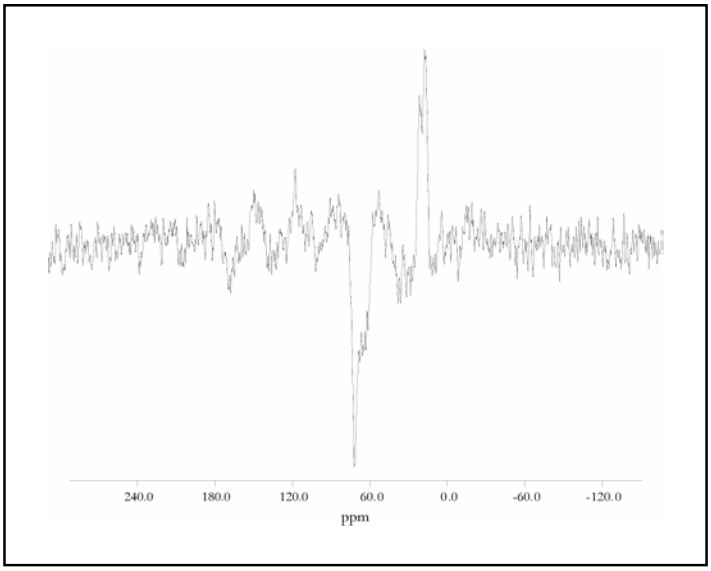

Figure 4.19 – ^{13}C spectral subtraction from rotational resonance experiments on the benzyl methylene/quinoline C3 spin pair: ω_r = 4550 Hz. A large proportion of signal is lost in sideband intensities, especially for the two aromatic resonances at 108 and 152 ppm, making deconvolution of peak intensities difficult.

4.4.3 Zero-quantum Relaxation Measurement

4.4.3.1 $^{13}C_2$-glycine

The variation of difference magnetisation intensity during the rotational resonance echo experiment was investigated using the sample of labelled glycine. The complex oscillatory behaviour of intensity around the echo position is illustrated in Figure 4.20. When the initial delay period (τ_1) is fixed at a value equivalent to 80 rotor cycles, a gross oscillation in intensity is observed across a range of τ_2 delays which are located on rotor cycles at 10 cycle intervals. The echo intensity varies from a normalised value of 1 (when $\tau_1 = \tau_2$) to as low as -0.85. An array of τ_2 delays over a shorter range, again located on rotor periods, suggests that the form of the gross oscillations is correct and is not a result of digitisation from of the 10 cycle steps. However, variation of τ_2 delays such that data points lay between rotor cycles indicates that a second smaller oscillation in difference magnetisation intensity (covering a normalised range of 0.15) is superimposed on the overall gross profile.

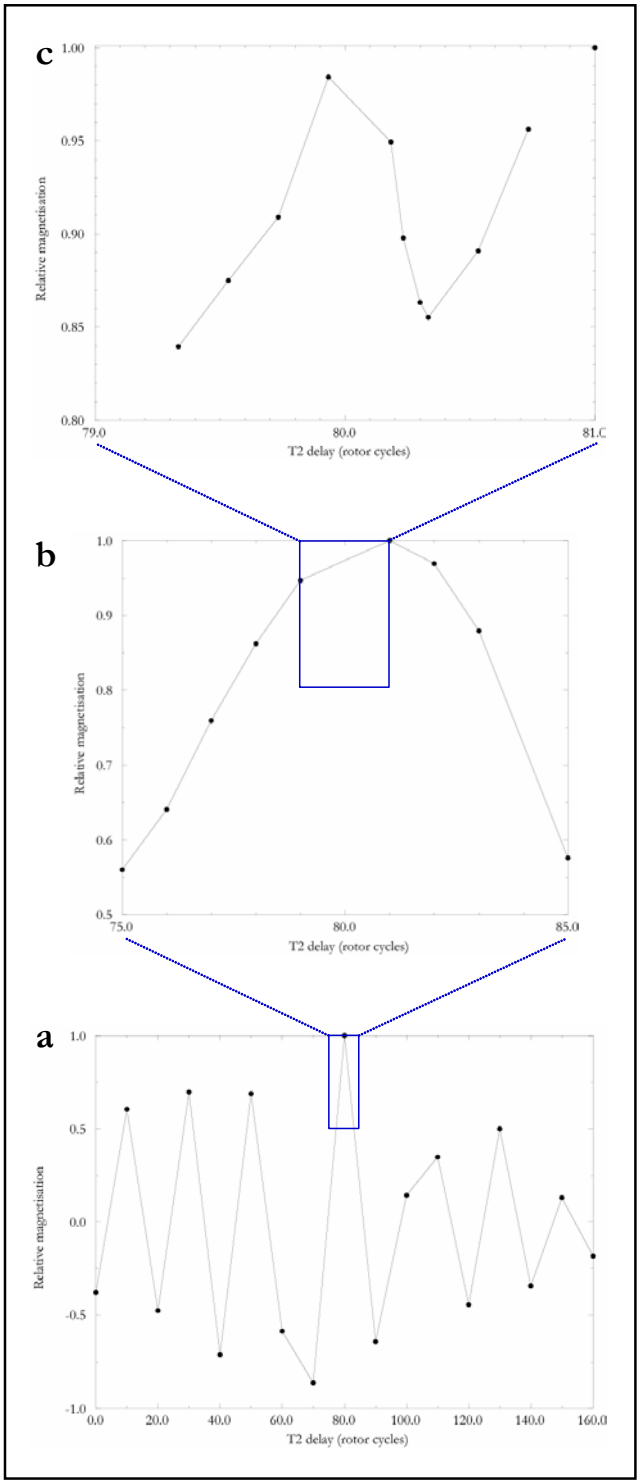

Figure 4.20 – Rotational resonance echoes from $^{13}C_2$-glycine: acquired at 125 MHz and the n = 1 rotational resonance condition. The initial delay, τ_1, is maintained at 80 rotor cycles (4.790 ms) with the second delay period, τ_2, varied between 0 and 160 rotor cycles, at intervals of 10 cycles (a) between 75 and 80 rotor cycles, on each rotor cycle (b) between 79 and 81 rotor cycles with values between complete rotor cycles (c).

Observation of rotational resonance echo intensity for a range of time delays such that $\tau_1 = \tau_2$ and fitting of the resulting data to a single exponential decay profile provides a direct measurement of zero-quantum relaxation (Figure 4.21). It should be noted that T_2^{ZQ} is actually half of the decay time constant determined from the experimental data (due to the zero-quantum vectors spending approximately 50% of their time in the transverse plane [220]) providing a value of 14.1 ms‡, this value is similar to that found in previous work on doubly labelled glycine (9.0 ms [233]). The discrepancy with earlier experiments may be explained through the fact that samples were not isotopically diluted, as was the case the current study (resulting in a faster rate of zero-quantum relaxation).

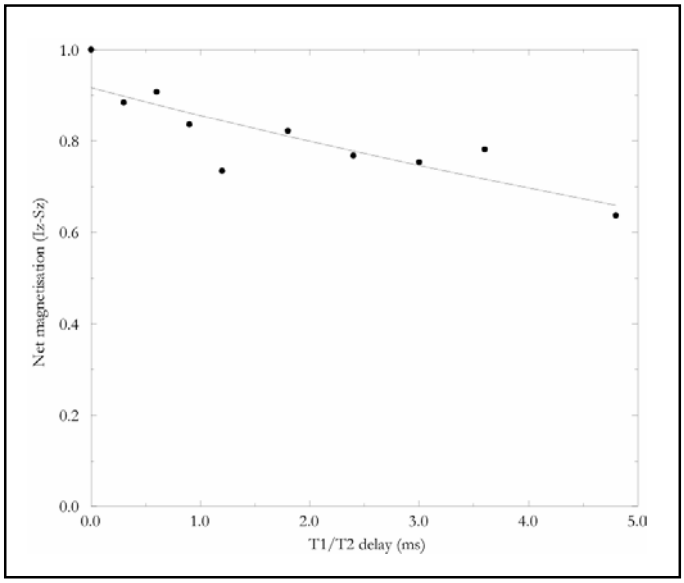

Figure 4.21 – Zero-quantum relaxation in $^{13}C_2$-glycine: applying the rotational resonance echo experiment at the n = 1 condition, normalised difference magnetisation intensity for a range of delay times (where $\tau_1 = \tau_2$) is shown as black dots, with a least squares exponential fit to the experimental data shown by a black line, R=0.8547.

‡ Based on the combined single quantum relaxation rates (determined earlier in Section 4.3.2.2) the zero-quantum relaxation rate is estimated to be 2.223 ms, a value significantly different from that measured directly.

4.4.3.2 $^{13}C_5$-R414983 bound to acetylcholinesterase

The benzyl methylene/2-methyl spin pair was selected for zero-quantum relaxation investigation as a representative example from the rotational resonance experiments performed previously (Section 4.4.2.2.2).

Use of the combined spectral linewidths to estimate T_2^{ZQ}, found to be the most appropriate method based on the calibration distance measurements, gave a value of 0.174 ms. However, application of the rotational resonance echo experiment to the benzyl methylene/2-methyl pair produced a result which conflicts with the linewidth based estimation method (Figure 4.22). While the data shows a relatively large error range, this is unlikely to have a serious effect on the overall form of the plot and it can be concluded that no significant loss of difference magnetisation occurs during the course of the experiment. This result is not unexpected since the time constant for zero-quantum relaxation can exceed 30 ms [233].

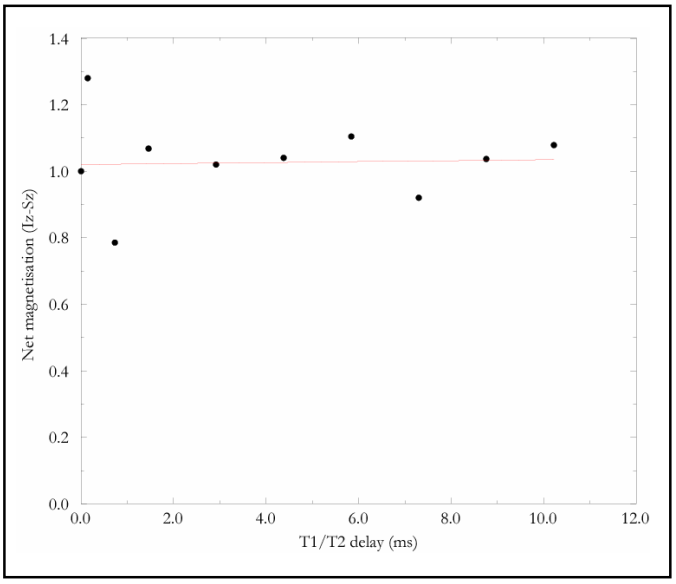

Figure 4.22 – Zero-quantum relaxation for benzyl methylene/2-methyl spin pair: acquired at 125 MHz, using the rotational resonance echo experiment at the n = 1 condition. The normalised difference magnetisation intensity for a range of delay times (where $\tau_1 = \tau_2$) is shown as black dots, with an exponential fit to the experimental data shown by a red line.

If T_2^{ZQ} was indeed 0.174 ms, it could be expected that difference magnetisation would only be refocused to much less than 1% of the initial level when both time delays are set at 5 ms (this includes a correction for the 50% lower decay rate observed in the echo experiment). Even if T_2^{ZQ} is based upon the single-quantum relaxation rates (1.79 ms), refocusing should still only reach slightly over 12% of the initial level. Taking this into consideration, the lack of any significant decay of difference magnetisation from loss of zero-quantum coherence may seem surprising at first but can be easily explained. It is likely that the degree of zero-quantum coherence from rotational resonance is limited as a result of the large linewidths, rather than T_2^{ZQ} undergoing unusual behaviour.

4.5 Discussion

The validation of NMR methodologies on ideal systems is an important step in the acceptance of new techniques into the field. Biological systems, however, are non-ideal and the desire to answer a specific biological problem creates a need to make compromises between the optimisation of experimental conditions and the collection of data.

Sample inhomogeneity, due to a degree of local structural variation in the environment of the bound inhibitor, resulted in extremely broad resonance linewidths. Rotational resonance experiments, though widely accepted as an accurate method for the determination of internuclear distances (see Section 4.2.2) and successfully demonstrated here using a sample of labelled glycine, have not been characterised under such unusual conditions. Additionally, the use of single-quantum relaxation rates and spectral linewidths have both been shown as a valid means for estimation of zero-quantum relaxation [151, 160, 185, 217], although a large sample inhomogeneity will lead to an increase in the discrepancy between these methods. It is therefore important to determine if the application of rotational resonance under extreme

inhomogeneous broadening can still produce reliable distance measurements and, if not, what corrective steps can be taken to improve accuracy.

In spite of the difficult experimental conditions both of the fixed internuclear distances were successfully determined to within 0.5 Å of the x-ray crystallography measurements (Section 4.4.2.2.1). Errors on this scale are acceptable in the current study, since the conformational freedom of the inhibitor can still be significantly restrained. The smallest distance errors are achieved through the use of spectral linewidths for estimation of the zero-quantum relaxation term, while the use of single-quantum relaxation rates for this purpose produced a larger error in both cases (which was consistently an underestimate of the internuclear distance). It is clear from a comparison of data spread with the simulated exchange profiles that random effects are unlikely to significantly affect the size of errors (see Appendix 5 for further details).

Rotational resonance is considered a narrow-banded method and exchange dynamics are sensitive to deviation from the match condition [232]. Inhomogeneity in resonance linewidths, in a similar manner to a small offset in spinning speed, results in reduced magnetisation exchange as the rotational resonance condition is not simultaneously met across all isochromats of the resonance. Earlier investigations of the impact of inhomogeneous linewidths (methods for its correction [218] and application to a biological problem [222]) relied upon the transfer of parameters discerned from short internuclear distances with well defined exchange profiles to the weaker exchange profiles where these parameters cannot be independently simulated. A number of points arise in the comparison of the current work to these earlier studies. Firstly, the extent of the inhomogeneous contribution to linewidths was not reported and it is not obvious whether the transfer of parameters would still be valid under the extreme conditions observed here. Secondly, despite incorporation of an inhomogeneity parameter from a strongly coupled standard, potential errors in the final distances determined

are not greatly reduced when compared to the errors found in the two calibration distance measurements made here. However, their approach is analytically more appropriate.

The success of the fixed distance measurements lies in the use of spectral linewidths for the estimation of the T_2^{ZQ} term in simulations. While inhomogeneity retards magnetisation exchange and should lead to an underestimate of the dipolar coupling, it additionally produces an overestimate of the rate of zero-quantum relaxation which, to a good approximation (under the current experimental conditions), compensates for the slower exchange observed. Estimation of zero-quantum relaxation using single-quantum relaxation rates produces a greater error in internuclear distance since it does not incorporate this 'internal' correction.

Evidence supporting the scenario of a corrected retarded exchange comes from the rotational resonance echo experiments. While the scheme was demonstrated on a sample of crystalline labelled glycine (low inhomogeneity), no significant zero-quantum relaxation was observed when applied to the acetylcholinesterase bound inhibitor during a total exchange period of 20 ms (Section 4.4.3). T_2^{ZQ} can be greater than 30 ms [233], however, the lack of observed zero-quantum relaxation is likely to be due to a low level of zero-quantum coherence (resulting from the broad lines and poor rotational resonance match) and therefore only a small portion of the difference magnetisation has the potential to relax.

With the ability to measure zero-quantum relaxation directly, it is clear that both of the currently accepted methods for estimation zero-quantum relaxation in rotational resonance simulations, using spectral linewidths or single quantum relaxation rates, produce values which substantially overestimate the true relaxation rate (suggesting a smaller time constant). Current simulation methodology must therefore already include some degree of inhomogeneity correction, however, both on- and off-resonance effects have been dealt with collectively in a fictitious zero-quantum relaxation term rather than through explicit definition of the exchange

phenomenon. Even under the extreme conditions observed in the present study, inhomogeneity is effectively compensated for by this mechanism. A full mathematical analysis of how inhomogeneity affects rotational resonance exchange and the subsequent simulation of dipolar couplings has not been published. It should now be possible to perform a simulation based on a single parameter fit which incorporates an independently determined inhomogeneity term (discerned from comparison of spectral linewidths and Hahn echo measured relaxation) and the directly measured T_2^{ZQ} value.

The use of rotational resonance echoes as a means of measuring T_2^{ZQ} has been illustrated previously only in examples where the time delays (τ_1, τ_2) fall on complete rotor periods [220, 234]. Behaviour identical to that previously demonstrated was observed on the sample of labelled glycine. The minor oscillation of difference magnetisation between rotor periods has not been shown previously and demonstrates that imprecise synchronisation of the delays to whole rotor periods will have relatively small affect on T_2^{ZQ} measurements.

The two variable distances measured (Figure 4.23), benzyl methylene/2-methyl (3.9 Å) and quinoline C2/benzyl methylene (3.5 Å), both fall within the range of values possible and suggest that the bound inhibitor demonstrates a partially folded conformation. These distances are discussed further during the development of a model for the conformation of the bound inhibitor (Chapter 6).

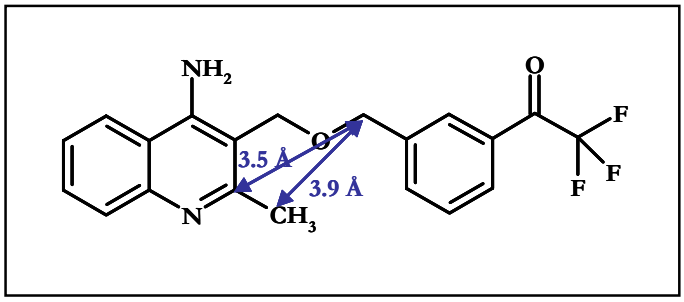

Figure 4.23 – Distances determined for acetylcholinesterase bound R414983 using rotational resonance.

The failure to quantify magnetisation exchange for the third pair of spins with a conformationally dependent separation is unlikely to be of practical significance, as it has the smallest range of potential values (only 0.65 Å). It would therefore be mainly of interest as further confirmation that the experimental methodology produces valid distance measurements. This particular spin pair may be a good candidate for the application of off-resonance techniques [225-228] which would allowing spinning at a higher speed, reducing sideband complexity and averaging residual homonuclear dipolar couplings.

Chapter 5 Rotational-Echo Double-Resonance Experiments

5.1 Overview

The measurment of ^{13}C-^{19}F internuclear distances provides an additional method for investigation of the structure of R414983 bound to acetylcholinesterase.

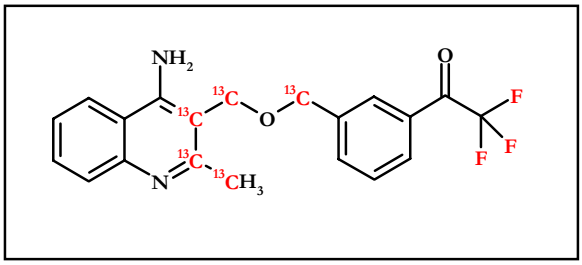

Figure 5.1 – $^{13}C_5$-R414983, 4-Amino-2-methyl-3-(3-triflouroacetylbenzyl-oxymethyl) quinoline.

Heteronuclear ^{13}C-^{19}F dipolar couplings are stronger than homonuclear ^{13}C-^{13}C couplings (due to the higher γ value for ^{19}F), enabling the measurement of accurate internuclear separations over a greater distance range. The isolated location of the trifluoromethyl function with respect to the rigid quinoline core means that heteronuclear distance measurements will significantly reduce the range of possible conformations in the development of a model for the bound state.

5.2 Introduction

5.2.1 Heteronuclear Recoupling Methods

Magic-angle spinning averages those heteronuclear dipolar interactions which are of biological importance, this averaging is subtly different from that of homonuclear dipolar interactions discussed earlier (the abundant proton heteronuclear couplings are an exception because of their homogeneous nature). In contrast to the broad range of homonuclear recoupling techniques available, the number of heteronuclear schemes is relatively small.

Relaxation based recoupling methods such as dipolar exchange-assisted recoupling (DEAR) [241] and the related relaxation-induced dipolar exchange with recoupling (RIDER) [242] have the advantage that only two spectrometer channels are required (for observation and decoupling - interaction with the third spins arises through trains of rotor synchronised π pulses applied on the observe channel to interrupt motional averaging). However, the dependency of these schemes on favourable relaxation rates and their susceptibility to dynamic effects are serious restrictions to their application for biological samples.

Lee-Goldburg cross-polarisation (LG-CP) [243] provides a route for the investigation of ^{1}H-^{13}C distances by the measurement of cross-polarisation rates in the presence of Lee-Goldburg homonuclear decoupling of protons [164]. While this scheme has obvious potential, it may not be possible to deconvolute the many contributions present in the current study (where the effect of both intramolecular couplings and protein-inhibitor couplings are unknown). With the conformation of the bound inhibitor in hand, the opportunity for investigation of inhibitor-protein interactions exists without the need for isotopic labelling of the protein.

The use of simultaneous frequency and amplitude modulation (SFAM) [244] has been shown to have a number of advantages over other methods in the investigation of ^{13}C-^{15}N heteronuclear distances [245], such as a reduced susceptibility to frequency offsets and RF

inhomogeneity. Complex RF pulse variation of this nature is unlikely to be feasible in ^{13}C-^{19}F NMR where inherent technical challenges are present because of the use of two high frequency channels.

To date, the most widely applied heteronuclear recoupling method is rotational-echo double-resonance (REDOR).

5.2.2 Rotational-Echo Double Resonance

5.2.2.1 The REDOR scheme

REDOR [246, 247] has been used extensively in solid state NMR for the recoupling of heteronuclear dipolar interactions under MAS and the subsequent determination of internuclear distances in spin systems which include: ^{13}C-^{15}N [248], ^{13}C-^{2}H [249], ^{15}N-^{31}P [250], ^{15}N-^{19}F [251],^{31}P-^{19}F [252] and also ^{13}C-^{19}F. ^{13}C-^{19}F REDOR has been used successfully in a range of studies, such as the investigation of: the conformation of inhibitors bound to H^+/K^+-ATPase in hydrated membranes [253]; host-guest distances in crystalline inclusion compounds [254]; inter-tryptophan distances in lyophilised rat cellular retinol binding protein [255]; the interfacial characteristics of polymer blends [256]; and the binding modes of antibiotics to lyophilised bacterial cell walls and whole cells [252].

As discussed earlier, the dipolar Hamiltonian for a heteronuclear interaction may be described by:

$$H_D^{het} = b_{IS}\left(1 - 3\cos^2\theta_{IS}\right) I_{I_Z} I_{S_Z} \qquad \text{Equation 1.13}$$

This interaction can be split into three key contributions: the space, I spin and S spin parts. Figure 5.2 illustrates how these three components behave after under normal MAS conditions; the dipolar interaction is averaged over each complete rotor cycle.

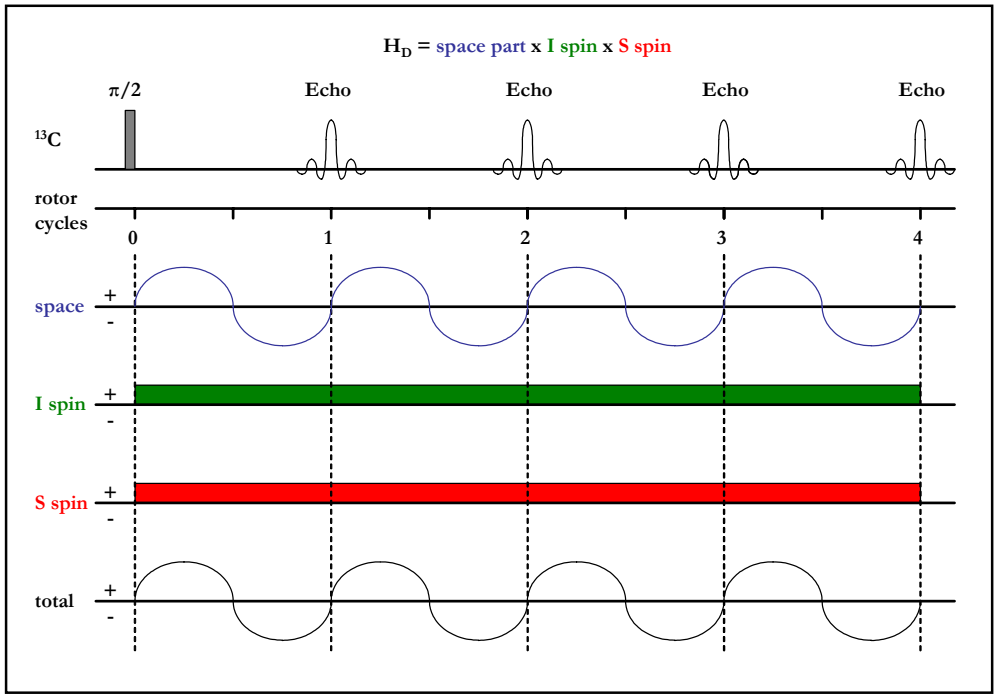

Figure 5.2 – The behaviour of the heteronuclear dipolar interaction under magic angle spinning.

REDOR is an extension of the static SEDOR scheme [257], adapted for MAS, and is conceptually simple. A typical REDOR sequence is shown in Figure 5.3 below. Initial proton magnetisation is first used to enhance the magnetisation of the observed spins through cross-polarisation, before the application of a train of rotor synchronised π pulses to the non-observed (dephasing) nuclei interrupts the spatial averaging of the heteronuclear dipolar coupling. A single π pulse on the observed nuclei is positioned in the centre of the evolution period to refocus the isotropic chemical shifts. Acquisition coincides with the completion of a rotor cycle. Strong proton decoupling is necessary during evolution and acquisition [258, 259].

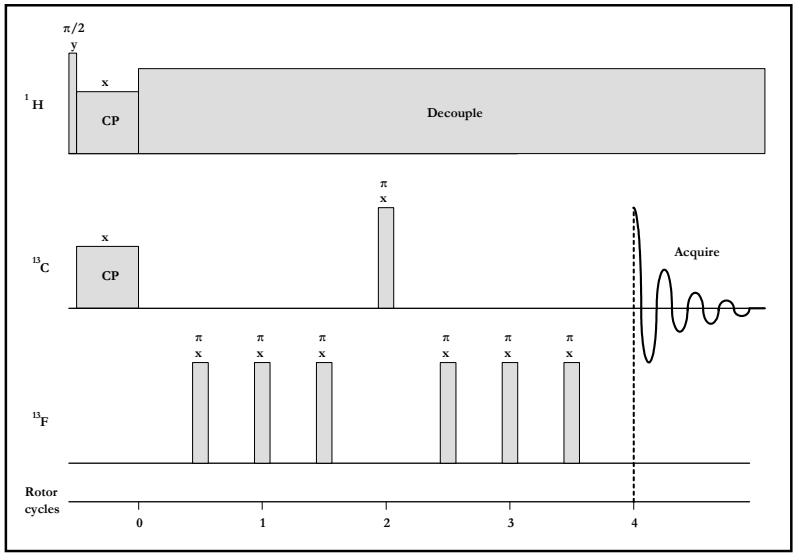

Figure 5.3 – A typical REDOR NMR pulse sequence: in this case demonstrating the scheme for the observation of ^{13}C with ^{19}F dephasing [246].

Figure 5.4 illustrates how the train of π pulses in the REDOR scheme leads to recoupling of the heteronuclear dipolar interaction.

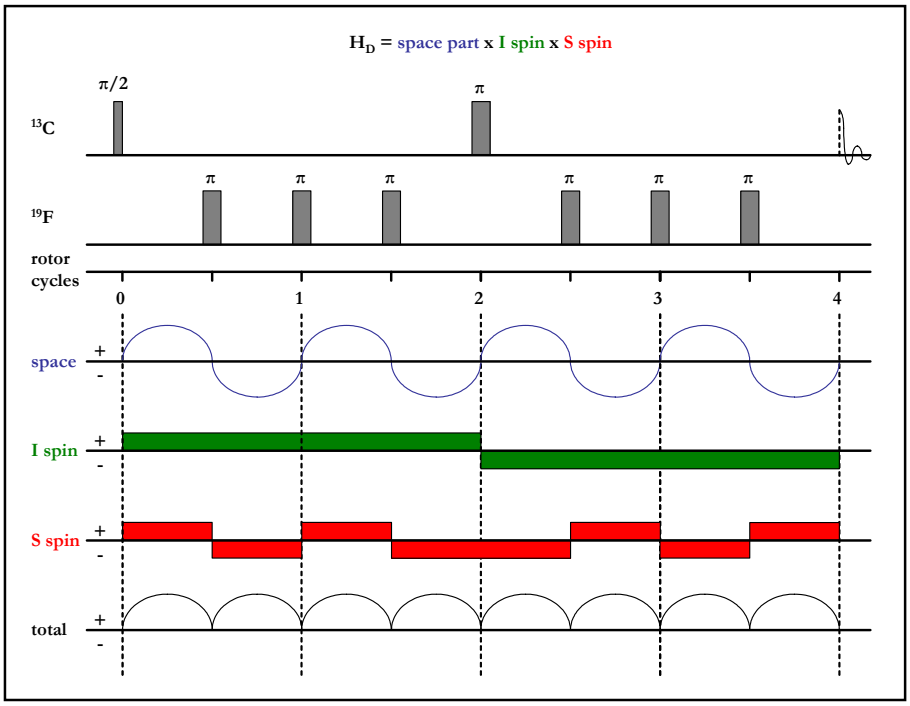

Figure 5.4 – Rotor synchronised radio-frequency pulses prevent MAS averaging of the heteronuclear dipolar interaction.

The sign change of the Hamiltonian in the later half of each rotor cycle, as a result of the oscillating space component, is cancelled through the application of a π pulse in the centre of each rotor period. π pulses positioned on rotor cycles ensure that the dipolar interaction is accumulated from one cycle to the next. The impact of the restored heteronuclear coupling during evolution is a reduction in observed echo intensity. To quantify the extent of this dephasing, experiments are performed with and without dephasing pulses. Section 5.2.2.2 discusses how the proportion of dephased signal may be correlated to a dipolar coupling strength and thereby an internuclear separation.

5.2.2.2 Data analysis and modelling of distances

Restating the heteronuclear dipolar Hamiltonian:

$$H_D^{het} = d(t) I_{I_Z} I_{S_Z} \qquad \text{Equation 5.1}$$

The time dependent space term, *d(t)*, can be defined in units of radians per second for a single pair of isolated spins [247]:

$$d(t) = d\left\{\sin^2\beta\cos 2(\alpha+\omega_r t) - \sqrt{2}\sin 2\beta\cos(\alpha+\omega_r t)\right\} \qquad \text{Equation 5.2}$$

where d is the dipolar coupling in rad/sec ($2\pi b_{IS}$), α is the azimuthal angle and β the polar angle of the internuclear vector, in a coordinate system where the z axis is aligned along the spinning axis (see Figure 5.5). The net dephasing angle, **Φ**, during a single rotor period is given by:

$$\phi = \int_0^{T_r/2} \omega_d(t)dt - \int_{T_r/2}^{T_r} \omega_d(t)dt \qquad \text{Equation 5.3}$$

where: $\omega_d = \pm\, d(t)/2$

T_r = rotor period

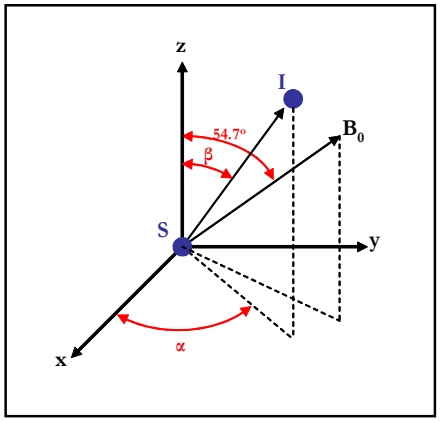

Figure 5.5 – The azimuthal (α) and polar (β) angles for a heteronuclear spin pair: B_0 is the applied magnetic field, I and S represent the pair of nuclei under investigation.

The negative sign for the second term in Equation 5.3 arises as a result of the π pulse applied in the centre of the rotor cycle (in the absence of this pulse the two terms cancel). Evaluation of over multiple rotor cycles (N_c) results in a general expression for the total phase accumulation:

$$\phi = \frac{N_c T_r d}{\pi} \sqrt{2} \sin 2\beta \sin \alpha \qquad \text{Equation 5.4}$$

The integral signal intensity in the absence of dephasing pulses (S_0) is dependent upon the transverse relaxation rate of the observed spin during evolution. However, the intensity in the presence of dephasing pulses (S) is a function of both relaxation and the extent of dipolar dephasing. The use of a term which defines the proportion of dephasing ($\Delta S/S_0$) enables the separation of the dipolar dephasing from relaxation effects.

$$\frac{\Delta S}{S_0} = \frac{S_0 - S}{S_0} \qquad \text{Equation 5.5}$$

For a single spin pair:

$$\frac{\Delta S}{S_0} = 1 - \cos \phi \qquad \text{Equation 5.6}$$

For a powder sample, with random orientations of the internuclear vector, all values of α and β must be considered.

Hence:

$$\frac{\Delta S}{S_0} = \frac{1}{2\pi} \int_{\alpha=0}^{\pi} \int_{\beta=0}^{\pi} \cos\phi \sin\beta \, d\alpha \, d\beta \qquad \text{Equation 5.7}$$

where (sin β) is a geometric weighting factor. A universal REDOR curve can be created using Equation 5.7, which relates the proportion of dephasing to a dimensionless term λ (Figure 5.6).

$$\lambda = N_c T_r b_{IS} \qquad \text{Equation 5.8}$$

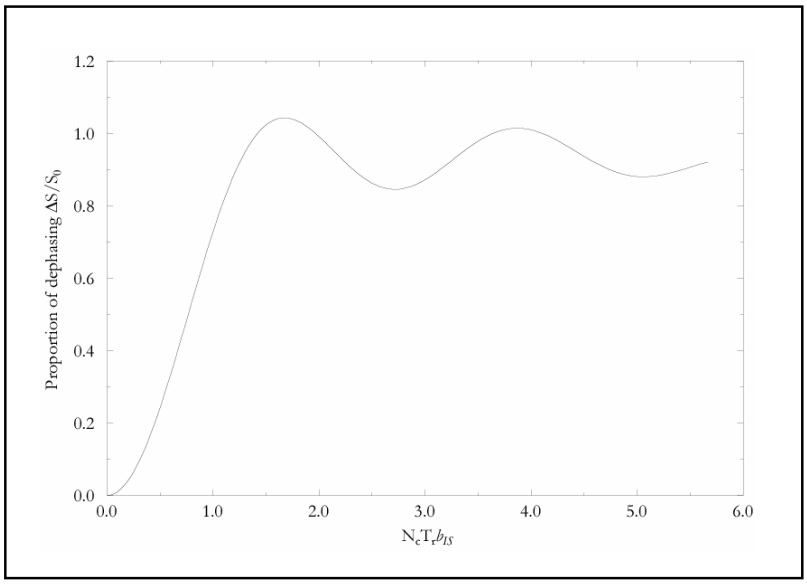

Figure 5.6 – The universal REDOR dephasing curve: the proportion of observed dephasing is correlated with the dimensionless parameter λ ($N_cT_r b_{IS}$).

Ideally, the evolution period is varied and multiple time points are used to determine an average value for the dipolar coupling strength. The dipolar coupling can then be correlated to an internuclear distance.

As stated previously:

$$b_{IS} = \left(\frac{\mu_0}{4\pi}\right)\frac{\gamma_I \gamma_S \eta}{r^3_{IS}} \qquad \text{Equation 1.12}$$

Which, for a $^{13}C/^{19}F$ spin pair, can be simplified to:

$$r_{IS} = \sqrt[3]{\frac{2.8412 \times 10^3}{b_{IS}}} \qquad \text{Equation 5.9}$$

where: b_{IS} is specified in Hz and r_{IS} in Å

Heteronuclear couplings between ^{13}C-^{19}F are stronger than homonuclear ^{13}C-^{13}C couplings, enabling accurate internuclear separations to be determined over a greater distance range (10-12 Å) [193, 255].

5.2.2.3 Improved REDOR sequences

The dependency of the original REDOR scheme on effective π pulses was quickly recognised, phase cycling of pulses (XY-8 and XY-16 schemes are among those commonly utilised [245, 260]) or the use of adiabatic pulses [261] can reduce the build-up of errors during the evolution period. The transfer of dephasing pulses to the observed spins rather than on the non-observed channel has been shown to reduce the susceptibility of the REDOR scheme to frequency off-sets [260], reduce homonuclear coupling effects between dephasing spins [262] and provide signal improvements where probe limitations restrict the power or quality of pulses on spectrometer channels [259]. A number of schemes are available which enable the investigation of systems containing multiple dephasing centres [263, 264] (the effects of which would otherwise be difficult to deconvolute), while a frequency selective scheme has enabled the determination of a single internuclear distance in uniformly labelled peptides [265].

Background filtered experiments can negate the requirement for a control sample in certain circumstances [266].

Experiments which are technically similar to REDOR also exist, such as transferred-echo double resonance (TEDOR) [267] and rotational-echo adiabatic passage double-resonance (REAPDOR) [268]. TEDOR additionally involves signal transfer between heteronuclear spins, while it is appropriate for the isolation of resonances in certain systems, it suffers from reduced sensitivity compared to REDOR. The REAPDOR scheme is optimised for measurements involving spin-1 nuclei.

5.3 Methodology

5.3.1 Sample Preparation

5.3.1.1 REDOR standard

A conformationally rigid REDOR standard was prepared in order to investigate the accuracy of REDOR distance measurements. Crude $^{13}C_4$-4-amino-5-fluoro-3-hydroxymethyl-2-methylquinoline (the 'labelled' component) and 4-amino-3-hydroxymethyl-2-methylquinoline (the 'unlabelled' component) were each purified by recrystallisation from hot ethanol (see Chapter 2 for information on their synthesis, Figure 5.7 illustrates their structures).

An aqueous solution was prepared with 5 mg of the purified labelled component and 136 mg of the unlabelled material (a 1:30 molar ratio). This solution was rapidly frozen in liquid nitrogen before freeze-drying to produce a homogeneous powder. Co-precipitation from hot ethanol was previously attempted, although NMR results suggested a poor level of incorporation was achieved for the labelled component.

25 mg of the powdered mixture was positioned in the centre of a 6 mm Chemagnetics MAS rotor, using custom made boron nitride inserts (boron nitride inserts were found to be superior to the commonly used Teflon or Delrin inserts, which lead to fluorine and carbon background signals respectively).

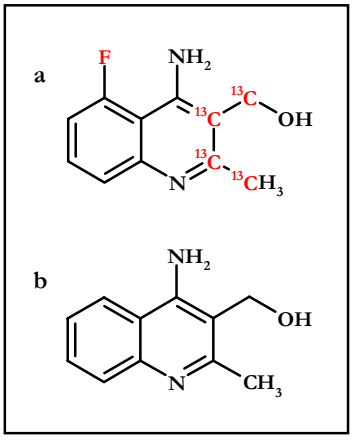

Figure 5.7 – REDOR standard compounds: $^{13}C_4$-4-amino-5-fluoro-3-hydroxymethyl-2-methylquinoline (a) and 4-amino-3-hydroxymethyl-2-methylquinoline (b).

5.3.1.2 Acetylcholinesterase

Samples of acetylcholinesterase with and without bound ^{13}C labelled R414983 used for the earlier rotational resonance studies were also utilised during REDOR experiments (their preparation is discussed in Section 4.3.1.2). Each sample was placed in the centre of a 6 mm Chemagnetics MAS rotor with the volume restricted appropriately using boron nitride inserts.

5.3.2 NMR Experiments

All experiments were performed on a Chemagnetics 500 MHz (^1H frequency, 125 MHz for ^{12}C) spectrometer using a 6 mm triple channel (HFX) Chemagnetics MAS probe. The temperature was maintained at -30 ^oC throughout all of the experiments.

The ability of three different REDOR pulse sequences (shown in Figure 5.8) to effectively restore heteronuclear couplings under MAS was first tested using the standard sample.

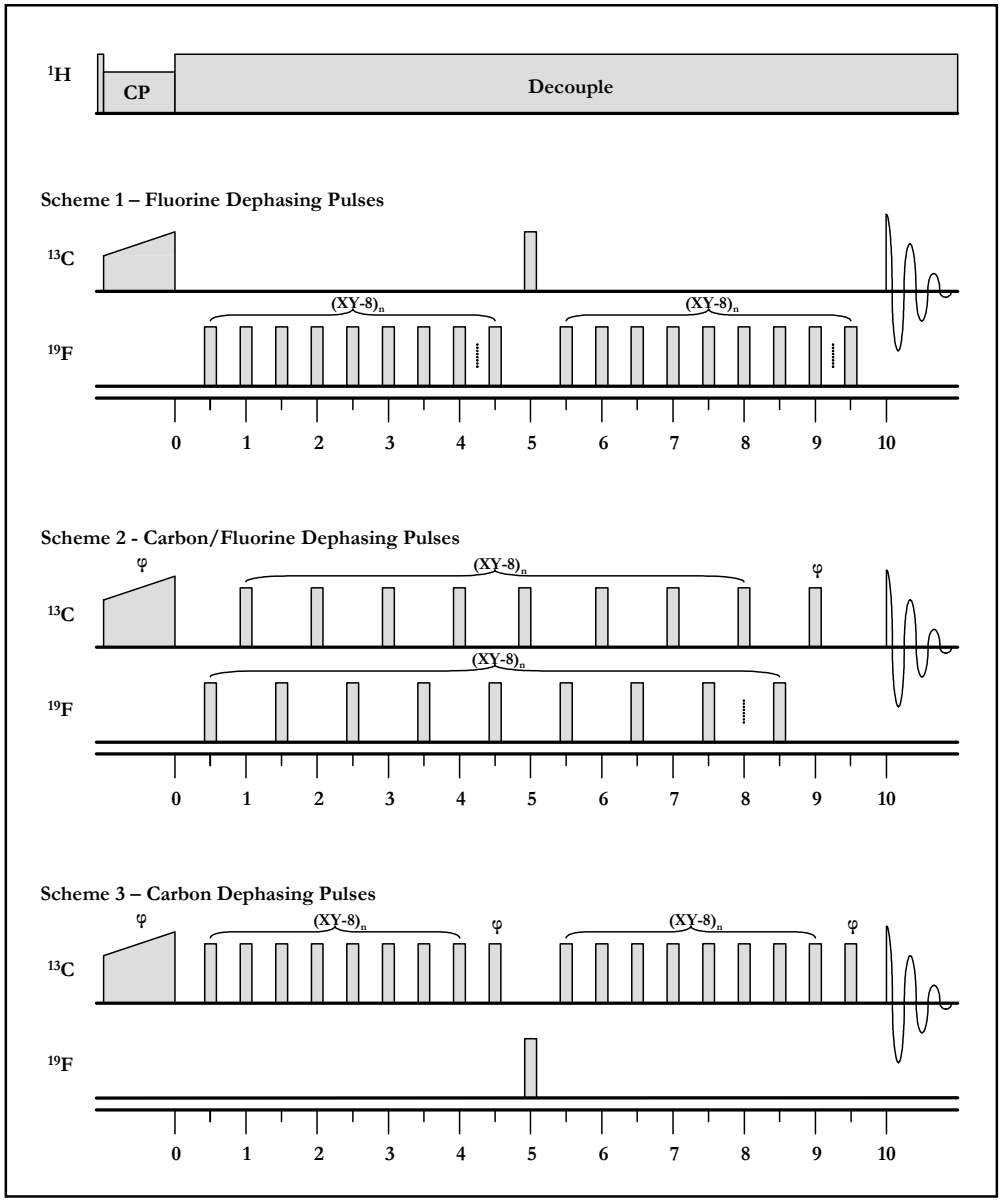

Figure 5.8 – REDOR sequences used during experiments.

A 63 kHz field was used to generate initial proton magnetisation and during CP, while an 83 kHz field was applied for decoupling during the evolution period and a 63 kHz field during acquisition. A carbon field strength of 63 kHz was applied during cross-polarisation, modulated by a 20% linear ramp, with a field strength of 42 kHz for π pulses on either the carbon or fluorine channel as required by the sequence (pulse widths were optimised on a sample containing 100% labelled material, such that maximum dephasing was observed). A

spinning speed of 9000 Hz was maintained throughout, selected to avoid rotational resonance match conditions for the multiple carbon labels present. 1536 transients were collected (for both non-dephased and dephased spectra, acquired alternately) at evolution times of approximately 4, 8 and 12 ms, with each of the three sequences.

The scheme found to provide the most accurate distance measurements (Scheme 3 – using carbon channel dephasing pulses) was applied to the acetylcholinesterase samples. Acquisition was restricted to a single evolution time, 26 rotor cycles/2.89 ms. 30,000 transients were acquired for the bound inhibitor and protein background samples (with non-dephased and dephased spectra acquired on alternate acquisitions), samples were exchanged after every 10,000 acquisitions to reduce the impact of instrument instability. Other acquisition parameters remained unchanged. Integral intensities were determined by peak fitting using the FELIX software package and corresponding dipolar couplings calculated using REDOR curves generated with the SIMPSON package [269].

5.4 Results

5.4.1 REDOR Standard

Figure 5.9 shows the NMR spectrum of the labelled standard (undiluted). Each of the four peaks arising from the site specific labelling of the molecule is easily discerned.

On dilution of the labelled material the spectrum becomes significantly more complex as a result of natural abundance contributions. Dipolar couplings within the REDOR standard were only determined for the methyl carbon/fluorine interaction. The methyl resonance occurs in an isolated region of the spectrum, requiring a simple correction for background contributions.

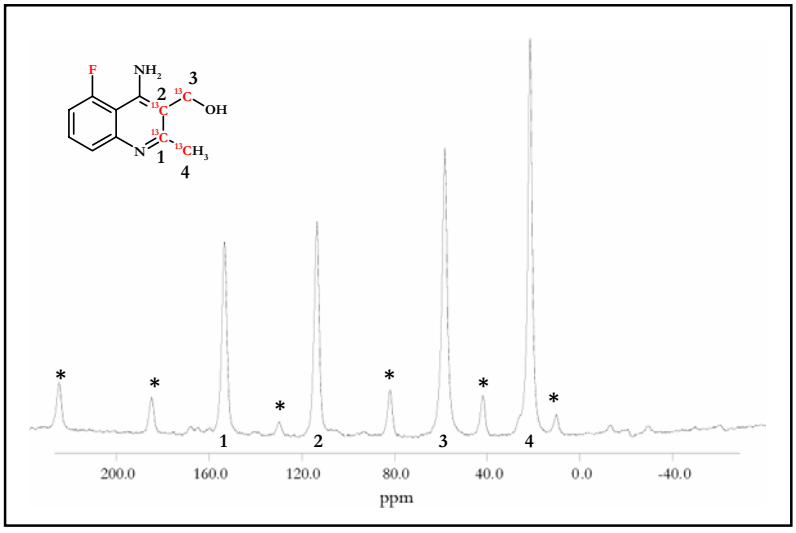

Figure 5.9 – ^{13}C spectra of the labelled REDOR standard: using a ramped cross-polarisation experiment, ω_r = 9000 Hz (* indicates a spinning sideband).

The expected internuclear distance for the methyl carbon/fluorine is illustrated in Figure 5.10, based on the crystal structure of enzyme bound R404435 [43]. The separation of 6.46 Å is at an intermediate range for ^{13}C-^{19}F heteronuclear measurements, which can be measured up to 12 Å [193, 255] for 'ideal' model compounds.

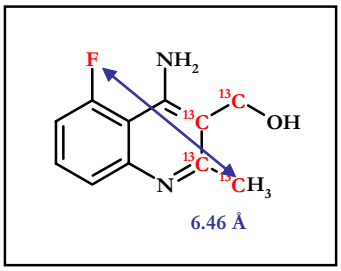

Figure 5.10 – The methyl carbon/fluorine internuclear distance measured using REDOR experiments.

Figure 5.11 shows a representative example of the REDOR results. This example is taken from the spectra generated using Scheme 2, with dephasing pulses on alternate channels. The effect of heteronuclear recoupling is visible on the overlay of non-dephased and dephased spectra (i),

but is most clear in (ii) where the methyl region has been expanded and a spectral subtraction included.

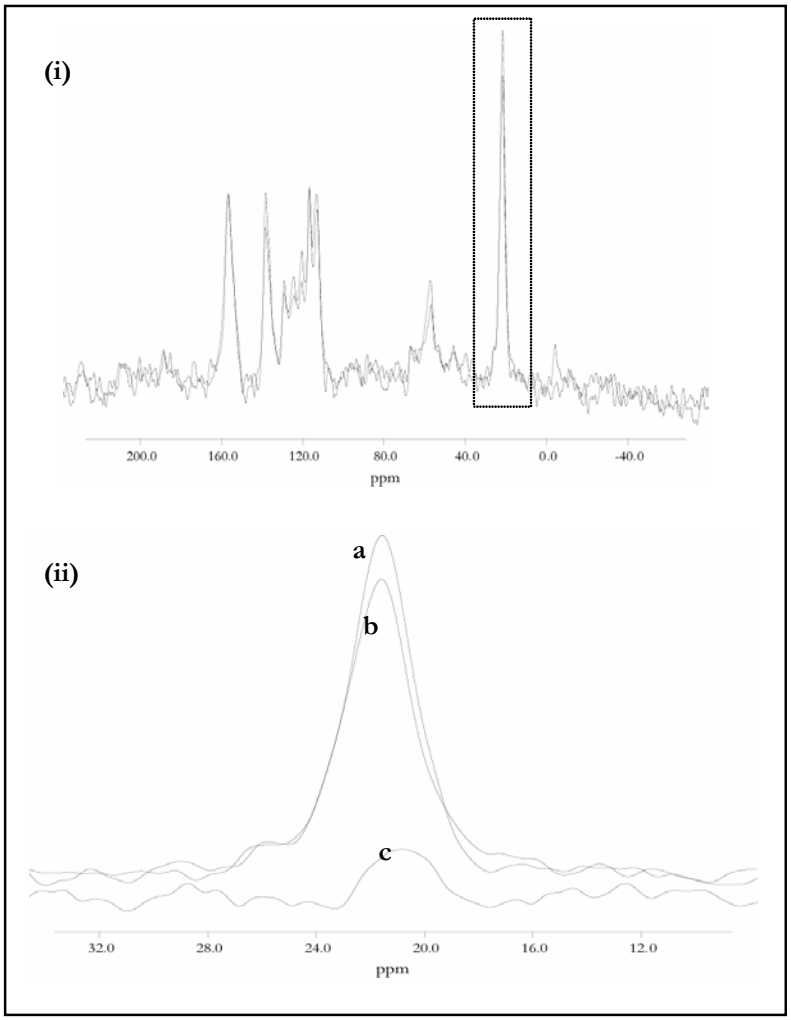

Figure 5.11 – REDOR spectra of the rigid distance standard (^{13}C observe, applying ^{13}C and ^{19}F dephasing pulses): acquired using Scheme 2, ω_r = 9000 Hz, with an evolution period of 32 rotor cycles (3.56 ms) - overlay of non-dephased and dephased spectra (i) expansion of the methyl region showing the non-dephased, dephased and difference spectra labelled a, b and c respectively (ii).

Table 5.1 summaries the REDOR results discussed below, which are also subsequently illustrated in Figure 5.12. The statistical error arising from noise levels is evaluated in Appendix 5.

Scheme 1- Fluorine channel dephasing pulses

Dipolar couplings were not calculated for the data generated using Scheme 1. The proportion of dephasing measured at all three evolution times is marginal and in fact decreases slightly with longer evolution periods. Signal to noise is reduced at longer evolution times, since magnetisation remains in the transverse plane, it is obvious that this standard REDOR sequence does not recouple the heteronuclear interaction to an appreciable degree.

Scheme 2- Alternate carbon/fluorine channel dephasing pulses

In contrast to Scheme 1, the use of carbon π pulses as a replacement for the fluorine pulses located on full rotor cycles produces an accurate value for the heteronuclear dipolar coupling at the shortest evolution time (32 rotor cycles, 3.56 ms). The corresponding internuclear distance, 6.43 Å, is within 0.03 Å of the expected value of 6.46 Å. However, as the evolution time is increased to 7.11 ms (64 cycles) and 10.67 ms (96 cycles), the efficiency of the scheme is reduced and dipolar couplings are progressively underestimated (providing distances of 7.10 and 7.84 Å respectively).

Scheme 3- Carbon channel dephasing pulses

The third REDOR scheme, in which only a single pulse remains on the fluorine channel, proved to be the most successful sequence. The shortest evolution time (34 cycles, 3.78 ms) produced dephasing which corresponded to a 6.51 Å ^{13}C-^{19}F distance (a 0.06 Å overestimate). The second time point also showed a reasonable degree of accuracy, providing a distance estimate of 6.61 Å (0.16 Å overestimate).

Analysis of the final evolution time for Scheme 3 was not practicable. At this time point the signal level in both dephased and non-dephased spectra is extremely low.

Table 5.1 – Summary of REDOR distance measurements for the standard sample.

REDOR scheme	Evolution time (ms)	$\Delta S/S_0$	Dipolar coupling (Hz)	Distance (Å)	Error (Å)
1 – ^{19}F pulses	4.00	0.076	-	-	-
1 – ^{19}F pulses	8.00	0.064	-	-	-
1 – ^{19}F pulses	12.00	0.031	-	-	-
2 – ^{13}C/^{19}F pulses	3.56	0.148	106.7	6.43	- 0.03
2 – ^{13}C/^{19}F pulses	7.11	0.303	79.5	7.10	+ 0.64
2 – ^{13}C/^{19}F pulses	10.67	0.359	58.9	7.84	+ 1.38
3 – ^{13}C pulses	3.78	0.157	103.2	6.51	+ 0.06
3 – ^{13}C pulses	7.33	0.450	98.2	6.61	+ 0.16
3 – ^{13}C pulses	10.89	-	-	-	-

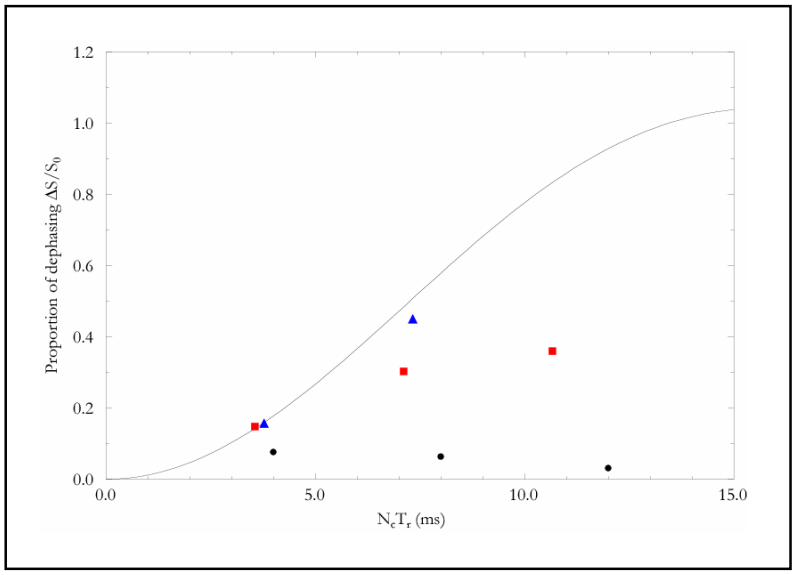

Figure 5.12 – Comparison of methyl dephasing using three different REDOR schemes: data for the ^{13}C observed ^{19}F dephasing pulse sequence is shown using black filled circles, for the ^{13}C/^{19}F dephasing pulse sequence by red squares and for the ^{13}C dephasing pulse sequence by blue triangles. A solid black line indicates the expected dephasing based on a dipolar coupling of 105.4 Hz (corresponding to the expected 6.46 Å internuclear distance). ω_r = 9000 Hz.

The extremely poor performance of the standard REDOR scheme may be explained by the technical challenges associated with fluorine NMR - it is difficult to effectively isolate each of the high frequency channels and phase transients become a significant issue. As a result, the quality and power of RF pulses on the fluorine channel is relatively low. Inversion of carbon spins therefore produces smaller errors, leading to more effective recoupling and higher levels

of observed dephasing. Problems are exacerbated by the need for an unusually high spinning frequency of 9 kHz, to avoid rotational resonance matches and remove residual dipolar couplings. While it has been shown that a finite pulse length does not have a detrimental effect on REDOR dephasing [270], the higher spinning frequency requires a greater rate of π pulses and pulse errors rapidly accumulate.

With respect to restoration of the heteronuclear coupling, the transfer of π pulses to the observed channel is theoretically equivalent to pulsing on the non-observed channel. However, three additional effects also arise:

- homonuclear dipolar couplings are partially restored. Resulting in increased relaxation of the carbon spins during the evolution period and a reduced signal to noise
- pulse imperfections not only provide a reduced level of recoupling (and therefore dephasing) but are also detrimental to the observed signal intensities in both the dephased and non-dephased spectra because of poor signal refocusing
- the final effect is positive in that a train of pulses on the observed channel more closely mimics a CPMG type echo [271] rather than the Hahn echo [235] of Scheme 1, producing a more effective refocusing of the signal

5.4.2 $^{13}C_5$-R414983 Bound to Acetylcholinesterase

The background subtracted REDOR spectra of labelled R414983 bound to acetylcholinesterase are shown in Figure 5.13. Even at an evolution time corresponding to 26 rotor cycles (2.89 ms at 9000 Hz) the fast T_2 relaxation rates, which result from the presence of the multiple ^{13}C labels in the inhibitor, are clearly apparent in the level of signal observed (see Section 4.4.1).

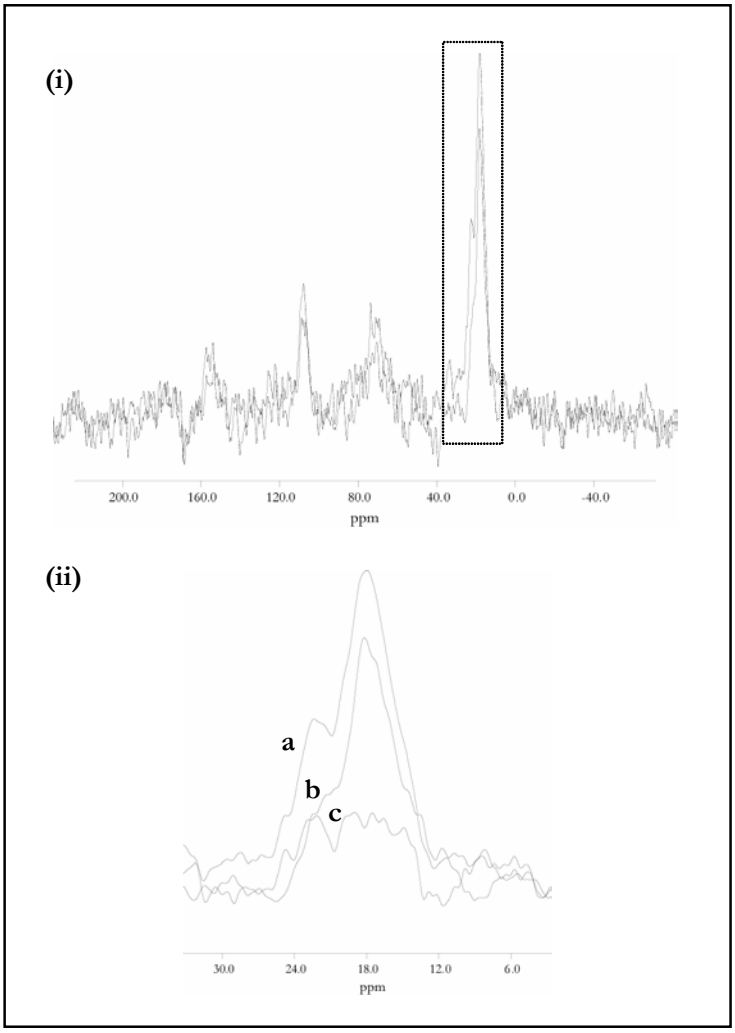

Figure 5.13 – REDOR spectra of labelled R414983 bound to acetylcholinesterase (^{13}C observe, applying ^{13}C dephasing pulses): acquired using Scheme 3, ω_r = 9000 Hz, with an evolution period of 26 rotor cycles (2.89 ms) - overlay of background subtracted non-dephased and dephased spectra (i), expansion of the methyl region showing the non-dephased, dephased and subtracted spectra labelled a, b and c respectively (ii).

Some degree of dephasing is observed across each of the resonances present, though because of the low signal to noise of the aromatic and methylene peaks only dephasing of the methyl spin has been quantified.

The integrated intensity of the dephased spectrum is reduced by 41.5% when compared with the non-dephased spectrum. This corresponds to a total dipolar coupling of 236.8 Hz between the methyl carbon and the trifluoromethyl function, which may be interpreted as a coupling of

78.9 Hz between the methyl and a single fluorine spin positioned centrally between the three fluorine atoms, providing a average distance measurement of 7.10 Å.

The earlier distance measurements performed on the REDOR standard using Scheme 3 provided an accuracy of at least ± 0.16 Å. However, the signal to noise level of the spectra for the protein bound inhibitor are reduced in comparison to the standard measurements and the result is based upon a single evolution time. Appendix 5 determines the statistical error arising from spectral noise, which is found to be ± 2%. Additional errors arising from peak fitting and incomplete recoupling are likely to dominate the statistical variation. For the creation of a model of the bound inhibitor utilising NMR derived distance restraints, an accuracy of ± 0.5 Å is acceptable and the result may be assumed to fall within this range.

5.5 Discussion

The use of a rigid molecule to investigate the accuracy of REDOR distance measurements demonstrates the importance of testing methodology on standards prior to the application to real systems. Although REDOR schemes typically involve dephasing pulses applied to the non-observed spectrometer channel, it has been shown that this approach (Scheme 1) is not effective in the present case, probably as a result of pulse imperfections on the non-observed fluorine channel. Modified REDOR schemes which transfer either alternate dephasing pulses (Scheme 2) or all dephasing pulses (Scheme 3) from fluorine to the carbon spins were more successful. While the alternated pulse scheme proved reliable only at shorter evolution periods, Scheme 3 provided accurate values for the dipolar coupling over the limited range tested. A reduced signal to noise level is one consequence of applying carbon dephasing pulses, although the need for a greater number of acquisitions is outweighed by the reliability of recoupling.

Following conformation of the quality of distance measurements, Scheme 3 was used to measure the heteronuclear coupling strength between the trifluoromethyl function and quinoline methyl in labelled R414983 bound to *Electrophorus electricus* acetylcholinesterase. The measured coupling corresponds to a distance separation of 7.10 Å, illustrated in Figure 5.14.

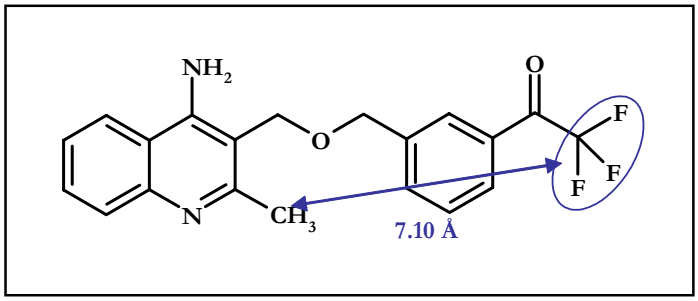

Figure 5.14 – Distance determined for acetylcholinesterase bound R414983 using REDOR.

The measurement on the bound ligand is based on a single evolution time, while the distance is likely to be within 0.5 Å of the true value, it would be advantageous to perform the experiment for both a greater number of acquisitions and at additional time points to quantify any error arising from imperfect recoupling (this has not been completed because of the long acquisition time required for such work).

The need for an accurate S_0 value means that both protein and protein/inhibitor samples must be examined to provide subtracted spectra of the inhibitor alone, doubling the time required for acquisition. Fluorine is extremely rare in natural systems; as such, the use of carbon dephased/fluorine observed REDOR has the potential to halve instrumental time. However, the performance of the current generation of NMR probes for the observation of fluorine means that this may be an unrealistic aim.

An advantage of REDOR over the earlier homonuclear rotational resonance measurements is that multiple internuclear distances can be determined through a single experiment, since

dephasing will occur independently on each of the observed spins. However, only dephasing of the methyl carbon was analysed because of the lower signal to noise ratio of the aromatic and methylene carbons. The single distance measurement weakens the contribution of the REDOR experiments in the creation of a model of the bound inhibitor, although the methyl carbon/trifluoromethyl distance can potentially reach 12 Å in a fully extended conformation, therefore this single restraint in itself is highly characteristic of the overall molecular arrangement.

Chapter 6 Modelling of R414983 Bound to Acetylcholinesterase

6.1 Overview

Computational studies have made a significant contribution to acetylcholinesterase research since the first crystal structure was published in 1991. The rapidly increasing processing capabilities of modern computers means that the complexity of the systems studied has been increased and the number of approximations made in calculations reduced, both of which have improved the level of information and accuracy which molecular modelling provides, in this system and generally.

This section discusses the contribution of molecular modelling to an understanding of acetylcholinesterase function and the binding modes of the two inhibitors (TMTFA and tacrine) which form basis of the Syngenta chimeras studied here. Energy minimisation is used to generate a conformation for R414983 alone and for the inhibitor bound to acetylcholinesterase (*in vacuo*), while molecular dynamics simulations enable investigation of the motional freedom for the inhibitor in both of these states. NMR derived distances for the bound ligand are compared to the modelling results and the range of structures fitting the NMR restraints is discussed.

6.2 Introduction

6.2.1 Computational Studies on Acetylcholinesterase

The publication of the first crystal structure of acetylcholinesterase [31] provided a basis for computational investigation of acetylcholinesterase. The contribution of electrostatic steering to the rate of ligand binding was one of the first topics studied using molecular modelling: rate constants for the binding of charged ligands were predicted to within an order of magnitude of those determined experimentally [53], while the presence of a net negative charge (-11e) was found to be only a minor factor in the large dipole exhibited by the enzyme, with the relative distribution of positive and negative charges throughout the protein being the main cause [52].

Selective mutation of up to seven negatively charged residues in the region of the gorge entrance showed little effect on the rate constants for the hydrolysis of cationic and neutral substrates, leading to the incorrect suggestion that electrostatic field is not responsible for the routing of cationic substrates to the binding site and that the process was simply diffusion based [75]. These results were later explained through simulation of the mutant enzymes which indicated that, even in the case where all seven residues have been substituted with uncharged amino-acids, the dipole of acetylcholinesterase is reduced by less than 40% [49].

Molecular dynamics simulations are computationally demanding. Early molecular dynamics simulations on *Tc*AChE were hampered by the relatively short timescales which could be modelled, with a simulation time of only 119 ps (compared to approximately 100 μs for the hydrolysis of one molecule of ACh) [21, 22, 51]. However, a small opening to the active site in the region of Trp84 was observed (although close to the active site, the wall of the protein is particularly thin in this region) [51].

A simulation on a *Tc*AChE dimer complexed with tacrine (500 ps) focused on the accessibility of the active site, both through the gorge and alternative routes [50]. It is clear that the system

had not converged, since deviation of the backbone compared to x-ray positions continued to rise over the time studied (although remains relatively small at 0.05 nm). An opening in the area of Cys67-Cys94 was observed (the 'side door') but not in the region of Trp84 (the 'back door'). Motions within the backbone were found to correspond well with B-factors from crystallography, with residues in the gorge and active site showing less mobility than was typical for the whole structure. The active site was accessible to a 2.4 Å probe (corresponding to the size of an acetylcholine molecule) during only 2.4% of the simulation time (Figure 6.1) [56], although the electrostatic field around the enzyme is relatively stable throughout [59].

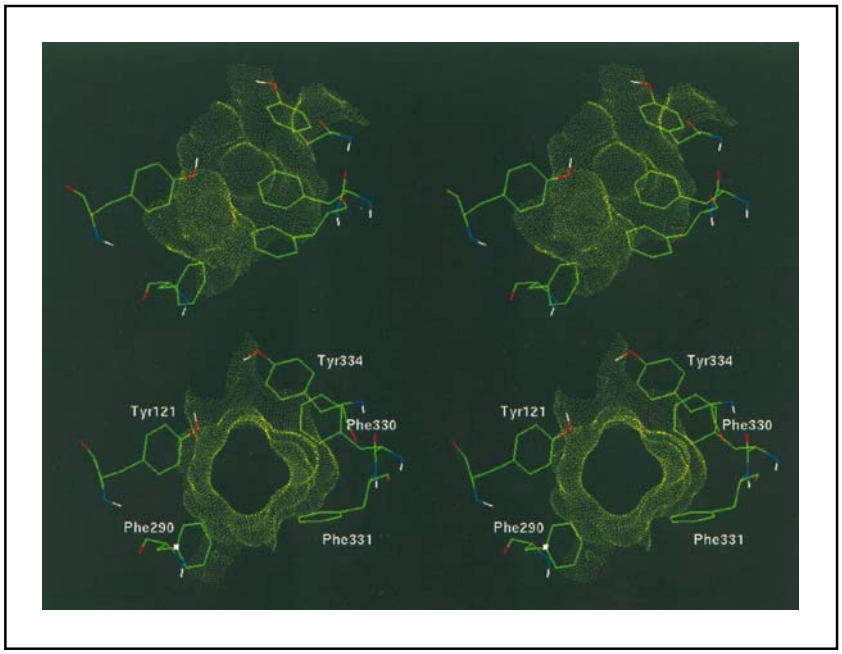

Figure 6.1 – Dynamics in the gate region: stereo images looking down the gorge to the catalytic site. Five residues are shown coloured by atom type in positions corresponding to the closed (above) and open states (below). The solvent accessible surface for a 1.4 Å probe is also shown. The state of the gate is determined by accessibility of a 2.6 Å probe. [56]

The latest generation of computer hardware and simulation techniques have further extended the timeframe of acetylcholinesterase simulations – a 10 ns simulation of mAChE [61] and a 5

ns simulation of the FAS II/mAChE complex [63] are now available. However, this timescale is still relatively short on a functional level.

In the simulation of mAChE alone, in addition to the main gorge entrance, 'back door' openings were observed in 78 of 10,000 frames analysed. The gorge was found to have an average radius of 1.52 Å with a complex distribution of probabilities [61] making it accessible to ACh during 20% of the simulation [66] (in contrast to the Gaussian probability distribution in the earlier 500 ps simulation of *Tc*AChE [50] which was accessible 2.4% of the time [56]). The population of water molecules in the gorge fluctuated from 16-22 molecules, with an average of 19.8 [62], closely matching the 18 water molecules present in the 1.8 Å *Tc*AChE crystal structure (PDB reference 1EA5), while 20 water molecules were located in isolated positions within the protein structure [67].

Simulation of the FAS II/mAChE complex showed a number of key changes in both overall structure and dynamic motions [63]. The imidazole ring of the catalytic histidine (His 447 for mAChE) is twisted in relation to the orientation found in simulations of the free enzyme [61]. In this twisted alignment the ring is positioned inappropriately for proton transfer during catalysis. Additionally, the sidechain of Glu334 is directed away from the two other residues of the catalytic triad (Figure 6.2). The distribution for the radius of the gorge opening in the FAS II complex, although following a similar profile, is shifted to a higher range of values (Figure 6.3). A more interesting difference in the two simulations involves the dynamics of secondary routes to the gorge. 'Back door' opening was observed in the simulation of mAChE in less than 1% of the sampled frames, while for the inhibitor complex further transient openings were also seen – the 'back door' was open in 18% of the frames, with a 'side door' open in 13%.

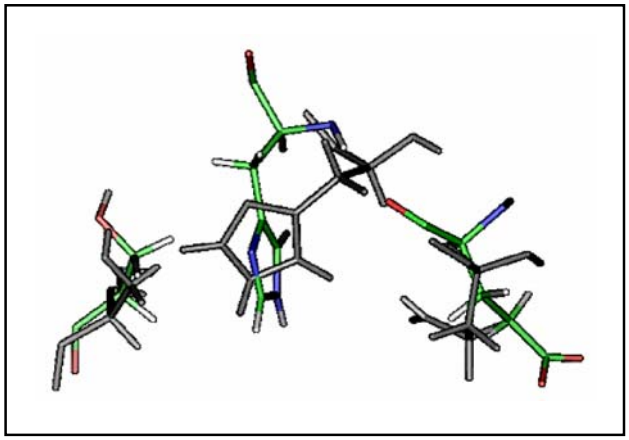

Figure 6.2 – Fasciculin induced movement of the catalytic triad: the average structures from simulations are shown. Results from the mAChE MD are shown in grey, those from the FAS II/mAChE MD are coloured by atom type. From left to right, residues are Ser203, His447 and Glu334 [63].

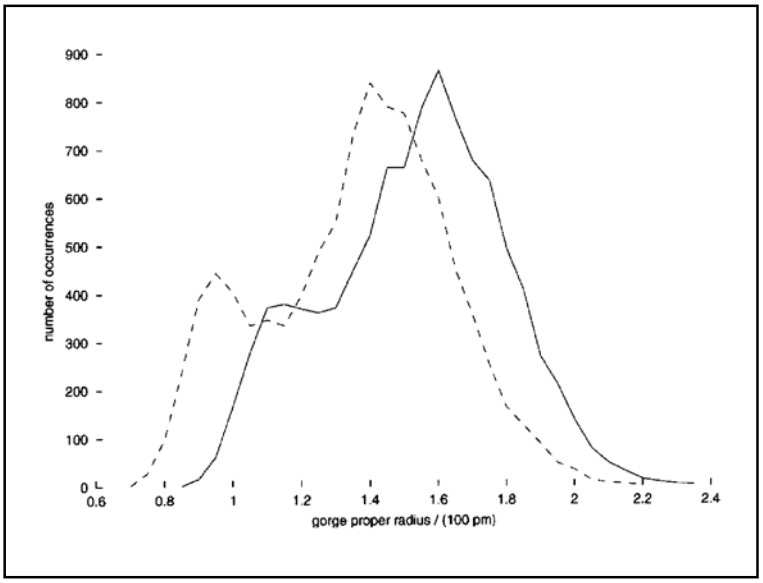

Figure 6.3 – Distribution of the gorge proper radius: data from the MD simulation of mAChE is shown by a dashed line, while that from the simulation of the FAS II/mAChE complex is shown by a solid line [63].

Modelling of inhibitor binding has proven to be a challenge for computational researchers. The Alzheimer's drug donepezil was developed after a comprehensive study involving the investigation of structure-activity relationships for a range of compounds and modelling of inhibitor binding [96]. Although donepezil was proven to be a potent inhibitor, the binding mode predicted during its development was found to be markedly different from the actual

bound conformation later derived using x-ray diffraction [36, 40]. Simulations of the binding of galanthamine, which is a rigid molecule, have only recently been able to produce a structure which matches x-ray crystallography data [41, 64].

6.2.2 The Binding of TMTFA and Tacrine to Acetylcholinesterase

Figure 6.4 shows the binding of TMTFA and tacrine to *Tc*AChE (the two inhibitors which form the basis of the series of Syngenta compounds). TMTFA binds covalently to the catalytic serine, forming a stable tetrahedral structure which is analogous to the first transition state formed during acetylcholine hydrolysis [27]. Tacrine binds non-covalently to the protein, close to the base of the gorge [30].

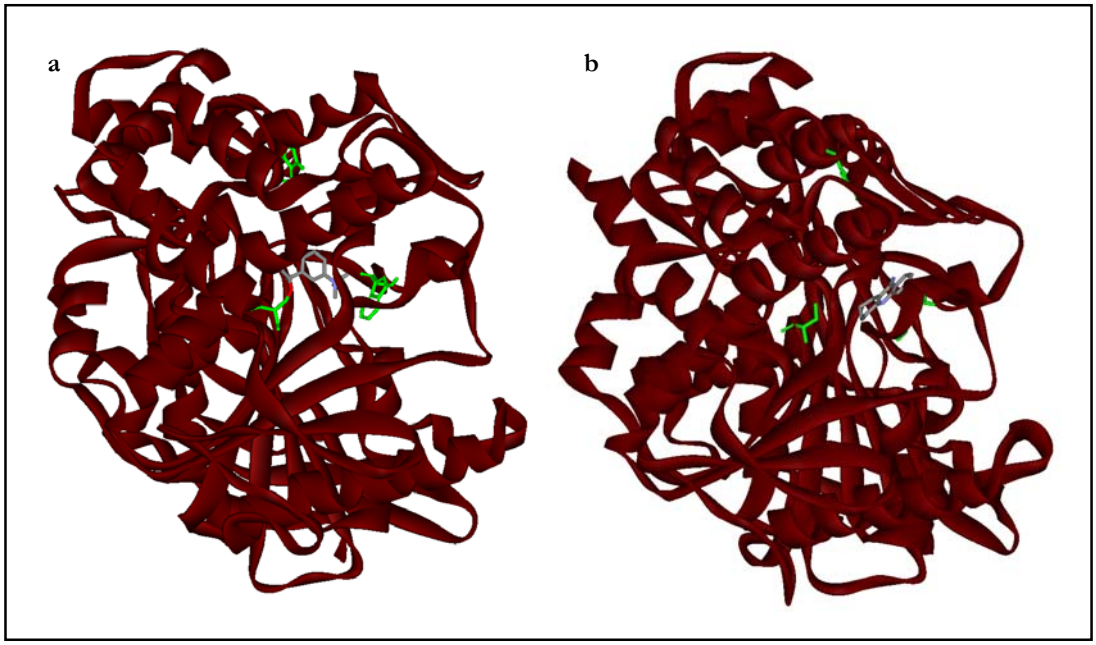

Figure 6.4 – The binding of TMTFA and tacrine to *Torpedo californica* acetylcholinesterase: based on the PDB structures 1AMN and 1ACJ. A dark red ribbon illustrates the protein backbone, with three key residues shown in green – Trp279 marks the gorge entrance at the top of the diagram, Ser200 marks the catalytic site in the centre and Trp84 marks the back door entrance on the right. Inhibitors are shown coloured by atom type, TMTFA (a) and tacrine (b).

In addition to covalent attachment to the protein, TMTFA is involved in a number of non-covalent interactions which stabilise the structure (Figure 6.5), these can be divided into three groups [30]. The quaternary ammonium, which is aligned towards the open face of Trp84 and also interacts with Phe330 (cation-π interactions), as expected for the quaternary ammonium function of the ACh substrate. Secondly, the oxy-anion is involved in hydrogen bonding to the backbone NH functions of Gly118, Gly119 and Ala201. Lastly, the trifluoromethyl group interacts with the aromatic rings of Trp233, Phe288, Phe290 and Phe331.

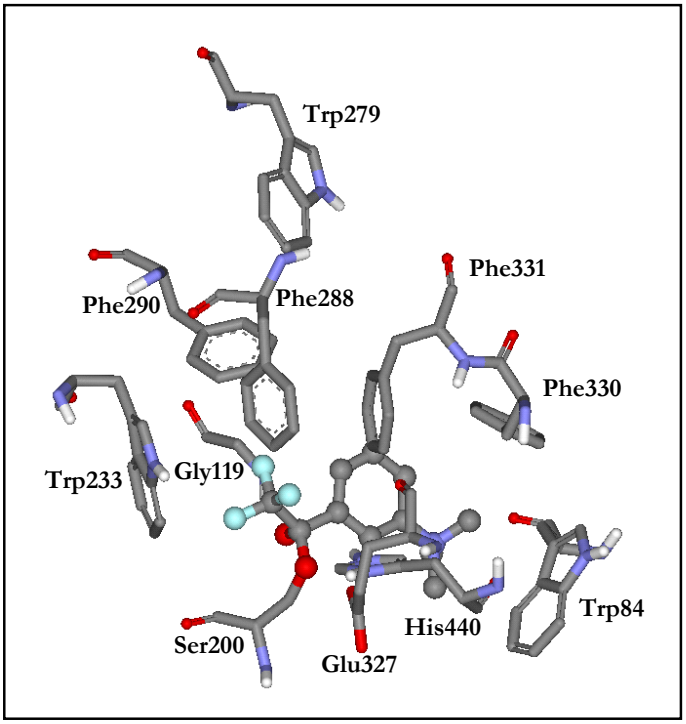

Figure 6.5 – TMTFA binding to *Torpedo californica* acetylcholinesterase: the inhibitor is shown as a ball and stick model. Key residues in the region of the binding site are shown with stick models. Created using the PDB file 1AMN.

The x-ray structure of tacrine bound to *Tc*AChE [30] shows that the acridine ring is stacked with the indole ring of Trp84 (Figure 6.6). This may explain why opening of the 'back door' was not observed in the 500 ps simulation of the *Tc*AChE/tacrine complex as discussed earlier, since Trp84 could be held in place through its interaction with the inhibitor [50]. Phe330 also

interacts with the acridine ring, while the tacrine ring nitrogen forms a hydrogen bond to the backbone oxygen of His440. The inhibitor occupies only part of the active site, with the region near the catalytic serine occupied by water molecules.

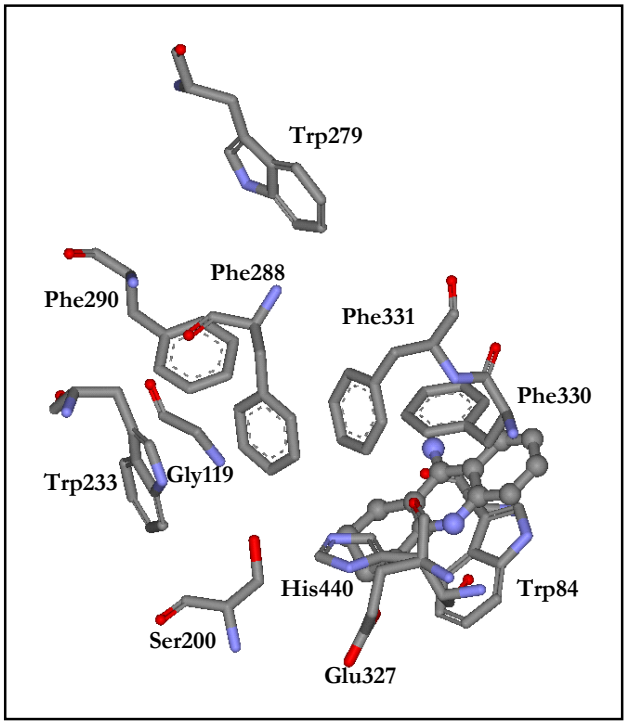

Figure 6.6 – Tacrine binding to *Torpedo californica* acetylcholinesterase: the inhibitor is shown as a ball and stick model. Key residues in the region of the binding site are shown with stick models. Created using the PDB file 1ACJ.

The rational for a chimera of TMTFA and tacrine as an inhibtor of AChE is clear. The binding site of each compound is positioned in a distinct region of the active site, and the combination of favourable binding interactions creates a more potent AChE inhibitor. Figure 6.7a shows an overlay of the crystal structures of TMTFA and tacrine bound to acetylcholinesterase; for clarity the relative position of the inhibitors alone is shown in Figure 6.7b. The main structural features of both inhibitors are included in the Syngenta compound R414983 (Figure 6.7c).

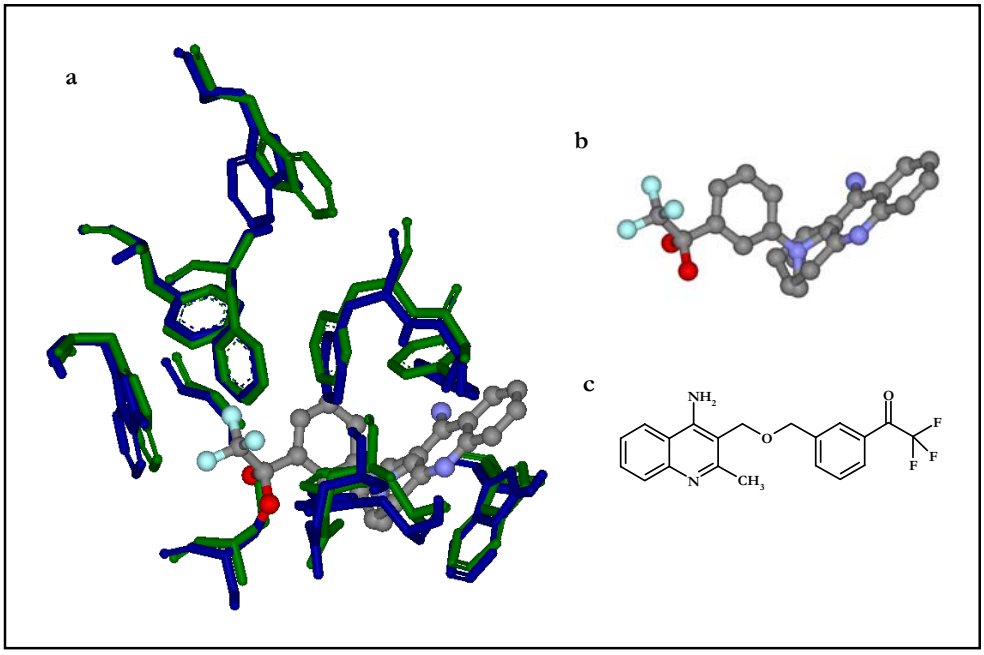

Figure 6.7 – Combination of TMTFA and tacrine: overlay of the crystal structures for the inhibitors bound to *Tc*AChE, residues from the TMTFA structure are shown in blue and from the and tacrine structure in green (a) an overlay of the inhibitors alone (b) R414983 (c).

6.3 Methodology

6.3.1 Molecular Dynamics Simulations

6.3.1.1 General

Energy minimisation and molecular dynamics were performed on a 1.4 GHz single processor machine with the Linux operating system and using GROMACS 3.1.3.

6.3.1.2 Modelling of R414983

A PDB file for the free inhibitor was created using DS ViewerPro 5.0 (Accelrys Inc.) and a topology for the molecule then generated using PRODRG [272]. A potential limitation of PRODRG is its bias towards typical biological molecules. The partial charges for R414983 assigned by the program were compared to those generated by DS Viewer, although small

differences were present, these were found to have no significant effect on the results from simulations.

The minimum energy conformation of the molecule was determined by the use of a steepest descent algorithm with the GROMACS forcefield. A maximum move per atom of 0.1 Å per step was allowed.

Using the energy minimised ligand structure, a 1 ns molecular dynamics simulation was performed *in vacuuo* (2 fs per step) using the GROMACS forcefield. Initial velocities were generated randomly using a Boltzman distribution at a temperature of 300K and a pressure of 1 bar (Berendsen methodology was used for the maintenance of temperature and pressure).

6.3.1.3 Modelling of R414983 bound to *Electrophorus electricus* acetylcholinesterase

R414983 was manually positioned at the active site of a single catalytic sub-unit of *Electrophorus electricus* AChE (PDB reference 1C2B), aligned in a similar manner to bound TMTFA and tacrine in their x-ray crystallography structures [27, 30] (Figure 6.8). The location of the protein backbone and sidechains were unaltered during this process.

A topology for the serine bound ligand was generated using PRODRG [272], where the inhibitor was covalently attached (in the correct chiral form) to a short chain from the protein backbone (comprising two additional residues on either side of the catalytic serine, Ser203 in *Ee*AChE). These structural parameters were included in the GROMACS forcefield as a new residue type, before a topology for the entire system was generated by GROMACS.

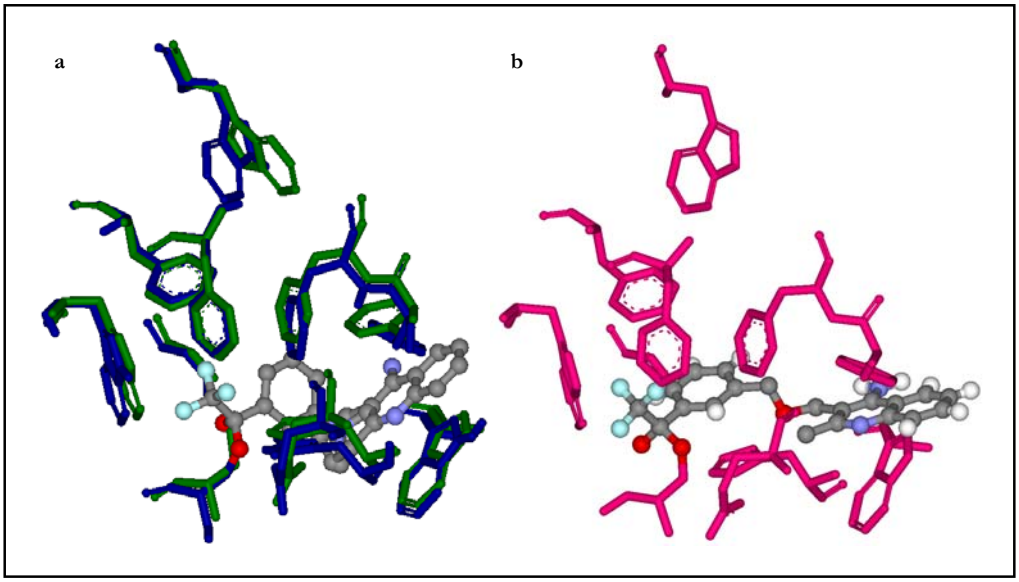

Figure 6.8 – Initial placement of R414983 within *Electrophorus electricus* AChE: overlay of the crystal structures for the inhibitors bound to *Tc*AChE, residues from the TMTFA structure are shown in blue and from the and tacrine structure in green (a) *Ee*AChE crystal structure with R414983 positioned in a similar location (b).

The energy of the complex was minimised using a steepest descent algorithm with a maximum move per atom of 0.1 Å per step. Subsequently, this energy minimised structure was used as the basis for a 1 ns molecular dynamics simulation (2 fs per step), *in vacuuo,* using the GROMACS forcefield.

Initial velocities were generated randomly using a Boltzman distribution at a temperature of 300K and a pressure of 1 bar (Berendsen methodology was used for the maintenance of temperature and pressure). The inhibitor and catalytic serine, together with any protein residues which had at least one atom within 5 Å, were allowed to move freely, the remaining parts of the structure were fixed. Five 20 ps simulations were performed to bring the system to equilibrium before the before the full 1 ns simulation was begun.

6.3.2 NMR Restrained Conformations

Using software developed specifically for this purpose by Dr Stephan Grage (Oxford), molecular conformations which matched the NMR derived distance restraints were determined. Each torsion angle was varied through 20 equal steps (15º) and, on the basis of typical bond lengths and angles from x-ray crystallography, the internuclear distances for pairs of atoms calculated. These distances were automatically compared to NMR restraints, with structures displaying a deviation above chosen threshold levels rejected – no threshold, 0.5 Å (the estimated error in the NMR restraints), 0.2 Å (a potentially achievable error with experimental optimisation) and 0.0108 Å (chosen to include only ten conformations).

6.4 Results

6.4.1 Molecular Dynamics Simulations

Sample structures and details of how the three distances investigated using NMR vary over time in the 1 ns molecular dynamics simulation of R414983 are shown in Figure 6.9. After a period of relative mobility during the first 200 ps of the simulation, the molecule reaches a stable state in which it remains until the later stages of the run. At approximately 900 ps the structure shows a sudden deviation and does not return to the previous conformation during the remainder of the simulation. The simulation time of 1 ns may therefore be insufficient to characterise the dynamic motions of the molecule in this state. However, structures sampled at 100 ps intervals are closely matched after the initial 200 ps.

Table 6.1, summarises the internuclear distances from molecular modelling and compares them with those determined using NMR and x-ray crystallography. Modelling of the inhibitor in free space results in an average distance between: the centroid of the trifluoromethyl and the 2-

methyl of 8.35 ± 0.72 Å; the benzyl methylene and the 2-methyl of 4.62 ± 0.14 Å; and for the benzyl methylene to the quinoline C2 of 4.54 ± 0.08 Å.

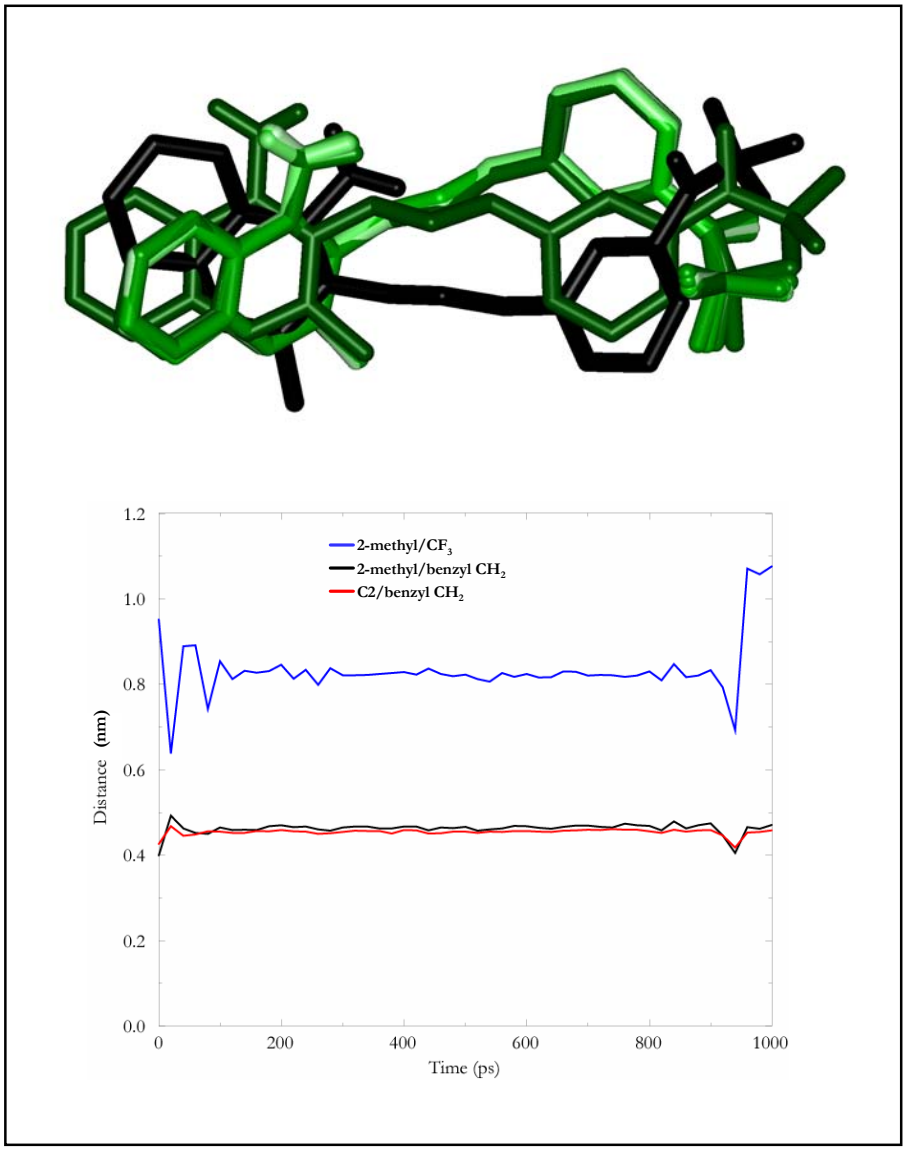

Figure 6.9 – Molecular dynamics simulation of R414983: overlay of structures, sampled every 100 ps during a 1 ns simulation, progressing from black at the start of the simulation (0 ps) to light green at the end (1000 ps). Variation of the three distances investigated by NMR is shown in the plot beneath.

In contrast to the free inhibitor, a reduced level of mobility is observed during the 1 ns simulation of the compound when bound to acetylcholinesterase (Figure 6.10), with each of the three distances having a lower RMSD value. The trifluoromethyl and the 2-methyl are

separated by 8.23 ± 0.20 Å, the benzyl methylene and the 2-methyl by 4.23 ± 0.08 Å, with the benzyl methylene to the quinoline C2 located 4.30 ± 0.06 Å apart. Sampled structures are closely matched throughout the 1 ns time period.

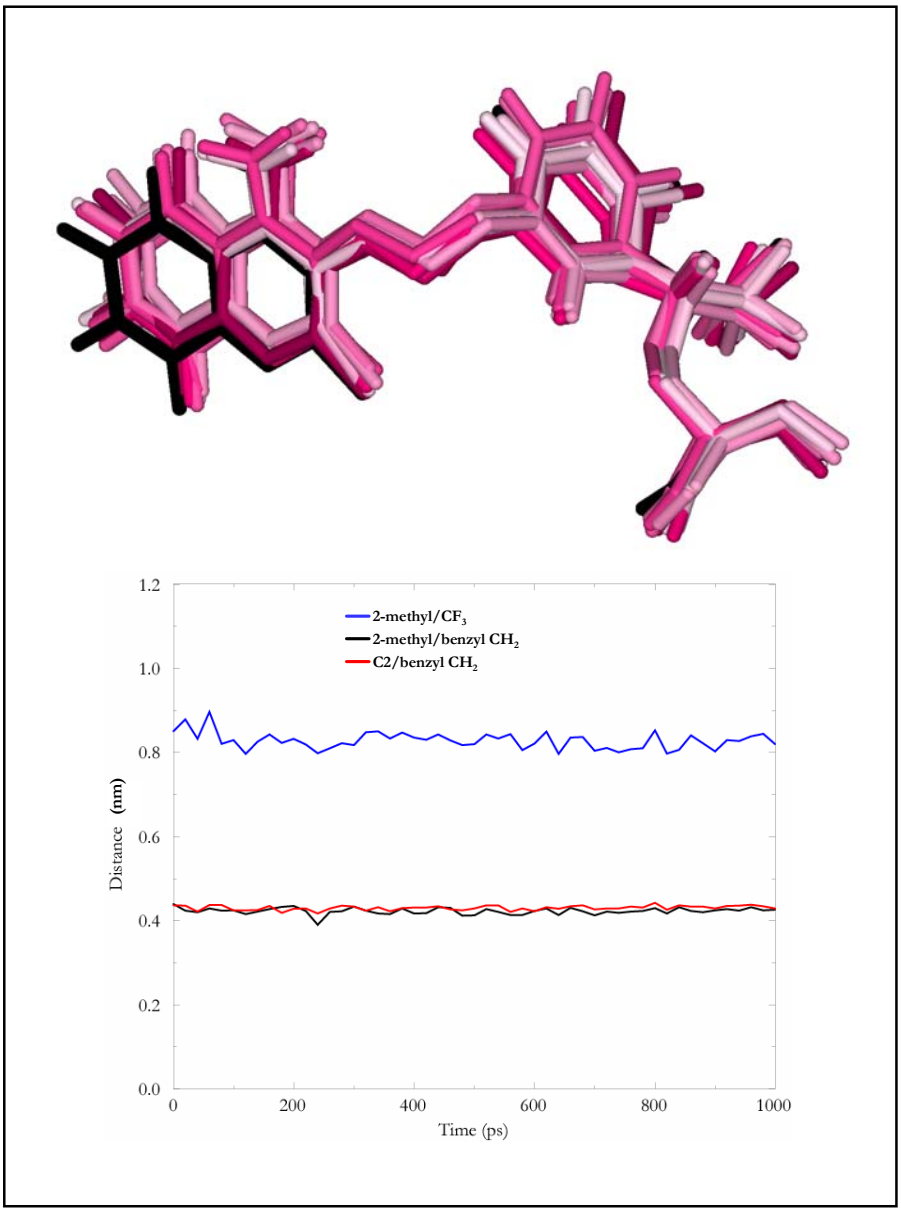

Figure 6.10 – Molecular dynamics simulation of R414983 bound to *Ee*AChE: overlay of the inhibitor and catalytic serine, sampled every 100 ps during a 1 ns simulation, progressing from black at the start of the simulation (0 ps) to light pink at the end (1000 ps). Variation of the three distances investigated by NMR is shown in the plot beneath.

The average distances during simulations do not correspond to those determined by NMR for R414983 bound to *Ee*AChE or by the earlier x-ray crystallographic investigation of R414983 analogues [43]. This discrepancy is most likely a result of the simplified methodology which was utilised. Residues greater than 5 Å from the inhibitor may be restricting local motions, trapping the system its current conformation (each of the distances changes by over 1 Å from their starting arrangement, therefore some degree of flexibility is present, although this may be insufficient). Additionally, longer simulation time could be necessary. The computationally demanding step of hydrating the system would provide an environment which approaches the natural state of the enzyme (how this may correspond to the lyophilised form examined by NMR is not known).

Table 6.1 – Summary of molecular modelling results, with previous NMR and x-ray derived measurements.

Inhibitor form	Structure	Internuclear distance (Å)			RMSD (from NMR data)
		2-methyl/benzyl CH_2	C2/benzyl CH_2	2-methyl/CF_3	
Free R414983	Initial form	3.84	4.28	9.53	1.47
"	Energy minimised	4.00	4.27	9.51	1.46
"	1 ns MD	4.62 ± 0.14	4.54 ± 0.08	8.35 ± 0.72	1.03
*Ee*AChE bound R414983	Initial form	3.35	3.71	7.63	0.46
"	Energy minimised	3.23	3.25	7.06	0.41
"	1 ns MD	4.23 ± 0.08	4.30 ± 0.06	8.23 ± 0.20	0.82
"	NMR restraints	3.9 ± 0.5	3.5 ± 0.5	7.1 ± 0.5	-
*Tc*AChE bound R404435	x-ray	4.11	3.55	6.57	0.33
*Dm*AChE bound R415657	x-ray	3.80	3.71	9.53	1.41

6.4.2 NMR Restrained Conformations

A large degree of conformation flexibility exists within the structure of R414983. Five distinct torsion angles must be determined to enable the selection of a single conformation for the bound inhibitor. The data in Table 6.2 indicates that the three internuclear distances which have been measured (Chapter 4 and Chapter 5) are insufficient for this purpose. Even in the case where NMR distances show unrealistically low errors (<0.0108 Å) a substantial number of possibilities remain, this number will be greater if the precision of torsion angles is increased (i.e. the number of steps). Figure 6.11 illustrates the structural basis for the values in Table 6.2.

Table 6.2 – Possible molecular conformations based on torsion angle searching (15° steps).

Data set	Number of structures
All possibilities	7,962,624
Model distances within 0.5 Å of NMR measurements	144,806
Model distances within 0.2 Å of NMR measurements	12,060
Model distances within 0.0108 Å of NMR measurements	10

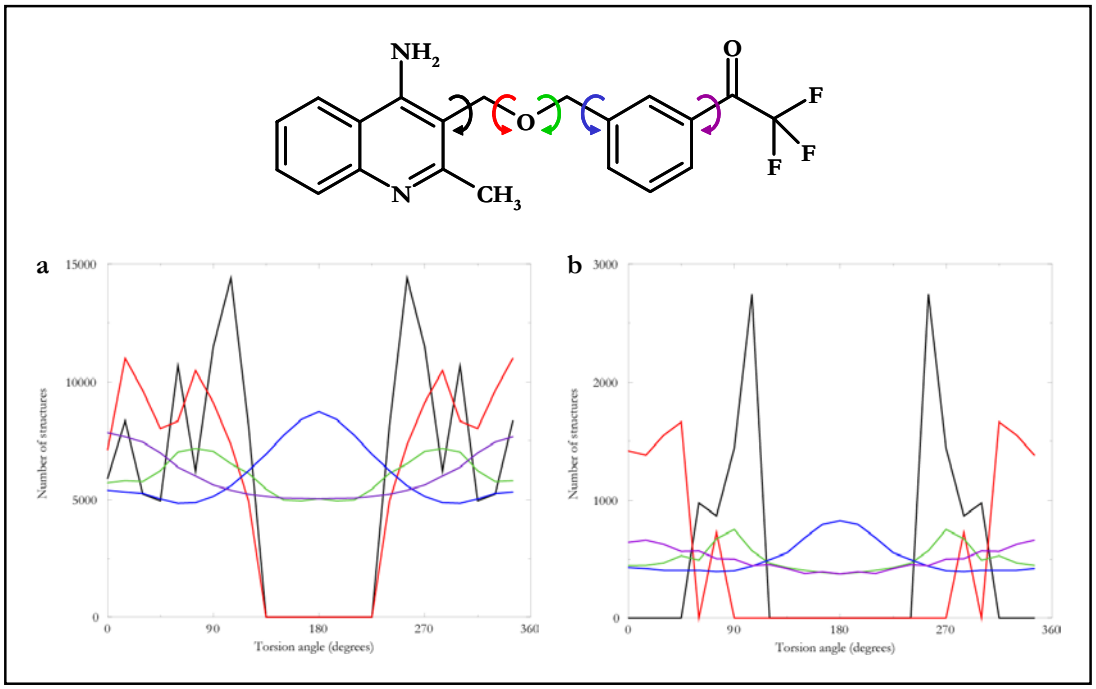

Figure 6.11 – Torsion angle occurrence in structures matching NMR restraints: each of the three model distances within 0.5 Å of NMR measurements (a) within 0.2 Å (b).

Inclusion of all structures within a maximum of 0.5 Å of the NMR determined distances (Figure 6.11a) only excludes a short range of angles for two of the five torsions (indicted by black and red). The two angles torsions closest to quinoline ring are restricted to a range of 255° (each excluding 7 torsion angle steps). Increasing the precision to include structures within 0.2 Å of the measured distances has a marked effect on their torsion angle distribution (Figure 6.11b), with a larger range of angles excluded.

The remaining three torsions, in the region of the benzyl ring, display a similar distribution profile for both the 0.5 Å and 0.2 Å thresholds, suggesting that the number of degrees of freedom is limiting rather than the quality of present measurements (i.e. more distance restraints are required, not a greater level of restraint precision, since a single REDOR distance covers the three torsions). Although certain angles show a slightly higher number of occurrences, for all three torsions the full range of angles is possible.

The method used in torsion angle searching is purely geometric and therefore does not consider steric effects. Of ten structures selected at random from those meeting the 0.5 Å threshold, four were positioned such that collisions occurred between atoms, while of the ten conformations determined to match the NMR restraints most closely (lowest RMSD), seven were positioned such that collisions occurred.

6.5 Discussion

The reliability of molecular modelling as a tool for structural analysis is limited by the accuracy with which a system is represented. Recently published simulations of acetylcholinesterase have been based on fully hydrated systems [61, 63] and analysis of water molecules within the gorge has shown that 16-20 water molecules are present (in crystal structures of *Tc*AChE 18 are

found in the gorge [62], out of 42 conserved water molecules in the complete enzyme [39]). It is not surprising that the conformation of enzyme bound R414983 in molecular dynamics simulations does not correspond to the internuclear distances measured using NMR (Table 6.1). Previous difficulties in the modelling of inhibitor binding [36, 40, 41, 43, 64] suggest that accurate representation of the system under study may be particularly critical in the case of acetylcholinesterase. The lack of a hydrated environment for the protein during simulation necessitated the restraint of a proportion of the enzyme structure to ensure it remained intact. The selection of a cut-off for mobile residues of 5 Å from the inhibitor or catalytic serine may result in an insufficient level of flexibility in the region of the inhibitor for it to assume a preferred conformation. Concerted 'breathing' motions of the enzyme have been observed during 10 ns simulations of the hydrated *Tc*AChE enzyme [61], such motions may be important for inhibitor positioning.

The PDB entry on which the present work was based (1C2B) is at a resolution of 4.5 Å [34]. As a result of the low resolution, the locations of amino-acid sidechains were determined through homology modelling with the mouse enzyme [34]. Use of the structure for simulations, especially where only a small region of the protein is mobile, is likely to contribute to the deviation of simulation results from NMR measurements.

Extending the current work to a fully hydrated system, where the complete structure is allowed motional freedom, may resolve the current discrepancy in distances. However, this step would be computationally demanding and could form a project in its own right.

At this time it is not realistic to present a single conformation, or even a small set of conformations, as being representative of R414983 bound to acetylcholinesterase using solely the internuclear distances measured using NMR in this study. A substantial degree of freedom remains within the molecule. Improving the accuracy of NMR measurements will reduce the

conformational freedom further but additional measurements are required if a single conformation is ultimately to be determined.

The two ^{13}C-^{13}C rotational resonance measurements help define torsions in the region of the quinoline ring (shown by black and red arrows in Figure 6.12). Increasing the precision of these measurements and the determination of the C3/benzyl methylene distance will increase the restriction placed on the range of possible angles for these two torsions.

The long-range REDOR measurement between the 2-methyl and trifluoromethyl function is dependent upon the orientation of all five torsions. While restricting the overall number of molecular conformations, the large number of torsions on which the distance depends means that none of the torsions is specifically constrained. Additional measurements are necessary to restrict torsions in the region of the benzyl ring (shown by green, blue and purple arrows in Figure 6.12), such as between the trifluoromethyl and the benzyl methylene or quinoline methylene.

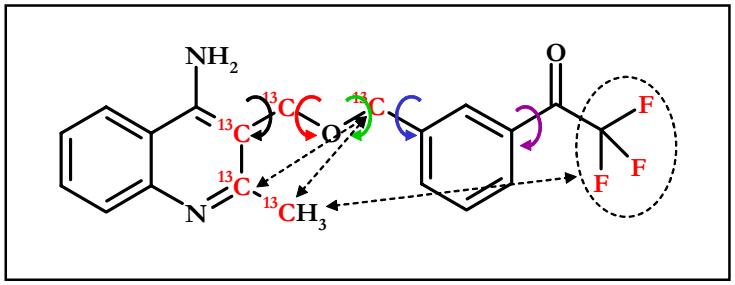

Figure 6.12 – Conformational freedom within the inhibitor R414983 and NMR distance measurements.

Despite the inability to determine a definitive structure using data presently available, it is interesting to note that of the two analogues which have been examined by x-ray crystallography (R404435 and R415657), only the conformation for R404435 falls within the error margins of the NMR based internuclear distances (Table 6.1). It is therefore possible that

R414983 adopts a similar conformation when bound to *Ee*AChE as is found with R404435 bound to *Tc*AChE.

Chapter 7 Conclusions

7.1 General Conclusions

Solid state NMR is a novel approach to the investigation of acetylcholinesterase and the binding of acetylcholinesterase inhibitors. This was demonstrated by studies on a series of compounds designed by Syngenta, based on a chimera of two previously known inhibitors, which are ideal candidates for such initial work. The compounds show a high level of potency, have structural flexibility and, as transition state analogues, have a known point of attachment to the enzyme.

As is often the case with structural studies on proteins, the availability of enzyme imposes restrictions on the experimental approach. The lack of an academic source of the enzyme means that material must be purchased from commercial suppliers. Under these circumstances, the selection of a single isotopic labelling scheme which enables the determination of multiple distance restraints is more appropriate than the use of multiple samples tailored for specific measurements.

Two compounds from the Syngenta series were chosen, 4-amino-5-fluoro-2-methyl-3-(3-trifluoroacetylbenzyl-oxymethyl)quinoline and 4-amino-2-methyl-3-(3-trifluoroacetylbenzyl-oxymethyl)quinoline, designated as R414425 and R414983. Both of these compounds were

subsequently synthesised with the incorporation of isotopic labels (^{13}C) which, in conjunction with the fluorine atoms already present in their structures, provides the potential for homonuclear ^{13}C-^{13}C, homonuclear ^{19}F-^{19}F and heteronuclear ^{13}C-^{19}F internuclear distance measurements. The availability of isotopically labelled starting materials restricted the selection of label positions in the final products. R414425 and R414983 were characterised as inhibitors of *Electrophorus electricus* acetylcholinesterase, with IC_{50} values determined to be 4.8 ± 1.2 nM and 4.4 ± 1.2 nM respectively.

Rotational resonance experiments on $^{13}C_5$-R414983 bound to *Ee*AChE are subject to errors arising from broad spectral linewidths and the presence of multiple ^{13}C labels in close proximity. Despite these difficulties, two measurements on internal calibration distances indicated an accuracy of 0.5 Å could be attained during experiments. Subsequently, the internuclear distance for the benzyl methylene/2-methyl spin pair was determined to be 3.9 ± 0.5 Å, with the benzyl methylene/quinoline C2 distance found to be 3.5 ± 0.5 Å. REDOR experiments were utilised to quantify the separation of the trifluoromethyl function and the ^{13}C atom at the 2-methyl position in $^{13}C_5$-R414983 bound to *Ee*AChE, providing a distance of 7.1 ± 0.5 Å.

The desire to answer a specific biological problem creates a need to make compromises between the optimisation of experimental conditions and the collection of data. The error level for each of the distance measurements is unfortunately high. However, the determination of a unique conformation for the bound inhibitor is restricted by the number of distance measurements presently available rather than the precision of the current values. Technical issues (such as the reliability of instrumentation) and theoretical issues (such as the complexity of the rotational resonance analysis in multi-spin systems with a large spectral linewidths) will have to be addressed if the precision of the present rotational resonance measurements is to be

improved, the third variable ^{13}C-^{13}C distance determined and supplementary ^{13}C-^{19}F distances measured using REDOR.

As such, this work forms a solid foundation which has the potential to provide a conclusive determination of the inhibitor conformation with further work. Significant progress has been made towards elucidation of the first structure of an inhibitor bound to *Electrophorus electricus* acetylcholinesterase and, for the first time, determination of the conformation of an inhibitor bound to acetylcholinesterase through means other than x-ray crystallography.

7.2 Future Experiments

Heterogeneity within the binding site is responsible for the broad spectral linewidths observed in ^{13}C spectra of $^{13}C_5$-R414983 bound to *Ee*AChE. Although it is possible that the binding site is promiscuous in its acceptance of different inhibitor conformations, the lyophilised state of NMR samples is a more likely explanation. The presence of 42 conserved water molecules in x-ray structures of the enzyme, 18 of which are in the region of the gorge and active site [39], suggests that water molecules are of structural importance. The preparation of NMR samples which contain micro-crystalline or partially hydrated enzyme may reduce spectral linewidths. In addition to the sensitivity benefit of smaller linewidths, heterogeneity effects during rotational resonance experiments would be decreased, enabling the determination of distances to a higher level of accuracy (presently, errors arise mainly through systematic rather than random effects).

The compensation for sample heterogeneity by the use of spectral linewidths to estimate zero-quantum relaxation parameters during rotational resonance experiments requires further investigation. In addition to the two rigid distances used to confirm the accuracy of rotational resonance measurements, a number of other rigid internuclear measurements can also be made, providing a basis for a more rigorous mathematical analysis of magnetisation exchange under these conditions, potentially increasing the precision of the rotational resonance

measurements already performed. The application of an off-resonance R2 scheme [225-228] should enable the measurement of the third and final conformationally dependent ^{13}C-^{13}C distance.

A series of REDOR experiments on standard samples will enable the full characterisation of the instrumentation, enabling the selection of experimental conditions such that reliable distance measurements can be obtained. Subsequently, the accuracy of the ^{13}C-^{19}F distance measured may be improved and additional interatomic distances determined.

Labelled R414425 has not yet been investigated when bound to acetylcholinesterase. The latest generation of solid state fluorine NMR probes should make more complex fluorine observed experiments viable, such as homonuclear distance measurement between the quinoline fluorine and trifluoromethyl in R414425. The previous performance of instrumentation for this purpose has been poor. The opportunity for homonuclear ^{13}C-^{13}C measurements on acetylcholinesterase bound R414425 also remains.

Deuterium NMR provides a method for the elucidation of dynamics in a system. Although not included here, deuterium labelled versions of the inhibitors R414425 and R414983 have also been synthesised (but not measured) and should allow the investigation of dynamics of in the region of the benzyl ring – whether it is tightly constrained or demonstrates a degree of motion, and the nature of any motions.

Once a specific conformation for the bound inhibitor has been determined (or a small number of possibilities), the opportunity for investigation of inhibitor-protein interactions exists without the need for isotopic labelling of the protein. Lee-Goldburg cross-polarisation (LG-CP) [243] provides a method for the investigation of heteronuclear ^{1}H-^{13}C distances.

The opportunity also exists for the development of more advanced molecular dynamics simulations of the bound inhibitors than undertaken here. However, such work is technically more difficult and is restricted by demands on computational time.

Knowledge of the interactions of acetylcholinesterase with acetylcholine is still of great interest. A small quantity of detergent solubilised GPI anchored *Tc*AChE has been provided by Israel Silman (Wizemann Institute). Once reconstituted into membranes, this material has the potential for rapid purification by centrifugation. It may therefore be possible to investigate the binding of carbamylcholine, a close analogue of acetylcholine, which is hydrolysed in a period of minutes at room temperature [273] and therefore not suitable for examination by x-ray crystallography.

Bibliography

1. J.F. Danielli and H. Davson (1935) A contribution to the theory of permeability of thin films. *J. Cell. Compar. Physl.*, **5**: 495-508.

2. S.J. Singer and G.L. Nicholson (1972) The fluid mosaic model of the structure of cell membranes. *Science*, **175** (23): 720-731.

3. C.K. Mathews and K.E. van Holde, *Biochemistry*. 1st ed. 1990: The Benjamin/Cummings Publishing Company Inc.

4. K. Simons and E. Ikonen (1997) Functional rafts in cell membranes. *Nature*, **387**: 569-572.

5. C.M. Fraser, J.D. Gocayne, O. White, M.D. Adams, R.A. Clayton, R.D. Fleischmann, C.J. Bult, A.R. Kerlavage, G. Sutton, J.M. Kelly, J.L. Fritchman, J.F. Weidman, S.K. V., M. Sandusky, J. Fuhrmann, D. Nguygen, T.R. Utterback, D.M. Saudek, C.A. Phillips, J.M. Merrick, J.-F. Tomb, B.A. Dougherty, K.F. Bott, P.-C. Hu, T.S. Lucier, S.N. Peterson, H.O. Smith, C.A. Hutchison III, and J.C. Venter (1995) The Minimal Gene Complement of Mycoplasma gentitalium. *Science*, **270**: 397-403.

6. A. Watts, I.J. Burnett, C. Glaubitz, G. Grobner, D.A. Middleton, P.J.R. Spooner, J.A. Watts, and P.T.F. Williamson (1999) Membrane protein structure determination by solid state NMR. *Nat. Prod. Rep.*, **16**: 419-423.

7. G.C. Terstappen and A. Reggiani (2001) *In silico* research in drug discovery. *Trends Pharmacol. Sci.*, **22** (1): 23-26.

8. P.-J. Corringer, N. Le Novere and J.-P. Changeux (2000) Nicotinic Receptors at the Amino Acid Level. *Annu. Rev. Pharmacol. Toxicol.*, **40**: 431-458.

9. J.R. Cooper, F.E. Bloom and R.H. Roth, *The Biochemical Basis of Neuropharmacology*. 7th ed. 1996, Oxford: Oxford University Press.

10. J. Minic, J. Molgo, E. Karlsson, and E. Krejci (2002) Regulation of acetylcholine release by muscarinic receptors at the mouse neuromuscular junction depends on the activity of acetylcholinesterase. *Eur. J. Neurosci.*, **15**: 439-448.

11. A.B. Smit, N.I. Syed, D. Schaap, J. van Minnen, J. Klumperman, K.S. Kits, H. Lodder, R.C. van der Schors, R. van Elk, B. Sorgedrager, K. Brejc, T.K. Sixma, and W.P.M. Geraerts (2001) A glia-derived acetylcholine-binding protein that modulates synaptic transmission. *Nature*, **411**: 261-268.

12. M.P. Cauflield and N.J.M. Birdsall (1998) International Union of Pharmacology. XVII. Classification of Muscarinic Acetylcholine Receptors. *Pharmacol. Rev.*, **50** (2): 279-290.

13. K. Palczewski, T. Kumasaka, T. Hori, C.A. Behnke, H. Motoshima, B.A. Fox, I. Le Trong, D.C. Teller, T. Okada, R.E. Stenkamp, M. Yamamoto, and M. Miyano (2000) Crystal Structure of Rhodopsin: A G protein-coupled receptor. *Science*, **277**: 687-690.

14. T.H. Ji, M. Grossman and I. Ji (1998) G Protein-coupled Receptors. I. Diversity of receptor-ligand interactions. *J. Biol. Chem.*, **273** (28): 17299-17302.

15. K. Brejc, W.J. van Dijk, R.V. Klaassen, M. Schuurmans, J. van der Oost, A.B. Smit, and T.K. Sixma (2001) Crystal structure of an ACh-binding protein reveals the ligand-binding domain of nicotinic receptors. *Nature*, **411**: 269-276.

16. A. Miyazawa, Y. Fujiyoshi, M. Stowell, and N. Unwin (1999) Nicotinic Acetylcholine Receptor at 4.6A Resolution: Transverse Tunnels in the Channel Wall. *J. Mol. Biol.*, **288**: 265-286.

17. N. Unwin (1993) Nicotinic Acetylcholine Receptor at 9A Resolution. *J. Mol. Biol.*, **229**: 1104-1124.

18. N. Unwin (1995) Acwtylcholine-Receptor Channel Imaged In The Open State. *Nature*, **373**: 37-43.

19. P.T.F. Williamson, G. Grobner, P.J.R. Spooner, K.W. Miller, and A. Watts (1998) Probing the agonist binding pocket in the nicotinic acetylcholine receptor: A high-resolution solid-state NMR approach. *Biochemistry*, **37**: 10854-10859.

20. P.T.F. Williamson, J.A. Watts, G.H. Addona, K.W. Miller, and A. Watts (2001) Dynamics and orientation of $N^+(CD_3)_3$-bromoacetylcholine bound to its binding site on the nicotinic acetylcholine receptor. *Proc. Natl. Acad. Sci. USA*, **98** (5): 2346-2351.

21. L. Styer, *Biochemistry*. 4th ed. 1995: W. H. Freeman and Company, New York.

22. P. Taylor (1991) The Cholinesterases. *J. Biol. Chem.*, **266** (7): 4025-4028.

23. G. Kryger, M. Harel, K. Giles, L. Toker, B. Velan, A. Lazar, C. Kronman, D. Barak, N. Ariel, A. Shafferman, I. Silman, and J.L. Sussman (2000) Structures of recombinant native and E202Q mutant human acetylcholinesterase complexed with the snake-venom toxin fasciculin-II. *Acta. Cryst. D*, **56** (11): 1385-1394.

24. M.L. Raves, M. Harel, Y.-P. Pang, I. Silman, A.P. Kozikowski, and J.L. Sussman (1997) Structure of acetylcholinesterase complexed with the nootropic alkaloid, (-)-huperzine A. *Nature Struct. Biol.*, **4** (1): 57-63.

25. C.B. Millard, G. Koellner, A. Ordentlich, A. Shafferman, I. Silman, and J.L. Sussman (1999) Reaction Products of Acetylcholinesterase and VX Reveal a Mobile Histidine in the Catalytic Triad. *J. Am. Chem. Soc.*, **121**: 9883-9884.

26. M. Harel, G.J. Kleywegt, R.B.G. Ravelli, I. Silman, and J.L. Sussman (1995) Crystal structure of an acetylcholinesterase-fasciculin complex: interaction of a three-fingered toxin from snake venom with its target. *Structure*, **3**: 1355-1366.

27. M. Harel, D.M. Quinn, H.K. Nair, I. Silman, and J.L. Sussman (1996) The X-ray Structure of a Transition State Analog Complex Reveals the Molecular Origins of the Catalytic Power and Substrate Specificity of Acetylcholinesterase. *J. Am. Chem. Soc.*, **118**: 2340-2346.

28. Y. Bourne, P. Taylor and P. Marchot (1995) Acetylcholinesterase Inhibition by Fasciculin: Crystal Structure of the Complex. *Cell*, **83**: 503-512.

29. J.L. Sussman, M. Harel and I. Silman (1993) Three-Dimensional Structure of Acetylcholinesterase and of its Complexes with Anticholinesterase Drugs. *Chem. Biol. Interact.*, **87**: 187-197.

30. M. Harel, I. Schalk, L. Ehret-Sabatier, F. Bouet, M. Goeldner, C. Hirth, P.H. Axelsen, I. Silman, and J.L. Sussman (1993) Quaternary ligand binding to aromatic residues in the active-site gorge of acetylcholinesterase. *Proc. Natl. Acad. Sci. USA*, **90**: 9031-9035.

31. J.L. Sussman, M. Harel, F. Frolow, C. Oefner, A. Goldman, L. Toker, and I. Silman (1991) Atomic Structure of Acetylcholinesterase from Torpedo californica: A Prototypic Acetylcholine-Binding Protein. *Science*, **253**: 872-879.

32. C.B. Millard, G. Kryger, A. Ordentlich, H.M. Greenblatt, M. Harel, M.L. Raves, Y. Segall, D. Barak, A. Shafferman, I. Silman, and J.L. Sussman (1999) Crystal Structures of Aged Phosphonylated Acetylcholinesterase: Nerve Agent Reaction Products at the Atomic Level. *Biochemistry*, **38** (22): 7032-7039.

33. Y. Bourne, P. Taylor, P.E. Bougis, and P. Marchot (1999) Crystal Structure of Mouse Acetylcholinesterase: A Peripheral Site-Occluding Loop in a Tetrameric Assembly. *J. Biol. Chem.*, **274** (5): 2963-2970.

34. Y. Bourne, J. Grassi, P.E. Bougis, and P. Marchot (1999) Conformational Flexibility of the Acetylcholinesterase Tetramer Suggested by X-ray Crystallography. *J. Biol. Chem.*, **274** (43): 30370.

35. C. Bartolucci, E. Perola, L. Cellai, M. Brufani, and D. Lamba (1999) "Back Door" Opening Implied by the Crystal Structure of a Carbamoylated Acetylcholinesterase. *Biochemistry*, **38**: 5714-5719.

36. G. Kryger, I. Silman and J.L. Sussman (1998) Three-dimensional structure of a complex of E2020 with acetylcholinesterase from Torpedo californica. *J. Physiology (Paris)*, **92**: 191-194.

37. R.B.G. Ravelli, M.L. Raves, Z. Ren, D. Bourgeois, M. Roth, J. Kroon, I. Silman, and J.L. Sussman (1998) Static Laue Diffraction Studies on Acetylcholinesterase. *Acta. Cryst. D*, **54**: 1359-1366.

38. M. Harel, G. Kryger, T.L. Rosenberry, W.D. Mallender, T. Lewis, R.J. Fletcher, J.M. Guss, I. Silman, and J.L. Sussman (2000) Three-dimensional structures of Drosophila melanogaster acetylcholinesterase and of its complexes with two potent inhibitors. *Protein Sci.*, **9** (6): 1063-1072.

39. G. Koellner, G. Kryger, C.B. Millard, I. Silman, J.L. Sussman, and T. Steiner (2000) Active-site gorge and buried water molecules in crystal structures of acetylcholinesterase from Torpedo californica. *J. Mol. Biol.*, **296**: 713-735.

40. G. Kryger, I. Silman and J.L. Sussman (1999) Structure of acetylcholinesterase complexed with E2020 (Aricept®): implications for the design of new anti-Alzheimer drugs. *Structure*, **7** (3): 297-307.

41. H.M. Greenblatt, G. Kryger, T. Lewis, I. Silman, and J.L. Sussman (1999) Structure of acetylcholinesterase complexed with (-)- galanthamine at 2.3 angstrom resolution. *FEBS Lett.*, **463**: 321-326.

42. C. Bartolucci, E. Perola, C. Pilger, G. Fels, and D. Lamba (2001) Three-dimensional structure of a complex of galanthamine (Nivalin®) with acetylcholinesterase from *Torpedo californica*: Implications for the design of new anti-Alzheimer drugs. *Proteins*, **42** (2): 182-191.

43. C. Doucet-Personeni, P.D. Bentley, R.J. Fletcher, A. Kinkaid, G. Kryger, B. Pirard, A. Taylor, R. Taylor, J. Taylor, R. Viner, I. Silman, J.L. Sussman, H.M. Greenblatt, and T. Lewis (2001) A Structure-Based Design Approach to the Development of Novel, Reversible AChE Inhibitors. *J. Med. Chem.*, **44**: 3203-3215.

44. G. Koellner, T. Steiner, C.B. Millard, I. Silman, and J.L. Sussman (2002) A Neutral Molecule in a Cation-binding Site: Specfic Binding of a PEG-SH to Acetylcholinesterase from *Torpedo californica*. *J. Mol. Biol.*, **320** (4): 721-725.

45. M. Weik, R.B.G. Ravelli, G. Kryger, S. McSweeney, M.L. Raves, M. Harel, P. Gros, I. Silman, J. Kroon, and J.L. Sussman (2000) Specific chemical and structural damage to proteins produced by synchrotron radiation. *Proc. Natl. Acad. Sci. USA*, **97** (2): 623-628.

46. P. Bar-On, C.B. Millard, M. Harel, H. Dvir, A. Enz, J.L. Sussman, and I. Silman (2002) Kinetic and Structural Studies on the Interaction of Cholinesterases with the Anti-Alzheimer Drug Rivastigmine. *Biochemistry*, **41**: 3555-3564.

47. H. Dvir, D.M. Wong, M. Harel, X. Barril, M. Orozco, F.J. Luque, D. Munoz-Torrero, P. Camps, T.L. Rosenberry, I. Silman, and J.L. Sussman (2002) 3D Structure of *Torpedo californica* Acetylcholinesterase Complexed with Huprine X at 2.1A Resolution: Kinetic and Molecular Dynamic Correlates. *Biochemistry*, **41**: 2970-2981.

48. H. Dvir, H.L. Jiang, D.M. Wong, M. Harel, M. Chetrit, X.C. He, G.Y. Yin, G.L. Yu, X.C. Tang, I. Silman, D.L. Bai, and J.L. Sussman (2002) X-ray Structures of Torpedo californica Acetylcholinesterase Complexed with (+)-Huperzine A and (-)-Huperzine B: Structural Evidence for an Active Site Rearrangement. *Biochemistry*, **41** (35): 10810-10818.

49. J. Antosiewicz and J.A. McCammon (1995) Simulation of Charge-Mutant Acetylcholinesterases. *Biochemistry*, **34**: 4211-4219.

50. S.T. Wlodek, T.W. Clark, L.R. Scott, and J.A. McCammon (1997) Molecular Dynamics of Acetylcholinesterase Dimer Complexed with Tacrine. *J. Am. Chem. Soc.*, **119**: 9513-9522.

51. M.K. Gilson, T.P. Straatsma, J.A. McCammon, D.R. Ripoll, C.H. Faerman, P.H. Axelsen, I. Silman, and J.L. Sussman (1994) Open 'Back Door' in a Molecular Dynamics Simulation of Acetylcholinesterase. *Science*, **263**: 1276-1278.

52. D.R. Ripoll, C.H. Faerman, P.H. Axelsen, I. Silman, and J.L. Sussman (1993) An electrostatic mechanism for the substrate guidance down the aromatic gorge of acetylcholinesterase. *Proc. Natl. Acad. Sci. USA*, **90**: 5128-5132.

53. R.C. Tan, T.N. Truong, J.A. McCammon, and J.L. Sussman (1993) Acetylcholinesterase: Electrostatic Steering Increases the Rate of Ligand Binding. *Biochemistry*, **32**: 401-403.

54. P. Deprez and N.C. Inestrosa (2000) Molecular modeling of the collagen-like tail of asymmetric acetylcholinesterase. *Protein Eng.*, **13** (1): 27-34.

55. A.H. Elcock, R.R. Gabdoulline, R.C. Wade, and J.A. McCammon (1999) Computer Simulation of Protein-Protein Association Kinetics: Acetylcholinesterase-Fasciculin. *J. Mol. Biol.*, **291** (1): 149-162.

56. H.-X. Zhou, S. Wlodek and J.A. McCammon (1998) Conformation gating as a mechanism for enzyme specificity. *Proc. Natl. Acad. Sci. USA*, **95**: 9280-9283.

57. P. Vagedes, B. Rabenstein, J. Åqvist, J. Marelius, and E.-W. Knapp (2000) The Deacylation Step of Acetylcholinesterase: Computer Simulation Studies. *J. Am. Chem. Soc.*, **122**: 12254-12262.

58. W. Sippl and H.-D. Holtje (2000) Structure-based 3D-QSAR - merging the accuracy of structure-based alignments with the computational efficiency of ligand-based methods. *J. Mol. Struct. (Theochem)*, **503**: 31-50.

59. S.T. Wlodek, T. Shen and J.A. McCammon (2000) Electrostatic steering of substrate to acetylcholinesterase: Analysis of field fluctuations. *Bioploymers*, **53** (3): 265-271.

60. P. Camps, E. Gomez, D. Munoz-Torrero, A. Badia, N.M. Vivas, X. Barril, M. Orozco, and F.J. Luque (2001) Synthesis, in Vitro Pharmacology, and Molecular Modelling of syn-Huprines as Acetylcholinesterase Inhibitors. *J. Med. Chem.*, **44**: 4733-4736.

61. K. Tai, T. Shen, U. Borjesson, M. Philippopoulos, and J.A. McCammon (2001) Analysis of a 10-ns Molecular Dynamics Simulation of Mouse Acetylcholinesterase. *Biophys. J.*, **81**: 715-724.

62. R.H. Henchman, K. Tai, T. Shen, and J.A. McCammon (2002) Properties of Water Molecules in the Active Site Gorge of Acetylcholinestease from Computer Simulation. *Biophys. J.*, **82**: 2671-2682.

63. K. Tai, T. Shen, R.H. Henchman, Y. Bourne, P. Marchot, and J.A. McCammon (2002) Mechanism of Acetylcholinesterase Inhibition by Fasciculin: A 5-ns Molecular Dynamics Simulation. *J. Am. Chem. Soc.*, **124**: 6153-6161.

64. C. Pilger, C. Bartolucci, D. Lamba, A. Tropsha, and G. Fels (2001) Accurate prediction of the bound conformation of galanthamine in the active site of *Torpedo californica* acetylcholinesterase using molecular docking. *J. Mol. Graph. Model.*, **19**: 288-296.

65. M. Ekholm (2001) Predicting relative free binding energies of substrates and inhibitors of acetylcholin- and butyrylcholinesterases. *J. Mol. Struct. (Theochem)*, **572**: 25-34.

66. T.Y. Shen, K. Tai and J.A. McCammon (2001) Statistical analysis of the fractal gating motions of the enzyme acetylcholinesterase. *Phys. Rev. E*, **63** (041902).

67. R.H. Henchman and J.A. McCammon (2002) Structural and dynamic properties of water around acetylcholinesterase. *Protein Sci.*, **11**: 2080-2090.

68. V. Marcel, L.G. Palacios, C. Pertuy, P. Masson, and D. Fournier (1998) Two invertebrate acetylcholinesterases show activation followed by inhibition with substrate concentration. *Biochem. J.*, **329**: 329-334.

69. S. Simon, A. Le Goff, Y. Frobert, J. Grassi, and J. Massoulie (1999) The binding sites of inhibitory monoclonal antibodies on acetylcholinesterase - Identification of a novel regulatory site at the putative "back door". *J. Biol. Chem.*, **274** (39): 27740-27746.

70. J. Pleiss, N. Mionetto and R.D. Schmid (1999) Probing the acyl binding site of acetylcholinesterase by protein engineering. *J. Mol. Catal. B-Enzym.*, **6**: 287-296.

71. T.L. Rosenberry, C.-R. Rabl and E. Neumann (1996) Binding of the Neurotoxin Fasciculin 2 to the Acetylcholinesterase Peripheral Site Drastically Reduces the Association and Dissociation Rate Constants for N-Methylacridinium Binding to the Active Site. *Biochemistry*, **35**: 685-690.

72. T. Szegletes, W.D. Mallender, P.J. Thomas, and T.L. Rossenberry (1999) Substrate Binding to the Peripheral Site of Acetylcholinesterase Initiates Enzymatic Catalysis. Substrate Inhibition Arises as a Secondary Effect. *Biochemistry*, **38**: 122-133.

73. Z. Radic, P.D. Kirchhoff, D.M. Quinn, J.A. McCammon, and P. Taylor (1997) Electrostatic Influence on the Kinetics of Ligand Binding to Acetylcholinesterase. *J. Biol. Chem.*, **272** (37): 23265-23277.

74. Z. Radic, D.M. Quinn, D.C. Vellom, S. Camp, and P. Taylor (1995) Allosteric Control of Acetylcholinesterase Catalysis by Fasciculin. *J. Biol. Chem.*, **270** (35): 20391-20399.

75. A. Shafferman, A. Ordentlich, D. Barak, C. Kronman, R. Ber, T. Bino, N. Ariel, R. Osman, and B. Velan (1994) Electrostatic attraction by surface charge does not contribute to the catalytic efficiency of acetylcholinesterase. *EMBO J.*, **13** (15): 3448-3455.

76. A. Ordentlich, D. Barak, C. Kronman, H.P. Benschop, L.P.A. De Jong, N. Ariel, R. Barak, Y. Segall, B. Velan, and A. Shafferman (1999) Exploring the Active Center of Human Acetylcholinesterase with Stereomers of an Organophosphorus Inhibitor with Two Chiral Centers. *Biochemistry*, **38**: 3055-3066.

77. T.L. Rosenberry, W.D. Mallender, P.J. Thomas, and T. Szegletes (1999) A steric blockade model for inhibition of acetylcholinesterase by peripheral site ligands and substrate. *Chem. Biol. Interact.*, **119-120**: 85-97.

78. T. Szegletes, W.D. Mallender and T.L. Rosenberry (1998) Nonequilibrium Analysis Alters the Mechanistic Interpretation of Inhibition of Acetylcholinesterase by Peripheral Site Ligands. *Biochemistry*, **37**: 4206-4216.

79. A. Saxena, R. Hur and B.P. Doctor (1998) Allosteric Control of Acetylcholinesterase Activity by Monoclonal Antibodies. *Biochemistry*, **37**: 145-154.

80. S. Malany, M. Sawai, R.S. Sikorski, J. Seravalli, D.M. Quinn, Z. Radic, P. Taylor, C. Kronman, B. Velan, and A. Shafferman (2000) Transition state structure and rate determination for the acylation stage of acetylcholinesterase catalyzed hydrolysis of (acetylthio)choline. *J. Am. Chem. Soc.*, **122** (13): 2981-2987.

81. A.E. Boyd, A.B. Marnett, L. Wong, and P. Taylor (2000) Probing the Active Center Gorge of Acetylcholinesterase by Fluorophores Linked to Substituted Cysteines. *J. Biol. Chem.*, **275** (29): 22401-22408.

82. W.D. Mallender, T. Szelgletes and T.L. Rosenberry (2000) Acetylthiocholine Binds to Asp74 at the Peripheral Site of Human Acetylcholinesterase as the First Step in the Catalytic Pathway. *Biochemistry*, **39**: 7753-7763.

83. D.M. Quinn, S.R. Feaster, H.K. Nair, N.A. Baker, Z. Radic, and P. Taylor (2000) Delineation and decomposition of energies involved in quaternary ammonium binding in the active site of acetylcholinesterase. *J. Am. Chem. Soc.*, **122** (13): 2975-2980.

84. V. Marcel, S. Estrada-Mondaca, F. Magne, J. Stojan, A. Klaebe, and D. Fournier (2000) Exploration of the Drosophila acetylcholinesterase substrate activation site using a reversible inhibitor (Triton X-100) and mutated enzymes. *J. Biol. Chem.*, **275** (16): 11603-11609.

85. D. Kraut, H. Goff, R.K. Pai, N.A. Hosea, I. Silman, J.L. Sussman, P. Taylor, and J.G. Voet (2000) Inactivation Studies of Acetylcholinesterase with Phenylmethylsulfonyl Fluoride. *Mol. Pharmacol.*, **57** (6): 1243-1248.

86. S. Malany, N. Baker, M. Verweyst, R. Medhekar, D.M. Quinn, B. Velan, C. Kronman, and A. Shafferman (1999) Theoretical and experimental investigations of electrostatic effects on acetylcholinesterase catalysis and inhibition. *Chem. Biol. Interact.*, **119-120**: 99-110.

87. G.V. De Ferrari, W.D. Mallender, N.C. Inestrosa, and T.L. Rosenberry (2001) Thioflavin T Is a Fluorescent Probe of the Acetylcholinesterase Peripheral Site That Reveals Conformational Interactions between the Peripheral and Acylation Sites. *J. Biol. Chem.*, **276** (26): 23282-23287.

88. D. Kaplan, A. Ordentlich, D. Barak, N. Ariel, C. Kronman, B. Velan, and A. Shafferman (2001) Does "Butyrylization" of Acetylcholinesterase through Substitution of the Six Divergent Aromatic Amino Acids in the Active Center Gorge Generate an Enzyme Mimic of Butyrylcholinesterase? *Biochemistry*, **40** (25): 7433-7445.

89. L. Brochier, Y. Pontie, M. Willson, S. Estrada-Mondaca, J. Czaplicki, A. Klaebe, and D. Fournier (2001) Involvement of Deacylation in Activation of Substrate Hydrolysis by *Drosophila* Acetylcholinesterase. *J. Biol. Chem.*, **276** (21): 18296-18302.

90. J. Shi, A.E. Boyd, Z. Radic, and P. Taylor (2001) Reversibly Bound and Covalently Attached Ligands Induce Conformational Changes in the Omega Loop, Cys(69)-Cys(96), of Mouse Acetylcholinesterase. *J. Biol. Chem.*, **276** (45): 42196-42204.

91. Z. Radic and P. Taylor (2001) Interaction Kinetics of Reversible Inhibitors and Substrates with Acetylcholinesterase and Its Fasciculin 2 Complex. *J. Biol. Chem.*, **276** (7): 4622-4633.

92. F. Zeng, H. Jiang, Y. Zhai, H. Zhang, K. Chen, and R. Ji (1999) Synthesis and acetylcholinesterase inhibitory activity of huperzine A-E2020 combined compound. *Bioorg. Med. Chem. Lett.*, **9**: 3279-3284.

93. J.-W. Chen, Y.-L. Luo, M.-J. Hwang, F.-C. Peng, and K.-H. Ling (1999) Territrem B, a tremorgenic mycotoxin that inhibits acetylcholinesterase with a noncovalent yet irreversible binding mechanism. *J. Biol. Chem.*, **274** (49): 34916-34923.

94. G. Lin, C.-Y. Lai and W.-C. Liao (1999) Molecular Recognition by Acetylcholinesterase at the Peripheral Anionic Site: Structure-Activity Relationships for Inhibitions by Aryl Carbamates. *Bioorg. Med. Chem.*, **7**: 2683-2689.

95. P.R. Carlier, E.S.-H. Chow, Y. Han, J. Liu, J. El Yazal, and Y.-P. Pang (1999) Heterodimeric Tacrine-Based Acetylcholinesterase Inhibitors: Investigating Ligand-Peripheral Site Interactions. *J. Med. Chem.*, **42**: 4225-4231.

96. Y. Kawakami, A. Inoue, T. Kawai, M. Wakita, H. Sugimoto, and A.J. Hopfinger (1996) The Rationale for E2020 as a Potent Acetylcholinesterase Inhibitor. *Bioorg. Med. Chem.*, **4** (9): 1429-1446.

97. S.Y. Kang, K.Y. Lee, S.H. Sung, M.J. Park, and Y.C. Kim (2001) Coumarins Isolated from *Angelica gigas* Inhibit Acetylcholinesterase: Structure-Activity Relationships. *J. Nat. Prod.*, **64** (5): 683-685.

98. A. Rampa, L. Piazzi, F. Belluti, S. Gobbi, A. Bisi, M. Bartolini, V. Andrisano, V. Cavrini, A. Cavalli, M. Recanatini, and P. Valenti (2001) Acetylcholinesterase inhibitors: SAR and kinetic studies on omega-[N-methyl-N-(3-alkylcarbamoyloxyphenyl)methyl]aminoalkoxyaryl derivatives. *J. Med. Chem.*, **44**: 3810-3820.

99. H.M. Greenblatt, I. Silman and J.L. Sussman (2000) Structural studies on vertebrate and invertebrate acetylcholinesterases and their complexes with functional ligands. *Drug Dev. Res.*, **50**: 573-583.

100. A. Rampa, A. Bisi, F. Belluti, S. Gobbi, P. Valenti, V. Andrisano, V. Cavrini, A. Cavalli, and M. Recanatini (2000) Acetylcholinesterase inhibitors for potential use in Alzheimer's disease: Molecular modeling, synthesis and kinetic evaluation of 11H-indeno-[1,2-b]-quinolin-10-ylamine derivatives. *Bioorg. Med. Chem.*, **8**: 497-506.

101. P. Camps, B. Cusack, W.D. Mallender, R. El Achab, J. Morral, D. Munoz-Torrero, and T.L. Rosenberry (2000) Huprine X is a novel high-affinity inhibitor of acetylcholinesterase that is of interest for treatment of Alzheimer's disease. *Mol. Pharmacol.*, **57**: 409-417.

102. A. Martinez, E. Fernadez, A. Castro, S. Conde, I. Rodriguez-Franco, J.-E. Bañosb, and A. Badia (2000) *N*-Benzylpiperidine derivatives of 1,2,4-thiadiazolidinone as new acetylcholinesterase inhibitors. *Eur. J. Med. Chem.*, **35** (10): 913-922.

103. P. Camps, R. El Achab, J. Morral, D. Muñoz-Torrero, A. Badia, J.E. Baños, N.M. Vivas, X. Barril, M. Orozco, and F.J. Luque (2000) New Tacrine-Huperzine A Hybrids (Huprines): Highly Potent Tight-Binding Acetylcholinesterase Inhibitors of Interest for the Treatment of Alzheimer's. *J. Med. Chem.*, **43** (24): 4657-4666.

104. M.L. Bolognesi, V. Andrisano, M. Bartolini, A. Minarini, M. Rosini, V. Tumiatti, and C. Melchiorre (2001) Hexahydrochromeno[4,3-*b*]pyrrole Derivatives as Acetylcholinesterase Inhibitors. *J. Med. Chem.*, **44** (1): 105-109.

105. L. Savini, G. Campiani, A. Gaeta, C. Pellerano, C. Fattorusso, L. Chiasserini, J.M. Fedorko, and A. Saxena (2001) Novel and potent tacrine-related hetero- and homobivalent ligands for acetylcholinesterase and butyrylcholinesterase. *Bioorg. Med. Chem. Lett.*, **11** (13): 1779-1782.

106. A.S. Dimoglo, N.M. Shvets, I.V. Tetko, and D.J. Livingstone (2001) Electronic-Topological Investigation of the Structure - Acetylcholinesterase Inhibitor Activity Relationship in the Series of N-Benzylpiperideine Derivatives. *Quant. Struct.-Act. Relat.*, **20**: 31-45.

107. V. Rajendran, S.-B. Rong, A. Saxena, B.P. Doctor, and A.P. Kozikowski (2001) Synthesis of a hybrid analogue of the acetylcholinesterase inhibitors huperzine A and huperzine B. *Tetrahedron Lett.*, **42**: 5359-5361.

108. K. Hogenaur, K. Baumann, A. Enz, and J. Mulzer (2001) Synthesis and Acetylcholinesterase Inhibition of 5-Desamino Huperzine A Derivatives. *Bioorg. Med. Chem. Lett.*, **11**: 2627-2630.

109. T. Sunazuka, M. Handa, K. Nagai, T. Shirahata, Y. Harigaya, K. Otoguro, I. Kuwajima, and S. Omura (2002) The First Total Synthesis of Arisugacin A, a Potent, Orally Bioavailable Inhibitor of Acetylcholinesterase. *Org. Lett.*, **4** (3): 367-369.

110. A. Andreani, A. Cavalli, M. Granaiola, M. Guardigli, A. Leoni, A. Locatelli, R. Morigi, M. Rambaldi, M. Recanatini, and A. Roda (2001) Synthesis and Screening for Antiacetylcholinesterase Activity of (1-Benzyl-4-oxopiperidine-3-ylidene)methylindoles and -pyrroles Related to Donepezil. *J. Med. Chem.*, **44**: 4011-4014.

111. H.K. Nair, J. Seravalli, T. Arbuckle, and D.M. Quinn (1994) Molecular Recognition in Acetylcholinesterase Catalysis: Free-Energy Correlations for Substrate Turnover and Inhibition by Trifluoro Ketone Transition-State Analogs. *Biochemistry*, **33** (8566-8576).

112. M. Sentjurc, S. Pecar, J. Stojan, P. Marchot, Z. Radic, and Z. Grubic (1999) Electron paramagnetic resonance reveals altered topography of the active site center gorge of acetylcholinesterase after binding of fasciculin to the peripheral site. *Biochim. Biophys. Acta*, **35856**: 349-358.

113. Z. Yingge, B. Chunli, W. Chen, and Z. Delu (2001) Force Spectroscopy between Acetylcholinesterase and Single Acetylcholinesterase Molecules and the Effects of Inhibitorsand Reactivators Studied by Atomic Force Microscopy. *J. Pharmacol. Exp. Ther.*, **297** (2): 798-803.

114. E. Elhanany, A. Ordentlich, O. Dgany, D. Kaplan, Y. Segall, R. Barak, B. Velan, and A. Shafferman (2001) Resolving Pathways of Interaction of Covalent Inhibitors with the Active Site of Acetylcholinesterases: MALDI-TOF/MS Analysis of Various Nerve Agent Phosphyl Adducts. *Chem. Res. Toxicol.*, **14**: 912-918.

115. G. Kato (1972) A Study by Nuclear Magnetic Resonance of the Acceleration of Acetylcholinesterase by Atropine and Inhibition by Eserine. *Mol. Pharmacol.*, **8**: 582-588.

116. C. Viragh, T.K. Harris, P.M. Reddy, M.A. Massiah, A.S. Mildvan, and I.M. Kovach (2000) NMR Evidence for a Short, Strong Hydrogen Bond at the Active Site of a Cholinesterase. *Biochemistry*, **39** (51): 16200-16205.

117. M.A. Massiah, C. Viragh, P.M. Reddy, I.M. KKKovach, J. Johnson, T.L. Rosenberry, and A.S. Mildvan (2001) Short, Strong Hydrogen Bonds at The Active Site of Human Acetylcholinesterase: Proton NMR Studies. *Biochemistry*, **40** (19): 5682-5690.

118. M. Delfini, R. Gianferri, V. Dubbini, C. Manetti, E. Gaggelli, and G. Valensin (2000) H-1 NMR relaxation investigation of inhibitors interacting with Torpedo californica acetylcholinesterase. *J. Mag. Res.*, **144**: 129-133.

119. Y. Segall, D. Waysbort, D. Barak, N. Ariel, B.P. Doctor, J. Grunwald, and Y. Ashani (1993) Direct Observation and Elucidation of the Structures of Aged and Nonaged Phosphorylated Cholinesterase by ^{31}P NMR Spectroscopy. *Biochemistry*, **32**: 13441-13450.

120. R.J. Linderman, J. Leazer, R.M. Roe, K. Venkatesh, B.S. Selinsky, and R.E. London (1988) ^{19}F-NMR Spectral Evidence That 3-Octylthio-1,1,1-trifluoropropan-2-one, at Potent Inhibitor of Insect Juvenile Hormone Esterase, Functions as a Transition State Analog Inhibitor of Acetylcholinesterase. *Pestic. Biochem. Physiol.*, **31**: 187-194.

121. C. Legay (2000) Why so many forms of acetylcholinesterase? *Micros. Res. Tech.*, **49**: 56-72.

122. J.G. Vontas, N. Cosmidis, M. Loukas, S. Tsakas, M. Jalil Hejazi, A. Ayoutanti, and J. Hemingway (2001) Altered Acetylcholinesterase Confers Organophosphate Resistance in the Olive Fruit Fly Bactrocera oleae. *Pestic. Biochem. Physiol.*, **71**: 124-132.

123. D. Grisaru, M. Sternfield, A. Eldor, D. Glick, and H. Soreq (1999) Structural roles of acetylcholinesterase variants in biology and pathology. *Eur. J. Biochem.*, **264**: 672-686.

124. J. Massoulie, A. Anselmet, S. Bon, E. Krejci, C. Legay, N. Morel, and S. Simon (1999) The polymorphism of acetylcholinesterase: post-translational processing, quaternary associations and localization. *Chem. Biol. Interact.*, **119-120**: 29-42.

125. A.L. Perrier, X. Cousin, N. Boschetti, R. Haas, J.-M. Chatel, S. Bon, W.L. Roberts, S.R. Pickett, J. Massoulié, T.L. Rosenberry, and E. Krejci (2000) Two Distinct Proteins Are Associated with Tetrameric Acetylcholinesterase on the Cell Surface. *J. Biol. Chem.*, **275** (44): 34260-34265.

126. S. Chatterjee and S. Mayor (2001) The GPI-anchor and protein sorting. *Cell Mol. Life Sci.*, **58** (14): 1969-1987.

127. A.H. Futerman, R.-M. Fiorini, E. Roth, M.G. Low, and I. Silman (1984) Physicochemical behaviour and structural characteristics of membrane-bound acetylcholinesterase from *Torpedo* electric organ. *Biochem. J.*, **226**: 369-377.

128. F. Coussen, A. Ayon, A. Le Goff, J. Leroy, J. Massoulie, and S. Bon (2001) Addition of a Glycophosphatidylinositol to Acetylcholinesterase. *J. Biol. Chem.*, **276** (30): 27881-27892.

129. D.R.D. Premkumar, Y. Fukuoka, D. Sevlever, E. Brunschwig, T.L. Rosenberry, M.L. Tykocinski, and M.E. Medof (2001) Properties of Exogenously Added GPI-Anchored Proteins Following Their Incorporation Into Cells. *journal of cellular bJournal of Cellular Biochemistry*, **82**: 234-245.

130. J.L. Sussman, M. Harel, F. Frolow, L. Varon, L. Toker, A.H. Futerman, and I. Silman (1988) Purification and Crystallization of a Dimeric Form of Acetylcholinesterase from Torpedo californica Subsequent to Solubilization with Phosphatidylinositol-specific Phospholipase C. *J. Mol. Biol.*, **203**: 821-823.

131. E. Doss-Pepe, P. Deprez, N.C. Inestrosa, and B. Brodsky (2000) Interaction of Collagen-Like Peptide Models of Asymmetric Acetylcholinesterase with Glycosaminoglycans: Spectroscopic Studies of Conformational Changes and Stability. *Biochemistry*, **39** (48): 14882-14892.

132. J.-R. Gao and K.Y. Zhu (2001) An acetylcholinesterase purified from the greenbug (*Schizaphis graminum*) with some unique enzymological and pharmacological characteristics. *Insect Biochem. Molec. Biol.*, **31**: 1095-1104.

133. K.V. Sharma, C. Koenigsberger, S. Brimijoin, and J.W. Bigbee (2001) Direct evidence for an adhesive function in the noncholinergic role of acetylcholinesterase in neurite outgrowth. *J. Neurosci. Res.*, **63** (2): 165-175.

134. K.P. Das and S. Barone Jr (1999) Neuronal Differentiation in PC12 Cells Is Inhibited by Chlorpyrifos and Its Metabolites: Is Acetylcholinesterase Inhibition the Site of Action? *Toxicol. Appl. Pharmacol.*, **160**: 217-230.

135. R.B. Anderson and B. Key (1999) Role of acetylcholinesterase in the development of axon tracts within the embryonic vertebrate brain. *Int. J. Devl. Neuroscience*, **17** (8): 787-793.

136. G.V. De Ferrari, M.A. Canales, I. Shin, L.M. Weiner, I. Silman, and N.C. Inestrosa (2001) A Structural Motif of Acetylcholinesterase That Promotes Amyloid B-Peptide Fibril Formation. *Biochemistry*, **40** (35): 10447-10457.

137. N.C. Inestrosa, A. Alvarez, C.A. Perez, R.D. Moreno, M. Vicente, C. Linker, O.I. Casanueva, C. Soto, and J. Garrido (1996) Acetylcholinesterase Accelerates Assembly of Amyloid-B-Peptides into Alzheimer's Fibrils: Possible Role of the Peripheral Site of the Enzyme. *Neuron*, **16**: 881-891.

138. W.G. Lewis, L.G. Green, F. Grynszpan, Z. Radic, P.R. Carlier, P. Taylor, M.G. Finn, and K.B. Sharples (2002) Click Chemistry In Situ: Acetylcholinesterase as a Reaction

Vessel for the Selective Assembly of a Femtomolar Inhibitor from an Array of Building Blocks. *Angew. Chem. Int. Edit.*, **41** (6): 1053-1057.

139. Y. Boublik, P. Saint-Aguet, A. Lougarre, M. Arnaud, F. Villatte, S. Estrada-Mondaca, and D. Fournier (2002) Acetylcholinesterase engineering for detection of insecticide residues. *Protein Eng.*, **15** (1): 43-50.

140. F. Cuevas, S. Di Stefano, J.O. Magrans, P. Prados, L. Mandolini, and J. de Mendoza (2000) Toward and Artificial Acetylcholinesterase. *Chem. Eur. J.*, **6** (17): 3228-3234.

141. M. Eddleston, L. Szinicz, P. Eyer, and N. Buckley (2002) Oximes in acute organophosphorus pesticide poisoning: a systematic review of clinical trials. *Q. J. Med.*, **95**: 275-283.

142. T.G. Beach, Y.-M. Kuo, C. Schwab, D.G. Walker, and A.E. Roher (2001) Reduction of cortical amyloid B levels in guinea pig brain after systemic administration of physostigmine. *Neurosci. Lett.*, **310**: 21-24.

143. M. Dooley and H.M. Lamb (2000) Donepezil - A review of its use in Alzheimer's disease. *Drugs Aging*, **16** (3): 199-226.

144. L.K. Unni (1998) Beyond Tacrine: Recently Developed Cholinesterase Inhibitors for the Treatment of Alzheimer's Disease. *CNS Drugs*, **10** (6): 447-460.

145. B.M. McGleenon, K.B. Dynan and A.P. Passmore (1999) Acetylcholinesterase inhibitors in Alzheimer's disease. *Br. J. Clin. Pharmacol.*, **48** (4): 471-480.

146. R. Wang, H.Y. Zhang and X.C. Tang (2001) Huperzine A attenuates cognitive dysfunction and neuronal degeneration caused by B-amyloid protein-(1-40) in rat. *Eur. J. Pharmacol.*, **421** (3): 149-156.

147. X.Q. Xiao, R. Wang and X.C. Tang (2000) Huperzine A and tacrine attenuate -amyloid peptide-induced oxidative injury. *J. Neurosci. Res.*, **61** (5): 564-569.

148. X.Q. Xiao, N.T.-K. Lee, P.R. Carlier, Y.-P. Pang, and Y.F. Han (2000) *Bis*(7)-tacrine, a promising anti-Alzheimer's agent, reduces hydrogen peroxide-induced injury in rat pheochromocytoma cells: comparison with tacrine. *Neurosci. Lett.*, **290** (3): 197-200.

149. P.G. Richards, M.K. Johnson and D.E. Ray (2000) Identification of Acylpeptide Hydrolase as a Sensitive Site for Reaction with Organophosphorus Compounds and a Potential Target for Cognitive Enhancing Drugs. *Mol. Pharmacol.*, **58** (3): 577-583.

150. E.G. Duysen, B. Li, W. Xie, L.M. Schopfer, R.S. Anderson, C.A. Broomfield, and O. Lockridge (2001) Evidence for Nonacetylcholinesterase Targets of Organophosphorus Nerve Agent: Supersensitivity of Acetylcholinesterase Knockout Mouse to VX Lethality. *J. Pharmacol. Exp. Ther.*, **299** (2): 528-535.

151. J.N.S. Evans, *Biomolecular NMR Spectroscopy*. 1995, Oxford: Oxford University Press.

152. R.R. Ernst, G. Bodenhausen and A. Wokaun, *Principles of nuclear magnetic resonance in one and two dimensions*. 1989: Oxford Science Publications.

153. E.R. Andrew, A. Bradbury and R.G. Eades (1958) Nuclear Magnetic Resonance Spectra from a Crystal rotated at High Speed. *Nature*, **182**: 1659.

154. I.J. Lowe (1959) Free Induction Decays of Rotating Solids. *Phys. Rev. Lett.*, **2** (7): 285-287.

155. M.M. Maricq and J.S. Waugh (1979) NMR in rotating solids. *J. Chem. Phys.*, **70** (7): 3300-3316.

156. A. Pines, M.G. Gibby and J.S. Waugh (1973) Proton-enhanced NMR of dilute spins in solids. *J. Chem. Phys.*, **59** (2): 569-590.

157. S.R. Hartmann and E.L. Hahn (1962) Nuclear Double Resonance in the Rotating Frame. *Phys. Rev.*, **128** (5): 2042-2053.

158. E.O. Stejskal, J. Schaefer and J.S. Waugh (1977) Magic-Angle Spinning and Polarization Transfer in Proton-Enhanced NMR. *J. Mag. Res.*, **28**: 105-112.

159. G. Metz, X. Wu and S.O. Smith (1994) Ramped-Amplitude Cross Polarization in Magic-Angle-Spinning NMR. *J. Magn. Reson. A*, **110**: 219-227.

160. O.B. Peersen and S.O. Smith (1993) Rotational Resonance NMR of Biological Membranes. *Concepts Mag. Res.*, **5**: 303-317.

161. S. Hediger, B.H. Meier and R.R. Ernst (1995) Rotor-synchronized amplitude-modulated nuclear magnetic resonace spin-lock sequences for improved cross polarization under fast magic angle sample spinning. *J. Chem. Phys.*, **102** (10): 4000-4011.

162. A.E. Bennett, C.M. Rienstra, M. Auger, K.V. Lakshmi, and R.G. Griffin (1995) Heteronuclear decoupling in rotating solids. *J. Chem. Phys.*, **103** (16): 6951-6958.

163. B.M. Fung, A.K. Khitrin and K. Ermolaev (2000) An Improved Broadband Decoupling Sequence for Liquid Crystals and Solids. *J. Mag. Res.*, **142**: 97-101.

164. M. Lee and W.I. Goldburg (1965) Nuclear-Magnetic-Resonance Line Narrowing by a Rotating rf Field. *Phys. Rev.*, **140** (4A): 1261-1271.

165. M. Ahmad, M.I. Arif, Z. Ahmad, and I. Denholm (2002) Cotton whitefly (*Bemisia tabaci*) restance to organophosphate and pyrethroid insecticides in Pakistan. *Pest. Manag. Sci.*, **58**: 203-208.

166. S.B. Walsh, T.A. Dolden, G.D. Moores, M. Kristensen, T. Lewis, A.L. Devonshire, and M.S. Williamson (2001) Identification and characterization of mutations in housefly (*Musca domestica*) acetylcholinesterase involved in insecticide resistance. *Biochem. J.*, **359**: 175-181.

167. A. Moretto and M. Lotti (1998) Poisoning by organophosphorus insecticides and sensory neuropathy. *J. Neurol. Neurosurg. Psychiatry*, **64**: 463-468.

168. Y. Wei and A.E. McDermott, *Effects of Hydrogen Bonding on 1H Chemical Shifts*, in *Modeling NMR chemical shifts: gaining insights into structure and environment*, J.C. Facelli and A.C. de Dios, Editors. 1999, American Chemical Society: Washington. p. 177-193.

169. K. Pervushin, R. Riek, G. Wider, and K. Wüthrich (1997) Attenuated T2 relaxation by mutual cancellation of dipole-dipole coupling and chemical shift anisotropy indicates an avenue to NMR structures of very large biological macromolecules in solution. *Proc. Natl. Acad. Sci. USA*, **94**: 12366-12371.

170. M.J.S. Kelly, L.J. Ball, C. Krieger, Y. Yu, M. Fischer, S. Schiffmann, P. Schmieder, R. Kühne, W. Bermel, A. Bacher, G. Richter, and H. Oschkinat (2001) The NMR structure of the 47-kDa dimeric enzyme 3,4-dihydroxy-2-butanone-4-phosphate synthase and ligand binding studies reveal the location of the active site. *Proc. Natl. Acad. Sci. USA*, **98**: 13025-13030.

171. G. Grobner, I.J. Burnett, C. Glaubitz, G. Choi, A.J. Mason, and A. Watts (2000) Observations of light-induced structural changes of retinal within rhodopsin. *Nature*, **405**: 810-813.

172. Y. Kim, K. Valentine, S.J. Opella, S.L. Schendel, and W.A. Cramer (1998) Solid-state NMR studies of the membrane-bound closed state of the colicin E1 channel domain in lipid bilayers. *Protein Sci.*, **7**: 342-348.

173. D. Huster, L. Xiao and M. Hong (2001) Solid-State NMR Investigation of the Dynamics of the Soluble and Membrane-Bound Colicin Ia Channel-Forming Domain. *Biochemistry*, **40**: 7662-7674.

174. S. Rozovsky and A.E. McDermott (2001) The Time scale of the Catalytic Loop Motion on Triosphosphate Isomerase. *J. Mol. Biol.*, **310** (1): 259-270.

175. J.D. van Beek, L. Beaulieu, H. Schafer, M. Demura, T. Asakura, and B.H. Meier (2000) Solid-state NMR determination of the secondary structure of Samia cynthia ricini silk. *Nature*, **405**: 1077-1079.

176. C. Guillou, A. Mary, D. Zafiarisoa, E. Gras, and C. Thal (2000) Potent acetylcholinesterase inhibitors: Design, synthesis and structure-activity relationships of alkylene linked bis-galanthamine and galanthamine-galanthaminium salts. *Bioorg. Med. Chem. Lett.*, **10**: 637-639.

177. J.J. Harrison, J.P. Pellegrini and C.M. Selwitz (1981) Bromination of Deactivated Aromatics Using Potassium Bromate. *J. Org. Chem.*, **46**: 2169-2171.

178. L.M. Harwood and C.J. Moody, *Experimental Organic Chemistry: Principles and Practice*. 1st ed. 1989: Blackwell Scientific.

179. G.L. Ellman, K.D. Courtney, V. Andres Jr., and R.M. Featherstone (1961) A New and Rapid Colorimetric Determination of Acetylcholinesterase Activity. *Biochem. Pharmacol.*, **7**: 88-95.

180. D. Voet, J.G. Voet and C.W. Pratt, *Fundamentals of Biochemistry*. 1999: John Wiley and Sons.

181. S. Schwarzinger, G.J.A. Kroon, T.R. Foss, J. Chung, P.E. Wright, and H.J. Dyson (2001) Sequence-Dependent Correction of Random Coil NMR Chemical Shifts. *J. Am. Chem. Soc.*, **123**: 2970-2978.

182. D.S. Wishart, B.D. Sykes and F.M. Richards (1992) The Chemical Shift Index: A Fast and Simple Method for the Assignment of Protein Secondary Structure through NMR Spectroscopy. *Biochemistry*, **31**: 1647-1651.

183. S. Spera and A. Bax (1991) Empirical Correlation between Protein Backbone Conformation and C-alpha and C-beta ^{13}C Nulcear Magnetic Resonance Shifts. *J. Am. Chem. Soc.*, **113**: 5490-5492.

184. G. Cornilescu, F. Delaglio and A. Bax (1999) Protein backbone angle restraints from searching a database for chemical shift and sequence homology. *J. Biomol. NMR*, **13**: 289-302.

185. P.J.R. Spooner, J.M. Sharples, M.A. Verhoeven, J. Lugtenburg, C. Glaubitz, and A. Watts (2002) Relative Orientation between the -Ionone Ring and the Polyene Chain for the Chromophore of Rhodopsin in Native Membranes. *Biochemistry*, **41** (24): 7549-7555.

186. J. Herzfeld and A.E. Berger (1980) Sideband intensities in NMR spectra of samples spinning at the magic angle. *J. Chem. Phys.*, **73** (12): 6021-6030.

187. O.N. Antzutkin, S.C. Shekar and M.H. Levitt (1995) Two-Dimensional Sideband Separation in Magic-Angle-Spinning NMR. *J. Mag. Res.*, **115** (1): 7-19.

188. M.H. Levitt, *Symmetry-Based Sequences in Magic-Angle Spinning Solid-State NMR*, in *Encyclopedia of Nuclear Magnetic Resonance*, 9: Advances in NMR, D.M. Grant and R.K. Harris, Editors. 2002, John Wiley & Sons Ltd: Chichester.

189. A. Brinkmann, M. Carravetta, X. Zhao, M. Eden, J. Schmedt auf der Gunne, and M.H. Levitt, *Using symmetry to design pulse sequences in solid-state NMR*, in *Perspectives on Solid State NMR in Biology*, S. Kiihne and H.J.M. de Groot, Editors. 2001, Kluwer: Dordrecht.

190. D.L. Beveridge, *Approximate Molecular Orbital Theory of Nuclear and Electron Magnetic Resonance Parameters*, in *Semi-empirical Methods of Electronic Structure Calculations*, B: Applications, G.A. Segal, Editor. 1977, Plenum Press: New York.

191. M. Hohwy, H.J. Jakobsen, M. Eden, M.H. Levitt, and N.C. Nielsen (1998) Broadband dipolar recoupling in the nuclear magnetic resonance of rotating solids: A compensated C7 pulse sequence. *J. Chem. Phys.*, **108** (7): 2686-2694.

192. Y.K. Lee, N.D. Kurur, M. Helmle, O.G. Johannessen, N.C. Nielsen, and M.H. Levitt (1995) Efficient dipolar recoupling in the NMR of rotating solids. A sevenfold symmetric radiofrequency pulse sequence. *Chem. Phys. Letters*, **242**: 304-309.

193. L.M. McDowell and J. Schaefer (1996) High-resolution NMR of biological solids. *Curr. Opin. Struct. Biol.*, **6**: 624-629.

194. R.G. Griffin (1998) Dipolar recoupling in MAS spectra of biological solids. *Nature Struct. Biol.*: 508-512.

195. R. Tycko and G. Dabbagh (1990) Measurement of nuclear magnetic dipole-dipole couplings in magic angle spinning NMR. *Chem. Phys. Letters*, **173**: 461-465.

196. A.E. Bennett, J.H. Ok, R.G. Griffin, and S. Vega (1992) Chemical shift correlation spectroscopy in rotating solids: Radio frequency-driven dipolar recoupling and longitudinal exchange. *J. Chem. Phys.*, **96** (11): 8624-8627.

197. O. Weintraub, S. Vega, C. Hoelger, and H.H. Limbach (1994) Distance Measurements between Homonuclear Spins in Rotating Solids. *J. Magn. Reson. A*, **109**: 14-25.

198. T. Gullion and S. Vega (1992) A simple magic angle spinning NMR experiment for the dephasing of rotational echoes of dipolar coupled homonuclear spin pairs. *Chem. Phys. Letters*, **194** (4-6): 423-428.

199. B.-Q. Sun, P.R. Costa, D. Kocisko, P.T. Lansbury Jr., and R.G. Griffin (1995) Internuclear distance measurements in solid state nuclear magnetic resonance: Dipolar recoupling via rotor synchronized spin locking. *J. Chem. Phys.*, **102** (2): 702-707.

200. W. Zhu, C.A. Klug and J. Schaefer (1994) Measurement of Dipolar Coupling Within Isolated Spin-½ Homonuclear Pairs by CEDRA NMR. *J. Magn. Reson. A*, **108**: 121-123.

201. M. Baldus, M. Tomaselli, B.H. Meier, and R.R. Ernst (1994) Broadband polarization-transfer experiments for rotating solids. *Chem. Phys. Letters*, **230**: 329-336.

202. D.M. Gregory, D.J. Mitchell, J.A. Stringer, S. Kiihne, J.C. Shiels, J. Callahan, M.A. Mehta, and G.P. Drobny (1995) Windowless dipolar recoupling: the detection of weak dipolar couplings between spin nuclei with large chemical shift anisotropies. *Chem. Phys. Letters*, **246** (6): 654-663.

203. G.J. Boender, J. Raap, S. Prytulla, H. Oschkinat, and H.J.M. de Groot (1995) MAS NMR structure refinement of uniformly 13C enriched chlorophyll a/water aggregates with 2D dipolar correlation spectroscopy. *Chem. Phys. Letters*, **237**: 502-508.

204. D.P. Weliky, A.E. Bennett, A. Zvi, J. Anglister, P.J. Steinbach, and R. Tycko (1999) Solid-state NMR evidence for an antibody-dependent conformation of the V3 loop of HIV-1 gp120. *Nature Struct. Biol.*, **6** (2): 141-145.

205. A.E. Bennett, C.M. Rienstra, J.M. Griffiths, W. Zhen, P.T. Lansbury Jr., and R.G. Griffin (1998) Homonuclear radio frequency-driven recoupling in rotating solids. *J. Chem. Phys.*, **108** (22): 9463-9479.

206. G. Goobes and S. Vega (2002) MAS NMR structure refinement of uniformly 13C enriched chlorophyll a/water aggregates with 2D dipolar correlation spectroscopy. *J. Mag. Res.*, **154** (2): 236-251.

207. N.C. Nielsen, H. Bildsoe, H.J. Jakobsen, and M.H. Levitt (1994) Double-quantum homonuclear rotary resonance: Efficient dipolar recovery in magic-angle spinning nuclear magnetic resonance. *J. Chem. Phys.*, **101** (3): 1805-1812.

208. R. Verel, M. Baldus, M. Ernst, and B.H. Meier (1998) A homonuclear spin-pair filter for solid-state NMR based on adiabatic-passage techniques. *Chem. Phys. Letters*, **287**: 421-428.

209. M. Hohwy, C.M. Rienstra, C.P. Jaroniec, and R.G. Griffin (1999) Fivefold symmetric homonuclear dipolar recoupling in rotating solids: Application to double quantum spectroscopy. *J. Chem. Phys.*, **110** (16): 7983-7992.

210. A. Brinkmann, M. Eden and M.H. Levitt (2000) Synchronous helical pulse sequences in magic-angle spinning nuclear magnetic resonance: Double quantum recoupling of multiple-spin systems. *J. Chem. Phys.*, **112** (19): 8539-8554.

211. P. Hodgkinson and L. Emsley (1999) The Accuracy of Distance Measurements in Solid-State NMR. *J. Mag. Res.*, **139**: 46-59.

212. E.R. Andrew, A. Bradbury, R.G. Eades, and V.T. Wynn (1963) Nuclear Cross-Relaxation Induced by Specimen Rotation. *Phys Lett*, **4** (2): 99-100.

213. E.R. Andrew, S. Clough, L.F. Farnell, T.D. Gledhill, and I. Roberts (1966) Resonant Rotational Broadening of Nuclear Magnetic Resonance Spectra. *Phys Lett*, **21** (5): 505-506.

214. D.P. Raleigh, M.H. Levitt and R.G. Griffin (1988) Rotational Resonance in Solid State NMR. *Chem. Phys. Letters*, **146**: 71-76.

215. P.J.E. Verdegem, M. Helmle, J. Lugtenburg, and H.J.M. de Groot (1997) Internuclear Distance Measurements up to 0.44 nm for Retinals in the Solid State with 1-D Rotational Resonance 13C MAS NMR Spectroscopy. *J. Am. Chem. Soc.*, **119**: 169-174.

216. P.J.E. Verdegem, P.H.M. Bovee-Geurts, W.J. de Grip, J. Lugtenburg, and H.J.M. de Groot (1999) Retinylidene Ligand Structure in Bovine Rhodopsin, Metarhodopsin-I, and 10-Methylrhodopsin from Internuclear Distance Measurements Using ^{13}C-Labeling and 1-D Rotational Resonance MAS NMR. *Biochemistry*, **38** (35): 11316-11324.

217. F. Creuzet, A.E. McDermott, R. Gebhard, K. van der Hoef, M.B. Spijker-Assink, J. Herzfeld, J. Lugtenburg, M.H. Levitt, and R.G. Griffin (1991) Determination of Membrane Protein Structure by Rotational Resonance NMR: Bacteriorhodopsin. *Science*, **251**: 783-786.

218. J. Heller, R. Larsen, M. Ernst, A.C. Kolbert, M. Baldwin, S.B. Prusiner, D.E. Wemmer, and A. Pines (1996) Application of rotational resonance to inhomogeneously broadened systems. *Chem. Phys. Letters*, **251**: 223-229.

219. P.R. Costa, B. Sun and R.G. Griffin (1997) Rotational Resonance Tickling: Accurate Internuclear Distance Measurements in Solids. *J. Am. Chem. Soc.*, **119**: 10821-10830.

220. T. Karlsson and M.H. Levitt (1998) Longitudinal rotational resonance echoes in solid state nuclear magnetic resonance: Investigation of zero quantum spin dynamics. *J. Chem. Phys.*, **109** (13): 5493-5507.

221. S.O. Smith and O.B. Peersen (1992) Solid-State NMR Approaches for Studying Membrane Protein Structure. *Annu. Rev. Biophys. Bio.*, **21**: 25-47.

222. J. Heller, A.C. Kolbert, R. Larsen, M. Ernst, T. Bekker, M. Baldwin, S.B. Prusiner, A. Pines, and D.E. Wemmer (1996) Solid-state NMR studies of the prion protein H1 fragment. *Protein Sci.*, **5**: 1655-1661.

223. D.A. Middleton, R. Robins, X. Feng, M.H. Levitt, I.D. Spiers, C.H. Schwalbe, D.G. Reid, and A. Watts (1997) The conformation of an inhibitor bound to the gastric proton pump. *FEBS Lett.*, **410**: 269-274.

224. Y.S. Balazs and L.K. Thompson (1999) Practical Methods for Solid-State NMR Distance Measurements on Large Biomolecules: Constant-Time Rotational Resonance. *J. Mag. Res.*, **139**: 371-376.

225. K. Takegoshi, K. Nomura and T. Terao (1995) Rotational resonance in the tilted rotating frame. *Chem. Phys. Letters*, **232**: 424-428.

226. T. Terao (1998) Structural measurements by solid-state NMR. *J. Mol. Struct.*, **441**: 283-294.

227. K. Takegoshi, K. Nomura and T. Terao (1997) Selective Homonuclear Polarization Transfer in the Tilted Rotating Frame under Magic Angle Spinning in Solids. *J. Mag. Res.*, **127**: 206-216.

228. K. Nomura, K. Takegoshi, T. Terao, K. Uchida, and M. Kainosho (1999) Determination of the Complete Structure of a Uniformly Labeled Molecule by Rotational Resonance Solid-State NMR in the Tilted Rotating Frame. *J. Am. Chem. Soc.*, **121**: 4064-4065.

229. T. Karlsson, C.E. Hughes, J. Schmedt auf der Günne, and M.H. Levitt (2001) Double-Quantum Excitation in the NMR of Spinning Solids by Pulse-Assisted Rotational Resonance. *J. Mag. Res.*, **148**: 238-247.

230. T. Karlsson, M. Edén, H. Luthman, and M.H. Levitt (2000) Efficient Double-Quantum Excitation in Rotational Resonance NMR. *J. Mag. Res.*, **145**: 95-107.

231. S. Dusold and A. Sebald (2000) Double-Quantum Filtration under Rotational-Resonance Conditions: Numerical Simulations and Experimental Results. *J. Mag. Res.*, **145**: 340-356.

232. M.H. Levitt, D.P. Raleigh, F. Creuzet, and R.G. Griffin (1990) Theory and simulations of homonuclear spin pair systems in rotating solids. *J. Chem. Phys.*, **92** (11): 6347-6364.

233. T. Karlsson, A. Brinkmann, P.J.E. Verdegem, J. Lugtenburg, and M.H. Levitt (1999) Multiple-quantum relaxation in the magic-angle-spinning NMR of 13C spin pairs. *Solid State NMR*, **14** (1): 43-58.

234. T. Karlsson, M. Helmle, N.D. Kurur, and M.H. Levitt (1995) Rotational Resonance echoes in the nuclear magnetic resonance of spinning solids. *Chem. Phys. Letters*, **247**: 534-540.

235. E.L. Hahn (1950) Spin echoes. *Phys. Rev.*, **80**: 580-594.

236. C. Glaubitz, *Magic Angle Sample Spinning NMR Spectroscopy on Biomembranes*, Ph.D. thesis, University of Oxford, 1998.

237. G. Albrecht and R.B. Corey (1939) The Crystal Structure of Glycine. *J. Am. Chem. Soc.*, **61**: 1087-1103.

238. P.-G. Jonsson and A. Kvick (1972) Precision neutron diffraction structure determination of protein and nucleic acid components. III. The crystal and molecular structure of the amino acid -glycine. *Acta. Cryst. B*, **28**: 1827-1833.

239. R.A. Haberkorn, R.E. Stark, H. van Willigen, and R.G. Griffin (1981) Determination of bond distances and bond angles by solid-state nuclear magnetic resonance. Carbon-13 and nitrogen-14 NMR study of glycine. *J. Am. Chem. Soc.*, **103** (10): 2534-2539.

240. P.T.F. Williamson, A. Verhoeven, M. Ernst, and B.H. Meier (2003) Determination of Internuclear Distances in Uniformly Labeled Molecules by Rotational-Resonance Solid-State NMR. *J. Am. Chem. Soc.*, (in press).

241. J.R. Sachleben, V. Frydman and L. Frydman (1996) Dipolar Determinations in Solids by Relaxation-Assisted NMR Recoupling. *J. Am. Chem. Soc.*, **118**: 9786-9787.

242. K. Saalwachter and K. Schmidt-Rohr (2000) Relaxation-Induced Dipolar Exchange with Recoupling - An MAS NMR Method for Determining Heteronuclear Distances without Irradiating the Second Spin. *J. Mag. Res.*, **145**: 161-172.

243. B.-J. van Rossum, C.P. de Groot, V. Ladizhansky, S. Vega, and H.J.M. de Groot (2000) A Method for Measuring Heteronuclear (^{1}H-^{13}C) Distances in High Speed MAS NMR. *J. Am. Chem. Soc.*, **122**: 3465-3472.

244. R. Fu, S.A. Smith and G. Bodenhausen (1997) Recoupling of heteronuclear dipolar interactions in solid state magic-angle spinning NMR by simultaneous frequency and amplitdue modulation. *Chem. Phys. Letters*, **272**: 361-369.

245. K. Nishimura, R. Fu and T.A. Cross (2001) The Effect of RF Inhomogeneity on Heteronuclear Dipolar Recoupling in Solid State NMR: Practical Performance of SFAM and REDOR. *J. Mag. Res.*, **152**: 227-233.

246. T. Guillon and J. Schaefer (1989) Rotational-Echo Double-Resonance NMR. *J. Mag. Res.*, **81**: 196-200.

247. T. Guillon (1998) Introduction to Rotational-Echo Double Resonance NMR. *Concepts Mag. Res.*, **10** (5): 277-289.

248. T. Kameda, Y. Nakazawa, J. Kazuhara, T. Yamane, and T. Asakura (2002) Determination of intermolecular distance for a model peptide of Bombyx mori silk fibroin, GAGAG, with rotational echo double resonance. *Biopolymers*, **64**: 80-85.

249. R.D. O'Connor, B. Poliks, D.H. Bolton, J.M. Goetz, J.A. Byers, K.L. Wooley, and J. Schaefer (2002) Chain Packing in Linear Phenol-Polycarbonate by ^{13}C{^{2}H} REDOR. *Macromolecules*, **35** (7): 2608-2617.

250. L. Kaustov, S. Kababya, S. Du, T. Baasov, S. Gropper, Y. Shoham, and A. Schmidt (2000) Direct Identification of Enzyme Active Site Residues by Solid-State REDOR NMR: Application to KDO8P Synthase. *J. Am. Chem. Soc.*, **122**: 2649-2650.

251. J.M. Goetz, B. Poliks, D.R. Studelska, M. Fischer, K. Kugelbrey, A. Bacher, M. Cushman, and J. Schaefer (1999) Investigation of the Binding of Fluorolumazines to the 1-MDa Capsid of Lumazine Synthases by $^{15}N\{^{19}F\}$ REDOR NMR. *J. Am. Chem. Soc.*, **121**: 7500-7508.

252. S.J. Kim, L. Cegelski, D.R. Studelska, R.D. O'Connor, A.K. Mehta, and J. Schaefer (2002) Rotational-Echo Double Resonance Characterization of Vancomycin Binding Sites in *Staphylococcus aureus*. *J. Am. Chem. Soc.*, **41**: 6967-6977.

253. J.A. Watts, A. Watts and D.A. Middleton (2001) A Model of Reversible Inhibitors in the Gastric H+/K+-ATPase Binding Site Determined by Rotational Echo Double Resonance NMR. *J. Biol. Chem.*, **276** (46): 43197-43204.

254. E.B. Brouwer, R.D.M. Gougeon, J. Hirschinger, K.A. Udachin, R.K. Harris, and J.A. Ripmeester (1999) Internuclear distance measurements in supramolecular solids: 13C-19F REDOR NMR spectroscopy of p-tert-butylcalix[4]arene-flurobenzene. *Phys. Chem. Chem. Phys.*, **1**: 4043-4050.

255. L.M. McDowell, S.M. Holl, S.-j. Qian, E. Li, and J. Schaefer (1993) Inter-Tryptophan Distances in Rat Cellular Retinol Binding Protein II by Solid-State NMR. *Biochemistry*, **32**: 4560-4563.

256. G. Tong and J. Schaefer (1997) Characterisation of the Interface of Heterogeneous Blends of Polycarbonate and Polyfluorostyrene by ^{13}C-^{19}F REDOR NMR. *Macromolecules*, **30**: 7522-7528.

257. P.-K. Wang and C.P. Slichter (1984) NMR Study of the Structure of Simple Molecules Adsorbed on Metal Surfaces: C_2H_2 on Pt. *Phys. Rev. Lett.*, **53** (1): 82-85.

258. D.J. Mitchell and J.N.S. Evans (1998) Improved heteronuclear decoupling in REDOR with the use of TPPM. *Chem. Phys. Letters*, **292**: 656-660.

259. A.K. Mehta, D.J. Hirsh, N. Oyler, G.P. Drobny, and J. Schaefer (2000) Carbon-Proton Dipolar Decoupling in REDOR. *J. Mag. Res.*, **145**: 158-158.

260. J.R. Garbow and T. Guillon (1991) Improvements in REDOR NMR Spectroscopy. Minimising Resonance-Offset Effects. *J. Mag. Res.*, **95**: 442-445.

261. B. Heise, J. Leppert and R. Ramachandran (2000) REDOR with Adiabatic Dephasing Pulses. *J. Mag. Res.*, **146**: 181-187.

262. J.M. Goetz and J. Schaefer (1997) REDOR Dephasing by Multiple Spins in the Presence of Molecular Motion. *J. Mag. Res.*, **127**: 147-154.

263. T. Guillon and C.H. Pennington (1998) Theta-REDOR: an MAS NMR method to simplify multiple coupled heteronuclear spin systems. *Chem. Phys. Letters*, **290**: 88-93.

264. O. Liivak and D.B. Zax (2000) Multiple simultaneous distance determinations: Application of rotational echo double resonance nuclear magnetic resonance to IS_2 spin networks. *J. Chem. Phys.*, **113** (3): 1088-1096.

265. C.P. Jaroniec, B.A. Tounge, J. Herzfeld, and R.G. Griffin (2001) Frequency Selective Heteronuclear Dipolar Recoupling in Rotating Solids: Accurate ^{13}C-^{15}N Distance Measurements in Uniformly ^{13}C, ^{15}N-labeled Peptides. *J. Am. Chem. Soc.*, **123**: 3507-3519.

266. F.G. Vogt, S.M. Mattingly, J.M. Gibson, and K.T. Mueller (2000) Measurement of Internuclear Distances in Solid-State NMR by a Background-Filtered REDOR Experiment. *J. Mag. Res.*, **147**: 26-35.

267. A.W. Hing, S. Vega and J. Schaefer (1992) Transferred-Echo Double-Resonance NMR. *J. Mag. Res.*, **96**: 205-209.

268. T. Guillon (1995) Measurment of diplolar interactions between spin-1/2 and quadrupolar nuclei by rotational-echo, adiabatic-passage, double-resonance NMR. *Chem. Phys. Letters*, **246**: 325-330.

269. M. Bak, J.T. Rasmussen and N.C. Nielsen (2000) SIMPSON: A General Simulation Program for Solid-State NMR Spectroscopy. *J. Mag. Res.*, **147** (2): 296-330.

270. C.P. Jaroniec, B.A. Tounge, C.M. Rienstra, J. Herzfeld, and R.G. Griffin (2000) Recoupling of Heteronuclear Dipolar Interactions with Rotational-Echo Double-Resonance at High Magic-Angle Spinning Frequencies. *J. Mag. Res.*, **146**: 132-139.

271. H.Y. Carr and E.M. Purcell (1954) Effects of Diffusion on Free Precession in Nuclear Magnetic Resonance Experiments. *Phys. Rev.*, **94** (3): 630-638.

272. D.M.F. van Aalten, R. Bywater, J.B.C. Findlay, M. Hendlich, R.W.W. Hooft, and G. Vriend (1996) PRODRG, a program for generating molecular topologies and unique molecular descriptors from coordinates of small molecules. *J. Comput. Aid. Mol. Des.*, **10**: 255-262.

273. D.E. Moore and G.P. Hess (1975) Acetylcholinesterase-Catalysed Hydrolysis of an Amide. *Biochemistry*, **14** (11): 2386-2389.

APPENDICES

Appendix 1

Acetylcholinesterase Publications

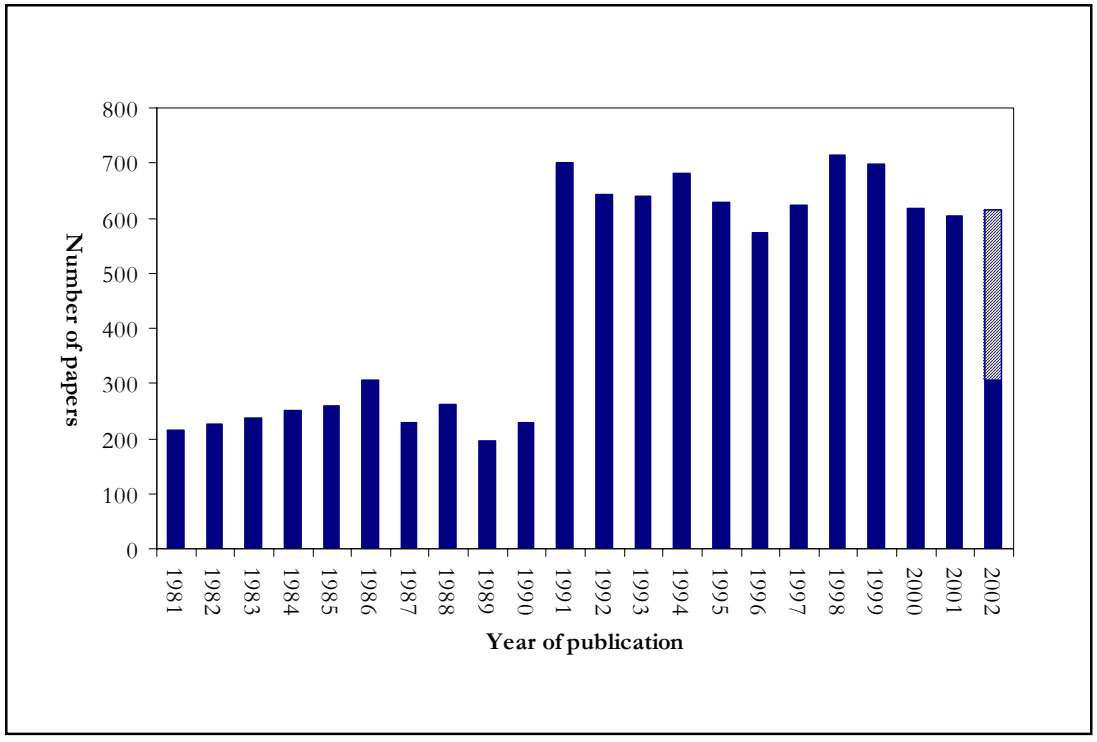

Figure A1.1 – Acetylcholinesterase publications: based on Science Citation Index search results for the term 'acetylcholinesterase' in article titles, keywords or abstracts. The first x-ray structure was published in 1991. Data for 2002 is based on an extrapolation of the number of publications during the first six months of the year.

Appendix 2

Published Acetylcholinesterase Structures

Table A2.1 – Summary of published acetylcholinesterase structures (Brookhaven Protein Data Bank, August 2002). Associated publications listed are those given in the Data Bank as the primary citation(s), if listed.

Esterase source	Comment	Technique	Associated publication	PDB code	Date
Drosophila melanogaster	-	x-ray (2.70 Å)	[38]	1QO9	1999
Drosophila melanogaster	9-(3-iodobenzylamino)-1,2,3,4-tetrahydroacridine complex	x-ray (2.72 Å)	[38]	1QON	1999
Drosophila melanogaster	9-(3-phenylmethylamino)-1,2,3,4-tetrahydroacridine complex	x-ray (2.70 Å)	[38]	1DX4	1999
Electophorus electricus	Single chain	x-ray (4.50 Å)	[34]	1C2B	1999
Electophorus electricus	Tetramer	x-ray (4.20 Å)	[34]	1C2O	1999
Electophorus electricus	-	x-ray (4.50 Å)	-	1EEA	1999
Human	Fasciculin-II complex	x-ray (2.76 Å)	[23]	1B41	1999
Human	Fasciculin-II complex with E202Q mutant	x-ray (2.90 Å)	[23]	1F8U	2000
Mus muculus	-	x-ray (2.90 Å)	[33]	1MAA	1998
Mus muculus	Fasciculin-II complex	x-ray (2.90 Å)	[28]	1MAH	1995
Torpedo californica	Radiation induced damage over nine time points	x-ray (2.1-3.0 Å)	[45]	1QID-1QIM	1999
Torpedo californica	-	x-ray (2.80 Å)	[31]	1ACE	1991
Torpedo californica	-	x-ray (2.50 Å)	[24]	2ACE	1996
Torpedo californica	-	x-ray (1.80 Å)	-	1EA5	2000
Torpedo californica	Bw284C51 complex	x-ray (2.85 Å)	-	1E3Q	2000
Torpedo californica	Decamethonium complex	x-ray (2.80 Å)	[30]	1ACL	1993
Torpedo californica	Diisopropyl-phosphoro-fluoridate	x-ray (2.30 Å)	[32]	2DFP	1998

Esterase source	Comment	Technique	Associated publication	PDB code	Date
Torpedo californica	3-[(1S)-1-(dimethylamino)ethyl]phenol complex	x-ray (3.00 Å)	[46]	1GQS	2001
Torpedo californica	E2020 (Aricept/Donepezil) complex	x-ray (2.50 Å)	[36, 40]	1EVE	1998
Torpedo californica	Edrophonium complex	x-ray (2.80 Å)	[37]	1AX9	1997
Torpedo californica	Edrophonium complex	x-ray (2.40 Å)	[37]	2ACK	1997
Torpedo californica	Fasciculin-II complex	x-ray (3.00 Å)	[26]	1FSS	1995
Torpedo californica	Galanthamine complex	x-ray (2.50 Å)	[42]	1QTI	1999
Torpedo californica	Galanthamine complex	x-ray (2.30 Å)	[41]	1DX6	1999
Torpedo californica	(-)-Huperzine-A complex	x-ray (2.50 Å)	[24]	1VOT	1996
Torpedo californica	Huprine-X complex	x-ray (2.10 Å)	[47]	1E66	2000
Torpedo californica	PEG-SH complex	x-ray (2.30 Å)	[44]	1JJB	2001
Torpedo californica	R404435 complex	x-ray (2.50 Å)	[43]	1HBJ	2001
Torpedo californica	Rivastigmine complex	x-ray (2.20 Å)	[46]	1GQR	2001
Torpedo californica	Mf268 complex	x-ray (2.70 Å)	[35]	1OCE	1998
Torpedo californica	Sarin complex (aged)	x-ray (2.60 Å)	[32]	1CFJ	1999
Torpedo californica	Soman complex (aged)	x-ray (2.20 Å)	[32]	1SOM	1999
Torpedo californica	Tacrine complex	x-ray (2.80 Å)	[30]	1ACJ	1993
Torpedo californica	m-(N,N,N-trimethylammonio)-2,2,2-trifluoroacetophenone complex	x-ray (2.80 Å)	[27]	1AMN	1996
Torpedo californica	Vx complex	x-ray (2.20 Å)	[25]	1VXR	1999
Torpedo californica	Vx complex (aged)	x-ray (2.40 Å)	[25]	1VXO	1999

Table A2.2 – Summary of acetylcholinesterase structures on hold (Brookhaven Protein Data Bank, August 2002).

Esterase source	Comment	Technique	Associated publication	PDB code	Date
Mus muculus	Fasciculin-II complex	x-ray	-	1KU6	Jan 2002
Torpedo californica	(+)-Huperzine A	x-ray	[48]	1GPK	Nov 2001
Torpedo californica	Huperzine B	x-ray	[48]	1GPN	Nov 2001
Not disclosed	Diisopropyl-phosphoryl enzyme with 1,7-heptylene-bis-N,N'-syn-2-pyridiniumaldoxime	theory	-	1JGA	June 2001
Not disclosed	Diisopropyl-phosphoryl enzyme with 1,3-propylene-bis-N,N'-syn-4-pyridiniumaldoxime	theory	-	1JGB	June 2001
Not disclosed	(S,S)-(-)-BIS(10)-Huperzine A complex	x-ray	-	1H22	July 2002
Not disclosed	(S,S)-(-)-BIS(12)-Huperzine A complex	x-ray	-	1H23	July 2002

Acetylcholinesterase Species Homology

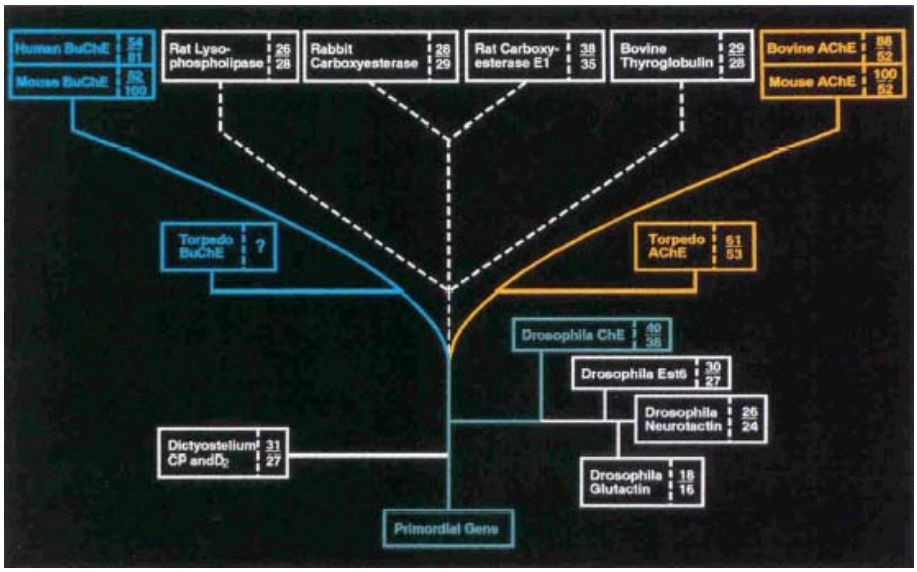

Figure A2.1 – Sequence relationships of proteins showing sequence identity to acetylcholinesterase: numbers reflect the fractional amino acid identities with mouse AChE (top) and BuChE (bottom) [22].

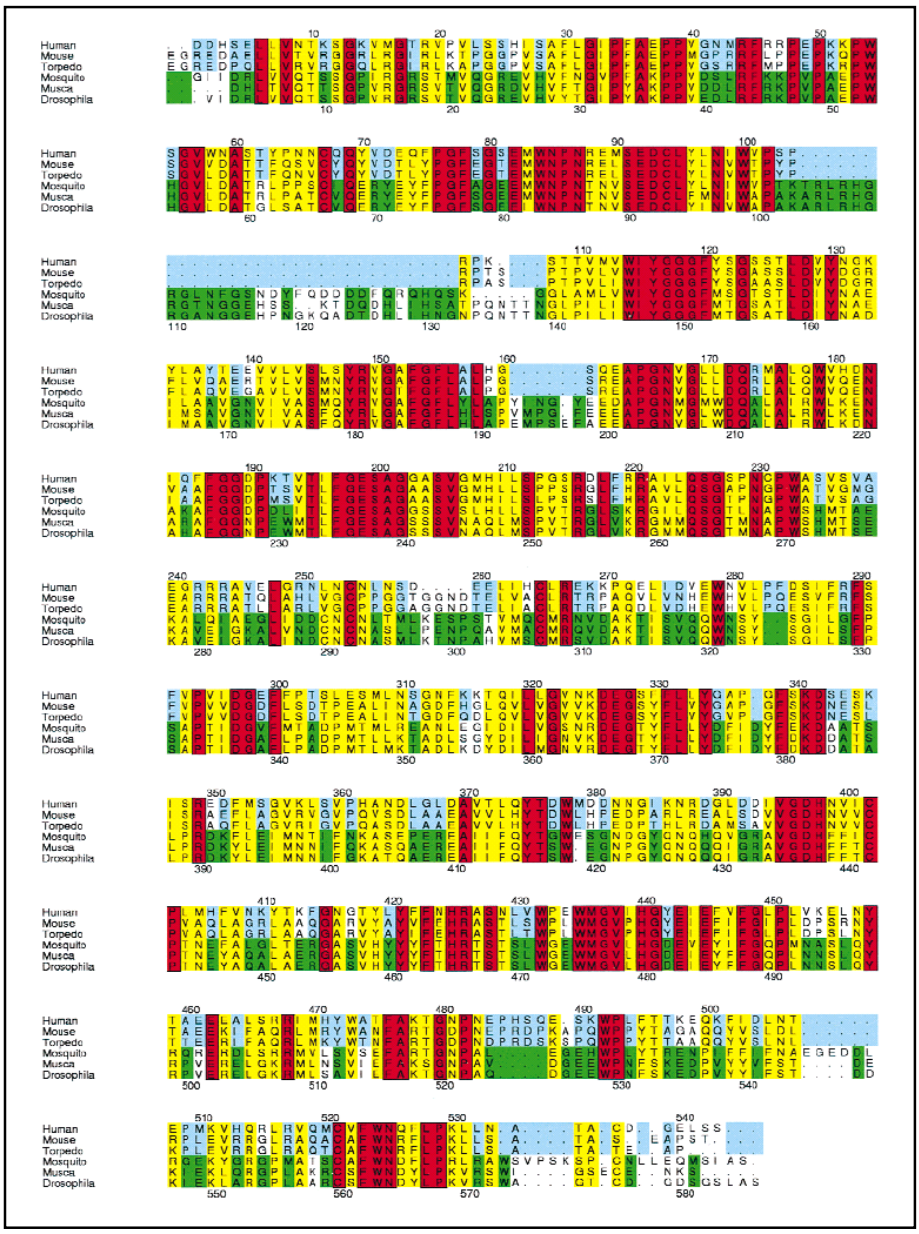

Figure A2.2 – Acetylcholinesterase species homology: comparison of three vertebrate and three insect acetylcholinesterase sequences. Insect/vertebrate identity is shown in red, insect/vertebrate similarity in yellow, insect only identity or similarity in green, and vertebrate only identity or similarity in blue. *Torpedo californica* numbering is shown above and *Drosophila melanogaster* numbering is shown below [38].

Appendix 3

Acetylcholinesterase Inhibitors

Nerve Agents:

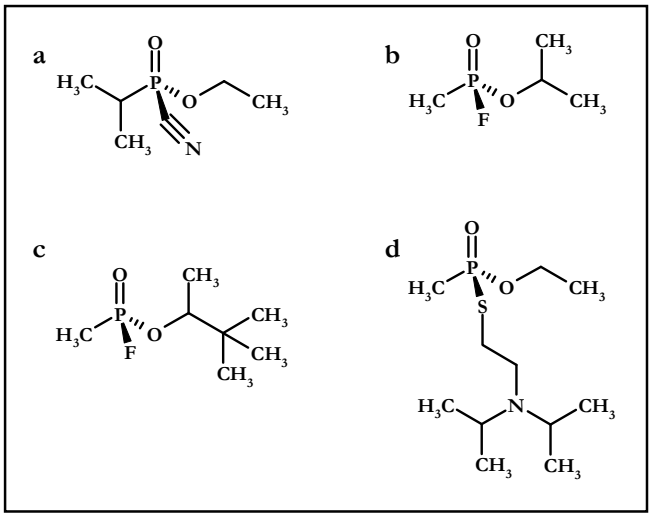

Figure A3.1 – Organophospahte nerve agents: tabun (a), sarin (b), soman (c), VX (d).

Pesticides:

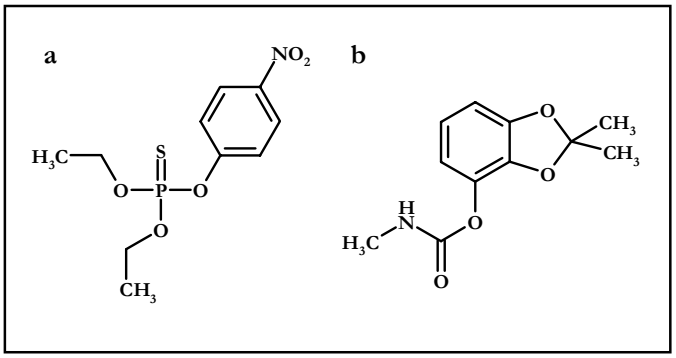

Figure A3.2 – Pesticides targeting acetylcholinesterase: parathion, an organophosphate (a), Bendiocarb, a carbamate (b).

Therapeutics:

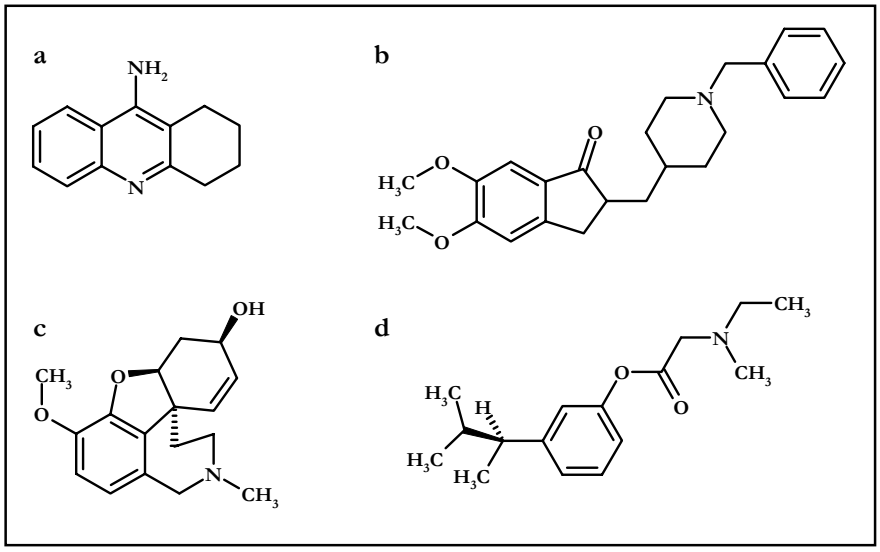

Figure A3.3 – Acetylcholinesterase inhibitors used in therapeutics: tacrine (a) donepezil (b) galanthamine (c) rivastigmine (d)

Other compounds discussed in the text:

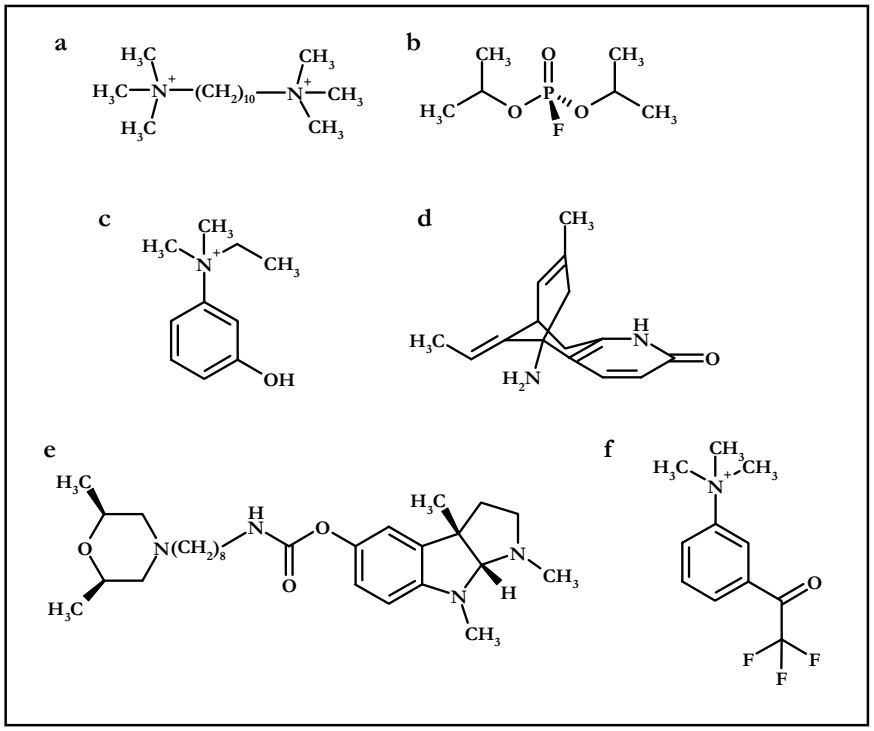

Figure A3.4 – Additional acetylcholinesterase inhibitors discussed in the text: decamethonium (a) DFP (b) edrophonium (c) (-)-Huperzine A (d) Mf268 (e) and TMTFA (f)

Appendix 4

^{13}C Spectra

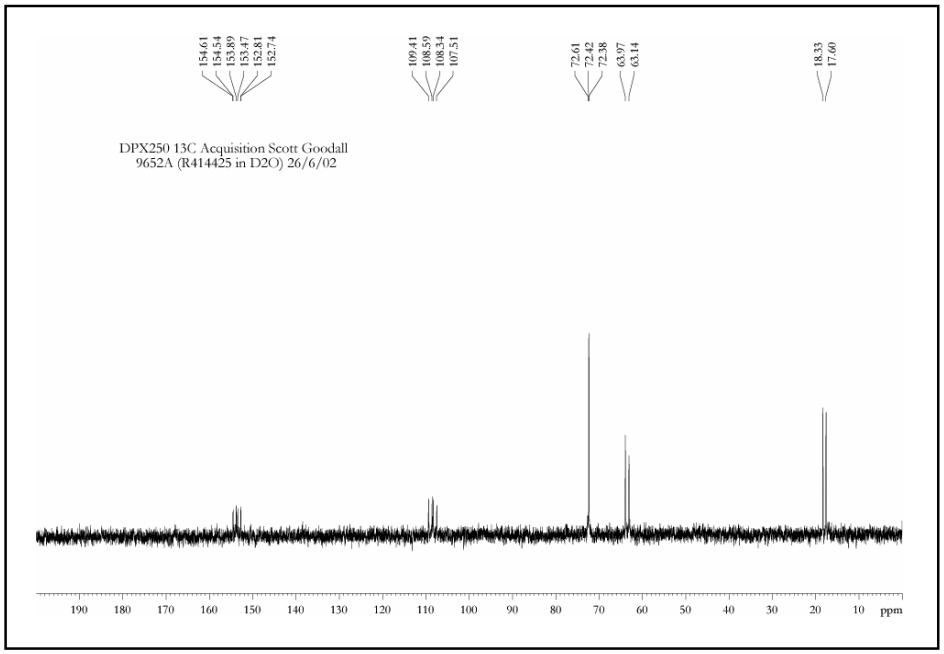

Figure A4.1 – ^{13}C solution NMR spectrum (63MHz) of $^{13}C_5$-R414425 in D_2O.

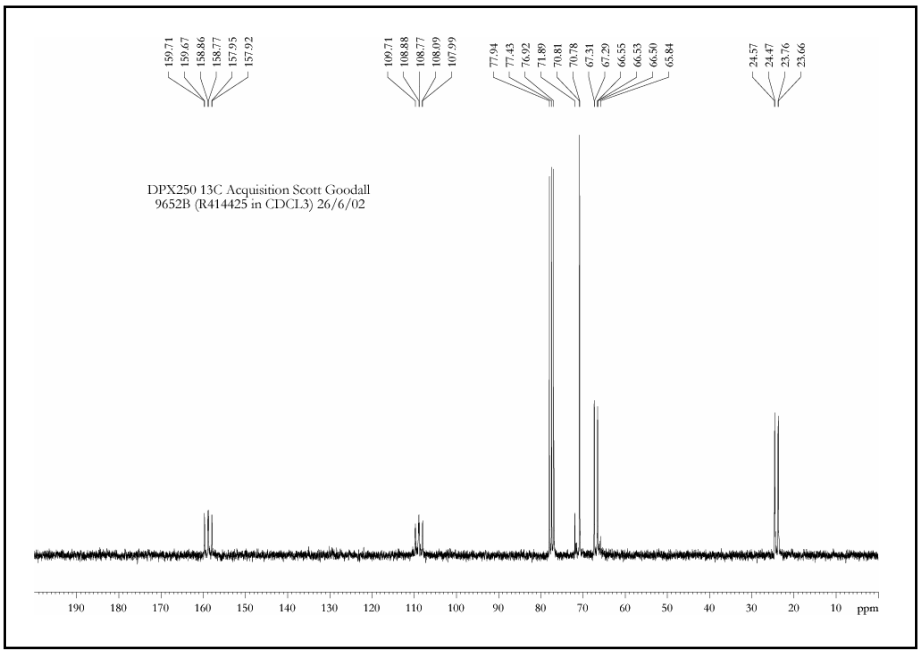

Figure A4.2 – ^{13}C solution NMR spectrum (63MHz) of $^{13}C_5$-R414425 in $CDCl_3$.

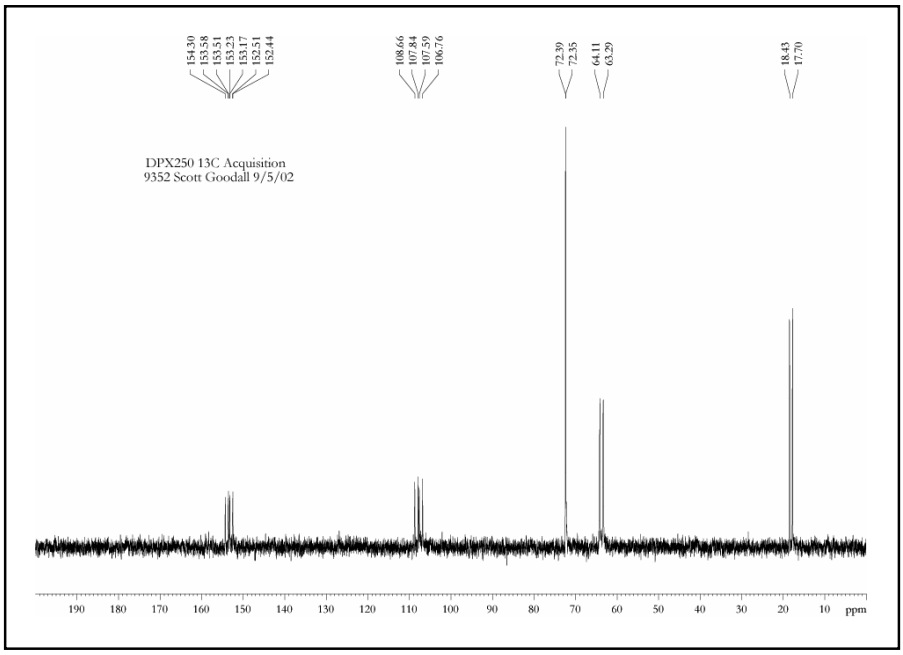

Figure A4.3 – ^{13}C solution NMR spectrum (63MHz) of $^{13}C_5$-R414983 in D_2O.

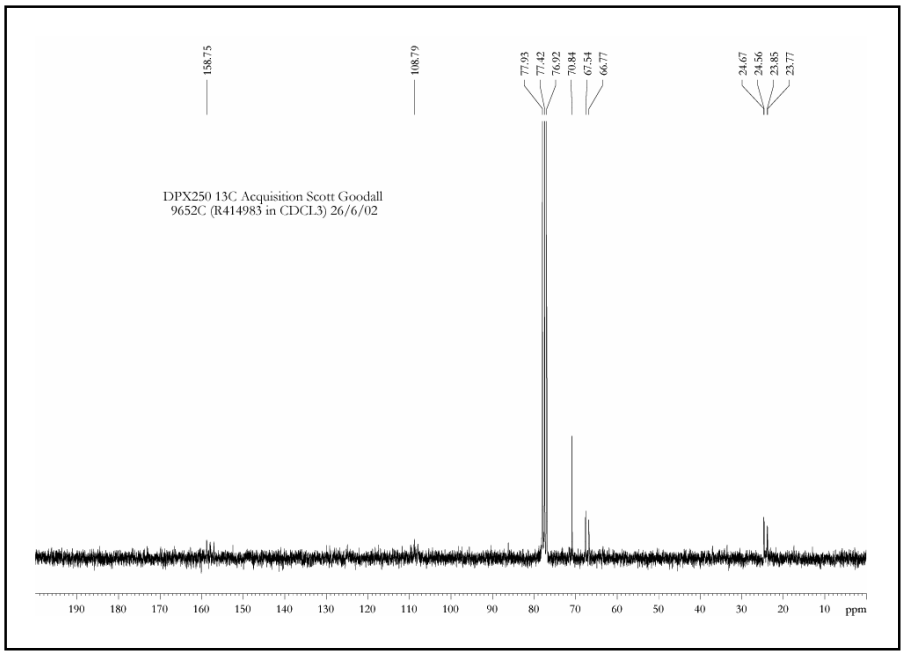

Figure A4.4 – ^{13}C solution NMR spectrum (63MHz) of $^{13}C_5$-R414983 in $CDCl_3$.

^{19}F Spectra

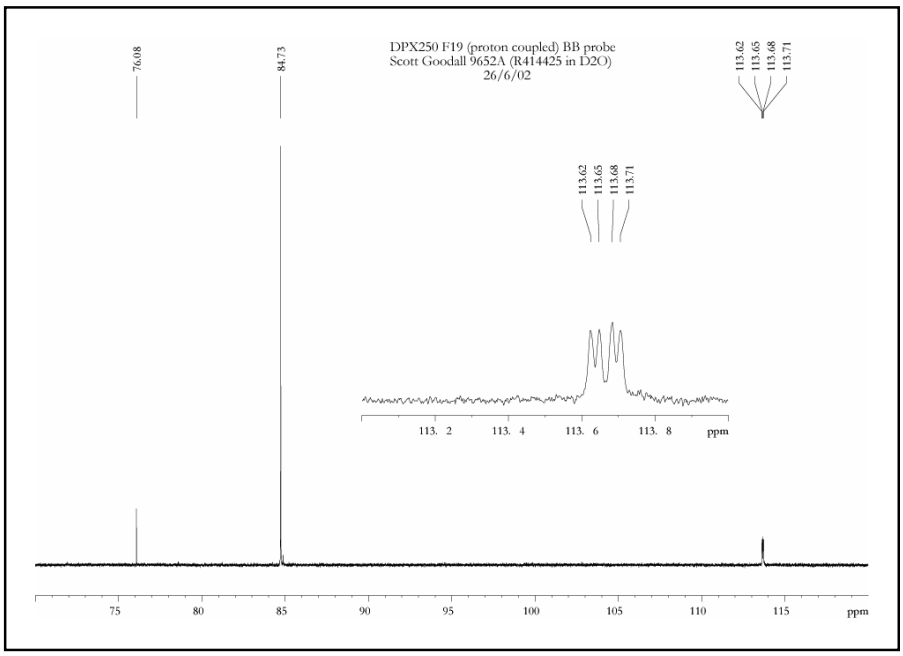

Figure A4.5 – ^{19}F solution NMR spectrum (235MHz) of $^{13}C_5$-R414425 in D_2O.

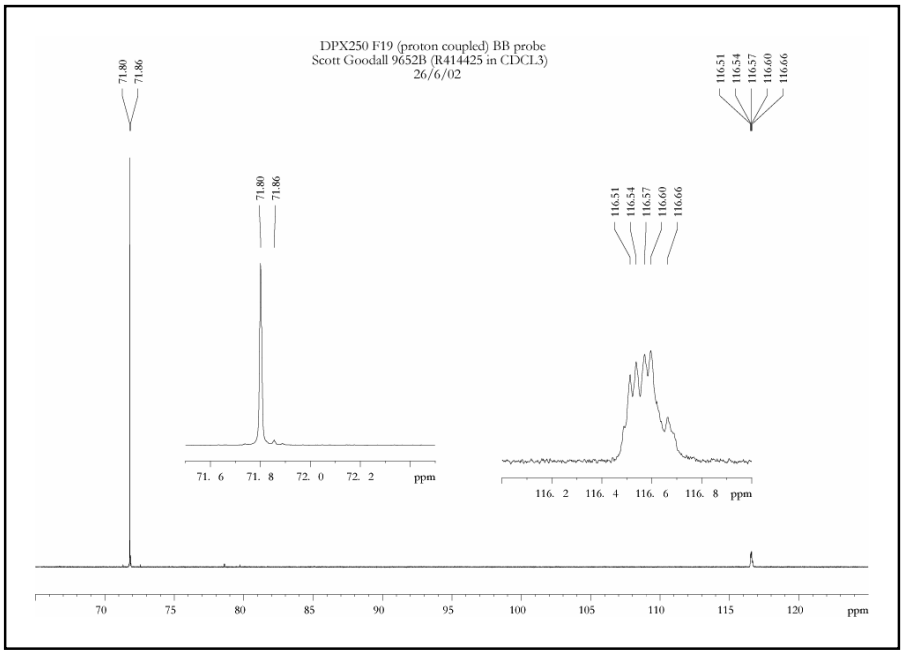

Figure A4.6 – ^{19}F solution NMR spectrum (235MHz) of $^{13}C_5$-R414425 in $CDCl_3$.

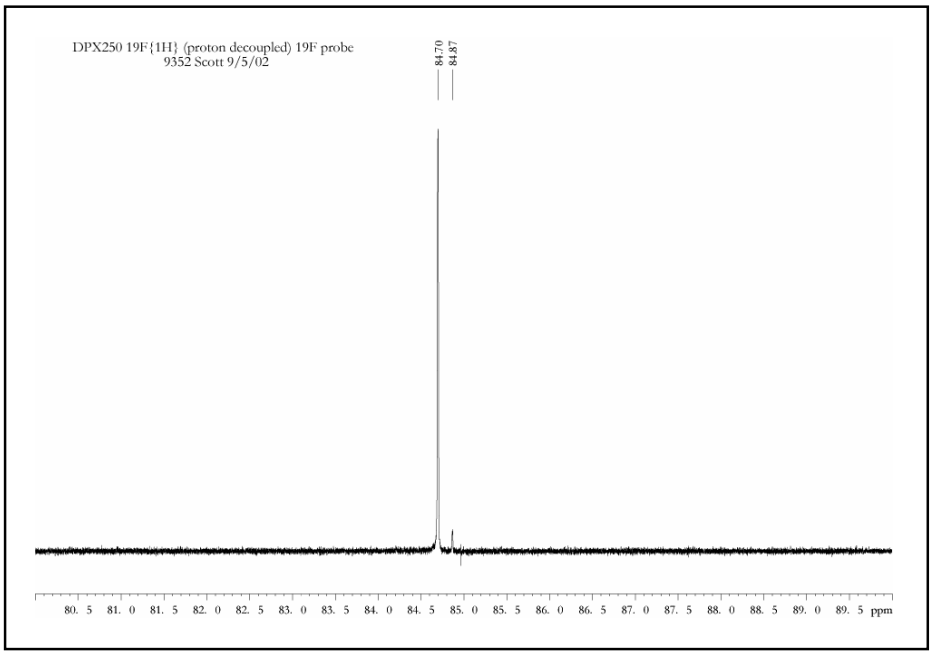

Figure A4.7 – ^{19}F solution NMR spectrum (235MHz) of $^{13}C_5$-R414983 in D_2O.

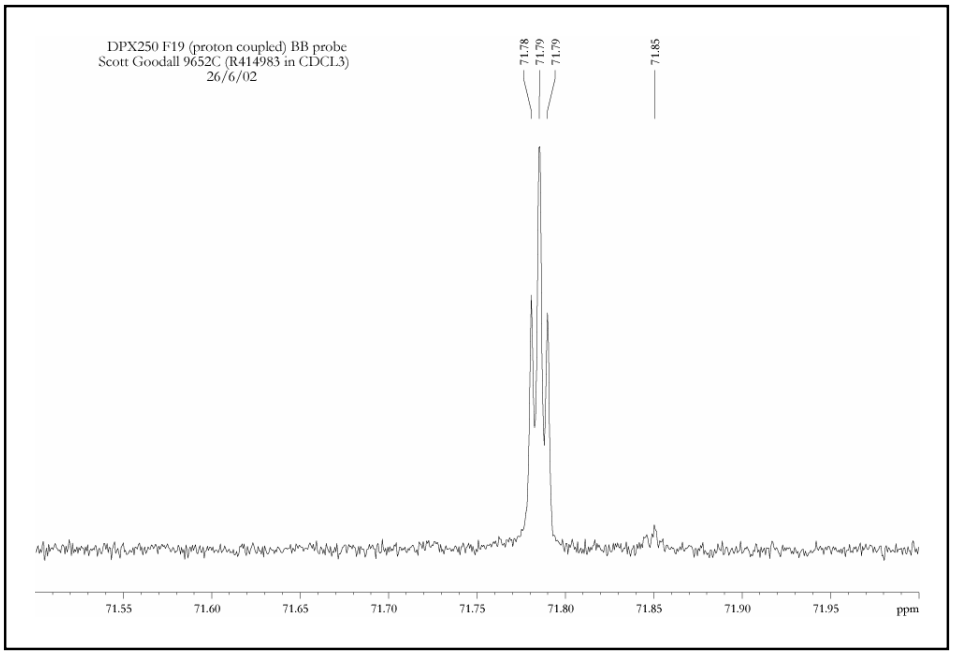

Figure A4.8 – ^{19}F solution NMR spectrum (235MHz) of $^{13}C_5$-R414983 in $CDCl_3$.

Appendix 5

Error Analysis

Rotational resonance experiments:

The uncertainty in any point of an NMR spectrum may be quantified by the root mean square deviation (RMSD) of the spectral noise (n). The plotted values used in the estimation of dipolar couplings are derived by addition of the integral areas for each peak in the spin pair under investigation. In order to estimate an error for the integrated area, it may by assumed that the number of points used to define a peak (N_p) can be related to the spectral width (Ω), the total number of points defining the spectrum (N_t) and the equivalent peak width (W):

$$N_p = \frac{W N_t}{\Omega} \qquad \text{Equation A5.1}$$

For simplicity, the peak width (W) may be approximated to that of an equivalent square (i.e. with the same integrated area) which is related to the full width at half height (L):

$$W = \frac{1}{2}\sqrt{\frac{\pi}{\ln 2}}\, L \qquad \text{Equation A5.2}$$

The statistical error (σ) in the area of a single peak as a result of spectral noise is then:

$$\sigma = \frac{n W}{\sqrt{N_p}} \qquad \text{Equation A5.3}$$

$$\sigma = \frac{\sqrt{N_p}\, \Omega\, n}{N_t} \qquad \text{Equation A5.4}$$

The error (σ_A) in net magnetisation (I_Z-S_Z) may be described in relation to the errors in the two areas (σ_I and σ_S) from which it is comprised:

$$\sigma_A = \sqrt{\sigma_I^{\,2} + \sigma_S^{\,2}} \qquad \text{Equation A5.5}$$

Since the linewidths, spectral width and acquisition length remain the same throughout each distance measurement the error arising from the noise is therefore identical for each data point (on an absolute, rather than proportional basis). Normalising the data with respect to the initial time point does not introduce a further error, it may be considered as a mathematical transformation necessary for the analysis software.

The level of signal to noise is lowest in experiments on the protein/inhibitor complex. As an example to demonstrate the spectral noise is not limiting in the determination of accurate internuclear distances, using the data for the quinoline methylene/2-methyl distance measurement (Section **Error! Reference source not found.**) provides an error in net magnetisation, in normalised units, of approximately $\pm$ 0.02 (errors in the initial point are lower, since the data from three time points are combined).

A number of assumptions are necessary in this calculation, such as the accurate knowledge of the linewidths, the appropriateness of approximating the peak to an equivalent square and that the processing of data does not introduce further errors. However, it is clear from the plotted results that data spread is generally low (exceptions are a single point in Figure 4.15 and two points in Figure 4.18), deviations from the fitted exchange curve match an oscillatory profile (most likely due to secondary couplings) and are thus not due to statistical variations.

REDOR experiments:

As stated previously, the statistical error (σ) in the area of a single peak as a result of spectral noise (n) is:

$$\sigma = \frac{\sqrt{N_p}\ \Omega\, n}{N_t} \qquad \text{Equation A5.4}$$

Each data point for a REDOR experiment represents the proportion of dephasing observed (A), determined from the integral intensities of the dephased (S) and non-dephased spectra (S_0). Both S and S_0 are considered as having errors.

Expanding Equation 5.5 from Chapter 5:

$$A = \frac{\Delta S}{S_0} = \frac{S_0 - S}{S_0} = 1 - \frac{S}{S_0} \qquad \text{Equation A5.6}$$

$$\sigma_A{}^2 = \left(\frac{\partial A}{\partial S}\right)^2 \sigma_S{}^2 + \left(\frac{\partial A}{\partial S_0}\right)^2 \sigma_{S_0}{}^2 \qquad \text{Equation A5.7}$$

$$\sigma_A{}^2 = \left(-\frac{1}{S_0}\right)^2 \sigma_S{}^2 + \left(\frac{S^2}{S_0{}^4}\right) \sigma_{S_0}{}^2 \qquad \text{Equation A5.8}$$

As both the dephased and non-dephased spectra are acquired with identical spectral width and acquisition length on the same instrument, the noise level in each spectrum should be comparable (i.e. $\sigma_S = \sigma_{S0} = \sigma$):

$$\sigma_A{}^2 = \frac{1}{S_0{}^2}\left(1 + \frac{S^2}{S_0{}^2}\right)\sigma^2 \qquad \text{Equation A5.9}$$

Using Equation A5.5:

$$\sigma_A{}^2 = \frac{1}{S_0{}^2}\left(1 + (1 - A)^2\right)\sigma^2 \qquad \text{Equation A5.10}$$

$$\sigma_A = \frac{\sigma}{S_0}\sqrt{1 + (1 - A)^2} \qquad \text{Equation A5.11}$$

Two additional factors must be included due to method of data manipulation. The RMSD noise is measured from a single spectrum in the series. However, a spectrum for the protein background is subtracted from a spectrum for the protein with inhibitor to create a value for S or S_0 (increasing noise by $2^{½}$), and three sets of such data were acquired (decreasing noise by a factor of $[1/3^{½}]$).

On this basis, the final data point used for determination of the 2-methyl/trifluoromethyl distance incorporates an error of less than ± 2% as a result of spectral noise.